THE MARMOUSI2 MODEL, ELASTIC SYNTHETIC DATA, AND AN ANALYSIS OF IMAGING AND AVO IN A STRUCTURALLY COMPLEX ENVIRONMENT

A Thesis

Presented to

the Faculty of the Department of Geosciences

University of Houston

In Partial Fulfillment

of the Requirements for the Degree

Master of Science

By

Gary Stuart Martin

May 2004

THE MARMOUSI2 MODEL, ELASTIC SYNTHETIC DATA, AND AN ANALYSIS OF IMAGING AND AVO IN A STRUCTURALLY COMPLEX ENVIRONMENT

Gary Stuart Martin

APPROVED:

Dr. Kurt Marfurt

Dr. Hua-Wei Zhou

Dr. Fred Hilterman

Dr. Chuan Yin

Dean, College of Natural Sciences and Mathematics

ACKNOWLEDGEMENTS

There have been many contributors to this project and I wish to thank everyone involved for their support, encouragement, and technical assistance. My thanks go to Aline Bourgeois at the Institut Français du Pétrôle who provided an initial dataset from which to begin construction of Marmousi2. Don Larson at GX Technology Corporation deserves a special mention. His technical assistance throughout has been invaluable, and his programming efforts to customize GXII to use the shear wave and density functions enabled the model to contain the desired complexity. My appreciation also goes to the management of GX Technology for their support of my efforts, and for the use of company algorithms and facilities. John Faragher, John Crowther, Susan Collins, and Mohamed Dolliazal, all from GX Technology also deserve my thanks for their technical contributions. Dr. Robert Wiley at the University of Houston warrants a special mention for his work which involved the setup and execution of the elastic modeling using the Sun cluster. He has also been involved with the storage, duplication, and distribution of data copies. My appreciation also goes to Cory Hoelting at the University of Houston for his assistance with the numerical modeling and other various tasks. This work would not have been possible without the contributions of my committee, and special thanks are due to Dr. Kurt Marfurt and Dr. Fred Hilterman. Last, but certainly not least, my deepest gratitude goes to my wife Rebecca and my daughter Kate who have had to endure many lonely evenings and weekends over the past three years.

THE MARMOUSI2 MODEL, ELASTIC SYNTHETIC DATA, AND AN ANALYSIS OF IMAGING AND AVO IN A STRUCTURALLY COMPLEX ENVIRONMENT

An Abstract of a Thesis

Presented to

the Faculty of the Department of Geosciences

University of Houston

In Partial Fulfillment

of the Requirements for the Degree

Master of Science

By

Gary Stuart Martin

May 2004

ABSTRACT

The reliability of AVO analysis is well established in relatively simple structural areas, but there remains some doubt as to the applicability of the technique in areas of complex velocity structure. To study this problem, I have created a 2D synthetic numerical model containing realistic hydrocarbons in a variety of structural settings. The new model, Marmousi2, is based on the structure and velocity of IFP's acoustic Marmousi model, but has been extended in width and depth, and is fully elastic.

High frequency, high fidelity elastic modeling was performed using state of the art modeling code and computational resources. Synthetic streamer, OBC, and VSP multi-component shot records were collected, including offsets up to 17km. Analysis of the data indicates that it is suitable for a wide variety of geophysical research including conventional imaging, AVO analysis, multiple attenuation, multi-component imaging, inversion, *etc.* The model and dataset have been made available to other researchers throughout the world.

Using a marine streamer subset, I applied some basic processing and surface multiple attenuation. I imaged the data with a suite of imaging algorithms using the known velocity model. The complex nature of the velocity dictates that for a good overall solution prestack depth imaging methods are required. The wavefield prestack imaging method produced the most impressive result.

In complex areas prestack imaging and AVO analysis are inextricably linked since more simple methods such as NMO and stacking are not sufficient to produce meaningful data. Events must be well imaged on the migrated stack section before AVO analysis is possible due to the much lower signal to noise ratio present in the image

gathers. The Marmousi2 hydrocarbons provide a challenge for both imaging and AVO analysis, due to their small scale, velocity complexity, and in some cases very small acoustic impedance contrasts with the surrounding rocks. As the complexity increases more rigorous imaging methods are required to identify the bodies on the stacked image, and corresponding image gathers. The well imaged events generally show the AVO expected from modeling.

The preliminary imaging and AVO analysis I have performed will serve as the 'baseline' for forthcoming studies by other researchers.

CONTENTS

FIGURES

TABLES

1. Introduction

This study is composed of two main goals, which have been simultaneously achieved. The initial objective was to investigate the impact of complex structure and imaging methodology on the reliability of AVO analysis. To do such a quantitative analysis, I needed a high quality fully elastic synthetic dataset on which to apply the proposed analysis. Working with colleagues at the Allied Geophysical Laboratory (AGL), Los Alamos National Laboratory, Lawrence Livermore National Laboratory, and industry partners, I expanded my scope to generate a 2D model that would allow calibration of modern seismic imaging and inversion technologies by the scientific community at large.

Some may argue that the value of 2D data for research is inappropriate, and that all new efforts should be targeted towards 3D. However, there are many reasons why 2D high fidelity synthetic data is still very attractive. The computational requirements for calculating an elastic dataset for a 3D model, of sufficient size, frequency bandwidth, and computational grid size are still effectively out of reach, at least without huge financial support. 3D models are also very challenging to construct if many layers and complexity are required. The generated data volume is large, which restricts use by many researchers who have limited storage and processing capabilities, and prohibits rapid testing of new concepts. In contrast, 2D models are relatively easy to construct, the data may include high frequencies and small cell sizes, and most researchers can adequately process and image the data on desktop workstations. In addition, most algorithmic development is usually initiated with 2D and later expanded to the 3D case.

The variation of seismic amplitude with offset (AVO) or angle (AVA) is widely used as a direct hydrocarbon indicator. It is based upon the physical changes to wave

propagation that occur when seismic waves travel through media of varying properties. The hydrocarbons present in the rocks affect the physical properties of the medium such that the recorded responses (when correctly processed and organized) can indicate their presence. The reliability of AVO is well established in relatively simple structural areas, and has become a workhorse of seismic exploration, particularly in Tertiary basins. However, in structurally complex areas there remains some doubt as to whether AVO is applicable due to the various imaging problems, and also because of amplitude variations that can be caused by effects such as focusing and defocusing that may mask, distort, or destroy the AVO signature. This study will attempt to quantify whether AVO is applicable in complex geological provinces where we know the exact velocity/depth model and have perfect amplitude recording, using standard and state of the art imaging tools.

The choice of a dataset presented several problems. Firstly, real data were rejected since the answer would remain ultimately unknown, and therefore it is impossible to test the efficacy of imaging algorithms, or to know whether any processed AVO signature is indeed related to the hydrocarbons that may or may not be present in the earth. Secondly, there is a paucity of publicly available, structurally complex, elastic models and synthetic data available. Given that the analysis of AVO is an objective, models based on raytracing, and acoustic finite difference methods must be rejected, since AVO is dependent upon accurate simulation of p-wave and s-wave mode conversion, head wave generation, interbed multiples, and interface waves. Finally, our team recognized and wished to emulate the success of the Marmousi model created by the French Petroleum Institute (IFP), as described by Versteeg, 1994. The much utilized Marmousi model (*e.g*. Ehinger *et al.*, 1996, Zhu and Lines, 1998, Alkhalifah, 2000, Hill,

2001, *etc*.) is an acoustic finite difference model and dataset that possesses complex structure and velocity variations. It therefore made sense for me to generate the 'next generation' of the IFP Marmousi model and synthetic dataset, which is now named Marmousi2 and forms the basis of this thesis.

Funding for the elastic model simulation was provided by the United States' Department of Energy's 'Next Generation Modeling and Imaging Project' coordinated through Los Alamos National Laboratory. The model and dataset constitute a work product for this project.

Our goal was to generate and make available the model and dataset for other researchers. This thesis, which is in complete form on the AGL website, and portions submitted to geophysical journals for publication, will serve as the baseline evaluation of imaging and AVO analysis for the new data. The true measure of my success will be a suite of scientific papers based on Marmousi2 that show significant improvement in modeling, imaging, and AVO analysis over what I present here.

The construction of the Marmousi2 model is thoroughly detailed in Chapter 2. The synthetic data acquisition is discussed and the raw results are presented in Chapter 3. Chapters 4 and 5 describe the processing, imaging and AVO analysis performed using a marine 6km streamer cable subset of the data.

2. The Marmousi2 Elastic Model

2.1 Rebuilding the Marmousi Structural Model

I created the Marmousi2 model by first reconstructing the original Marmousi model. This was then extended and modified. I acquired assistance from Aline Bourgeois at the Institut Français du Pétrôle (French Petroleum Institute, or IFP), and she supplied the initial files, which included the property grids (P-wave velocity and density), a “facies” grid (basically a grid containing the layer number), a set of SEP horizon files, and a table of layer properties. The original model was generated in Sierra software, but the specific Sierra horizon files have since been lost, and as such I had to recreate the model from the gridded representations of the model. The familiar Marmousi model and its P-wave velocity are shown in Figure 2.1.

I created the Marmousi2 model using GX Technology Corporation’s GXII modeling software, which allows the construction of 2D models from segments of horizons. The model definition required the reconstruction of horizon segments from the gridded (SEP format) horizon files.

First, I converted the binary SEP format horizon files into ASCII format using standard Unix commands (od), and then reformatted them into standard column delimited format using additional Unix tools such as awk and sed. An awk script was used to reformat the files into GXII standard import format, and then I inserted the horizon names using sed. I then concatenated the files to produce a single ASCII file containing all of the horizons.

Many hours of manual editing were necessary in GXII in order to construct the model. This results from the differences in the way the original model was defined

compared to the method used by GXII. Figure 2.2 shows how the horizons were modified. The edits were especially numerous for the faults, the waterbottom, and the base salt unconformity. In addition to the manual editing I smoothed each horizon in order to remove the granularity of the original gridding (the SEP horizon files are regular grids with a 4m spacing). This was performed in GXII. The effects of the smoothing can be seen in Figure 2.2 and 2.3.

2.2 Structural Model modification

I have modified the original model to ensure that the model fulfills its objectives.

- Physical expansion. The sizes of the two Marmousi models are shown in Table 2.1, and graphically in Figure 2.4. The original Marmousi model is located close to the center of Marmousi2.

	Marmousi	**Marmousi2**
Line length (X)	0 - 9.2 km	0 - 17 km
Depth (Z)	0 - 3 km	0 - 3.5 km

Table 2.1 Marmousi model sizes

- Extension of horizons. I extended the horizons in the original model to fit the expanded model. Forty-one new horizons were introduced, bringing the total number of horizons to 199. The horizons were expanded with two main aims. The first was to reduce the structural complexity in the expanded area in order to produce a model with both structurally complex and structurally simple components. The second was to create a plausible geological expansion. The expanded model horizons are shown in Figure 2.4.

- Deep-water setting. In order to make the model more suitable for deep-water acquisition and processing, I modified the depth of the horizons, shifting them 468m deeper in order to place the waterbottom (previous average depth ~32m) to a depth of 500m. Later I straightened the horizon to make it perfectly flat, with a depth of 505m.

- Transition layers above the waterbottom. In order to reduce the "hard waterbottom" effect, I added two transitional layers above the original waterbottom. These layers are perfectly flat with thicknesses of 25m and 30m, creating a new waterbottom at a depth of exactly 450m, Figure 2.5.

- Traps. I introduced additional horizons in order to create new locations in which to insert hydrocarbons to the model. The hydrocarbons will be discussed in detail in section 2.4.

The structural elements of Marmousi2 are shown in Figure 2.6 and 2.7. Due to the geometry of Marmousi2 most of the figures contain considerable vertical exaggeration. Figure 2.6 shows the model horizons and P-wave velocity at true 1:1 scale.

Layer thickness was not changed from the original model, but a brief discussion of thickness is necessary in the context of seismic resolution. Figure 2.8 shows a small part of the model and highlights some layers and their approximate thickness. Typically the sediment layers have a thickness in the range of 20-100m, although minimum thickness ultimately approaches zero at pinchouts and truncations.

Seismic resolution is defined in terms of seismic wavelength, $\lambda = \frac{V}{f}$, where λ is the seismic wavelength, V is the velocity, and f is the dominant frequency.

Table 2.2 shows some values of seismic resolution for the shallow, middle depths, and deeper part of the model. A range of dominant frequencies are used for illustration.

	V (m/s)	f (Hz)	λ(m)
shallow	1800	20	90
		30	60
		40	45
		50	36
middle	3000	20	150
		30	100
		40	75
		50	60
deep	4000	20	200
		30	133
		40	100
		50	80

Table 2.2. Seismic resolution for different depths in the model and varying dominant frequency.

Table 2.2 and Figure 2.9 show that the model includes some events that will be individually distinguishable. However, the majority of reflection events will be composites consisting of the interference of more than one event in the earth model. Although the layering of the model is coarser than the real earth, the model events are realistic since most will be composites.

2.3 Defining the layer properties

The original Marmousi model was an acoustic model, *i.e.* it possessed compressional wave velocities (P-wave velocities) and densities (ρ). The Marmousi2 model is an elastic model and therefore must also possess shear wave velocities (S-

wave velocity). I determined the layer properties based upon the Marmousi P-wave velocity and by an assigned lithology.

The initial step was to assign lithologies to the layers. The Marmousi model was based upon real geology from the North Quenguela Trough in the Quanza Basin of Angola, and although the lithologies were not assigned in the model (except for salt and water), the lithologies are described (Versteeg, 1994). The section is primarily composed of shale units, with occasional sand layers. The core of the complex faulted area is an anticline that is composed of marl. An unconformity and a partially evacuated salt layer separate the marls from the deeper anticlinal units, which are also mostly shales with some sand.

I assigned lithology to Marmousi2 (Figure 2.7) using the following policy:

- The salt and water layers from the original model are preserved.
- The first two layers (transitional layers) are shale, and possess properties consistent with soft modern sediments.
- All layers containing hydrocarbons must be sand.
- The anticline above the salt is composed of marl (carbonate rich shales, defined in this model as 70% shale, 30% limestone).
- All other layers are either sand or shale, with the majority of layers being shale. The sand layers were picked out by assuming that sands are typically less dense than shale.

Regardless of the designated lithology, the layers were initially given an identical P-wave velocity to the original Marmousi model. The P-wave velocity is defined as

either a constant velocity or using a standard velocity gradient definition ($V = V_0+kZ$). It is assumed that actual velocities of the layers will remain unchanged by the increase in water depth, since velocity gradients account for compaction due to overburden loading (and thus water depth is irrelevant). I adjusted the velocity definitions accordingly using the following equation:

$$V_{0\ new} = V_{0\ old} - (k*468).$$

The gradients (k) are unchanged, but the intercepts at datum (Vo) values are reduced. The new layers were assigned P-wave velocities similar to the neighboring units.

I applied standard industry transforms to create shear wave velocities and densities for the layers. I applied the commonly used Greenburg and Castagna (1992) transforms for obtaining shear wave velocity from P-wave velocity, and Castagna *et al*'s (1993) "ARCO transforms" for obtaining the density from the P-wave velocity. These transforms (which are defined for water-wet sediments) are shown in Table 2.3, which also shows the values for the other lithologies in the model.

	Vp (m/s)	**Vs (m/s)**	**ρ (g/cm3)**
Water	1500	0	1.01
Sand	From Marmousi	Vs = 0.804Vp – 856	ρ = 0.2736Vp.261
Shale	From Marmousi	Vs = 0.770Vp – 867	ρ = 0.2806Vp.265
Salt	4500	2600	2.14
Limestone	From Marmousi	$Vs = 1.017Vp – 0.055Vp^2 – 1030$	ρ = 0.3170Vp.225

Table 2.3. Velocities and density for the lithologies

The P-wave velocity of the salt layer was reduced significantly from the value in the original model (5500m/s). I reduced the value to 4500 m/s, which is a more commonly-used velocity for salt. Correspondence with velocity modeling experts in Angola confirmed that the previous figure was probably too fast.

I calculated the properties for the marl units using the equations given above for shale and limestone. The marls are described as 70% shale, 30% limestone. The values for the marls were calculated using the Voight-Reuss-Hill method as described by Hilterman (2001):

$$\frac{1}{V_{SReuss}} = \frac{0.7}{V_{Sshale}} + \frac{0.3}{V_{Slimestone}}$$

$$V_{SVoight} = 0.7 * V_{Sshale} + 0.3 * V_{Slimestone}$$

$$V_S = \frac{V_{SReuss} + V_{Slimestone}}{2}$$

The Reuss and Voight methods produced almost identical values of S-wave velocity for the marls.

2.4 Adding hydrocarbons to the model

I introduced a series of hydrocarbon layers to the structural model. These are shown as red (gas) and green (oil) on Figure 2.10. They are distributed within the complex faulted zone at different depths, and also in the simple structure at the flanks. These layers vary in their size, shape, structural complexity, and hydrocarbon content, see Table 2.4.

- One shallow gas sand in a simple structural area (A)
- One relatively shallow oil sand in a structurally simple area (B)
- Four faulted trap gas sands at varying depths (C1, C2, C3, C4)
- Two faulted trap oil sands at medium to deep depths (D1, D2)
- One deep oil and gas sand anticlinal trap (E1, E2)

ID	Index	Feature Length (m)	Avg. Vertical Thickness (m)	Avg. Thickness (m)	Hydrocarbon Content
A	013_GAS	780	38	38	Gas
B	033_OIL	2940	40	40	Oil
C1	049_GAS	135	26	22	Gas
C2	051_GAS	133	55	45	Gas
C3	053_GAS	435	53	45	Gas
C4	071_GAS	340	75	60	Gas
D1	071_OIL	255	75	45	Oil
D2	071_OIL	540	49	38	Oil
E1	177_GAS	1395	50	50	Gas
E2	178_OIL	1890	42	42	Oil

Table 2.4. Dimensions of hydrocarbon layers

Gas and varying GOR oil have been introduced using standard fluid substitution techniques, performed by Geophysical Development Corporation's GDCMOD software.

I assigned each hydrocarbon bearing layer a single value for P-wave velocity by calculating the value at the average depth of the unit. This was necessary to simplify the fluid substitution calculations. Additional assumptions for all hydrocarbon layers are that all units are normally pressured, temperature is 200°F, mud weight is 10lb/gallon, water saturation is 30%, and the API is 30. The gas/oil ratio is expressed as cubic feet of gas per barrel at the surface (used/maximum).

ID	Fluid	Gas Oil Ratio	Thickness (m)	Depth (m)	Water Wet Sand			Hydrocarbon Charged Sand		
					Vp (ms)	Vs (m/s)	ρ (g/cc)	Vp (ms)	Vs (m/s)	ρ (g/cc)
A	GAS	-	38	1080	1753	553	1.92	1028	607	1.59
B	OIL	250/609	40	1700	1855	635	1.94	1640	652	1.85
C1	GAS	-	26	1250	2210	921	2.04	1770	988	1.77
C2	GAS	-	55	1300	2480	1138	2.10	2131	1209	1.86
C3	GAS	-	53	1150	2080	816	2.00	1584	881	1.72
C4	GAS	-	75	1900	3025	1576	2.21	2783	1645	2.03
D1	OIL	270/686	75	1900	3025	1576	2.21	2874	1604	2.14
D2	OIL	270/686	49	1900	3025	1576	2.21	2874	1604	2.14
E1	GAS	-	50	3000	4200	2521	2.44	4045	2564	2.36
E2	OIL	300/1100	42	3050	4200	2521	2.44	4123	2538	2.41

Table 2.5. Fluid substitution results

Table 2.5 shows the results of fluid substitution. Figure 2.11 shows that hydrocarbon substitution results in a drop of the P-wave velocity, a minor increase of the S-wave velocity, and a small decrease of the density. The Vp/Vs ratio and acoustic impedance values both decrease after fluid substitution. Comparison of the fluid substitution results for the anticlinal hydrocarbons and the original Marmousi model is shown in Table 2.6. It is clear that the original model possessed incredibly large changes in velocity and density that cannot be supported by fluid substitution, Figure 2.12. It is assumed that these extreme values were emplaced into the model to ensure a very strong reflectivity response for these units.

ID	Marmousi2 model						Marmousi model	
	Water Wet			Hydrocarbon Charged				
	Vp (ms)	Vs (m/s)	ρ (g/cc)	Vp (ms)	Vs (m/s)	ρ (g/cc)	Vp (ms)	ρ (g/cc)
E1	4200	2520.8	2.44	4045	2564	2.36	2700	1.80
E2	4200	2520.8	2.44	4123	2538	2.41	3230	2.05

Table 2.6. Marmousi and Marmousi2 hydrocarbon properties in layers E1 and E2 are very different. Fluid substitution cannot support such large changes in the properties of Marmousi at this depth.

2.4.1 AVO Responses

In order to ascertain what effect the substituted fluids would have I calculated synthetic AVO responses for each hydrocarbon unit. I used the University of Houston's Tips program to calculate the synthetic responses for a simple two layer model consisting of a shale overlying a sand. The P-wave velocity, S-wave velocity, and density for the shale, water saturated sand, and hydrocarbon saturated sand were entered for each unit. The appropriate depth, thicknesses, temperature, mud weight, water saturation, API, and GOR, for the sand were also entered. The program

calculated the responses shown in Figures 2.13 – 2.22. The figures show a velocity-density crossplot and the expected amplitude curves for both a gas and an oil saturated sand. An NMO corrected synthetic seismogram shows the expected CDP gather given a water saturated state and the hydrocarbon saturated state. A summary of the expected theoretical AVO responses is given in Table 2.7.

ID	Fluid	AVO response	Top	Base	X
A	GAS	A very bright spot. Large amplitudes at all offsets, moderate increase of amplitude with offset	trough	peak	no
B	OIL	A bright spot. Medium-large amplitudes at all offsets, no increase of amplitude with offset	trough	peak	yes
C1	GAS	No increase or decrease of amplitude with offset, higher amplitudes than water saturated state	trough	peak	yes
C2	GAS	Large increase of amplitude with offset	trough	peak	no
C3	GAS	Small increase of amplitude with offset	trough	peak	no
C4	GAS	Large increase of amplitude with offset	trough	peak	no
D1	OIL	Medium-large increase of amplitude with offset from almost zero amplitude at zero offset. Amplitudes represent a phase reversal compared to the water saturated state at zero offset	trough	peak	no
D2	OIL	Medium sized increase of amplitude with offset. Amplitudes represent a phase reversal compared to the water saturated state at zero offset	trough	peak	yes
E1	GAS	Large increase of amplitude with offset	trough	peak	yes
E2	OIL	Large increase of amplitude with offset from almost zero amplitude at zero offset	trough	peak	yes

Table 2.7. Predicted AVO responses for Marmousi2 hydrocarbons. X represents whether top and base amplitudes interfere (cross).

2.5 Other Features

The model also contains some sand units that should not be detectable by P-wave data alone. The units have identical P-wave and density values to the surrounding layers so that there is no P-wave impedance change. The shear wave values were

modified from the values given by the transforms so that it exhibits a small shear wave impedance change, Figure 2.23.

The complete set of properties for the layers is presented in Table 2.8. The model properties are shown graphically in Figures 2.24 – 2.29.

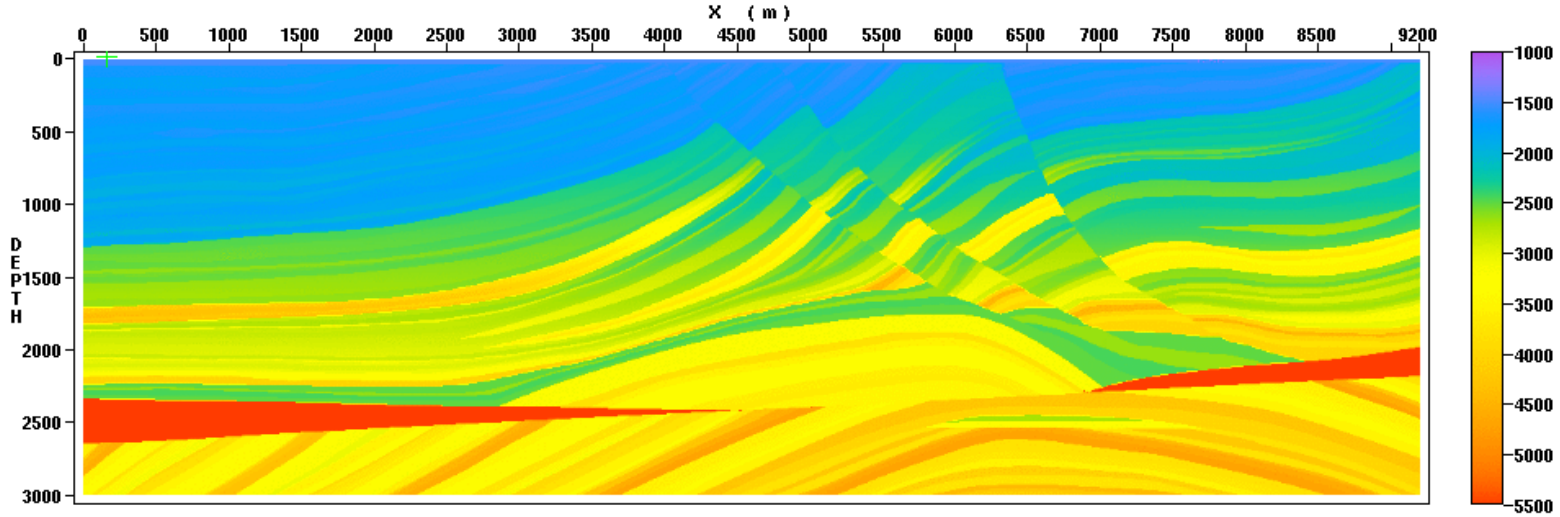

Figure 2.1. The original Marmousi model P-wave velocity. Model is shown to scale without vertical exaggeration.

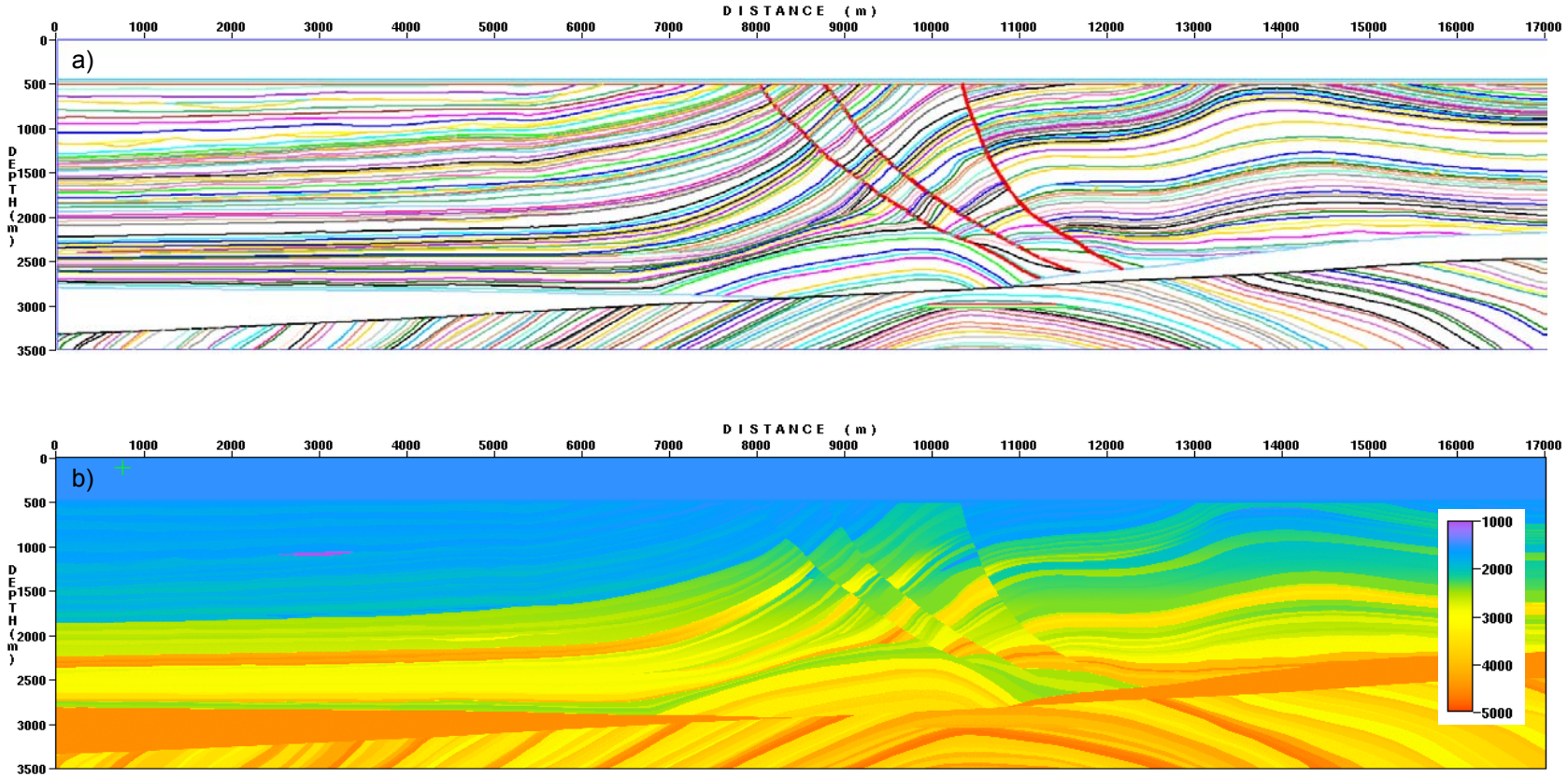

Figure 2.6. Marmousi2. a) model horizons, b) P-wave velocity. Model is shown to scale without vertical exaggeration.

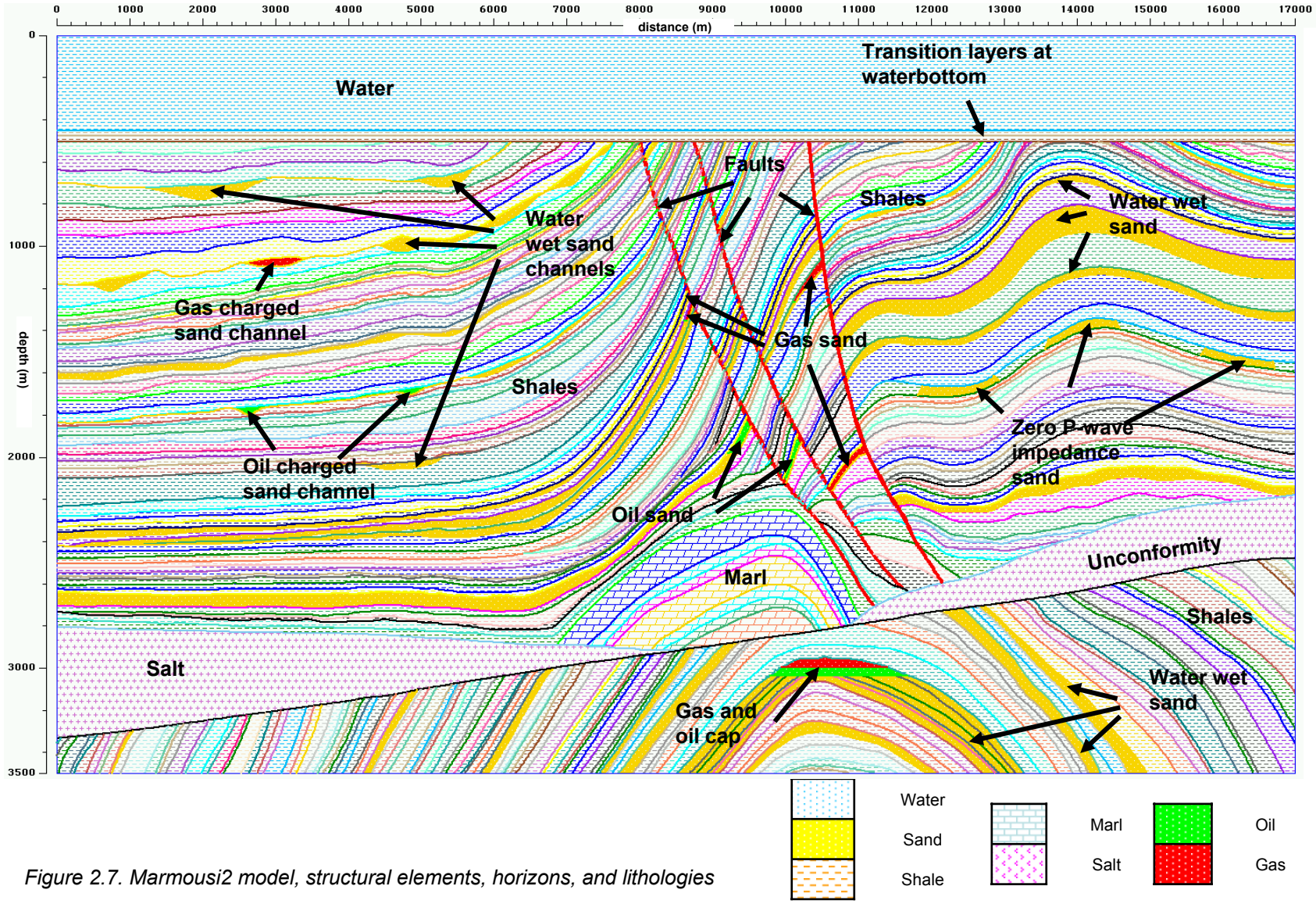

Figure 2.7. Marmousi2 model, structural elements, horizons, and lithologies

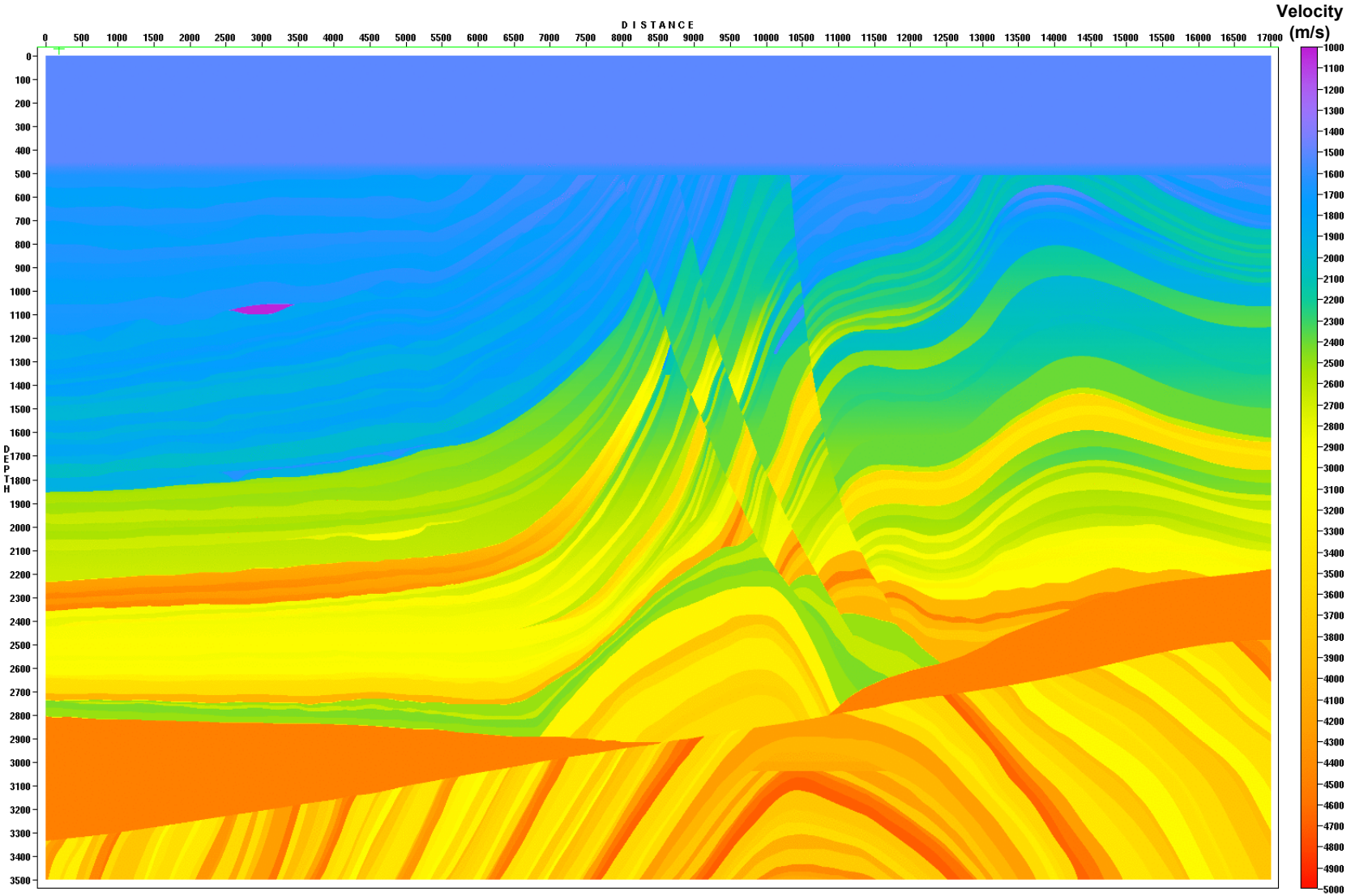

Figure 2.24. Marmousi2 P-wave velocity

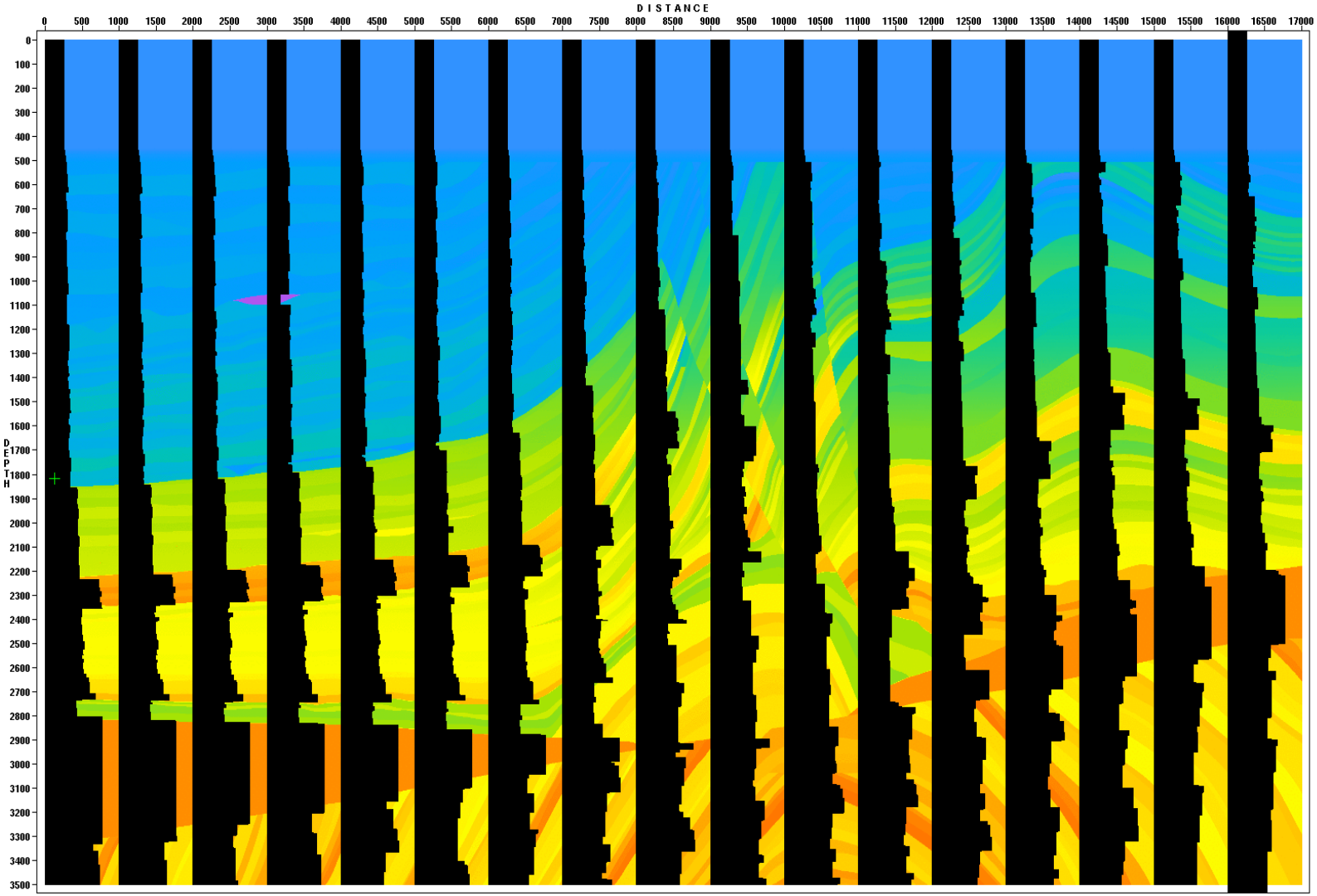

Figure 2.25. Marmousi2 P-wave velocity (m/s), columns overlaying the gridded model

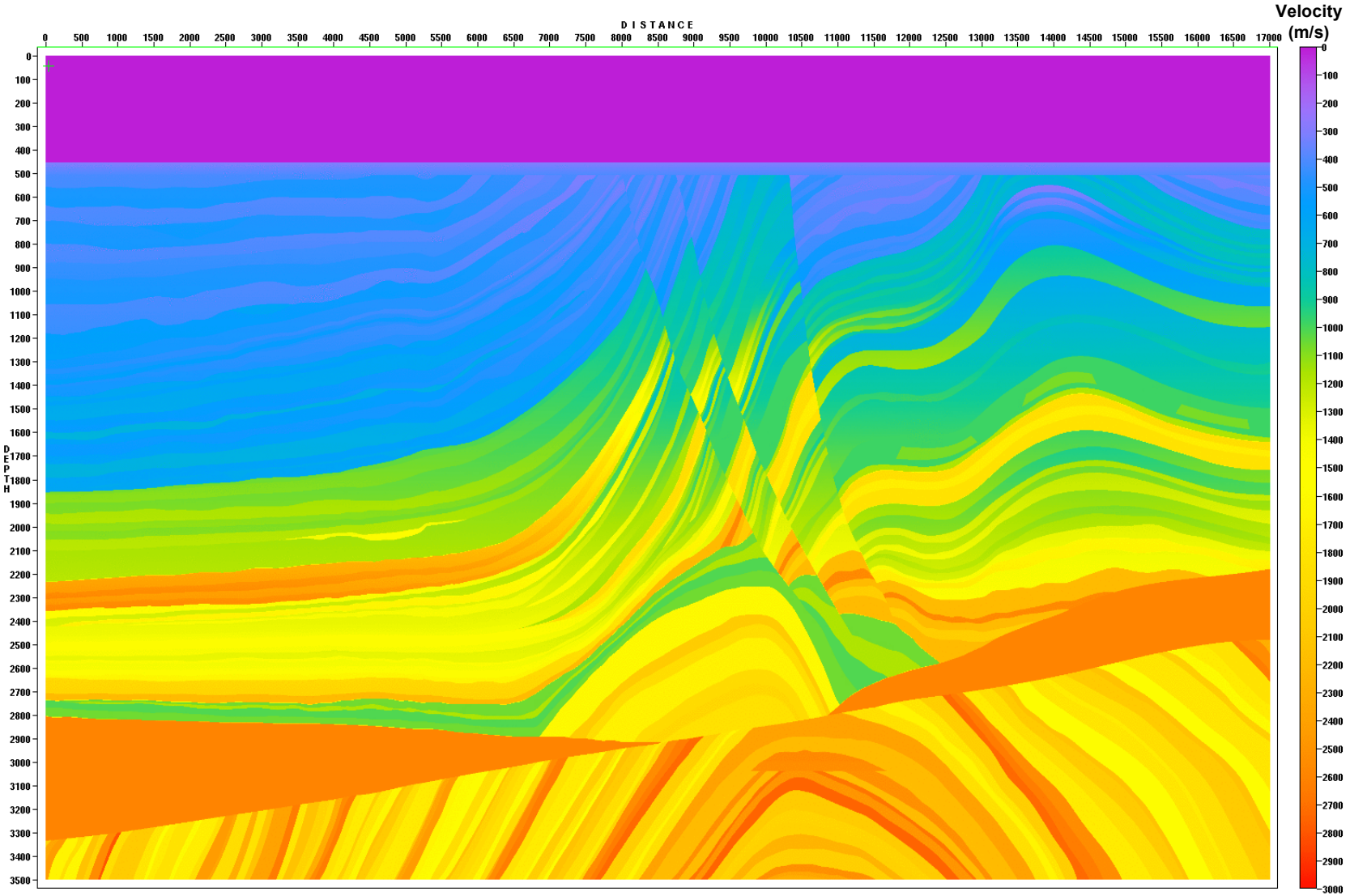

Figure 2.26. Marmousi2 S-wave velocity

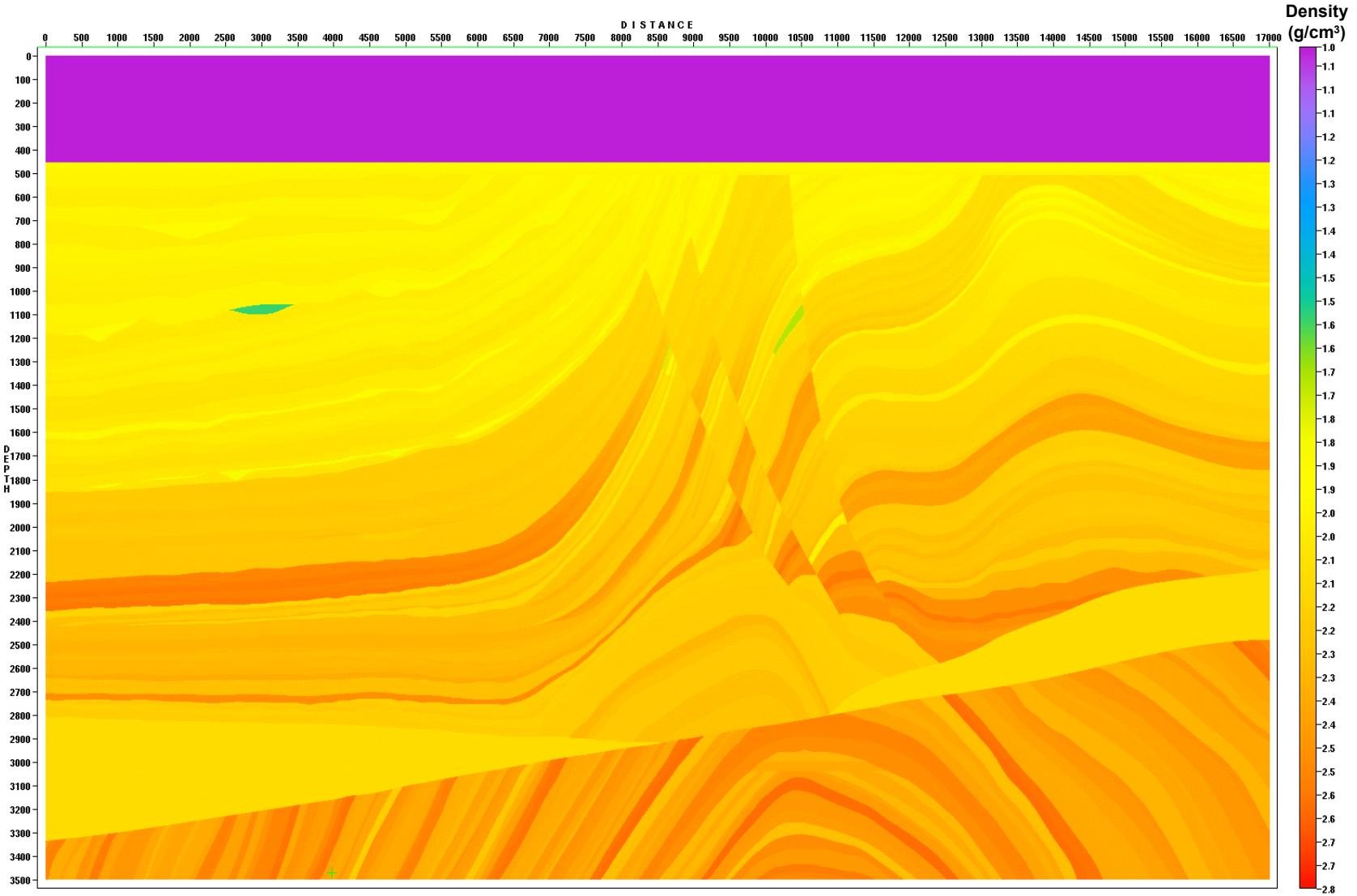

Figure 2.27. Marmousi2 density

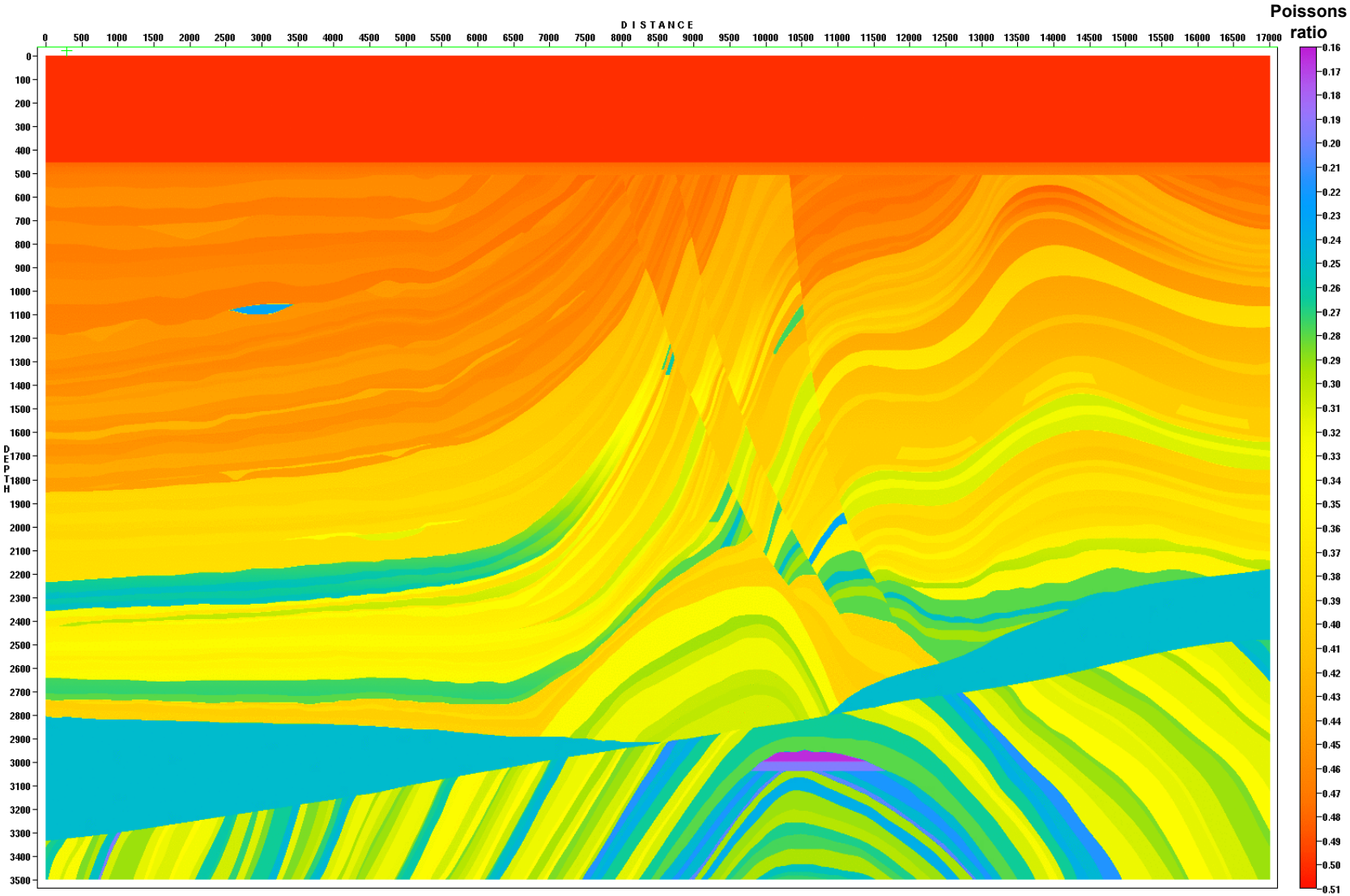

Figure 2.28. Marmousi2 Poissons ratio

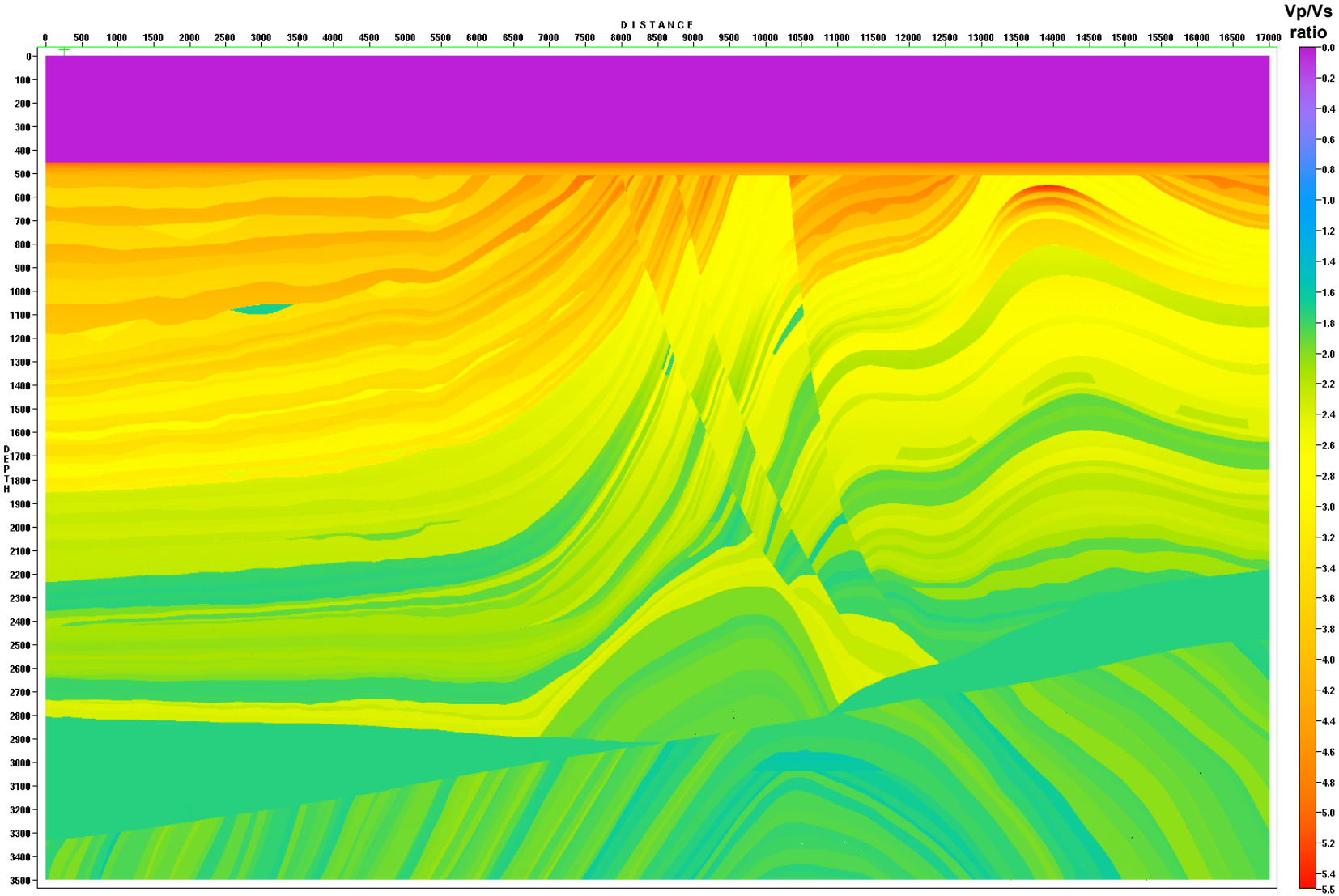

Figure 2.29. Marmousi2 Vp-Vs ratio

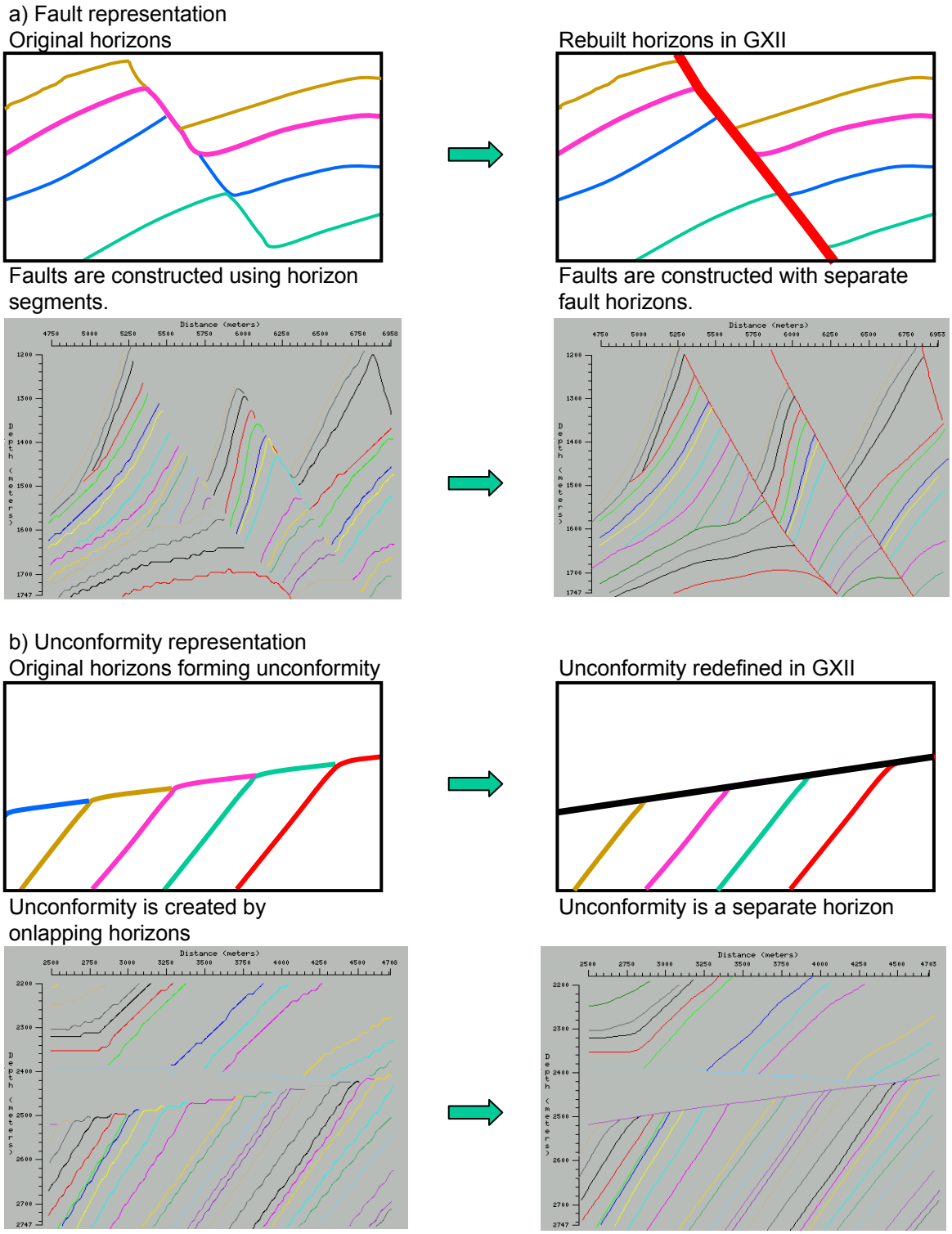

Figure 2.2. Rebuilding the Marmousi structural model from the gridded horizons. a) shows the representations of faults in the original model and how they were modified in the construction of Marmousi2, b) shows a similar modification for unconformity reconstruction.

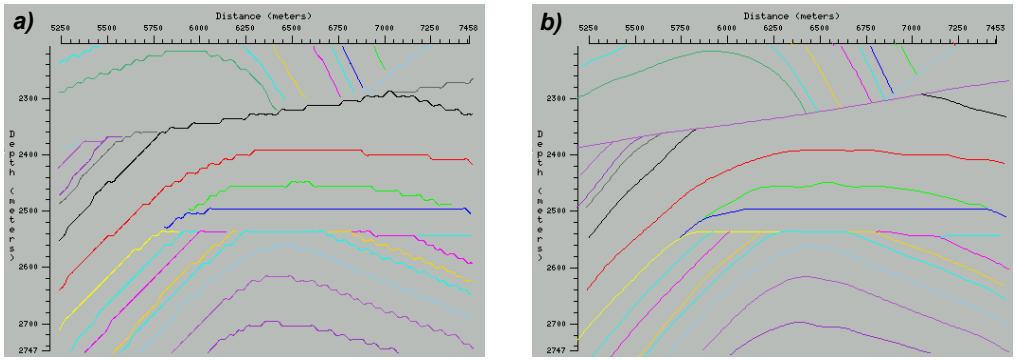

Figure 2.3. Smoothing the reconstructed horizons. a) shows the stepping artifact caused by the 4mx4m gridding in the original Marmousi model, b) is smoothed to remove artifact.

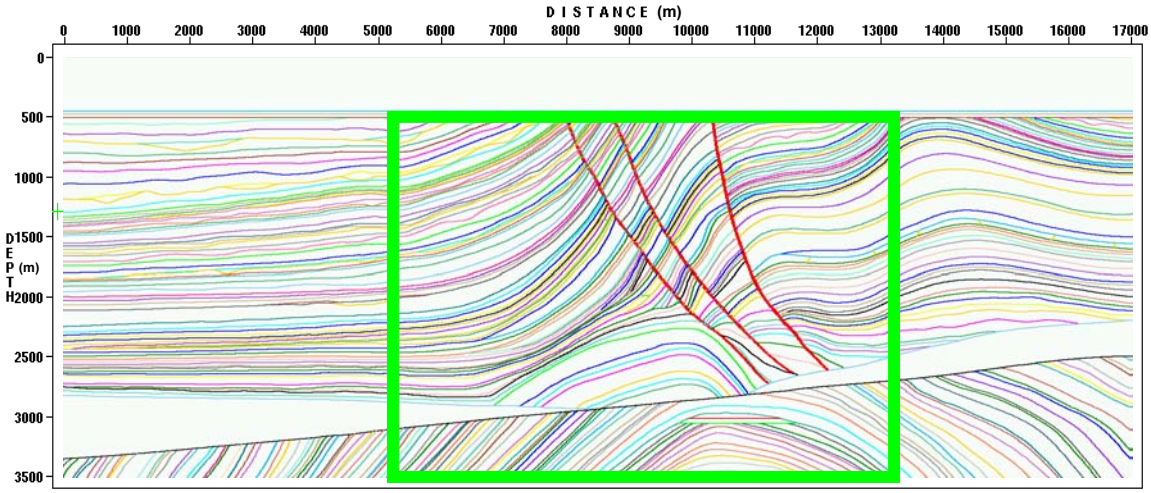

Figure 2.4. The Marmousi2 model with the area of the original model shown as a green rectangle.

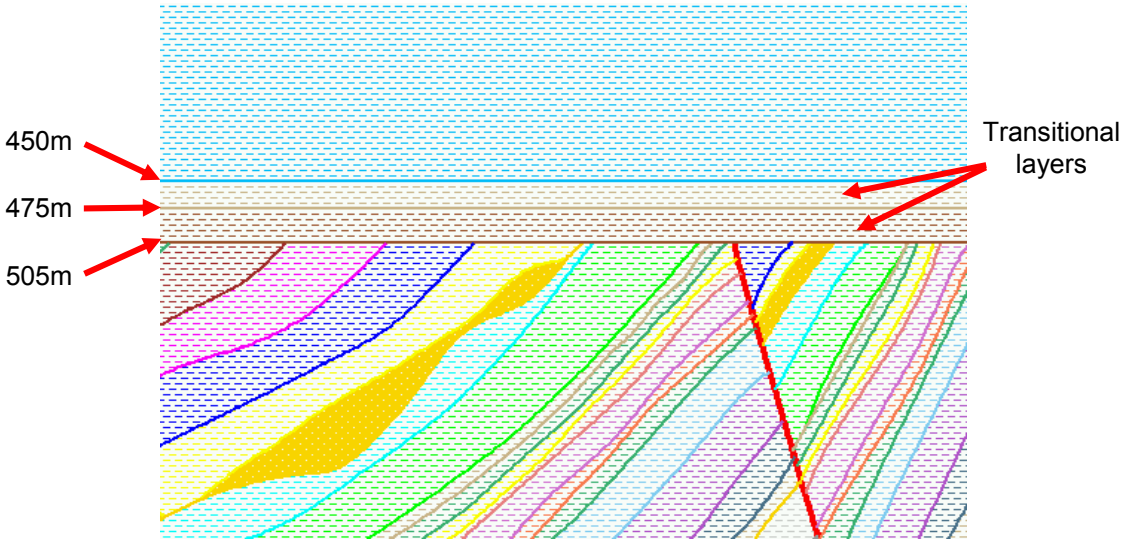

Figure 2.5. Transitional soft sedimentary layers at the waterbottom

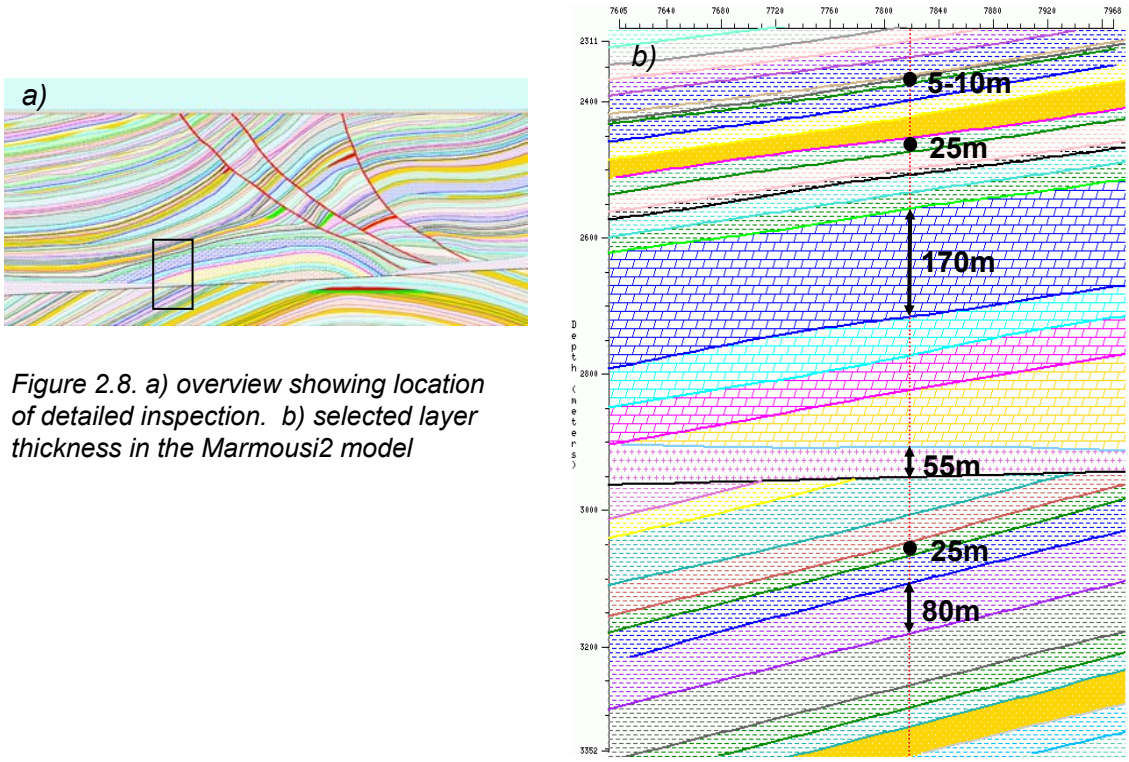

Figure 2.8. a) overview showing location of detailed inspection. b) selected layer thickness in the Marmousi2 model

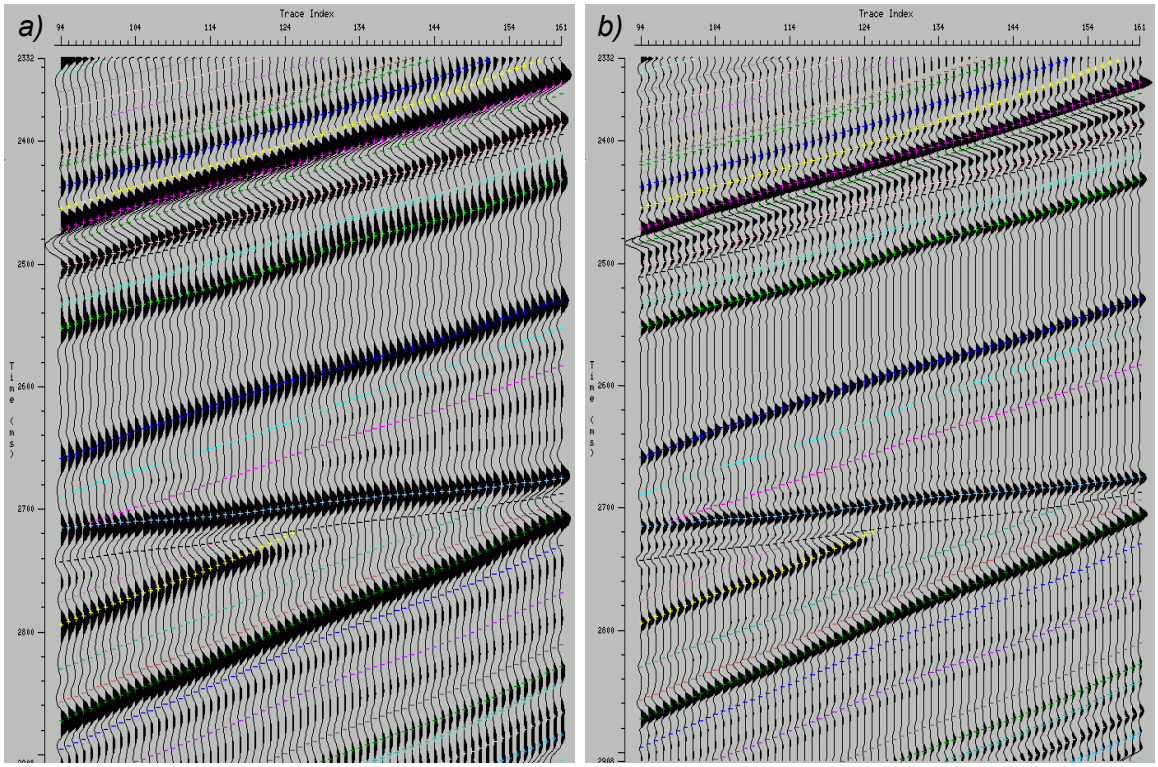

Figure 2.9. Simple synthetic convolved with a) 5-10-30-40 Hz bandpass filter and b) 5-10-60-80Hz bandpass filter. Area is identical to that shown in Figure 2.7. Thick layers show no interference with adjacent layers. Thin layers are not distinguishable even with the higher frequency band.

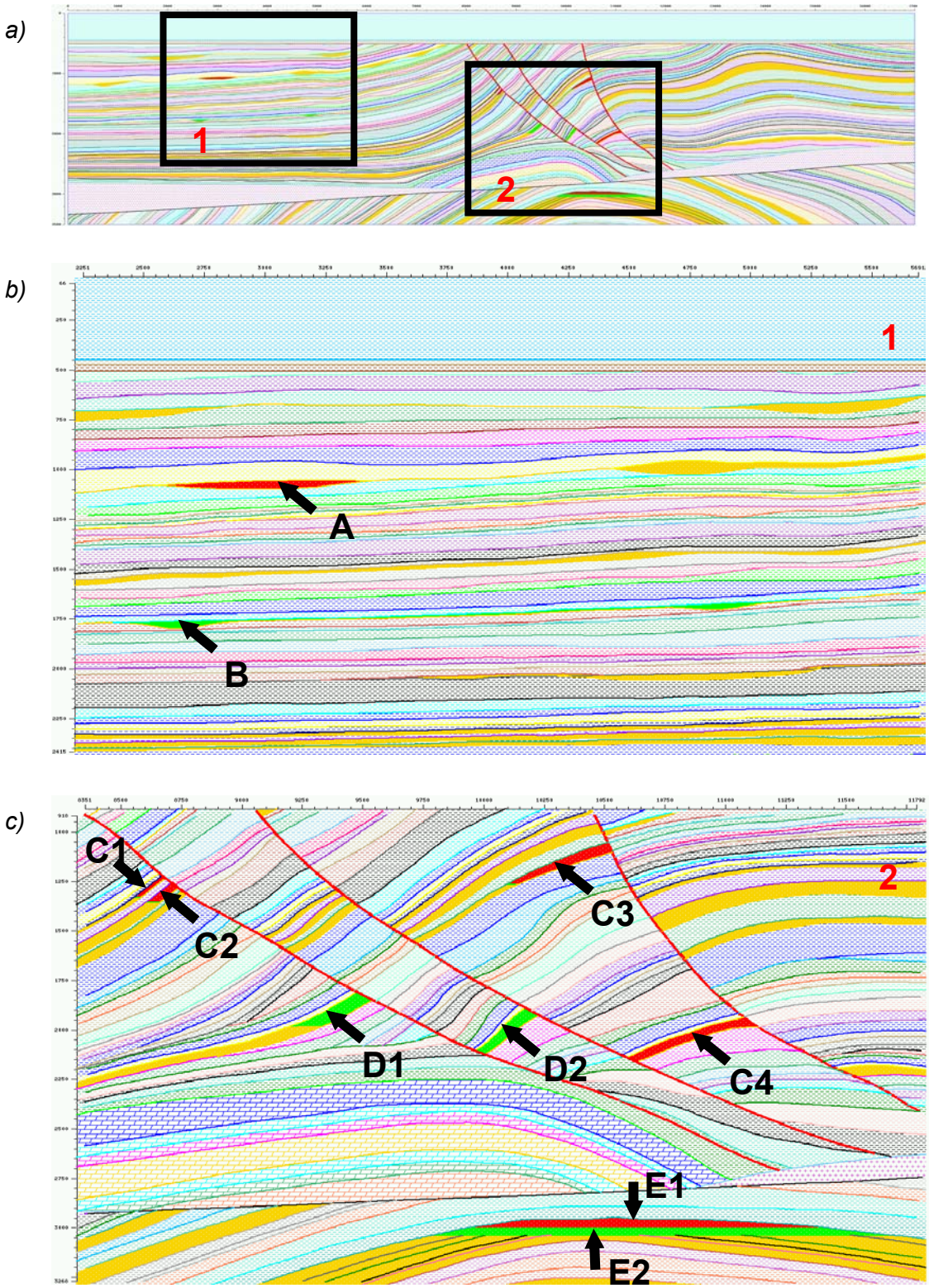

Figure 2.10. Hydrocarbon units. a) overview shows location of hydrocarbon units and areas shown in greater detail in b) and c), b) location of hydrocarbon units in relatively simple structural setting, c) location of hydrocarbon units in structurally more complex locations.

a)

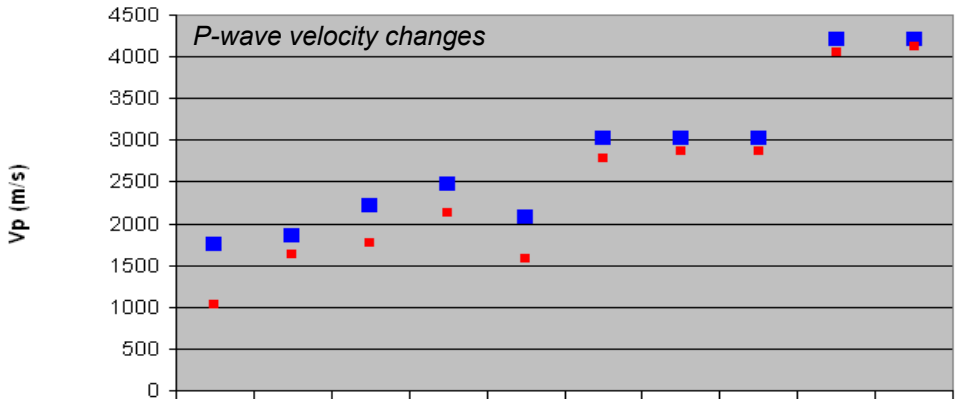

	A	B	C1	C2	C3	C4	D1	D2	E1	E2
Water Wet	1753	1855	2210	2480	2080	3025	3025	3025	4200	4200
Hydrocarbons	1028	1640	1770	2131	1584	2783	2874	2874	4045	4123
% change	-41.4	-11.6	-19.9	-14.1	-23.8	-8.0	-5.0	-5.0	-3.7	-1.8

b)

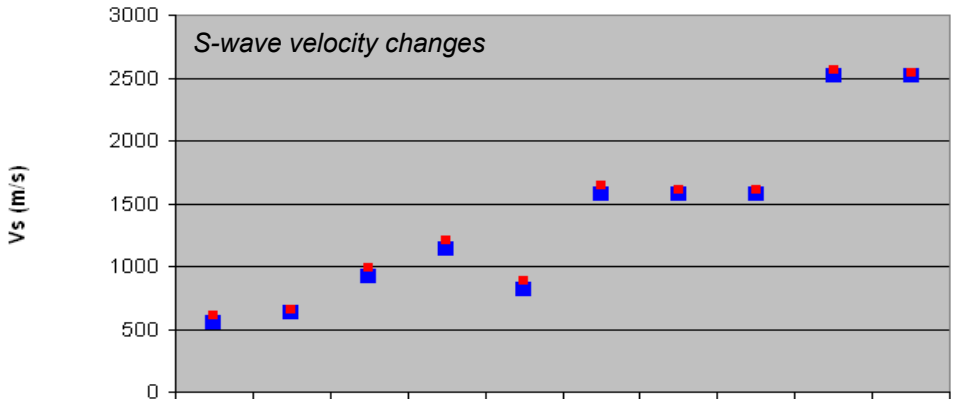

	A	B	C1	C2	C3	C4	D1	D2	E1	E2
Water Wet	553	635	921	1138	816	1576	1576	1576	2521	2521
Hydrocarbons	607	652	988	1209	881	1645	1604	1604	2564	2538
% change	9.7	2.6	7.3	6.2	7.9	4.4	1.8	1.8	1.7	0.7

c)

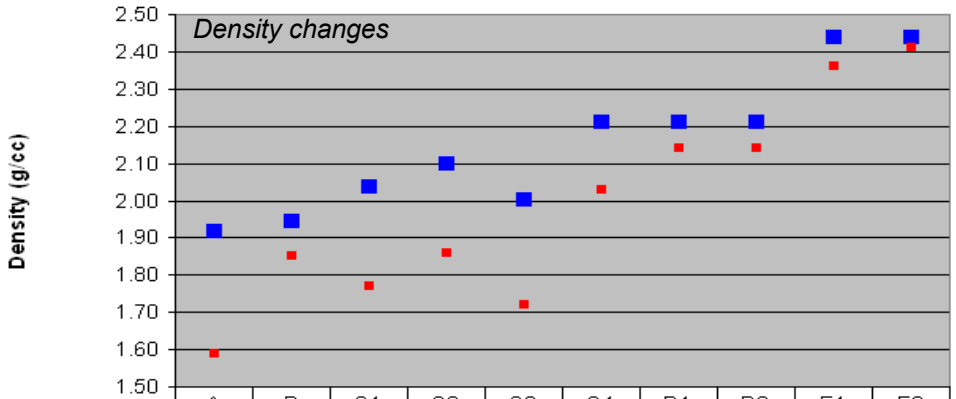

	A	B	C1	C2	C3	C4	D1	D2	E1	E2
Water Wet	1.92	1.94	2.04	2.10	2.00	2.21	2.21	2.21	2.44	2.44
Hydrocarbons	1.59	1.85	1.77	1.86	1.72	2.03	2.14	2.14	2.36	2.41
% change	-17.0	-4.8	-13.0	-11.3	-14.1	-8.1	-3.1	-3.1	-3.3	-1.2

Figure 2.11. Graphs and tables showing the changes to a) P-wave velocity, b) S-wave velocity, and c) density when hydrocarbons are substituted into the sands.

d)

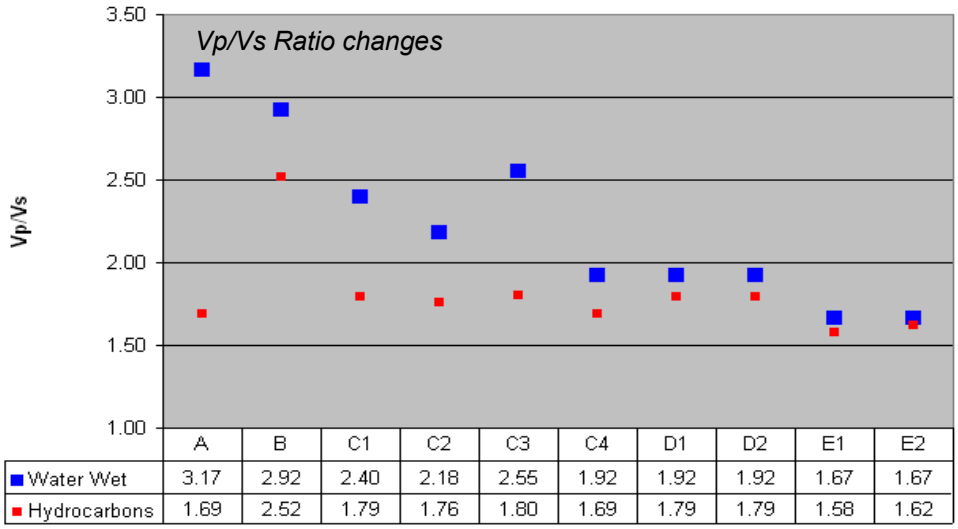

	A	B	C1	C2	C3	C4	D1	D2	E1	E2
Water Wet	3.17	2.92	2.40	2.18	2.55	1.92	1.92	1.92	1.67	1.67
Hydrocarbons	1.69	2.52	1.79	1.76	1.80	1.69	1.79	1.79	1.58	1.62

e)

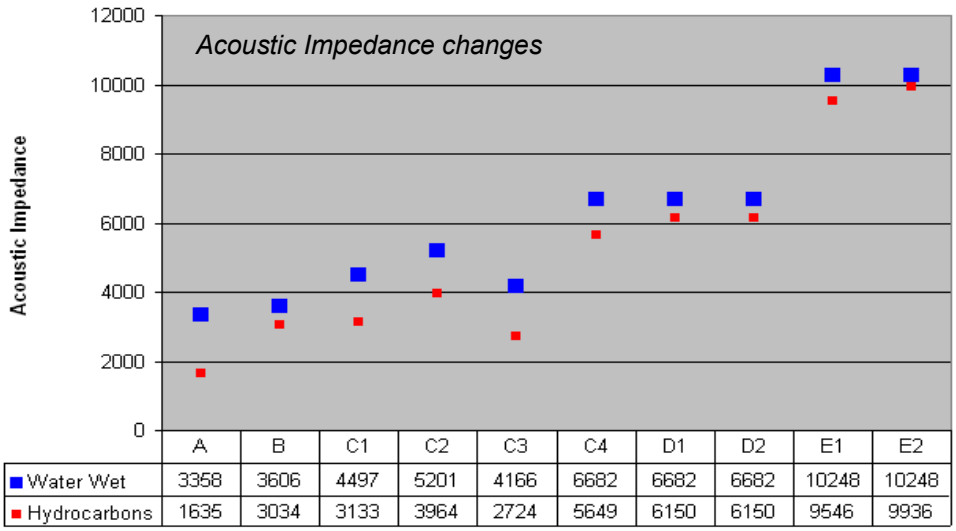

	A	B	C1	C2	C3	C4	D1	D2	E1	E2
Water Wet	3358	3606	4497	5201	4166	6682	6682	6682	10248	10248
Hydrocarbons	1635	3034	3133	3964	2724	5649	6150	6150	9546	9936

Figure 2.11. Graphs and tables showing the changes to d) Vp/Vs ratio, b) acoustic impedance when hydrocarbons are substituted into the sands.

a)

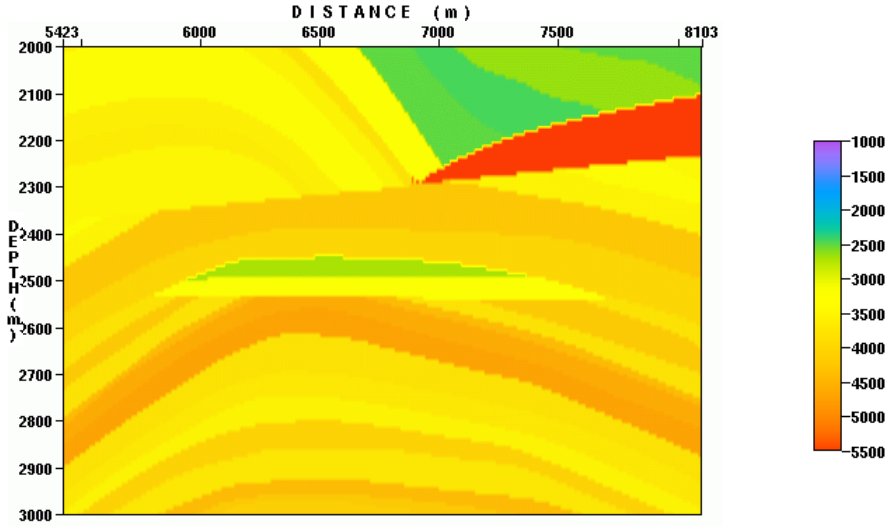

b)

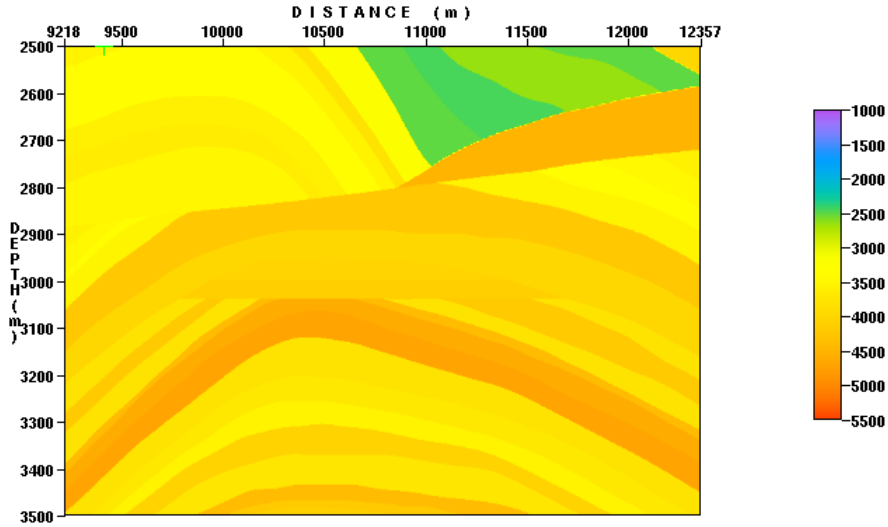

Figure 2.12. Comparison of the P-wave velocity for a) Marmousi, and b) Marmousi2. The large decrease of velocity due to the oil and gas cap in the Marmousi model can not be supported by fluid substitution, and is therefore absent in Marmousi2.

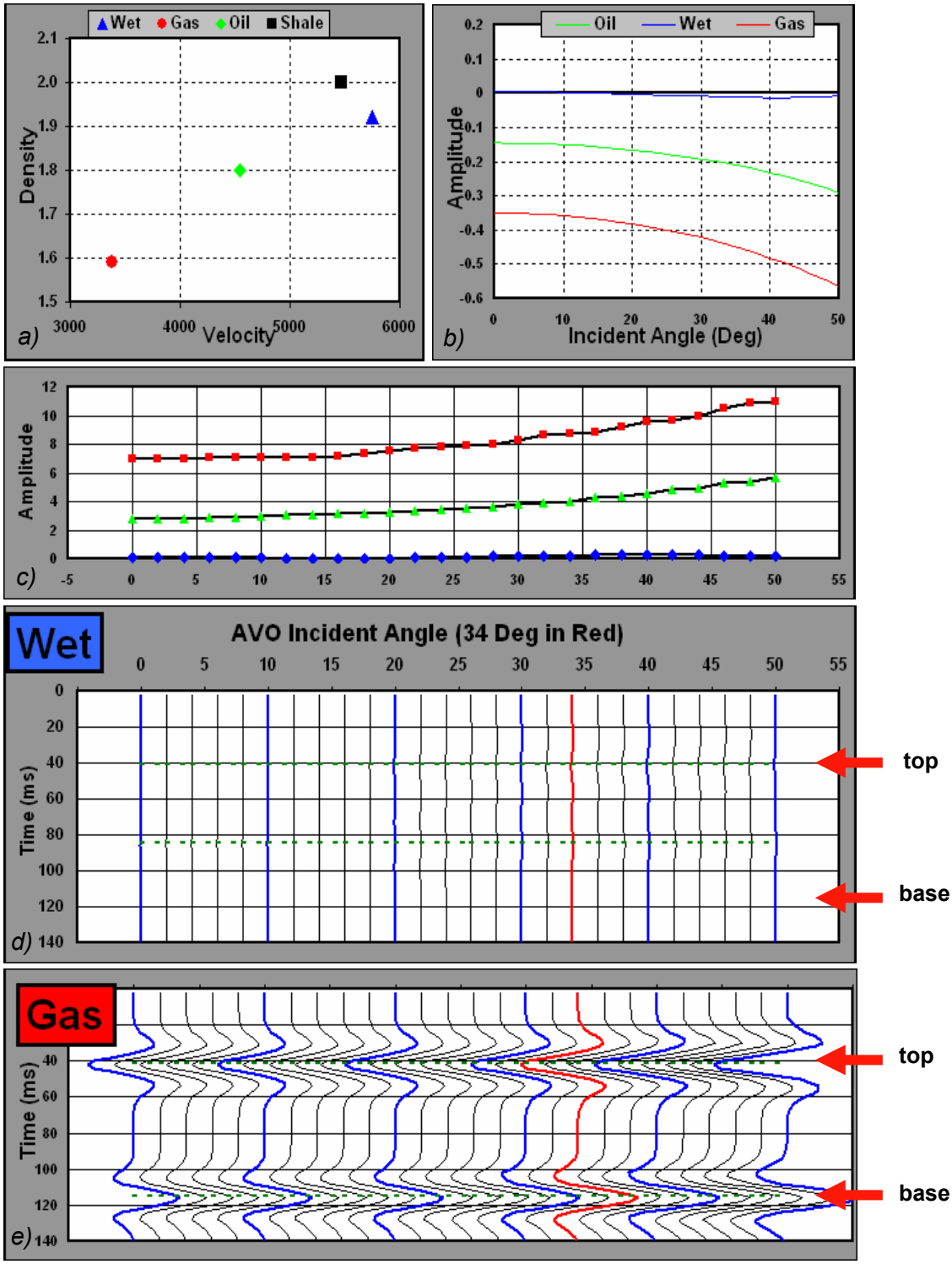

Figure 2.13. Fluid substitution and theoretical AVO for hydrocarbon A. a) velocity and density crossplot for the shale, gas filled sand, oil filled sand, and water wet sand, b) and c) amplitude variation with incident angle for fluid filled sands, d) amplitude variation with angle (offset) for the water wet sand (before fluid substitution), e) amplitude variation with angle (offset) for the hydrocarbon saturated sand. Arrows indicate top and base of sand layer, redline in d) and e) indicates offset=depth.

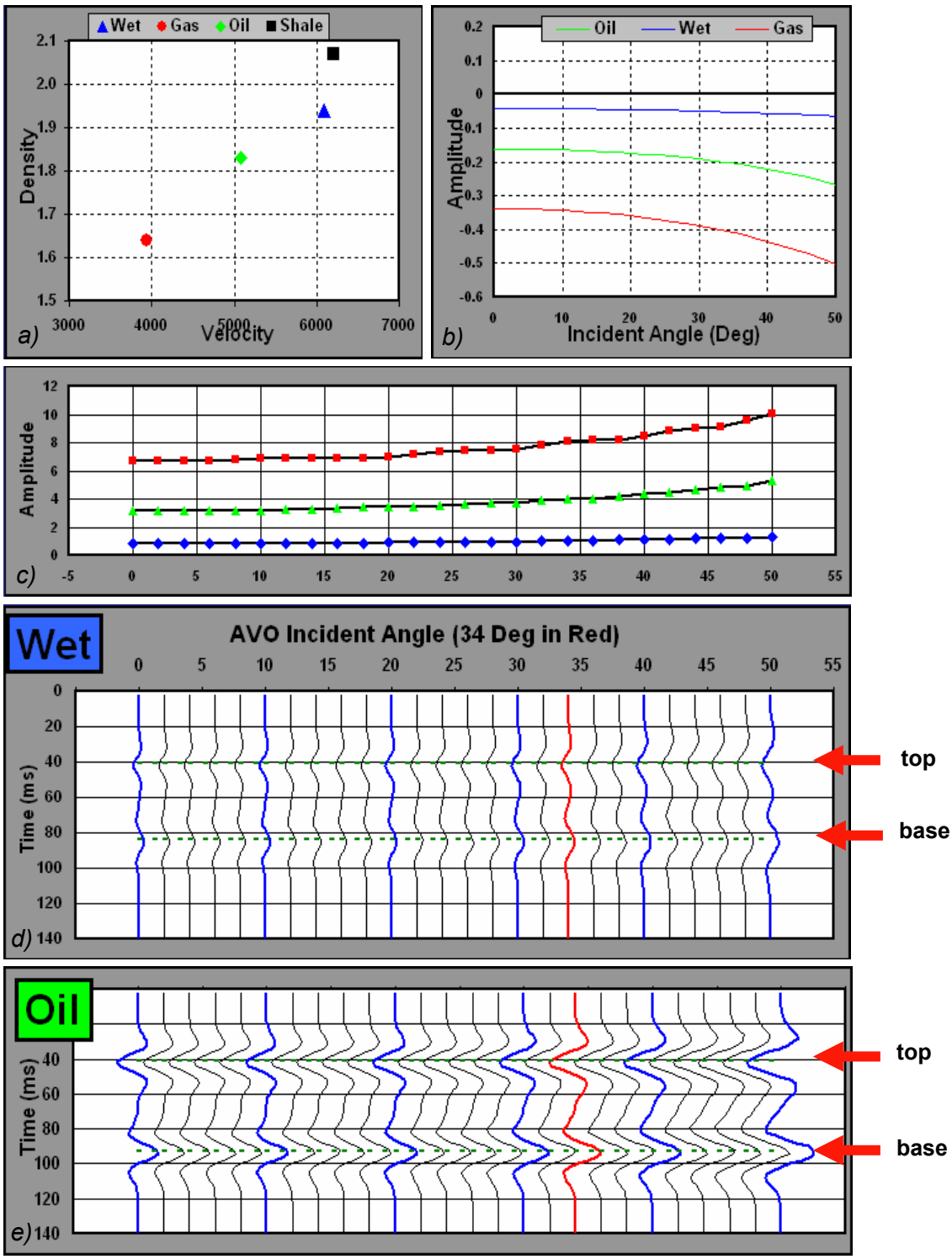

Figure 2.14. Fluid substitution and theoretical AVO for hydrocarbon B. a) velocity and density crossplot for the shale, gas filled sand, oil filled sand, and water wet sand, b) and c) amplitude variation with incident angle for fluid filled sands, d) amplitude variation with angle (offset) for the water wet sand (before fluid substitution), e) amplitude variation with angle (offset) for the hydrocarbon saturated sand. Arrows indicate top and base of sand layer, redline in d) and e) indicates offset=depth.

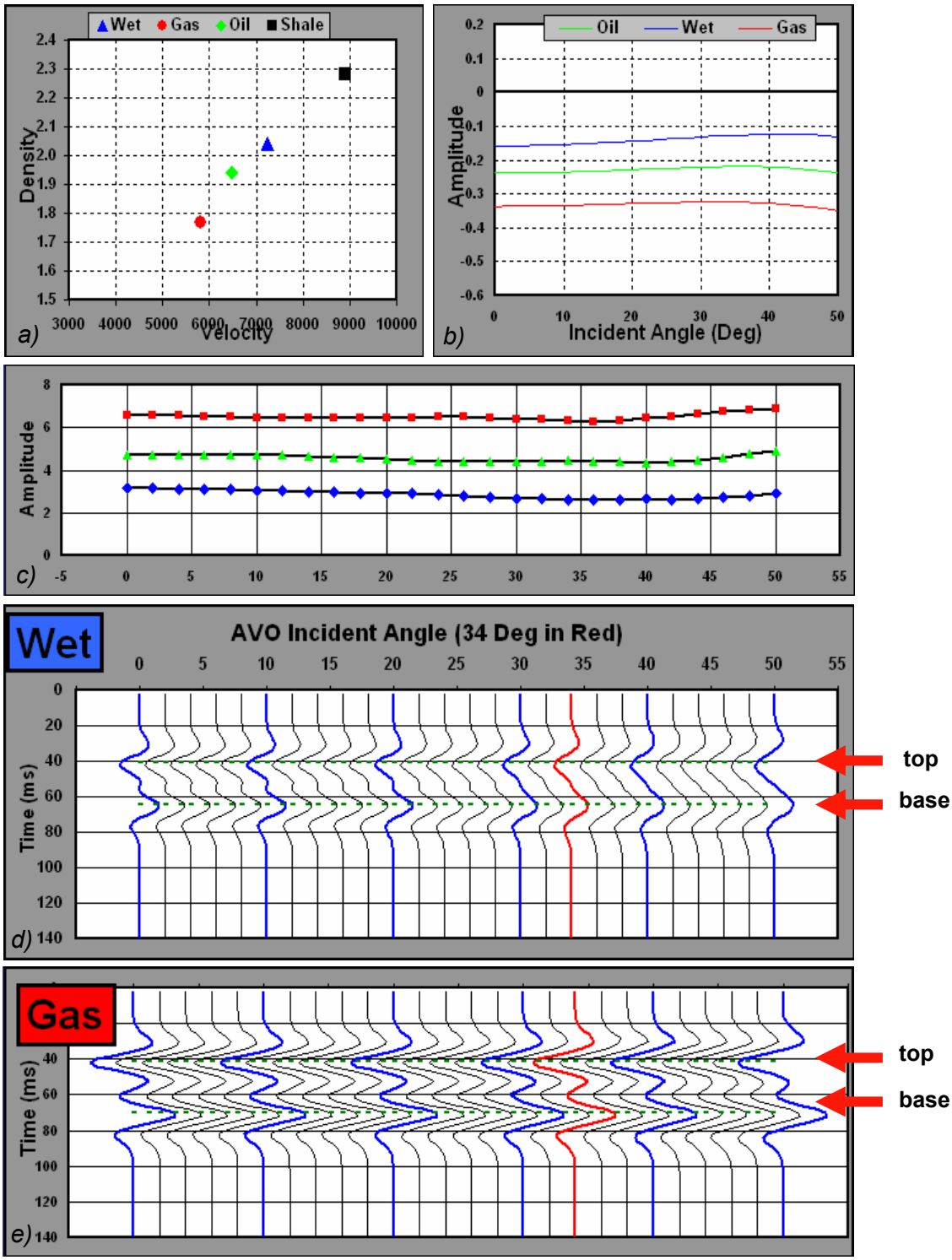

Figure 2.15. Fluid substitution and theoretical AVO for hydrocarbon C1. a) velocity and density crossplot for the shale, gas filled sand, oil filled sand, and water wet sand, b) and c) amplitude variation with incident angle for fluid filled sands, d) amplitude variation with angle (offset) for the water wet sand (before fluid substitution), e) amplitude variation with angle (offset) for the hydrocarbon saturated sand. Arrows indicate top and base of sand layer, redline in d) and e) indicates offset=depth.

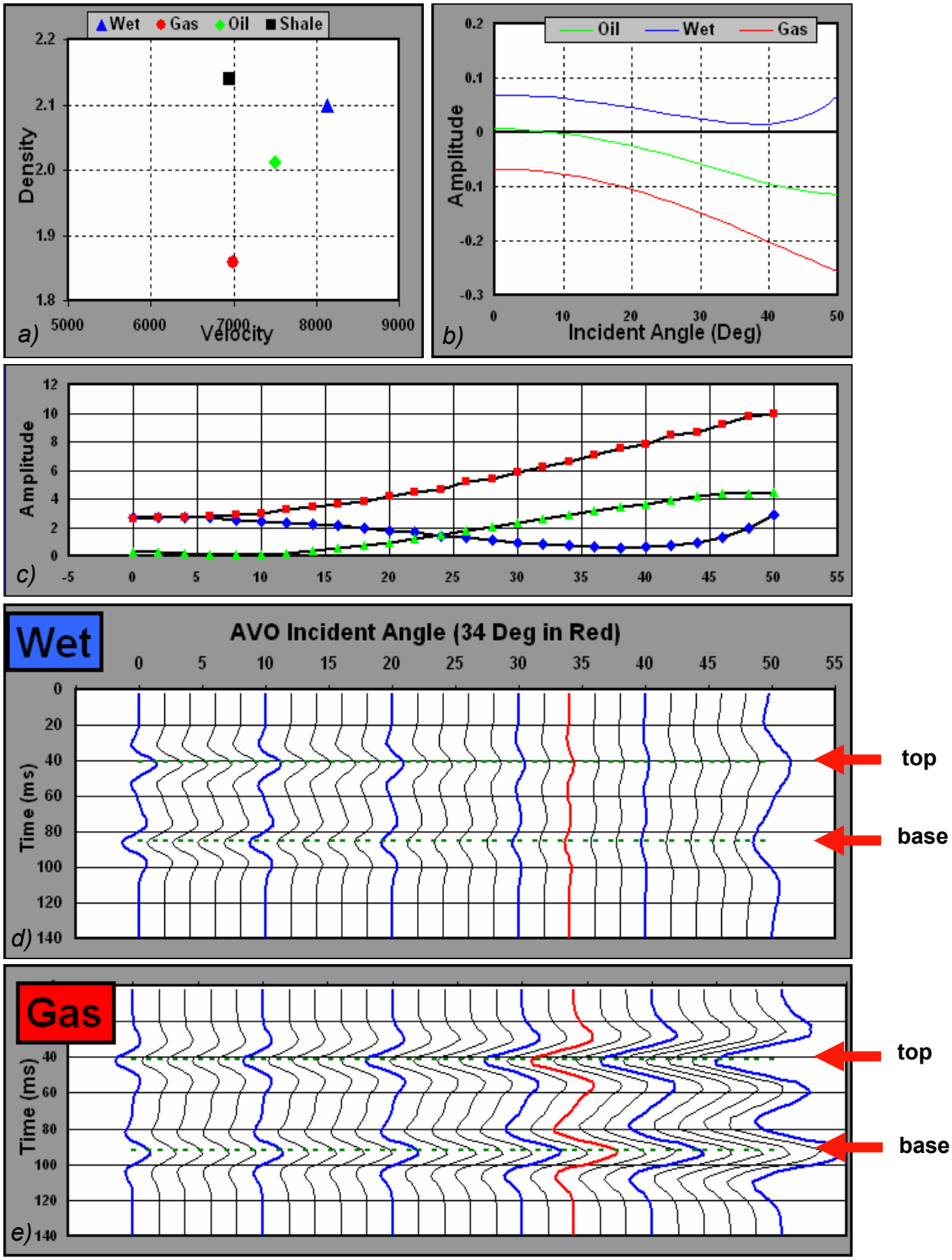

Figure 2.16. Fluid substitution and theoretical AVO for hydrocarbon C2. a) velocity and density crossplot for the shale, gas filled sand, oil filled sand, and water wet sand, b) and c) amplitude variation with incident angle for fluid filled sands, d) amplitude variation with angle (offset) for the water wet sand (before fluid substitution), e) amplitude variation with angle (offset) for the hydrocarbon saturated sand. Arrows indicate top and base of sand layer, redline in d) and e) indicates offset=depth.

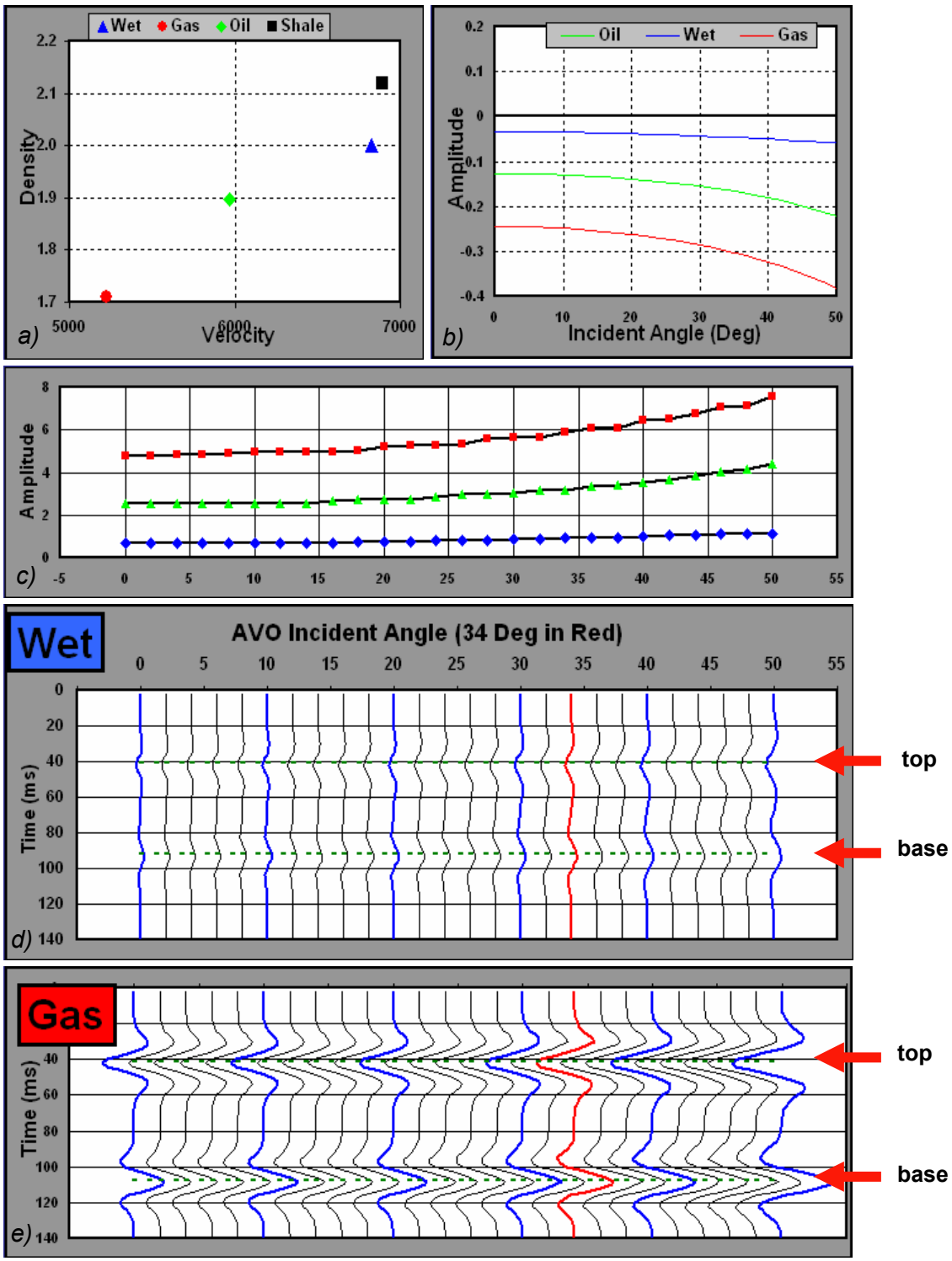

Figure 2.17. Fluid substitution and theoretical AVO for hydrocarbon C3. a) velocity and density crossplot for the shale, gas filled sand, oil filled sand, and water wet sand, b) and c) amplitude variation with incident angle for fluid filled sands, d) amplitude variation with angle (offset) for the water wet sand (before fluid substitution), e) amplitude variation with angle (offset) for the hydrocarbon saturated sand. Arrows indicate top and base of sand layer, redline in d) and e) indicates offset=depth.

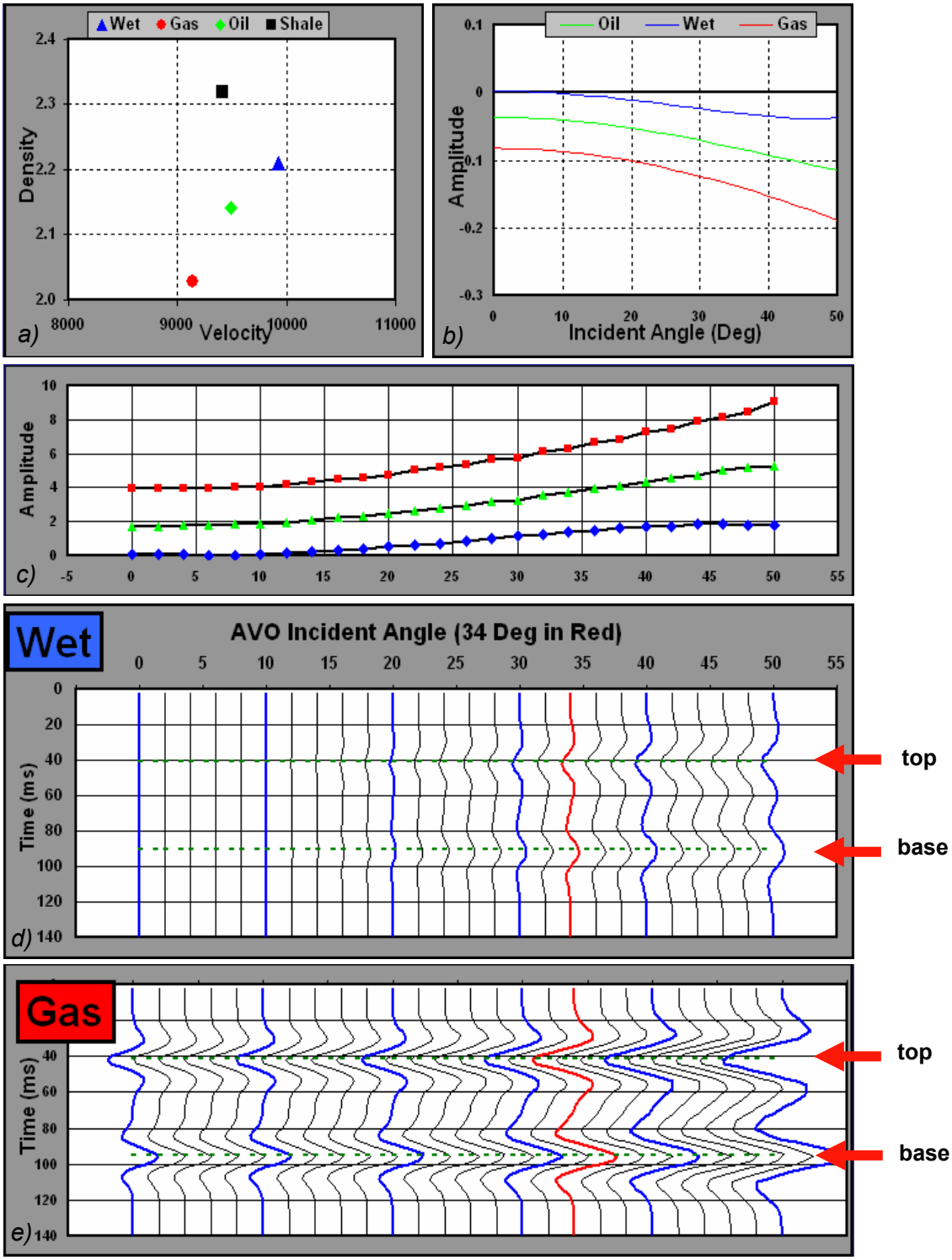

Figure 2.18. Fluid substitution and theoretical AVO for hydrocarbon C4. a) velocity and density crossplot for the shale, gas filled sand, oil filled sand, and water wet sand, b) and c) amplitude variation with incident angle for fluid filled sands, d) amplitude variation with angle (offset) for the water wet sand (before fluid substitution), e) amplitude variation with angle (offset) for the hydrocarbon saturated sand. Arrows indicate top and base of sand layer, redline in d) and e) indicates offset=depth.

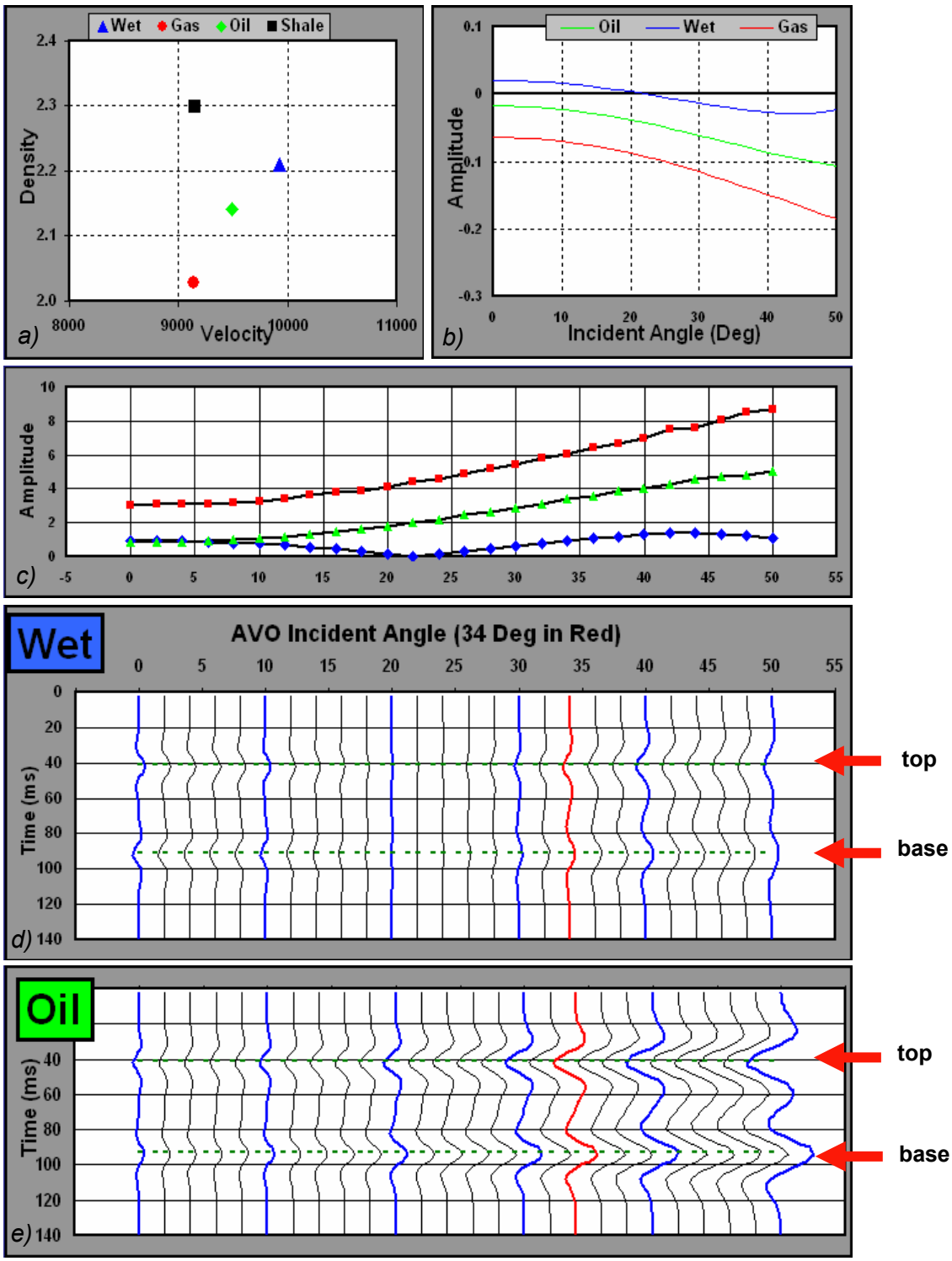

Figure 2.19. Fluid substitution and theoretical AVO for hydrocarbon D1. a) velocity and density crossplot for the shale, gas filled sand, oil filled sand, and water wet sand, b) and c) amplitude variation with incident angle for fluid filled sands, d) amplitude variation with angle (offset) for the water wet sand (before fluid substitution), e) amplitude variation with angle (offset) for the hydrocarbon saturated sand. Arrows indicate top and base of sand layer, redline in d) and e) indicates offset=depth.

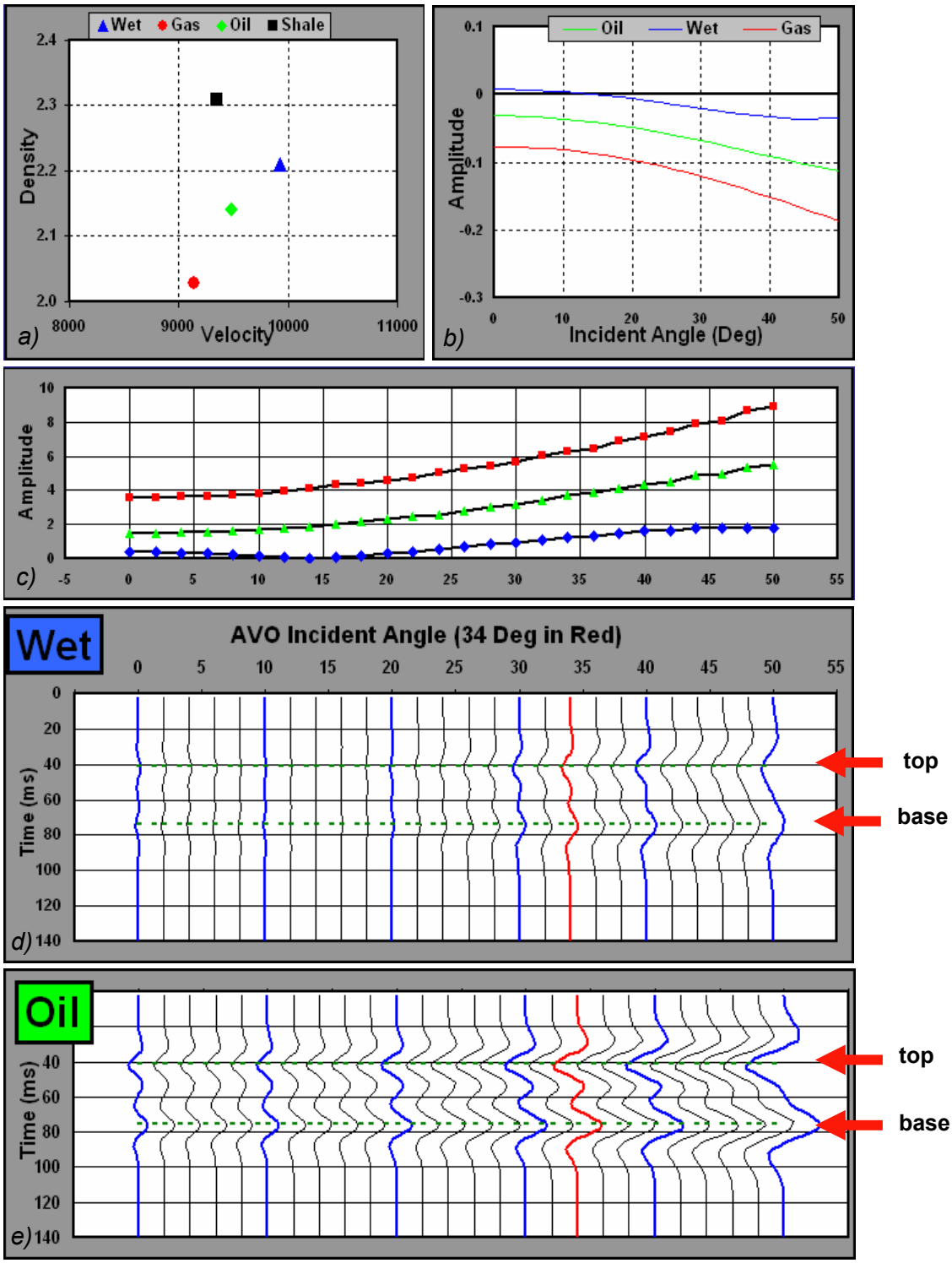

Figure 2.20. Fluid substitution and theoretical AVO for hydrocarbon D2. a) velocity and density crossplot for the shale, gas filled sand, oil filled sand, and water wet sand, b) and c) amplitude variation with incident angle for fluid filled sands, d) amplitude variation with angle (offset) for the water wet sand (before fluid substitution), e) amplitude variation with angle (offset) for the hydrocarbon saturated sand. Arrows indicate top and base of sand layer, redline in d) and e) indicates offset=depth.

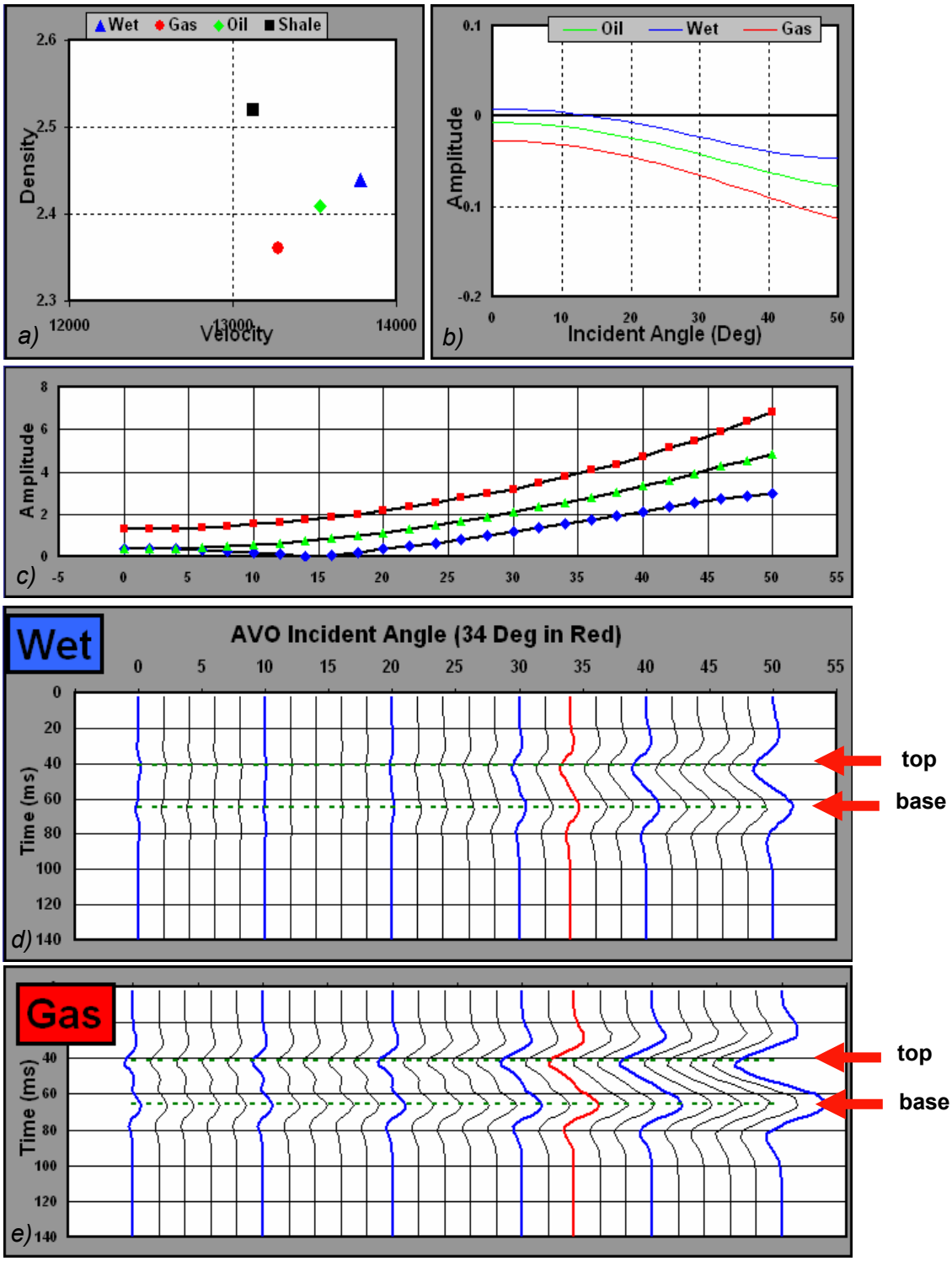

Figure 2.21. Fluid substitution and theoretical AVO for hydrocarbon E1. a) velocity and density crossplot for the shale, gas filled sand, oil filled sand, and water wet sand, b) and c) amplitude variation with incident angle for fluid filled sands, d) amplitude variation with angle (offset) for the water wet sand (before fluid substitution), e) amplitude variation with angle (offset) for the hydrocarbon saturated sand. Arrows indicate top and base of sand layer, redline in d) and e) indicates offset=depth.

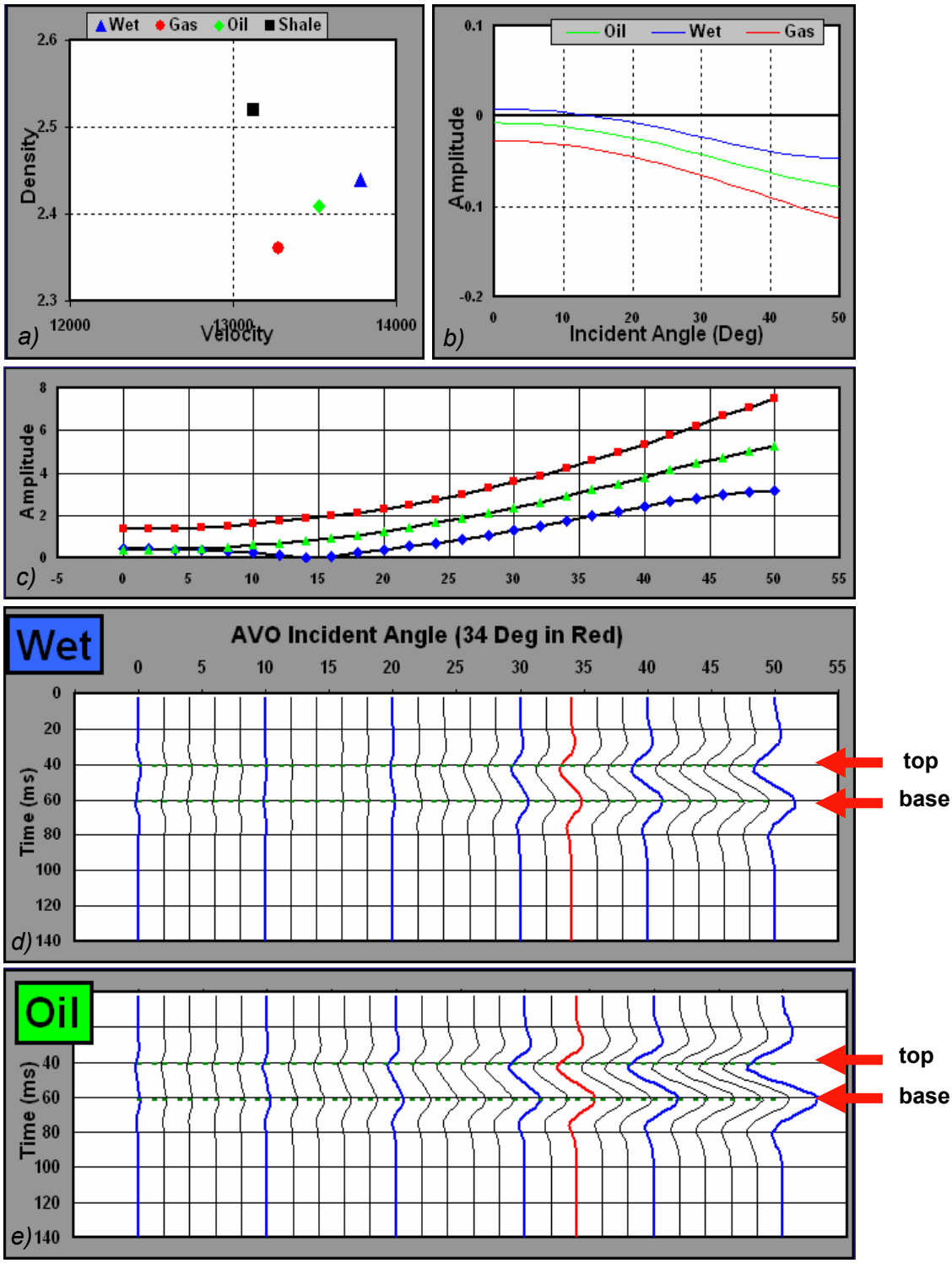

Figure 2.22. Fluid substitution and theoretical AVO for hydrocarbon E2. a) velocity and density crossplot for the shale, gas filled sand, oil filled sand, and water wet sand, b) and c) amplitude variation with incident angle for fluid filled sands, d) amplitude variation with angle (offset) for the water wet sand (before fluid substitution), e) amplitude variation with angle (offset) for the hydrocarbon saturated sand. Arrows indicate top and base of sand layer, redline in d) and e) indicates offset=depth.

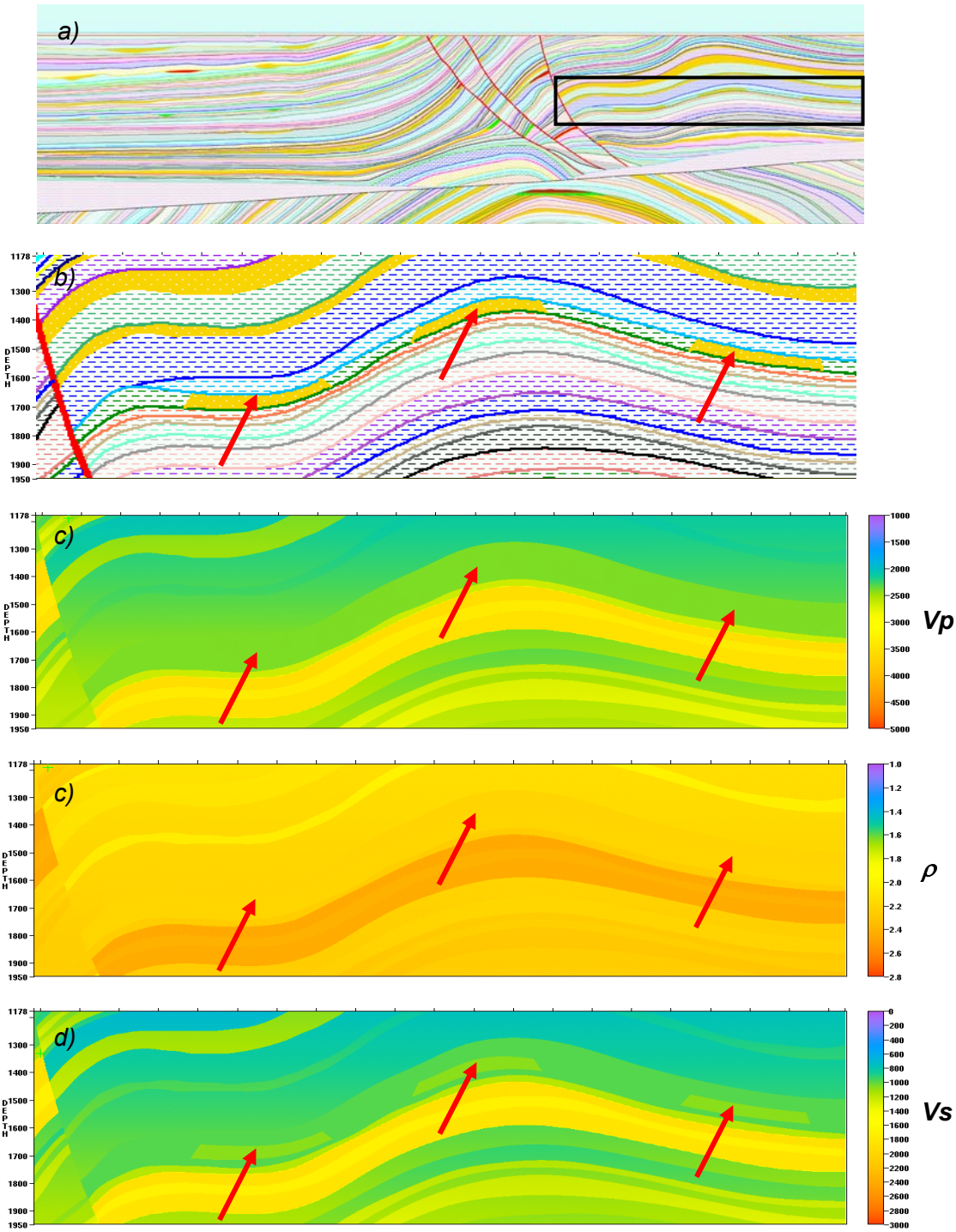

Figure 2.23. Zero P-impedance contrast sands. Sands and encasing shales have identical P-wave velocity and density. S-wave velocity of sands differs from the encasing shale. a) location of unit within Marmousi2, b) layering and lithology, c) P-wave velocity is identical for the sand and the encasing shale, d) density is identical for the sand and the encasing shale, e) S-wave velocity for the sand is slightly lower than the encasing shale. Sand layer of interest is yellow in a) and b) and is highlighted by the red arrows.

Layer Number	Horizon at base	Horizon at top	Rock Type	Fluid	k	Vo	Vs	Density
001_Water	H001-wb	-	water	water	0	1500	0	1.01
002	002	H001-wb	shale	water	3.2	60	Vs transform	ρ transform
003	003	002	shale	water	2.333	472	Vs transform	ρ transform
004	004	003	shale	water	0.25	1534	Vs transform	ρ transform
005	005	004	shale	water	0.25	1634	Vs transform	ρ transform
006	006	005	shale	water	0.25	1484	Vs transform	ρ transform
007	007	006	sandstone	water	0.25	1534	Vs transform	ρ transform
008	008	007	shale	water	0.25	1584	Vs transform	ρ transform
009	009	008	shale	water	0.25	1444	Vs transform	ρ transform
010	010	009	shale	water	0.25	1484	Vs transform	ρ transform
011	011	010	shale	water	0.25	1534	Vs transform	ρ transform
012	012	011	shale	water	0.25	1404	Vs transform	ρ transform
013_wet	013	012	sandstone	water	0.25	1484	Vs transform	ρ transform
013_gas	013	012	sandstone	gas	0	1028	607	1.59
014	014	013	shale	water	0.25	1564	Vs transform	ρ transform
015	015	014	shale	water	0.25	1484	Vs transform	ρ transform
016	016	015	shale	water	0.25	1414	Vs transform	ρ transform
017	017	016	shale	water	0.25	1464	Vs transform	ρ transform
018	018	017	shale	water	0.25	1534	Vs transform	ρ transform
019	019	018	shale	water	0.25	1454	Vs transform	ρ transform
020	020	019	shale	water	0.25	1414	Vs transform	ρ transform
021	021	020	shale	water	0.25	1444	Vs transform	ρ transform
022	022	021	shale	water	0.25	1584	Vs transform	ρ transform
023	023	022	shale	water	0.25	1534	Vs transform	ρ transform
024	024	023	shale	water	0.25	1604	Vs transform	ρ transform
025	025	024	shale	water	0.25	1474	Vs transform	ρ transform
026	026	025	shale	water	0.25	1444	Vs transform	ρ transform
027	027	026	sandstone	water	0.25	1554	Vs transform	ρ transform
028	028	027	shale	water	0.25	1484	Vs transform	ρ transform
029	029	028	shale	water	0.25	1414	Vs transform	ρ transform
030	030	029	shale	water	0.25	1484	Vs transform	ρ transform
031	031	030	shale	water	0.25	1604	Vs transform	ρ transform
032	032	031	shale	water	0.25	1474	Vs transform	ρ transform
033_wet	033	032	sandstone	water	0.25	1424	Vs transform	ρ transform
033_oil	033	032	sandstone	oil	0	1640	652	1.85
034	034	033	shale	water	0.25	1484	Vs transform	ρ transform
035	035	034	shale	water	0.375	1826	Vs transform	ρ transform
036	036	035	shale	water	0.375	1856	Vs transform	ρ transform
037	037	036	shale	water	0.375	1806	Vs transform	ρ transform
038	038	037	shale	water	0.375	1916	Vs transform	ρ transform
039	039	038	shale	water	0.375	1826	Vs transform	ρ transform
040	040	039	shale	water	0.375	1786	Vs transform	ρ transform
041	H041_levee	040	shale	water	0.375	1906	Vs transform	ρ transform
042-levee	H042	H041_levee	sandstone	water	0	2800	1395	2.30
043-channel	H043_channel	H042	sandstone	water	0	3000	1556	2.21
044	044	H043_channel	shale	water	0.375	1846	Vs transform	ρ transform
045	045	044	shale	water	1.625	584	Vs transform	ρ transform
046	046	045	shale	water	1.625	724	Vs transform	ρ transform
047	047	046	shale	water	1.625	544	Vs transform	ρ transform
048	048	047	shale	water	1.625	644	Vs transform	ρ transform
049_wet	049	048	sandstone	water	0.625	1409	Vs transform	ρ transform
049_gas	H048-049_GAS	H048	sandstone	gas	0	1770	988	1.77
050	050	049	shale	water	0.625	1309	Vs transform	ρ transform
051_wet	051	050	sandstone	water	0.625	1659	Vs transform	ρ transform
051_gas	H050-051_GAS	H050	sandstone	gas	0	2131	1209	1.86
052	052	051	shale	water	0.625	1389	Vs transform	ρ transform
053_wet	053	052	sandstone	water	0.625	1359	Vs transform	ρ transform
053_gas	H052-053_GAS	H052	sandstone	gas	0	1584	881	1720.00
054	054	053	shale	water	0.625	1389	Vs transform	ρ transform
055	055	054	shale	water	0	2400	981	2.20

Layer Number	Horizon at base	Horizon at top	Rock Type	Fluid	k	Vo	Vs	Density
056	056	055	sandstone	water	0	2400	981	2.20
056_noAlp	H055-056_noAlp	H055	sandstone	water	0	2400	1074	2.20
057	057	056	shale	water	0	2400	981	2.20
058	058	057	shale	water	0	2650	1174	2.26
059	059	058	shale	water	0	3550	1867	2.44
060	060	059	shale	water	0	3350	1713	2.40
061	061	060	shale	water	0	3500	1828	2.43
062	062	061	shale	water	0.625	1409	Vs transform	ρ transform
063	063	062	shale	water	0.625	1289	Vs transform	ρ transform
064	064	063	shale	water	0.625	1559	Vs transform	ρ transform
065	065	064	shale	water	0.625	1409	Vs transform	ρ transform
066	066	065	shale	water	0.625	1609	Vs transform	ρ transform
067	067	066	shale	water	0.625	1409	Vs transform	ρ transform
068	068	067	shale	water	0.625	1339	Vs transform	ρ transform
069	069	068	shale	water	0.625	1409	Vs transform	ρ transform
070	070	069	shale	water	0.625	1609	Vs transform	ρ transform
071_wet	071	H070	sandstone	water	0.625	1809	Vs transform	ρ transform
071_oil	H071-070_OIL	H070	sandstone	oil	0	2874	1604	2.14
071_gas	H071	H070	sandstone	gas	0	2783	1645	2.03
072	072	071	shale	water	0.625	1609	Vs transform	ρ transform
073	073	072	shale	water	0	4000	2213	2.52
074	074	073	shale	water	0	4450	2560	2.59
075	075	074	shale	water	0	4000	2213	2.52
076	076	075	shale	water	0	3770	2036	2.48
077	077	076	shale	water	0	4000	2213	2.52
078	078	077	shale	water	0	2500	1058	2.22
079	079	078	shale	water	0	2650	1174	2.26
080	080	079	shale	water	0	2440	1012	2.21
081	081	080	shale	water	0	2500	1058	2.22
082	082	081	marl	water	0	3200	1616	2.24
083	083	082	marl	water	0	3800	2053	2.34
084	084	083	marl	water	0	3550	1873	2.30
085	085	084	marl	water	0	3300	1690	2.25
086	086	085	marl	water	0	3600	1909	2.31
087	087	086	marl	water	0	3650	1945	2.31
088	088_Top_Salt	087	marl	water	0	3500	1836	2.29
089_salt	089_UC	088_Top_Salt	salt	water	0	4500	2600	2.14
090	090	089_UC	shale	water	0	3750	2021	2.47
091	091	90	shale	water	0	4200	2367	2.55
092	092	091	shale	water	0	4300	2444	2.57
093	093	092	shale	water	0	3300	1674	2.39
094	094	093	shale	water	0	3550	1867	2.44
095	095	094	shale	water	0	3250	1636	2.38
096	096	095	shale	water	0	3900	2136	2.50
097	097	096	shale	water	0	3700	1982	2.47
098	098	097	shale	water	0	4440	2552	2.59
099	099	098	shale	water	0	4550	2637	2.60
100	100	099	sandstone	water	0	3540	1990	2.30
101	101	100	shale	water	0	3800	2059	2.48
102	102	101	shale	water	0	3450	1790	2.42
103	103	102	shale	water	0	3120	1535	2.36
104	104	103	shale	water	0	3380	1736	2.41
105	105	104	shale	water	0	3500	1828	2.43
106	106	105	shale	water	0	3200	1597	2.37
107	107	106	shale	water	0	3350	1713	2.40
108	108	107	shale	water	0	3540	1859	2.44
109	109	108	shale	water	0	4300	2444	2.57
110	110	109	shale	water	0	4200	2367	2.55
111	111	110	shale	water	0	3550	1867	2.44
112	112	111	shale	water	0	4120	2305	2.54

Layer Number	Horizon at base	Horizon at top	Rock Type	Fluid	k	Vo	Vs	Density
113	113	112	shale	water	0	3500	1828	2.43
114	114	113	shale	water	0	3900	2136	2.50
115	115	114	shale	water	0	4230	2390	2.55
116	116	115	shale	water	0	4560	2644	2.61
117	117	116	shale	water	0	3450	1790	2.42
118	118	117	shale	water	0	3900	2136	2.50
119	119	118	shale	water	0	3700	1982	2.47
120	120	119	shale	water	0	3600	1905	2.45
121	121	120	shale	water	0	4120	2305	2.54
122	122	121	shale	water	0	4440	2552	2.59
123	123	122	shale	water	0	4550	2637	2.60
124	124	123	shale	water	0	3500	1828	2.43
125	125	124	shale	water	0	3380	1736	2.41
126	126	125	shale	water	0	3750	2021	2.47
127	127	126	shale	water	0	3450	1790	2.42
128	128	127	shale	water	0	3120	1535	2.36
129	129	128	sandstone	water	0	3900	2280	2.36
130	130	129	shale	water	0	3800	2059	2.48
131	131	130	shale	water	0	3540	1859	2.44
132	132	131	shale	water	0	3380	1736	2.41
133	133	132	shale	water	0	3400	1751	2.41
134	134	133	shale	water	0	3900	2136	2.50
135	135	134	shale	water	0	4200	2367	2.55
136	136	135	shale	water	0	4300	2444	2.57
137	137	136	shale	water	0	3300	1674	2.39
138	138	137	shale	water	0	3200	1597	2.37
139	139	138	shale	water	0	3050	1482	2.34
140	140	139	shale	water	0	3550	1867	2.44
141	141	140	shale	water	0	3250	1636	2.38
142	142	141	shale	water	0	3900	2136	2.50
143	143	142	shale	water	0	3700	1982	2.47
144	144	143	shale	water	0	3600	1905	2.45
145	145	144	shale	water	0	3350	1713	2.40
146	146	145	sandstone	water	0	3200	1717	2.24
147	147	146	shale	water	0	3600	1905	2.45
148	148	147	shale	water	0	4120	2305	2.54
149	149	148	shale	water	0	4440	2552	2.59
150	150	149	shale	water	0	4550	2637	2.60
151	151	150	shale	water	0	3500	1828	2.43
152	152	151	shale	water	0	3380	1736	2.41
153	153	152	shale	water	0	3200	1597	2.37
154	154	153	shale	water	0	3750	2021	2.47
155	155	154	shale	water	0	3450	1790	2.42
156	156	155	shale	water	0	3120	1535	2.36
157	157	156	shale	water	0	3900	2136	2.50
158	158	157	shale	water	0	3800	2059	2.48
159	159	158	shale	water	0	3540	1859	2.44
160	160_UC	159	shale	water	0	3380	1736	2.41
161	161	160	shale	water	0	3450	1790	2.42
162	162	161	shale	water	0	3120	1535	2.36
163	163	162	shale	water	0	3900	2136	2.50
164	164	163	shale	water	0	3800	2059	2.48
165	165	164	shale	water	0	3540	1859	2.44
166	166	165	shale	water	0	3380	1736	2.41
167	167	160_UC	shale	water	0	3700	1982	2.47
168	168	166	sandstone	water	0	4230	2545	2.41
169	169	168	shale	water	0	4560	2644	2.61
170	170	169	shale	water	0	4670	2729	2.62
171	171	170	sandstone	water	0	3580	2022	2.31
172	172	171	shale	water	0	3470	1805	2.42

Layer Number	Horizon at base	Horizon at top	Rock Type	Fluid	k	Vo	Vs	Density
173	173	172	shale	water	0	3300	1674	2.39
174	174	173	shale	water	0	3530	1851	2.44
175	175	174	shale	water	0	4230	2390	2.55
176	176	175	shale	water	0	4000	2213	2.52
177_gas	177	176	sandstone	gas	0	4045	2564	2.36
178_oil	178	177	sandstone	oil	0	4123	2538	2.41
179	179	178	sandstone	water	0	3800	2199	2.34
180	180	179	sandstone	water	0	4200	2521	2.41
181	181	180	sandstone	water	0	3800	2199	2.34
182	182	181	sandstone	water	0	4400	2682	2.44
183	183	182	sandstone	water	0	4600	2482	2.46
184	184	183	shale	water	0	4700	2752	2.63
185	185	184	shale	water	0	3800	2059	2.48
186	186	185	shale	water	0	3700	1982	2.47
187	187	186	sandstone	water	0	3550	1998	2.30
188	188	187	shale	water	0	4050	2252	2.53
189	189	188	shale	water	0	3750	2021	2.47
190	190	189	shale	water	0	4400	2521	2.58
191	191	190	shale	water	0	4200	2367	2.55
192	-	191	shale	water	0	4100	2290	2.53

Key

shale
wet sand
gas sand
oil sand
water
marl
salt

Vs transform — **Greenburg and Castagna (1992) shear wave transform**
ρ transform — **Castagna *et al*. (1993) density transform**

Table 2.8. Marmousi2 horizons, layers, and elastic properties. Details of the shear wave velocity and density transforms are presented in Table 2.3

3. Synthetic Data Generation

3.1 Acquisition Objectives

The major acquisition objectives for Marmousi2 were to create a high quality, multi-component, high frequency, elastic synthetic dataset over a complex structural model.

3.2 Seismic Modeling

In order for seismic model data to be useful for calibrating data processing and algorithms it must accurately emulate the physical experiment. At the very least, the forward modeling methods must be more accurate than the inverse methods that will be tested, Gray *et al.*, 2001.

Seismic modeling takes one of two forms, physical modeling or numerical modeling. Physical modeling requires the construction of a scaled earth model with sources, receivers, wavelengths, and recording times all scaled in such a way that the length of model features in terms of their wavelengths are preserved. Physical models tend to possess few layers due to the difficult nature of creating the models, and are best suited to 3D modeling where numerical methods are outrageously CPU intensive.

Numerical modeling involves the creation of a seismic model in the computer, and as such can be precisely defined with as many layers as desired. The results are as exact as the computation algorithm, which should avoid numerical problems such as instability and numerical dispersion. Numerical models also allow us to record the wavefield within the model (so called “snapshots”) at little additional cost. For complex 2D models numerical methods are preferred to physical methods.

Traditionally, numerical modeling for the creation of synthetic seismic data has utilized ray based techniques. These methods use the equations of Zoeppritz (1919) to partition the energy at boundaries inside the Earth that are caused by changes in the material property. The calculations are fast enough for desktop workstations and sufficiently flexible to model complex ray-paths including multiples and mode conversions. Although these equations are quite accurate, the ray tracing method tends to break down under the presence of large velocity variations and complex structure. In these cases the velocity must be heavily smoothed to achieve reasonable ray coverage. Seismic energy travels as waves in the subsurface, and a ray approximation is not appropriate for areas of complex velocity variation. In particular, ray methods do not accurately predict head wave amplitudes, which may strongly influence AVO at farther offsets. Ray-based methods are therefore not suitable for the task of creating synthetic data for modern seismic processing calibration, or the investigation of AVO in the presence of structure.

Wave-equation methods are preferred in these complex areas because they describe wave propagation, which is how the seismic energy actually travels. In addition, wave equation methods handle arbitrary velocity variations in the model (no smoothing is required), and all waveforms are incorporated implicitly.

Wave equation propagation can be described by the scalar wave equation (also called the acoustic wave equation), or by the elastic wave equation. The acoustic wave equation describes the propagation of compressional waves (P-waves), and therefore ignores the propagation of shear waves (S-waves) and mode conversion (the conversion of energy traveling as compressional waves into energy traveling as shear waves and *vice-versa*). The elastic wave equation describes the propagation of both compressional

and shear waves, and implicitly handles mode conversions. Forward modeling with the elastic wave equation should therefore provide data with all the seismogram events including primaries, multiples, head wave events, and also anisotropic and mode conversion effects. The modeling is typically performed using a discrete approximation of the differential equations, *i.e.* a finite difference approach. Using wave based techniques for AVO calibration requires that full elastic propagation be used, since mode conversion and shear propagation are essential to the AVO process.

Interestingly, runtimes for ray based and wave based modeling for complex models such as Marmousi2 reverses the conventional wisdom. Testing showed that in order to get meaningful raytracing results extremely dense ray coverage was required, and the CPU time to compute standard reflection rays for 10 layers was similar to the CPU time required to compute the full waveform modeling with finite difference techniques! There are almost 200 layers in Marmousi2, and therefore modeling with ray-based methods would take much longer.

3.3 Synthetic Data Acquisition

3.3.1 Geometry

A full set of elastic shot records have been acquired over the model. The spacing of the sources and receivers are shown in Table 3.1, and Figure 3.1.

Sources	X (m) origin	end	inc.	#	Depth	Type
Towed source	3000	14975	25	480	10m	Airgun

Streamer & OBC Receivers	X (m) origin	end	inc.	#	Depth	pressure	Vz	Vx
Streamer	0	17000	12.5	1361	5	yes	no	no
OBC	0	17000	12.32	1381	450	yes	yes	yes

VSP Receivers	X (m) location	#	Z (m) origin	end	inc.	#	pressure	Vz	Vx	shear
VSPs	10300	1	0	3500	12.5	281	yes	yes	yes	yes

Table 3.1. Source and receiver geometry for Marmousi2 acquisition.

The source is a synthetic air gun with a firing depth of 10m. The sailing direction for the source vessel is from low X (left) to high X (right).

The source signature is a zero-phase 5-10-60-80 Ormsby wavelet with frequencies up to 80Hz, as shown in Figure 3.2. The computation of 2D models typically involves the use of a 'line source' due to the nature of the modeling. A line source differs considerably from a 'point source'. Real 2D data is of course acquired in a 3D world with 3D spherical divergence, *etc.*, and is therefore a point source which makes it necessary to correct the source for Marmousi2. The modification takes the form of a 45 degree phase rotation, time shift, and frequency filter. Most of the change occurs in near field signature; the far field wavelet and frequency spectra are not changed, Figure 3.2.

The data were recorded using receivers located on two horizontal surfaces (the streamer and OBC surfaces), and one vertical surface (the VSP surface).

The “streamer” cable recorded a hydrophone response (pressure) at 1361 locations with a group interval of 12.5m, representing a currently unrealistic 17km cable. The cable was fixed at a depth of 5m, and was also fixed in space during the acquisition.

The “OBC” cable recorded pressure, the vertical component of particle velocity (Vz), and the horizontal component of particle velocity (Vx), using a hydrophone and two orthogonal geophones respectively. The cable was fixed at the waterbottom (450m) and was fixed in space, having 1381 locations and a group interval of 12.32m. The unusual grouping distance resulted from parameterization difficulties within the modeling software.

The vertical cables recorded a simulated VSP response. The “VSP” cable recorded both the hydrophone and two-component geophone responses. In addition a theoretical “shear phone” was used. Shear phones do not exist in the real world, but can be simulated in the modeling software, recording only the shear wave component of the energy. The vertical cable started at the free surface and the receiver groups were spaced at 12.5m in depth and were recorded to the depth of 3500m, making a total of 281 receiver groups. The cable was located at X=10300m.

Every receiver was “live” (recorded data) for every shot, so the offset distribution of the data has not been limited to standard streamer lengths or geometries.

3.3.2 Model Boundaries

The data were acquired with a reflecting free surface, which simulates an air water interface. The reflecting free surface is commonly the most significant source of multiples in marine data. The remaining boundaries are absorbing, that is energy

passing out of the model does not reflect back into the model. Clayton Engquist (1990) boundary conditions were employed by E3D to provide absorbing model margins.

3.3.3 Calculation Grid

The calculation grid size was evaluated by testing and practical limitations. The grid sampling can be calculated using the equation below,

$$grid.sampling = \frac{\min.velocity}{\max.frequency * samples.per.wavelength}$$

In order to avoid numerical dispersion approximately 5 samples per wavelength are required for the slowest velocity in the model (Levander, 1988).

The slowest velocity is approximately 270 m/s (shear wave velocity), and the maximum frequency is 80Hz. Theoretically, using 5 samples per wavelength, this requires a grid size of 0.42m, which was impractical for the assigned computational resources. However, looking more closely at the model it is clear that only a very small portion of the model has velocities with values this low. A more reasonable average minimum shear wave velocity is around 400m/s. The required grid size becomes 1m for 80Hz, 1.14m for 70Hz, and 1.33m for 60Hz.

Practical memory and runtime limitations result in a compromise. The final grid spacing was 1.25m. This gives only 2.7 samples per wavelength for the very highest frequency and absolute minimum velocity, which will result in some dispersion of the wavefield. However, for all velocities over 400m/s and all frequencies below ~65Hz, there should be no dispersion.

3.3.4 Computation

The University of Houston provided the computational resources to create the synthetic data, with funding from Next Generation Modeling and Imaging Project. I used twenty nodes of a Sun 6800 Starfire system for a total of five months.

The E3D modeling algorithm developed at Lawrence Livermore National laboratory was used to perform the finite difference calculations. E3D (Larson and Grieger, 1998) is a general wave propagation algorithm applicable to diverse problems of wave propagation including those outside of the geophysical industry. The algorithm uses a finite difference scheme that is second order accurate in time and fourth order accurate in space.

The computation time averaged about 20 hours per shot using 6 nodes of the system, *i.e.* about 4 ½ CPU days per shot. The data were acquired between September 2002 and January 2003, using a total of five CPU months, which is equivalent to 70,000 CPU hours, or approximately 8 CPU years!

3.4 Results

The following data were acquired:

- Wavefront snapshots
- Surface seismic shot records
- OBC seismic shot records
- VSP seismic shot records

3.4.1 Wavefront Snapshots

The snapshots were recorded on a 1.25m grid covering the entire model. The time interval between snapshots is 100ms, making a total of 50 snapshots within the time range of 0.1 seconds – 5.0 seconds. There are two snapshots for each shot, representing P-waves and S-waves. Snapshots were only recorded for every 40th shot, due to their large size and storage requirements. The fourteen snapshot locations are spaced evenly every 1000m, from 3000m to 15000m.

The snapshot figures use a custom color wheel and blending to combine the P-waves and S-waves, as shown in Figure 3.3. The P-waves appear with a blue-yellow colorscale, and the S-waves appear with a pink-green colorscale. The Marmousi2 P-wave interval velocity model is also mapped to a greyscale image behind the wavefronts.

Figure 3.4 shows a zoomed image of one snapshot (t=1.4s) with certain features labeled. The full set of wavefront snapshots for shot #201 (X=5000m) are shown in Figures 3.5 – 3.54.

The snapshots clearly show that the water bottom is a strong multiple generator. The high velocity beds reflect a large amount of energy, which reduces energy propagating to the deeper parts of the model. There is also an abundance of mode conversion of energy taking place within the subsurface. The stronger (higher acoustic impedance) events tend to be the source for much of the mode conversion.

3.4.2 Streamer and OBC Shot Records

The shot records were recorded with a time sampling of 2ms and a record length of 5 seconds. Figure 3.55 shows the surface seismic shot record for shot #285

(X=7100m). Figures 3.56 – 3.58 show the OBC shot records, also for shot #285 (X=7100m). Certain features are identified and labeled in the figures.

The shot records closely resemble real field shot records, both in terms of the number of events and complexity. The elastic modeling has appeared to create very realistic data from the synthetic model.

3.4.3 VSP Shot Records

The single vertical cable, located at X=10300m, recorded data for every shot. Therefore there are 480 records for each of the hydrophone, Vz geophone, Vx geophone, and shear phone receivers. A suite of VSP records for a near-offset location (shot #412, X=10275m, source to receiver offset of 25m) is shown in Figures 3.59. A suite of VSP records for a relatively far-offset location (shot #212, X=5275m, source to receiver offset of 5025m) is shown in Figures 3.60. Certain features are identified and labeled for the near offset VSP in Figures 3.61 – 3.64.

The near offset VSP records show that energy propagating into the earth is dominantly P-wave energy, but that considerable mode conversion is taking place.

3.4.4 Summary

The acquired data appear to have satisfied the acquisition objectives. This has been achieved by:

- Simultaneously recording streamer, OBC, and VSP acquisition
- Recording multi-component data for OBC and VSPs
- Employing an elastic simulation method using a high order finite difference scheme with a high frequency input wavelet and a very dense computational grid

- Recording wave-front snapshots for P-waves and S-waves

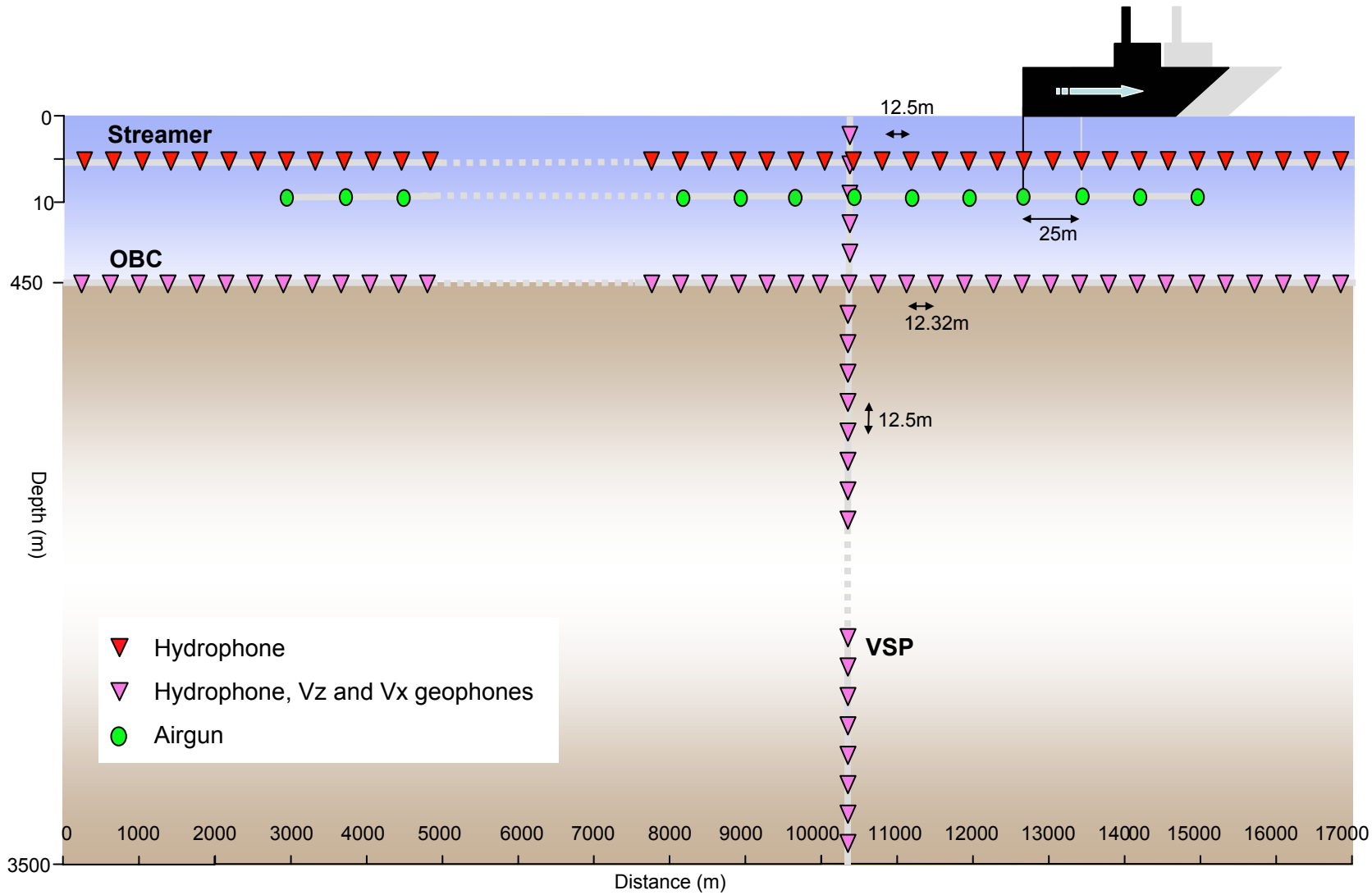

Figure 3.1. Acquisition Geometry for Marmousi2. Diagram is schematic, and not to scale.

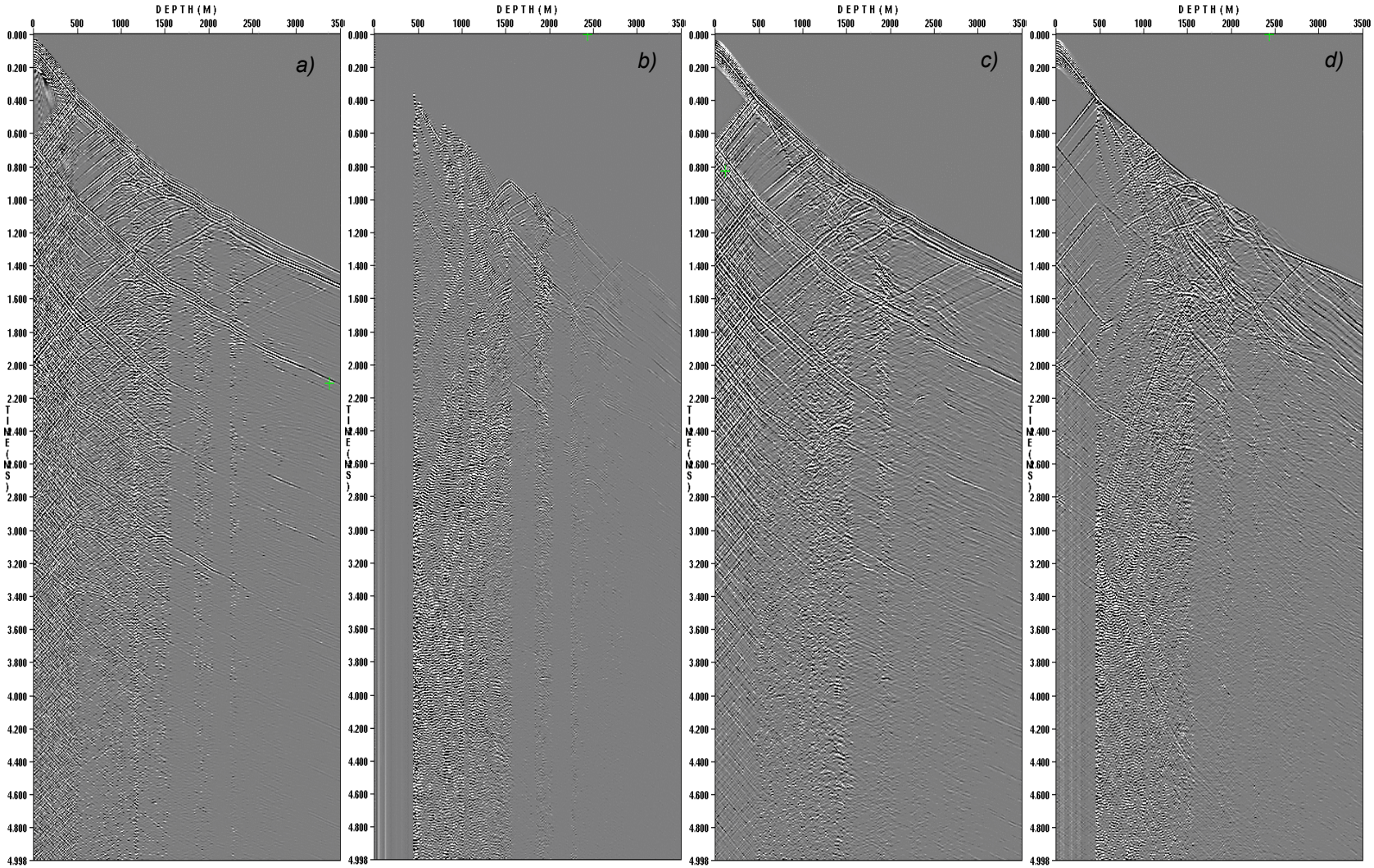

Figure 3.59. VSP for shot #412, (at 10275m, CDP 1645). Source to VSP offset is 25m. Downgoing energy is dipping to the right side of the figures, upgoing energy is dipping to the left side. a) hydrophone records P-waves, b) theoretical shear phone records S-waves, c) vertical component geophone records both P-waves and S-waves, d) horizontal component geophone also records both P-waves and S-waves.

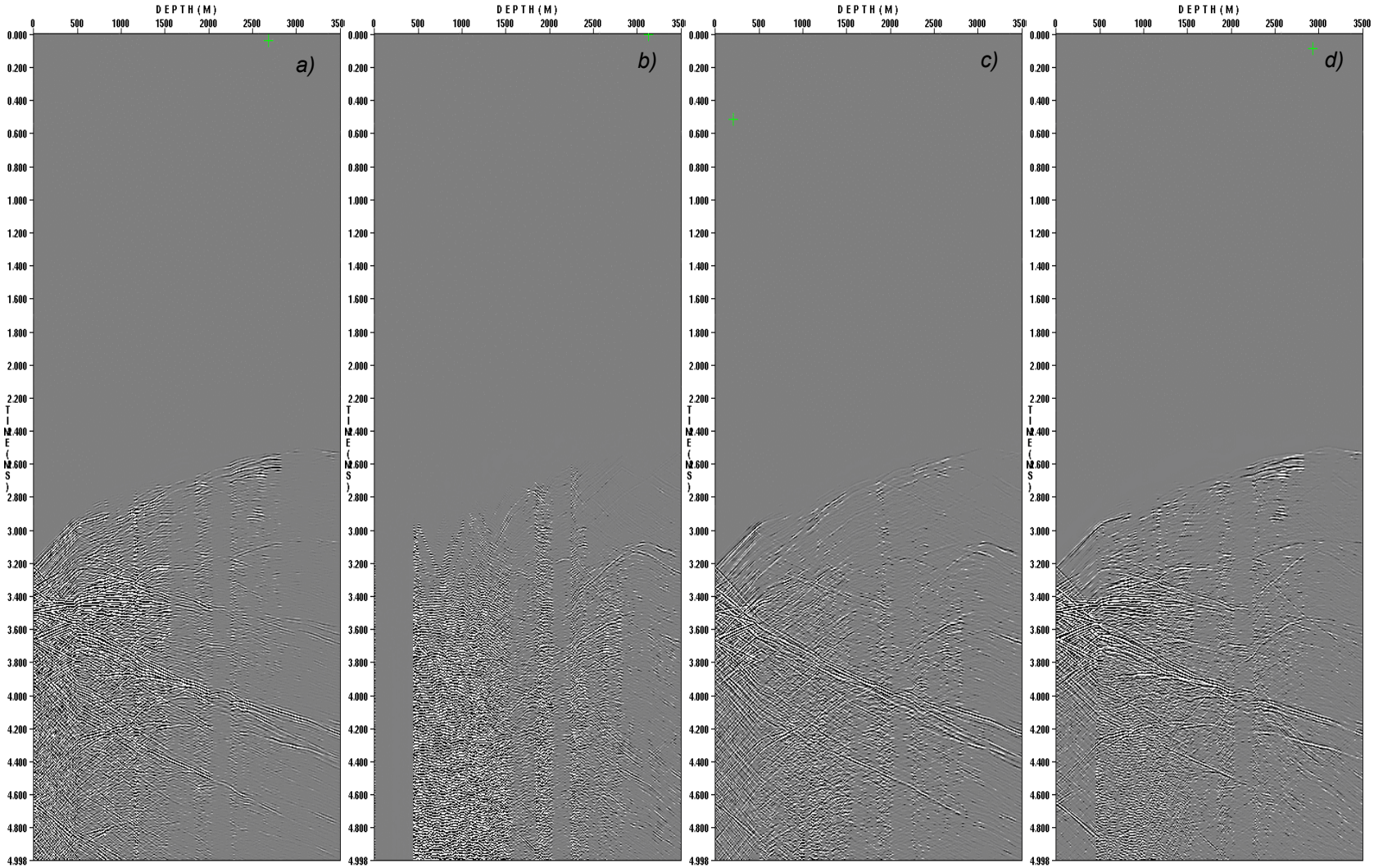

Figure 3.60. VSP for shot #212, (at 5275m, CDP 845). Source to VSP offset is 5025m. Downgoing energy is dipping to the right side of the figures, upgoing energy is dipping to the left side. a) hydrophone records P-waves, b) theoretical shear phone records S-waves, c) vertical component geophone records both P-waves and S-waves, d) horizontal component geophone also records both P-waves and S-waves.

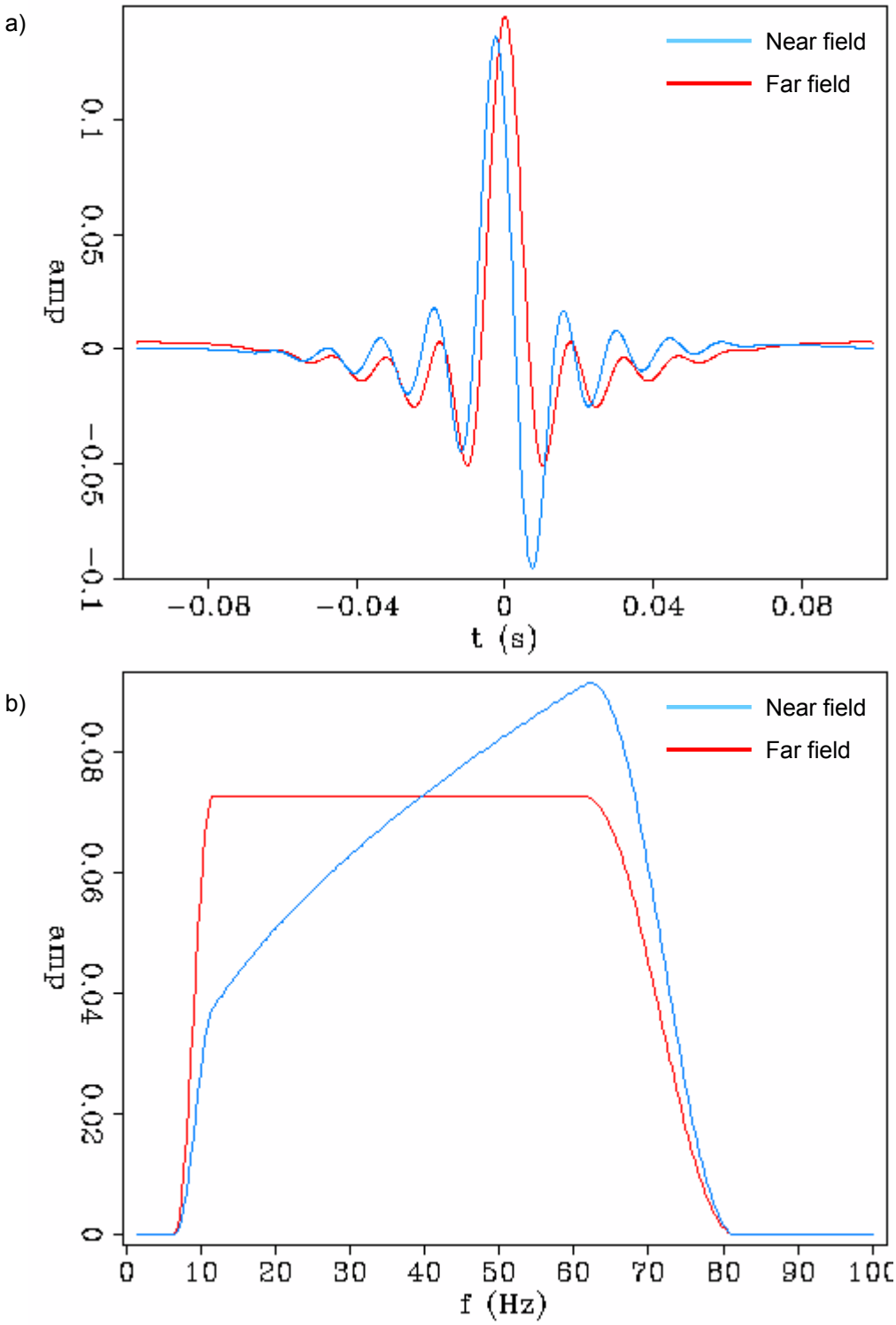

Figure 3.2. a) wavelet and b) amplitude spectra for the source. The blue line represents the actual modeling source wavelet and also characterizes the signature in the near field. It was derived from the 5-10-60-80 Hz Ormsby wavelet (red line) by applying modifications to produce a point source rather than a line source. The red line is the initial 5-10-60-80Hz Ormsby wavelet, and also represents the modeling signature in the far field.

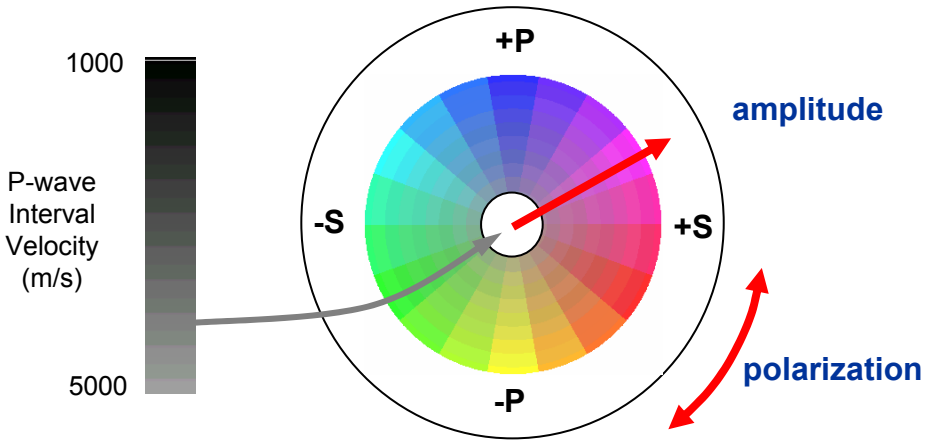

Figure 3.3 Wavefront snapshots are displayed with a custom color wheel, enabling P-waves and S-waves to be combined. Interval velocity is mapped to zones of low seismic amplitude to allow a structural representation of the model to be included.

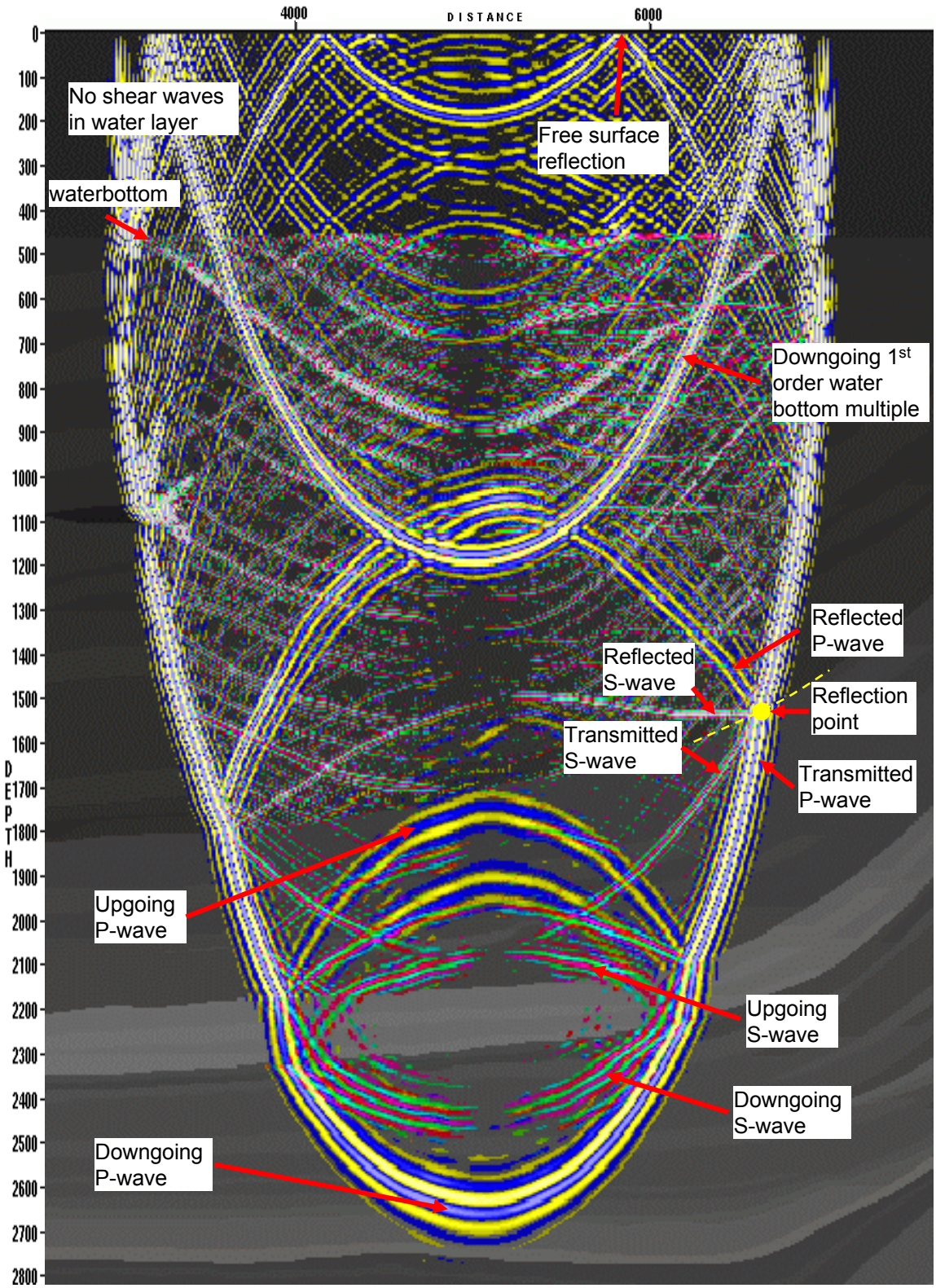

Figure 3.4. Wavefront snapshot for source #201 (at X=5000m), and t=1.4s. Certain downgoing and upgoing P-waves (blue-yellow) and S-waves (red-green) are labeled.

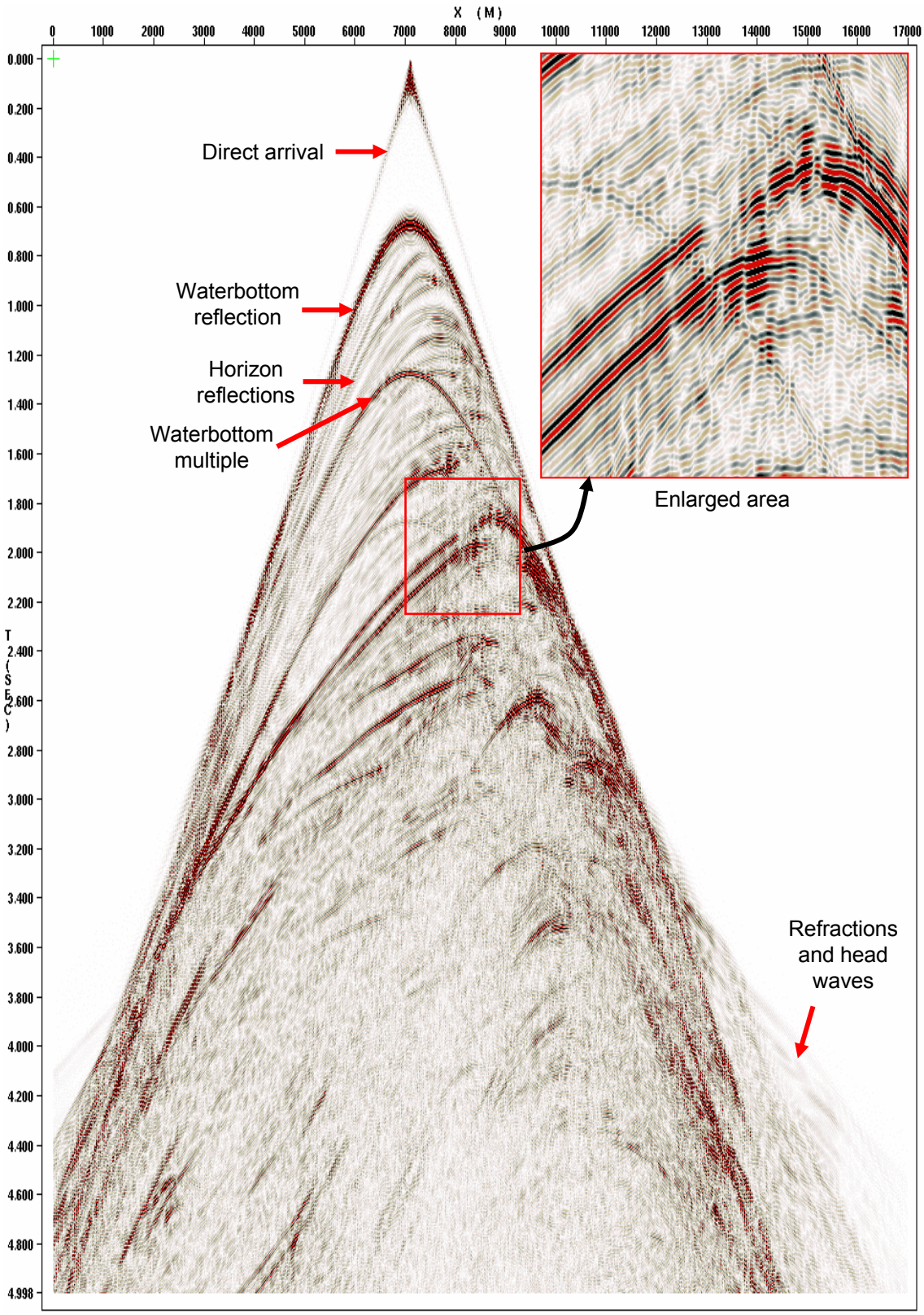

Figure 3.55. Streamer pressure, shot record #285 (X=7100m)

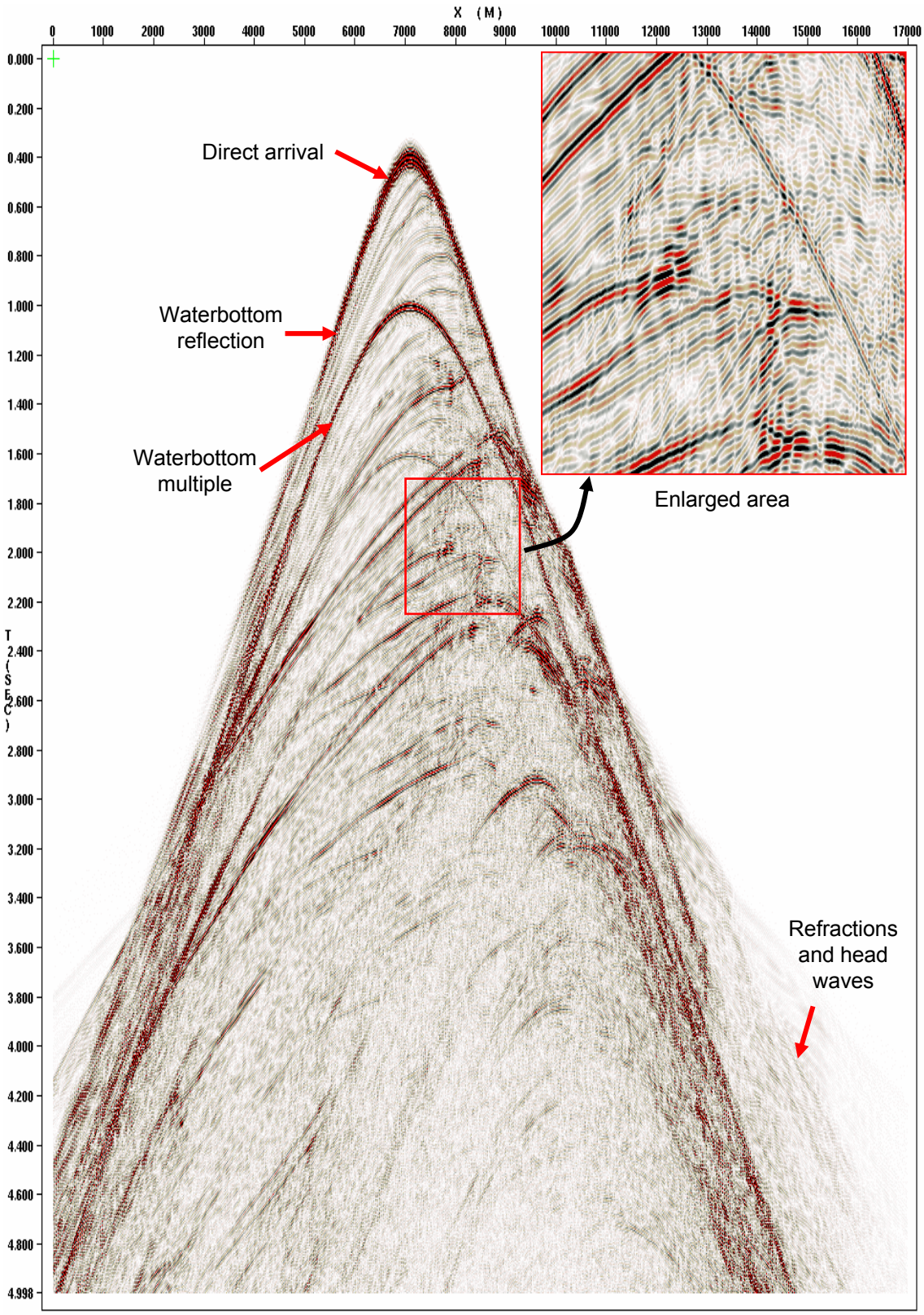

Figure 3.56. OBC pressure, shot record #285 (X=7100m)

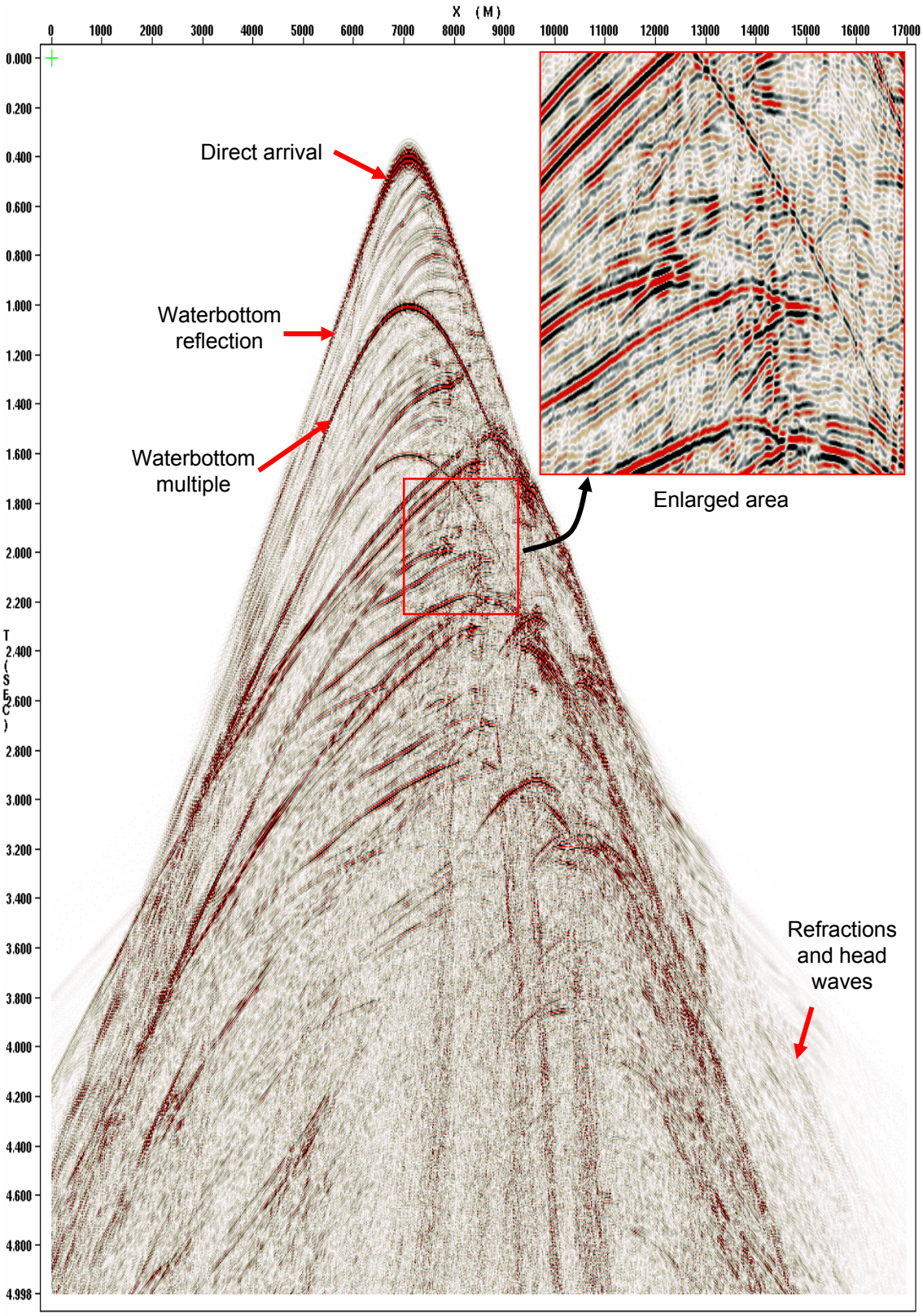

Figure 3.57. OBC vertical velocity, shot record #285 (X=7100m)

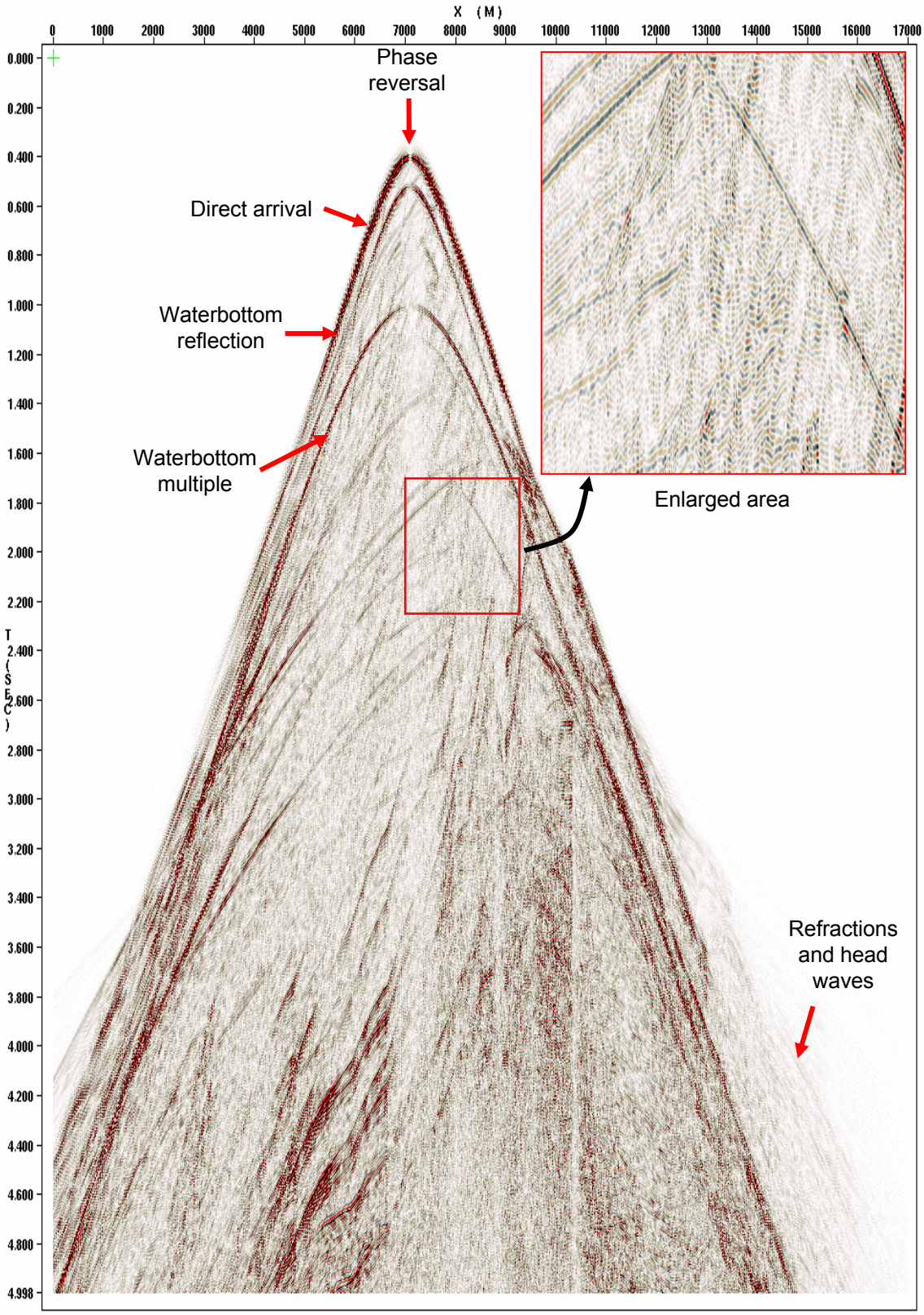

Figure 3.58. OBC horizontal velocity, shot record #285 (X=7100m)

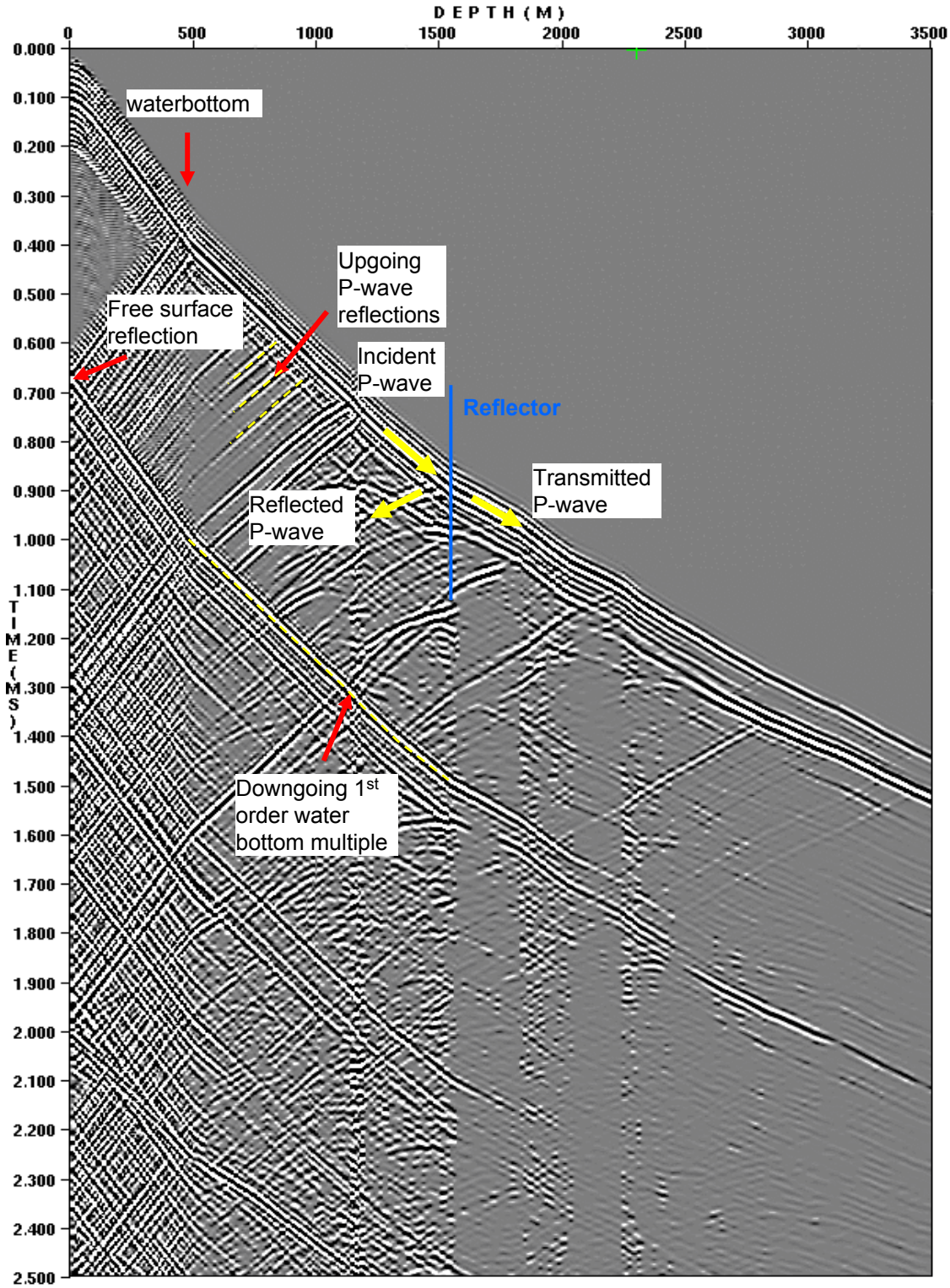

Figure 3.61. VSP for shot #412, (at 10275m, CDP 1645), hydrophone instrument. Source to VSP offset is 25m. Only P-waves are recorded by the hydrophone. Downgoing energy is dipping to the right side of the figure, upgoing energy is dipping to the left side. Various features are labeled.

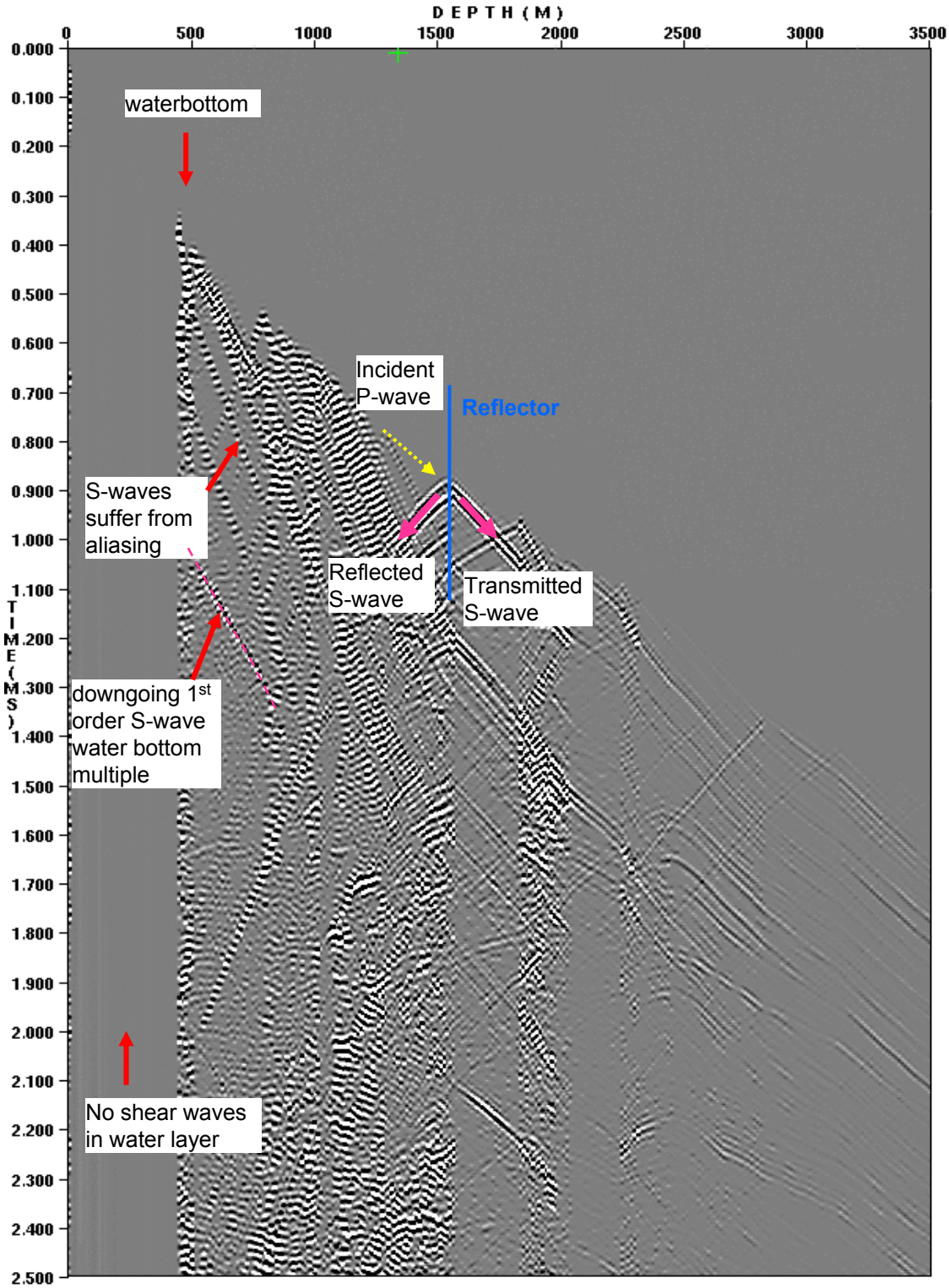

Figure 3.62. VSP for shot #412, (at 10275m, CDP 1645), synthetic shear wave instrument. Source to VSP offset is 25m. Only S-waves are recorded by the theoretical device. Downgoing energy is dipping to the right side of the figure, upgoing energy is dipping to the left side. Various features are labeled.

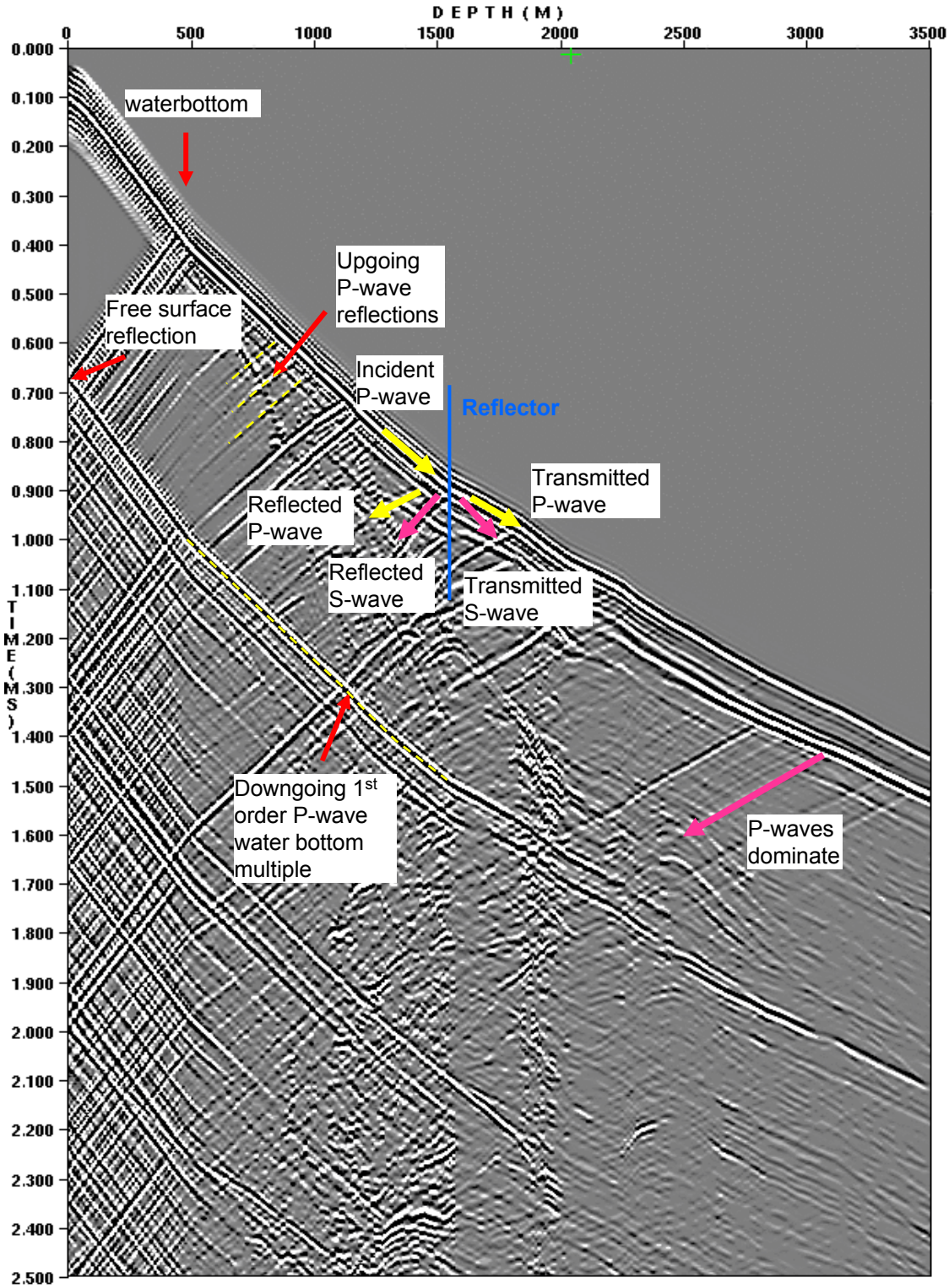

Figure 3.63. VSP for shot #412, (at 10275m, CDP 1645), vertical geophone instrument. Source to VSP offset is 25m. Both P-waves and S-waves are recorded by the geophone, but P-waves dominate. Downgoing energy is dipping to the right side of the figure, upgoing energy is dipping to the left side. Various features are labeled.

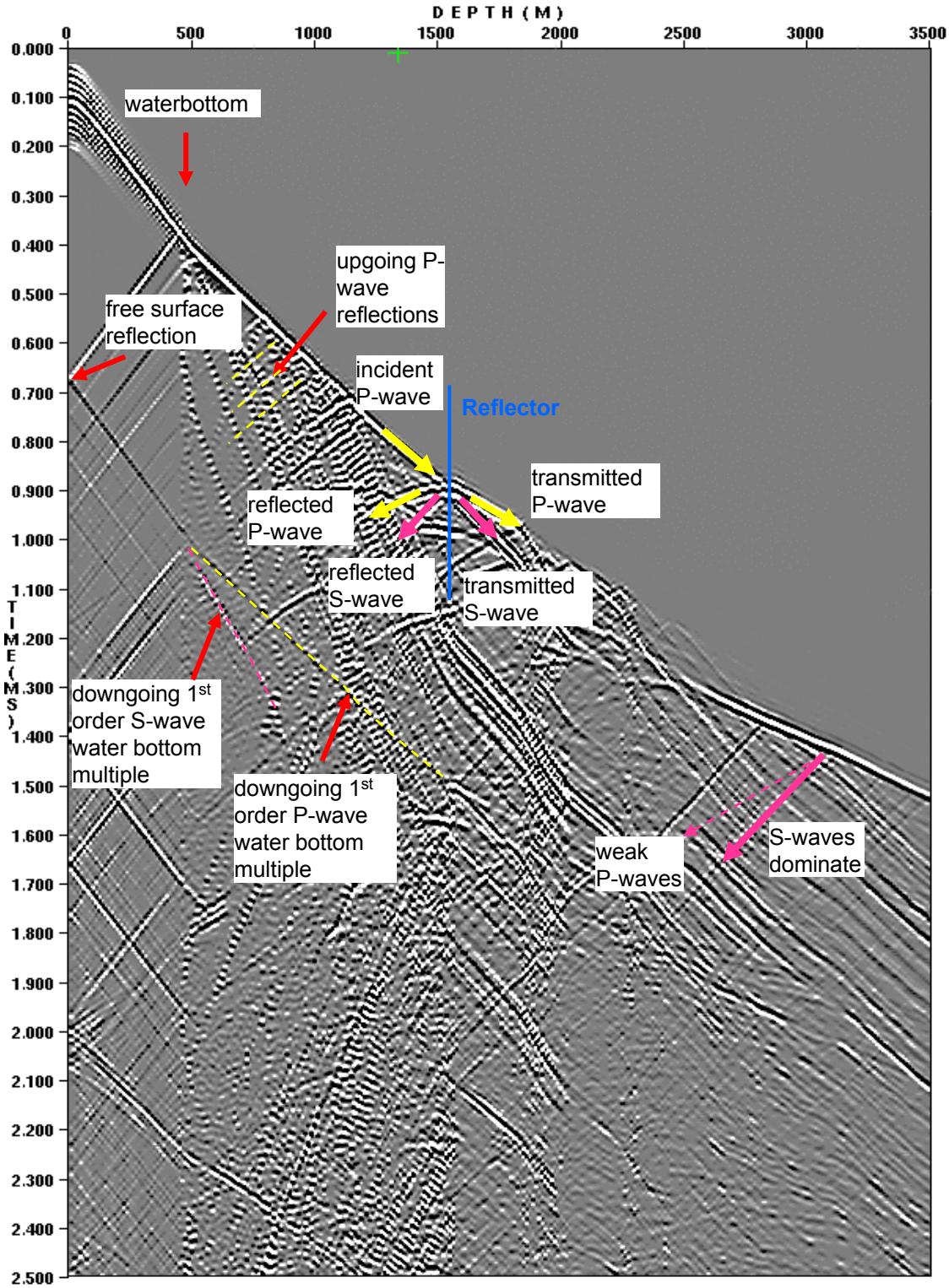

Figure 3.64. VSP for shot #412, (at 10275m, CDP 1645), horizontal geophone instrument. Source to VSP offset is 25m. Both P-waves and S-waves are recorded by the geophone, but S-waves dominate outside of the water column. Downgoing energy is dipping to the right side of the figure, upgoing energy is dipping to the left side. Various features are labeled.

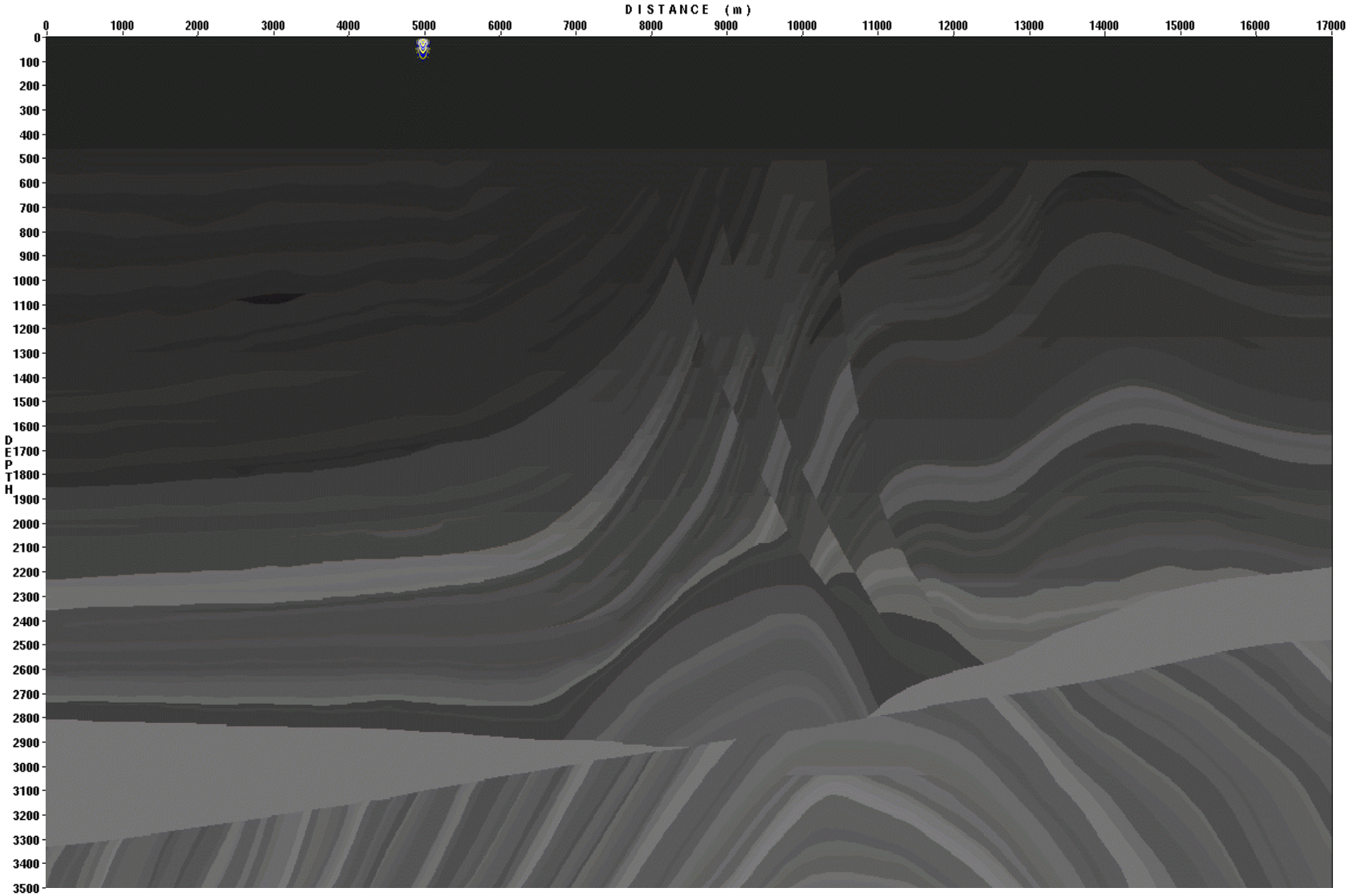

Figure 3.5. Wave propagation snapshot at t=0.1s. P-waves are blue-yellow, S-waves are red-green, model is greyscale

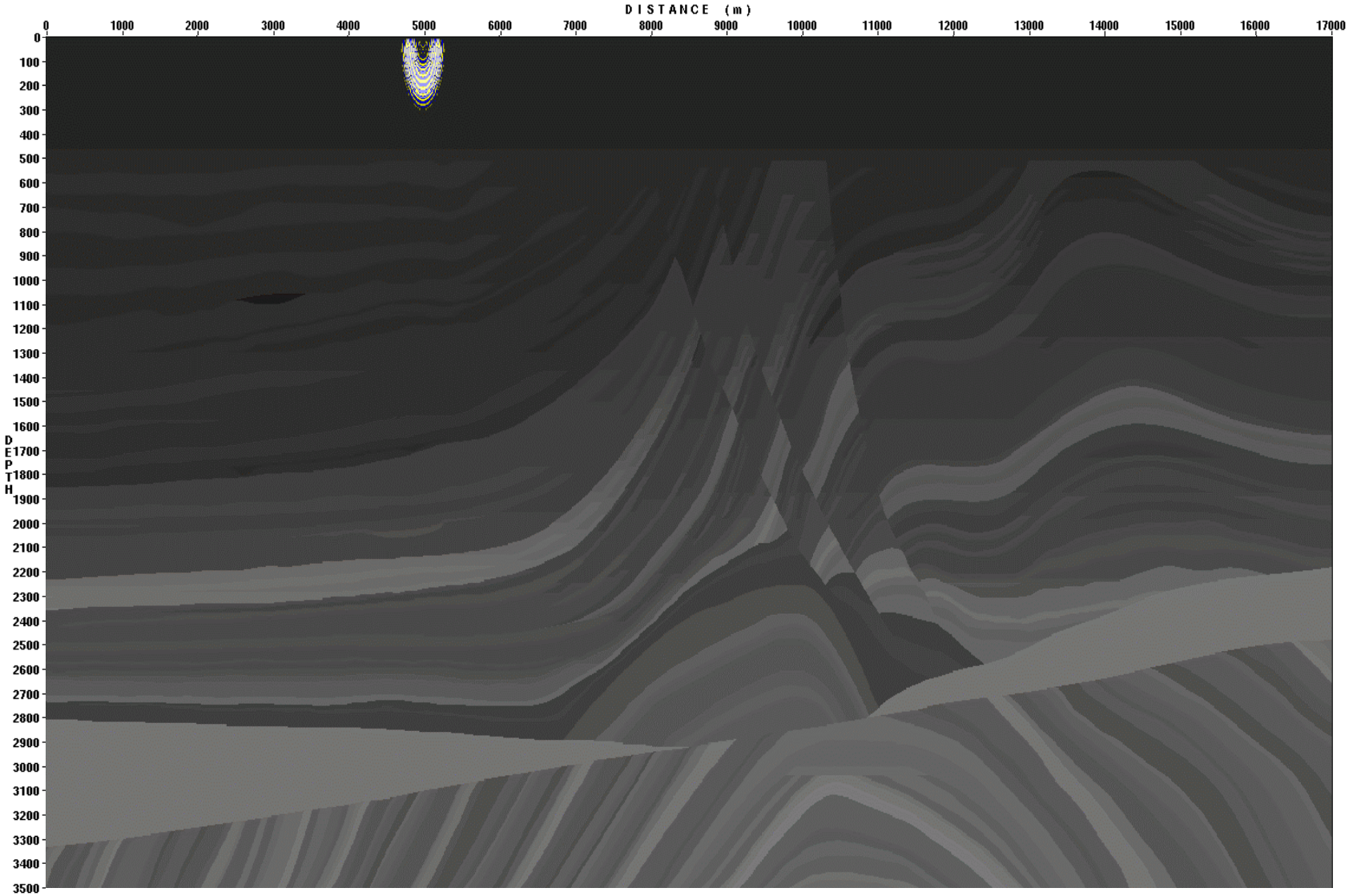

Figure 3.6. Wave propagation snapshot at t=0.2s. P-waves are blue-yellow, S-waves are red-green, model is greyscale

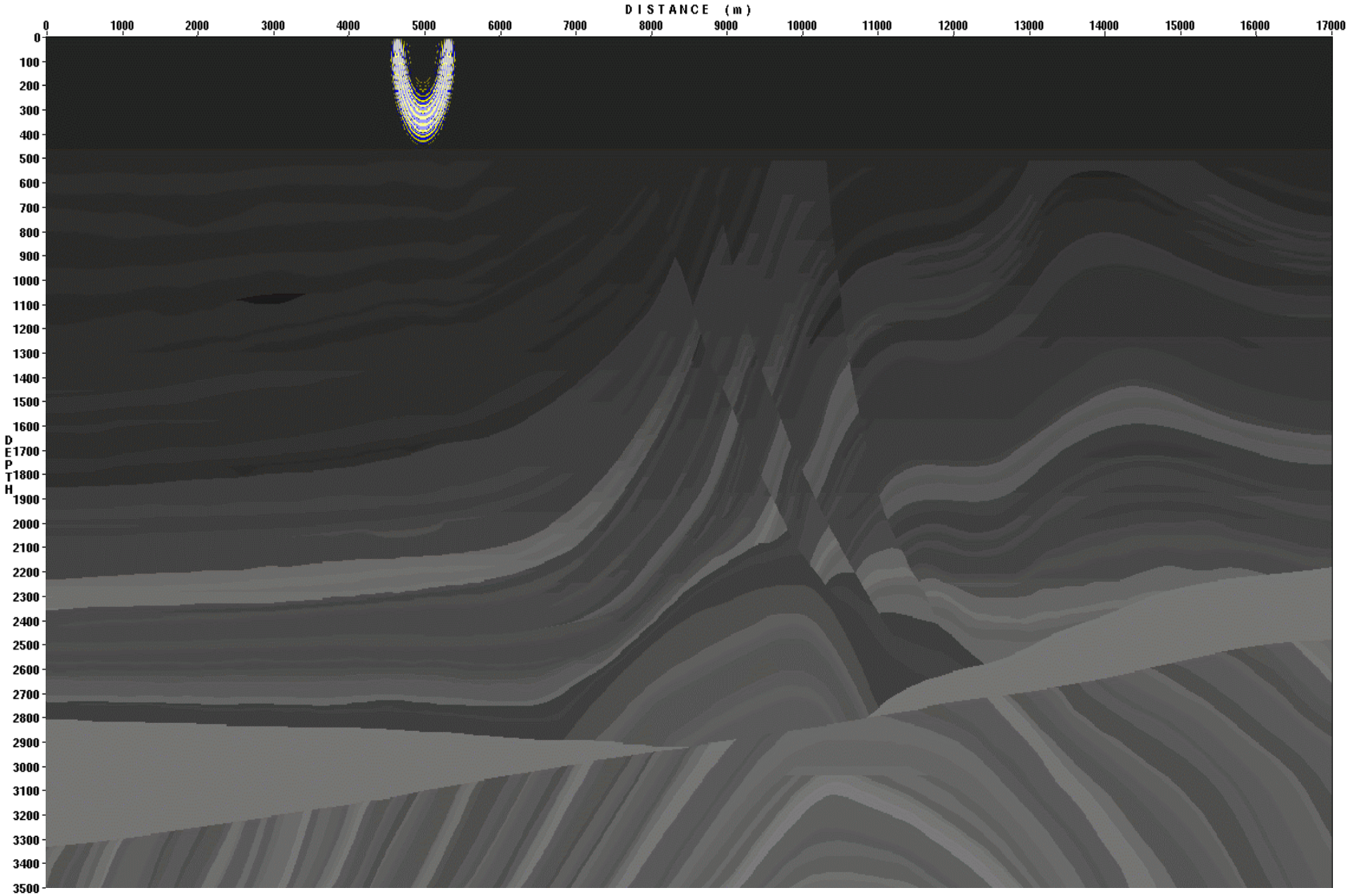

Figure 3.7. Wave propagation snapshot at t=0.3s. P-waves are blue-yellow, S-waves are red-green, model is greyscale

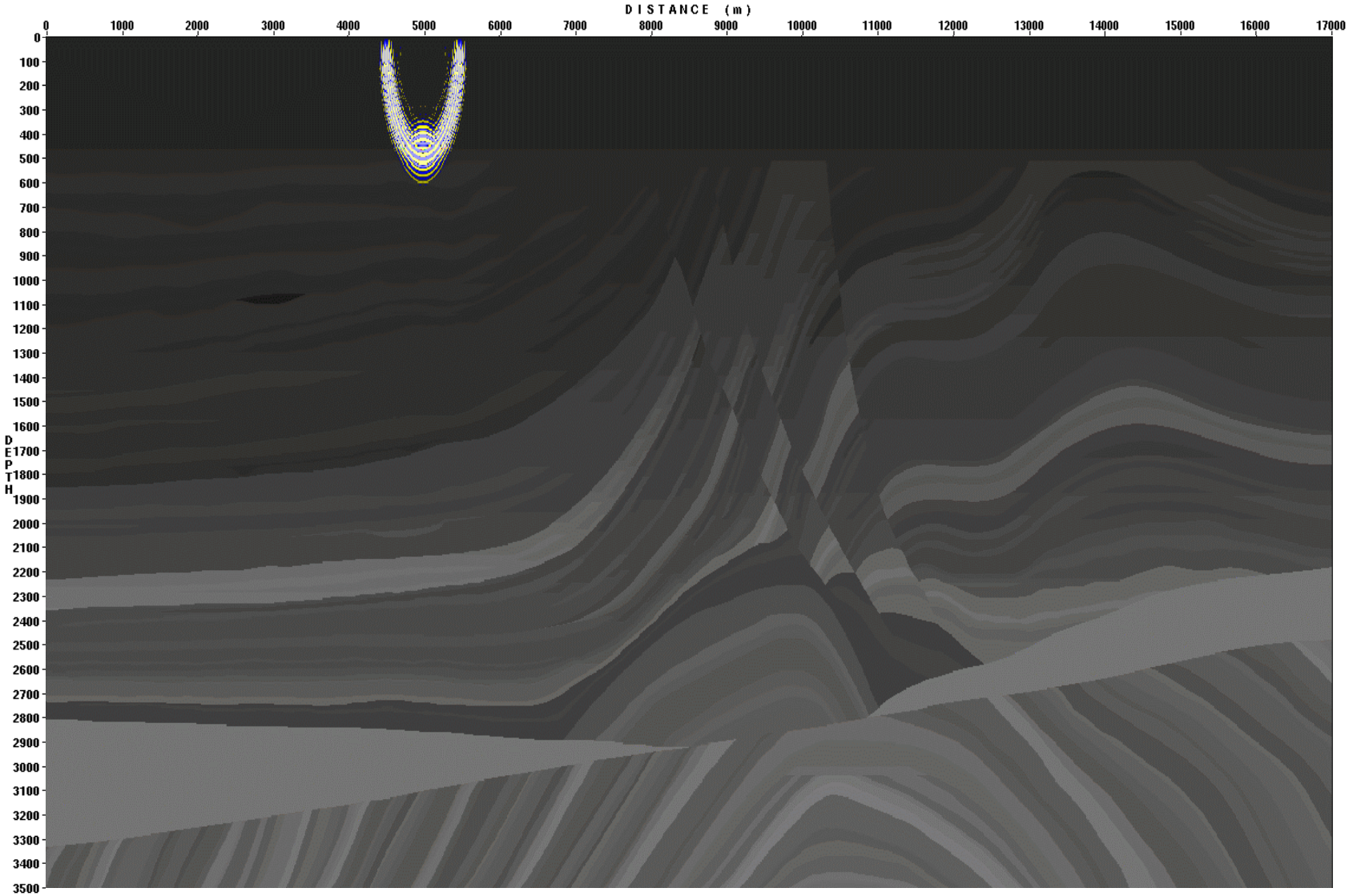

Figure 3.8. Wave propagation snapshot at t=0.4s. P-waves are blue-yellow, S-waves are red-green, model is greyscale

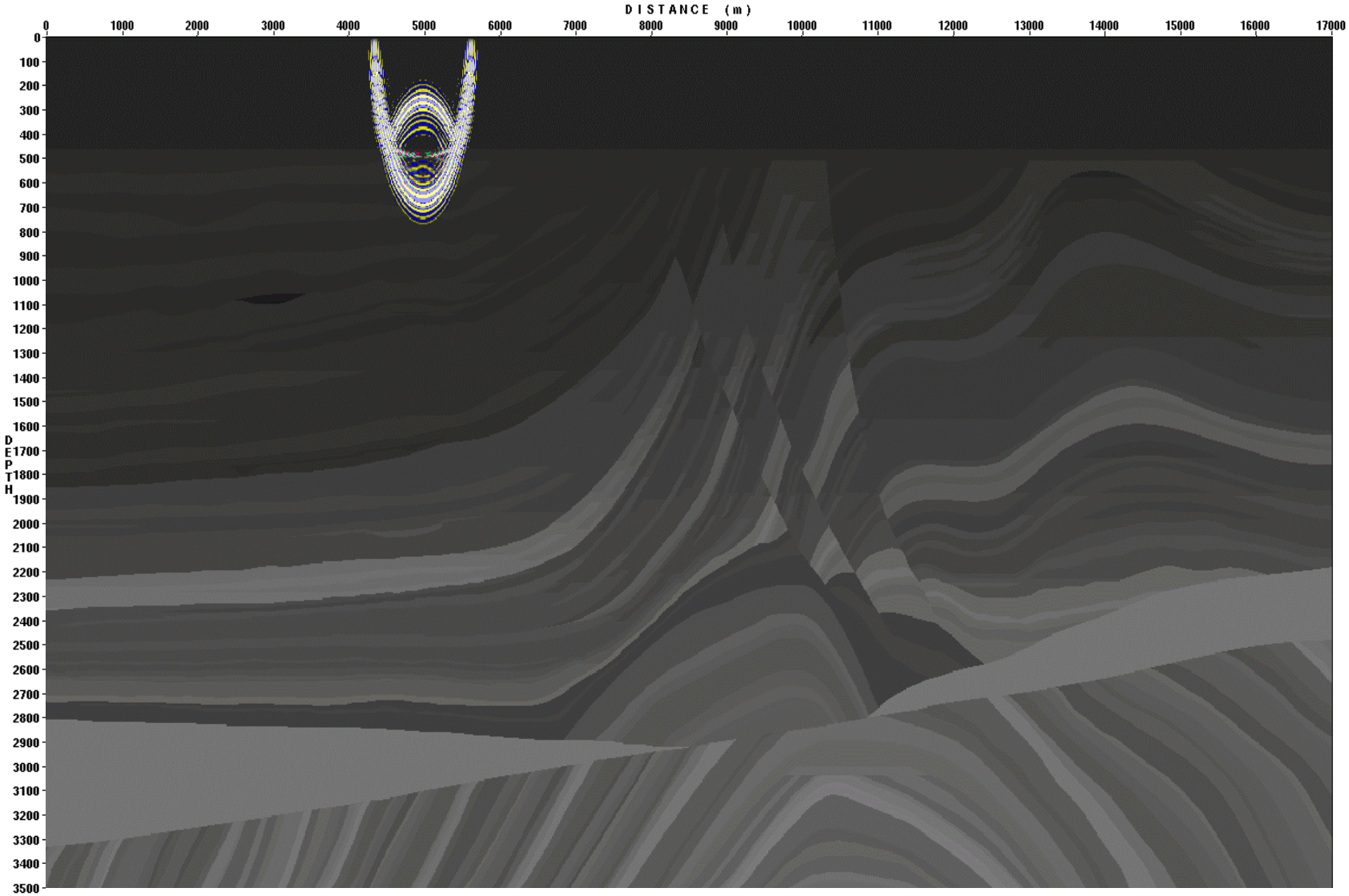

Figure 3.9. Wave propagation snapshot at t=0.5s. P-waves are blue-yellow, S-waves are red-green, model is greyscale

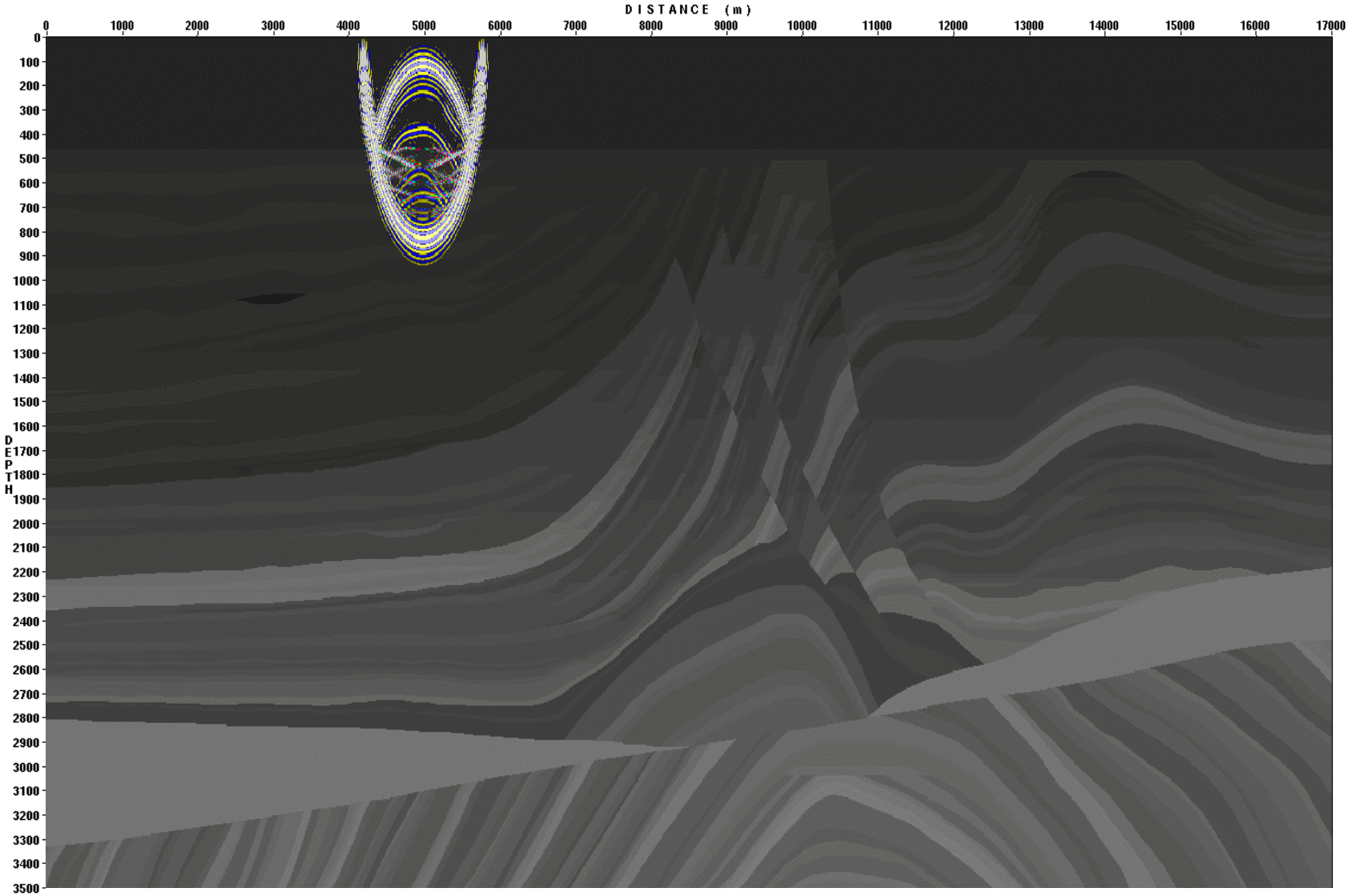

Figure 3.10. Wave propagation snapshot at t=0.6s. P-waves are blue-yellow, S-waves are red-green, model is greyscale

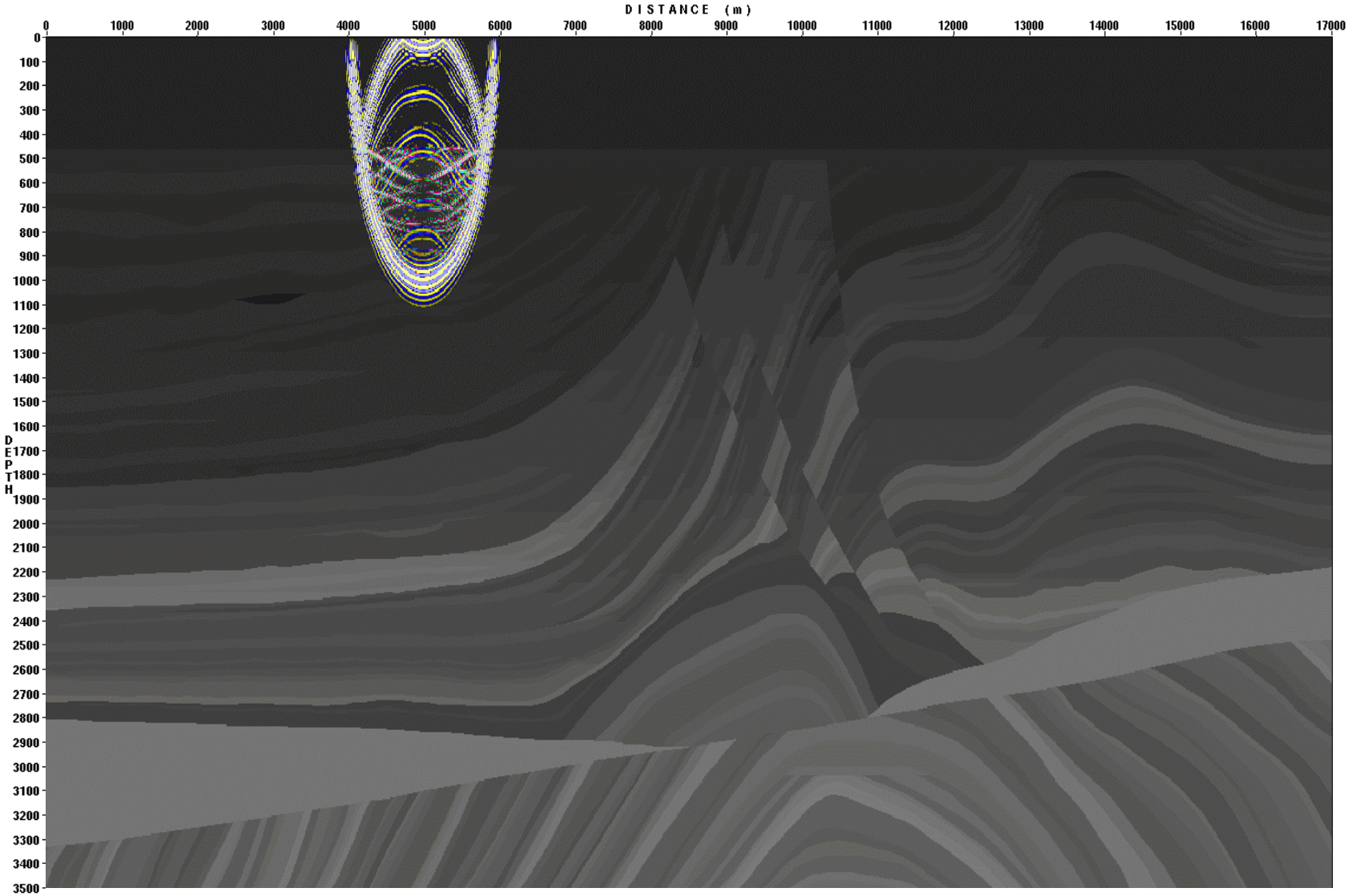

Figure 3.11. Wave propagation snapshot at t=0.7s. P-waves are blue-yellow, S-waves are red-green, model is greyscale

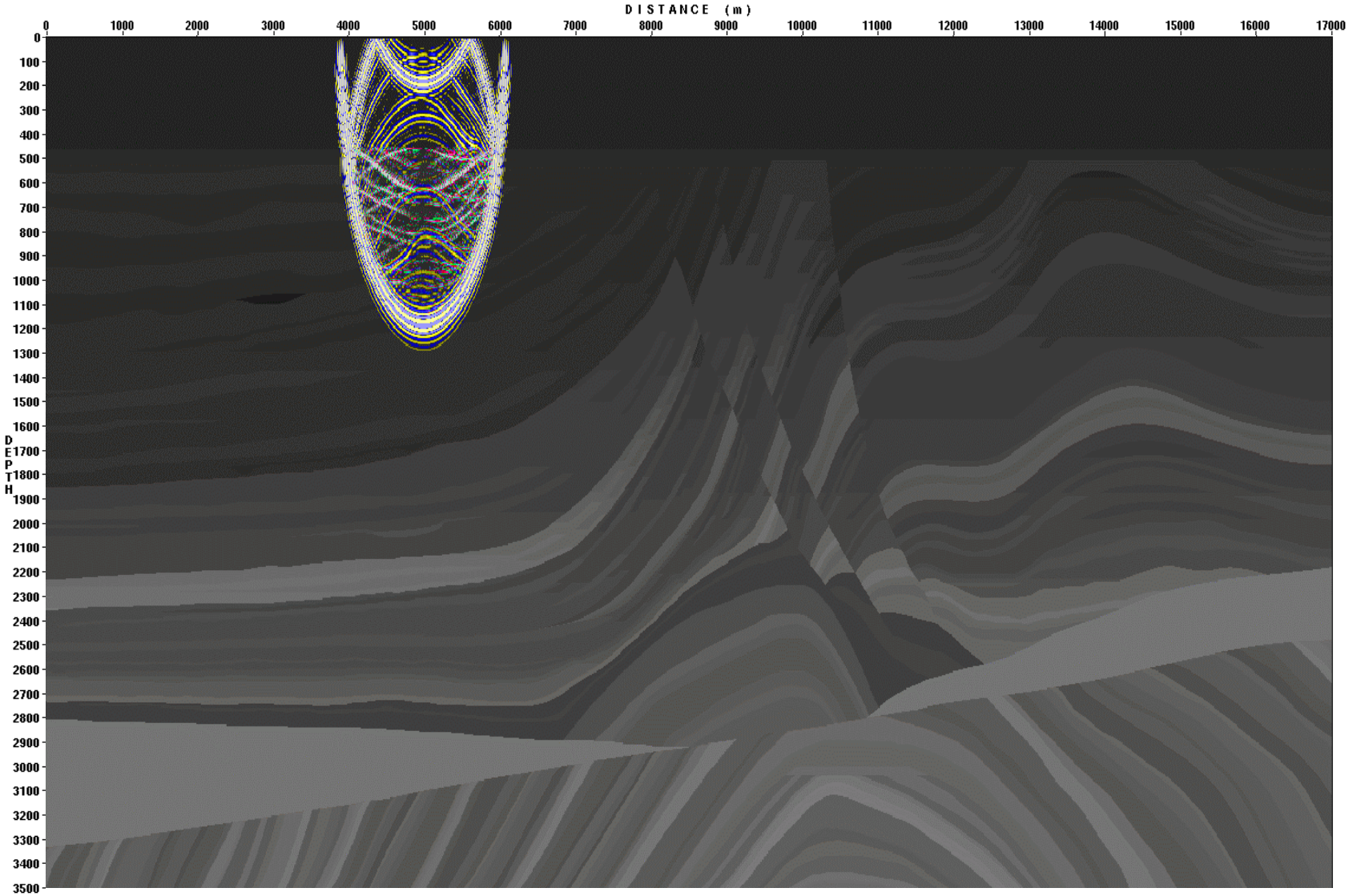

Figure 3.12. Wave propagation snapshot at t=0.8s. P-waves are blue-yellow, S-waves are red-green, model is greyscale

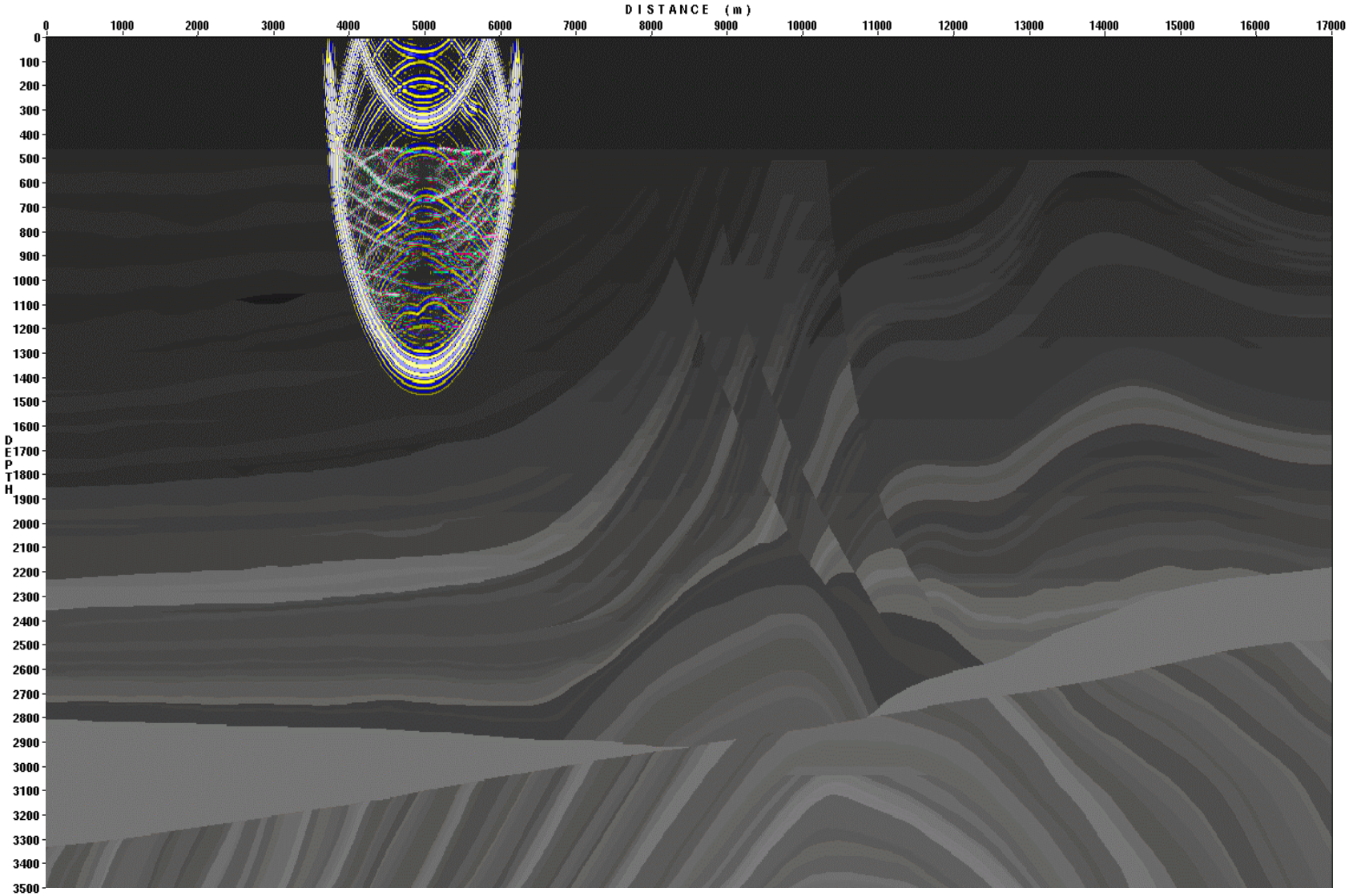

Figure 3.13. Wave propagation snapshot at t=0.9s. P-waves are blue-yellow, S-waves are red-green, model is greyscale

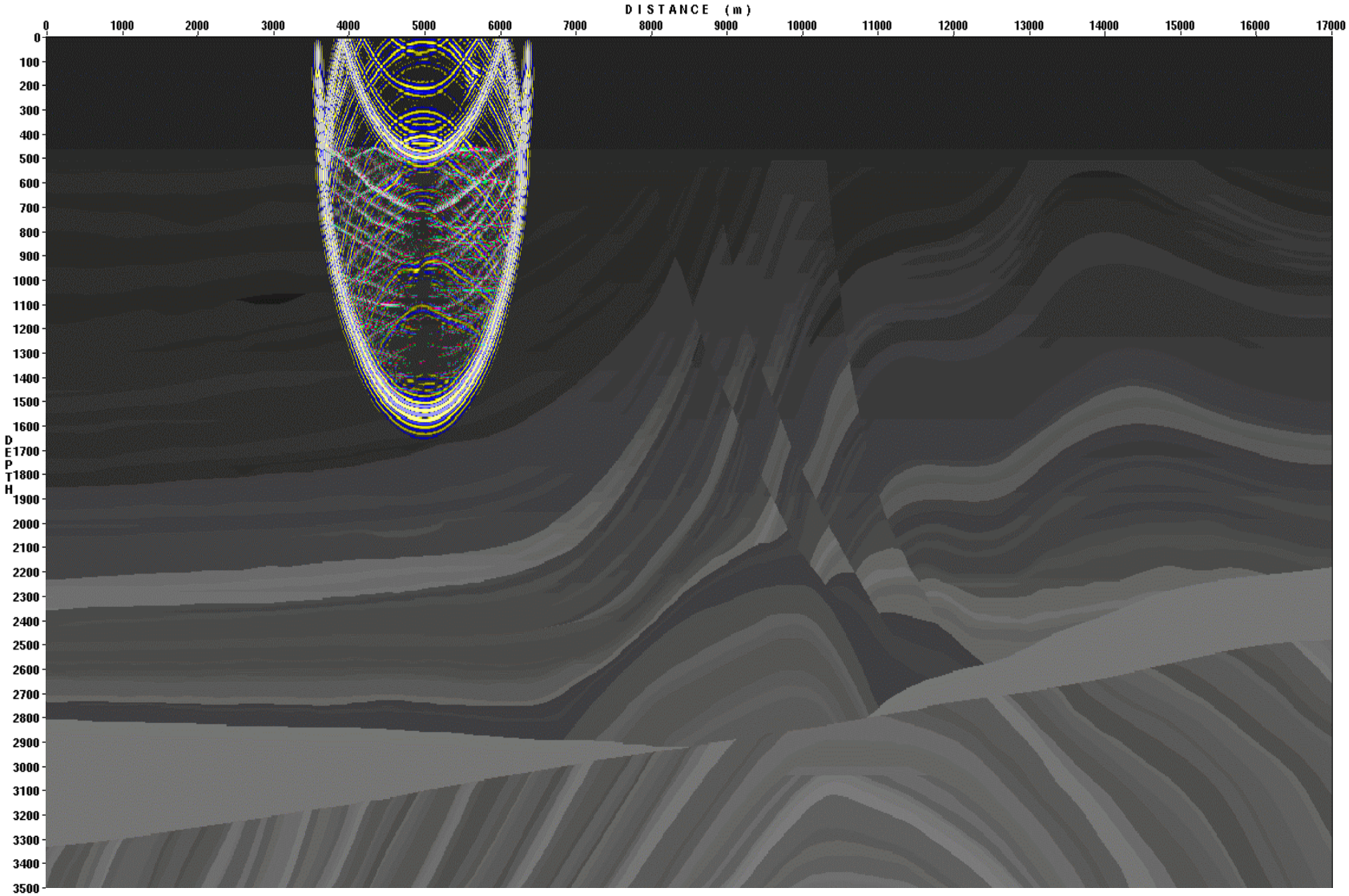

Figure 3.14. Wave propagation snapshot at t=1.0s. P-waves are blue-yellow, S-waves are red-green, model is greyscale

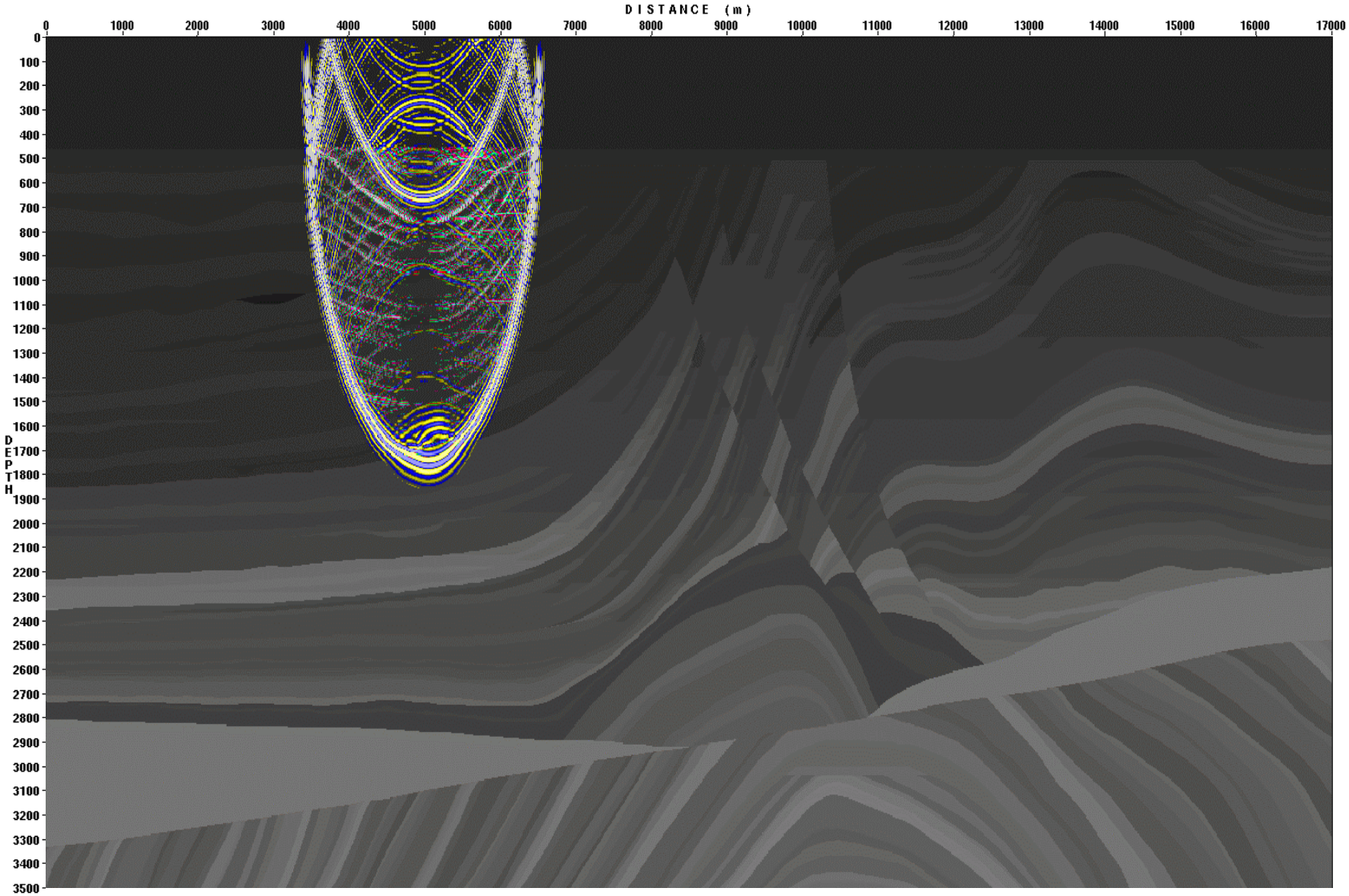

Figure 3.15. Wave propagation snapshot at t=1.1s. P-waves are blue-yellow, S-waves are red-green, model is greyscale

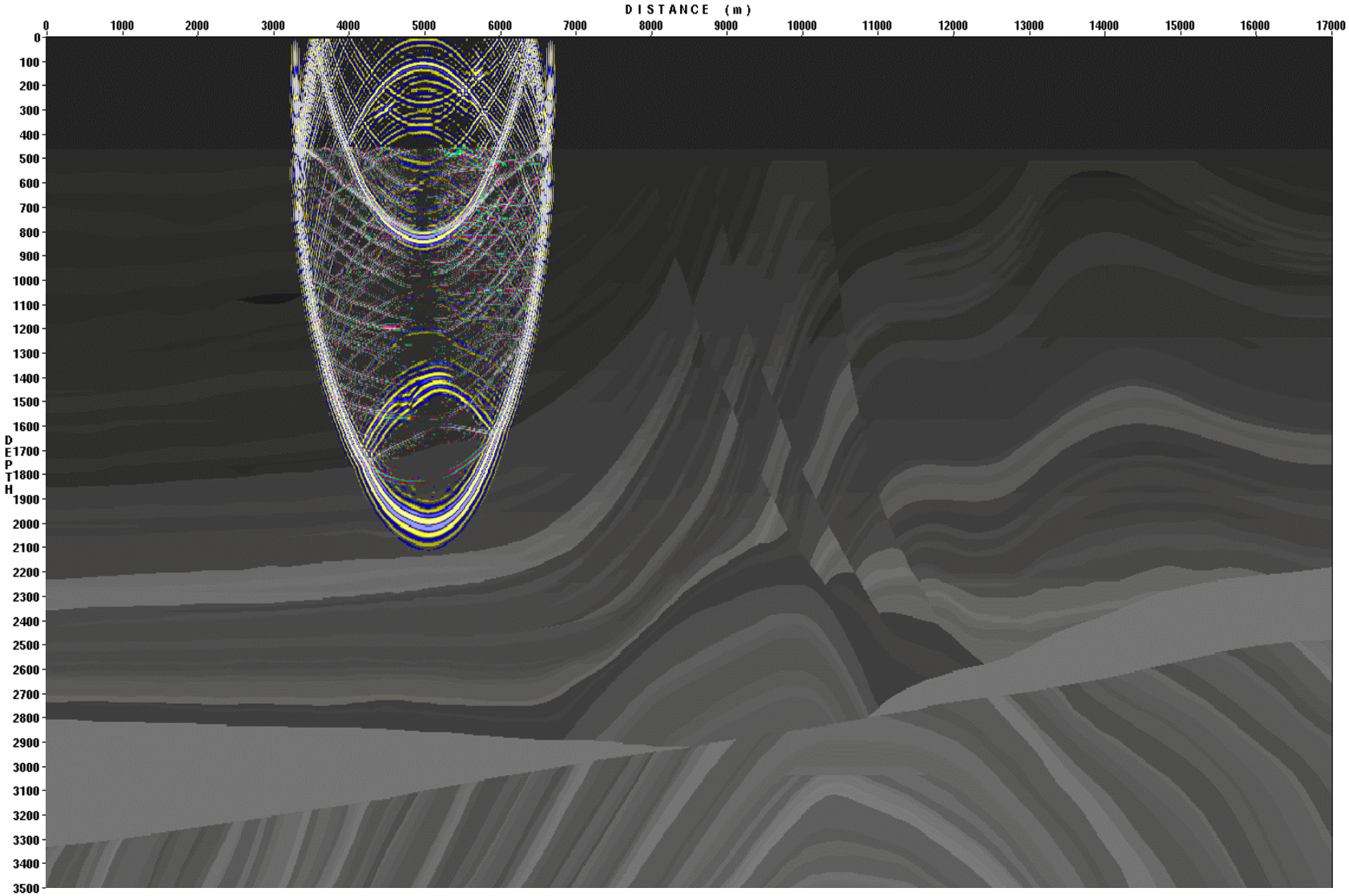

Figure 3.16. Wave propagation snapshot at t=1.2s. P-waves are blue-yellow, S-waves are red-green, model is greyscale

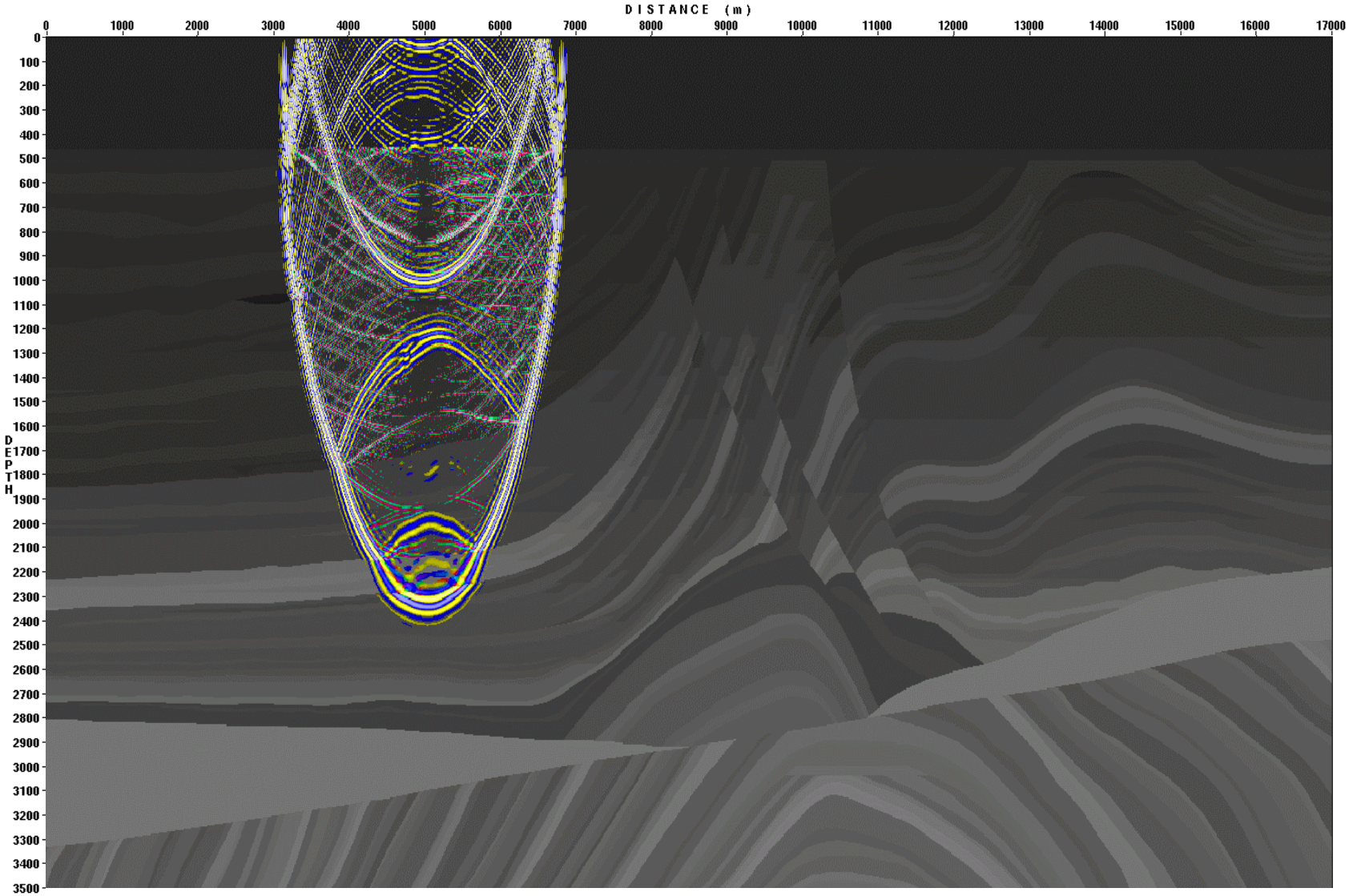

Figure 3.17. Wave propagation snapshot at t=1.3s. P-waves are blue-yellow, S-waves are red-green, model is greyscale

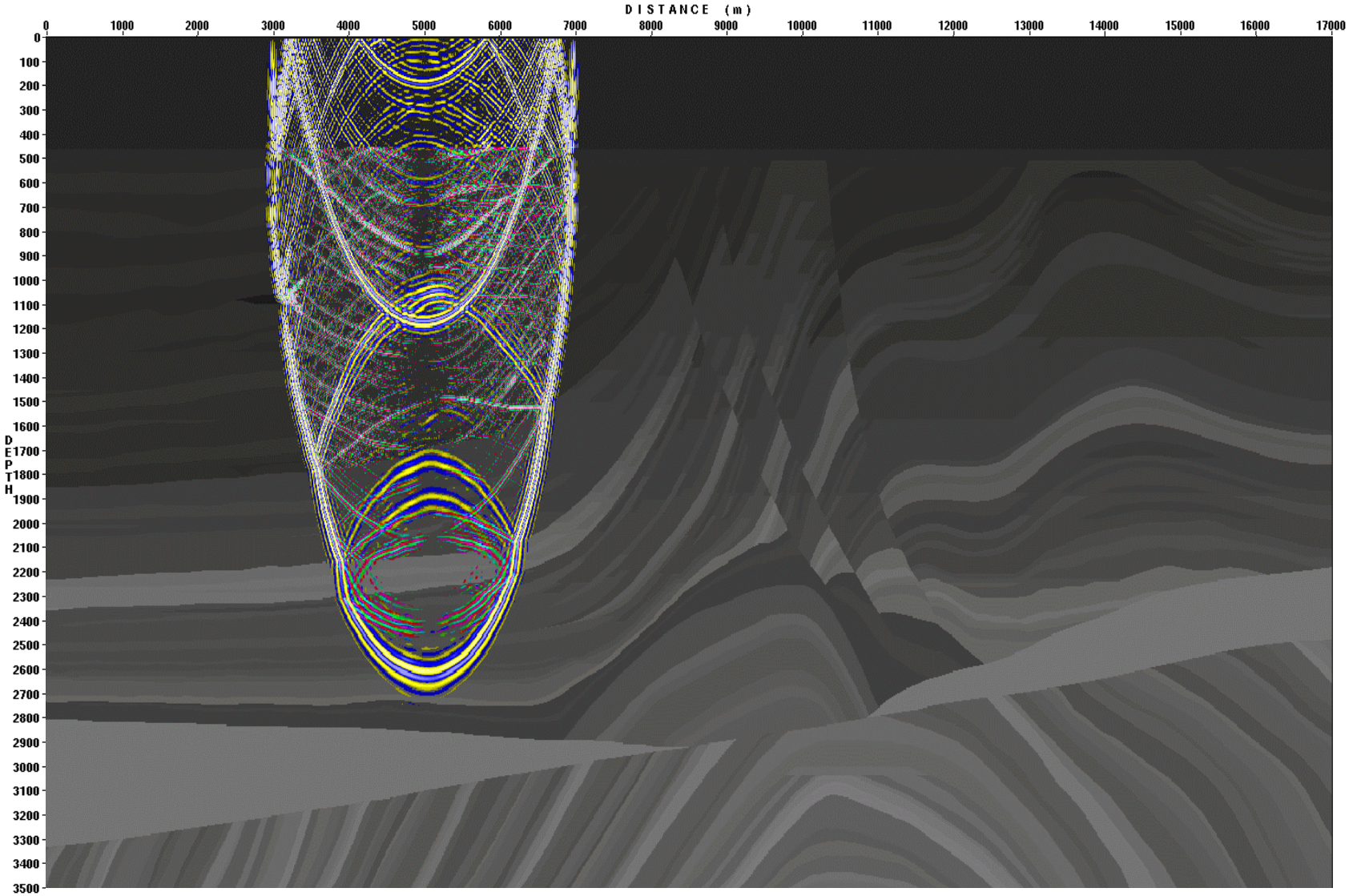

Figure 3.18. Wave propagation snapshot at t=1.4s. P-waves are blue-yellow, S-waves are red-green, model is greyscale

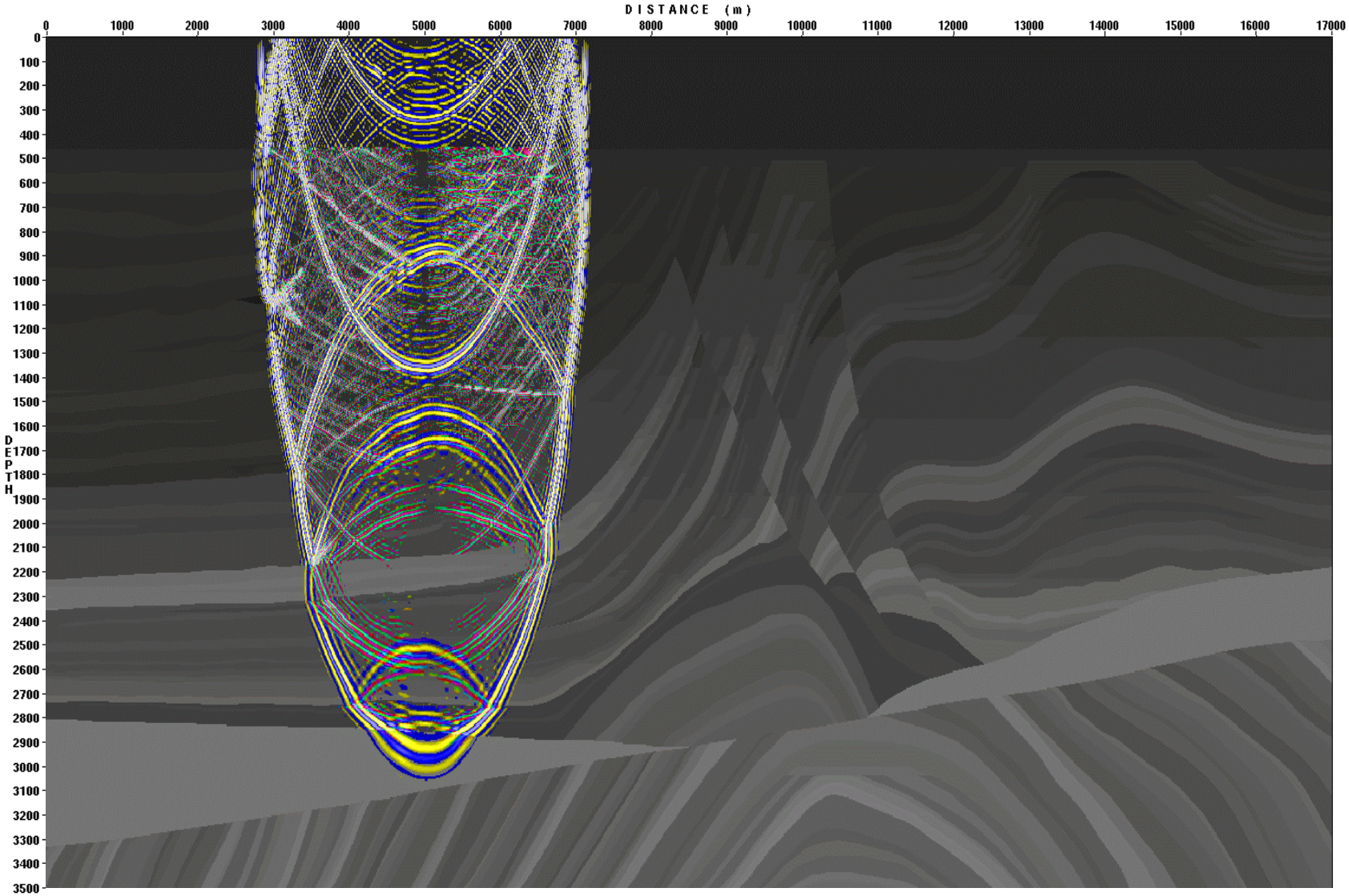

Figure 3.19. Wave propagation snapshot at t=1.5s. P-waves are blue-yellow, S-waves are red-green, model is greyscale

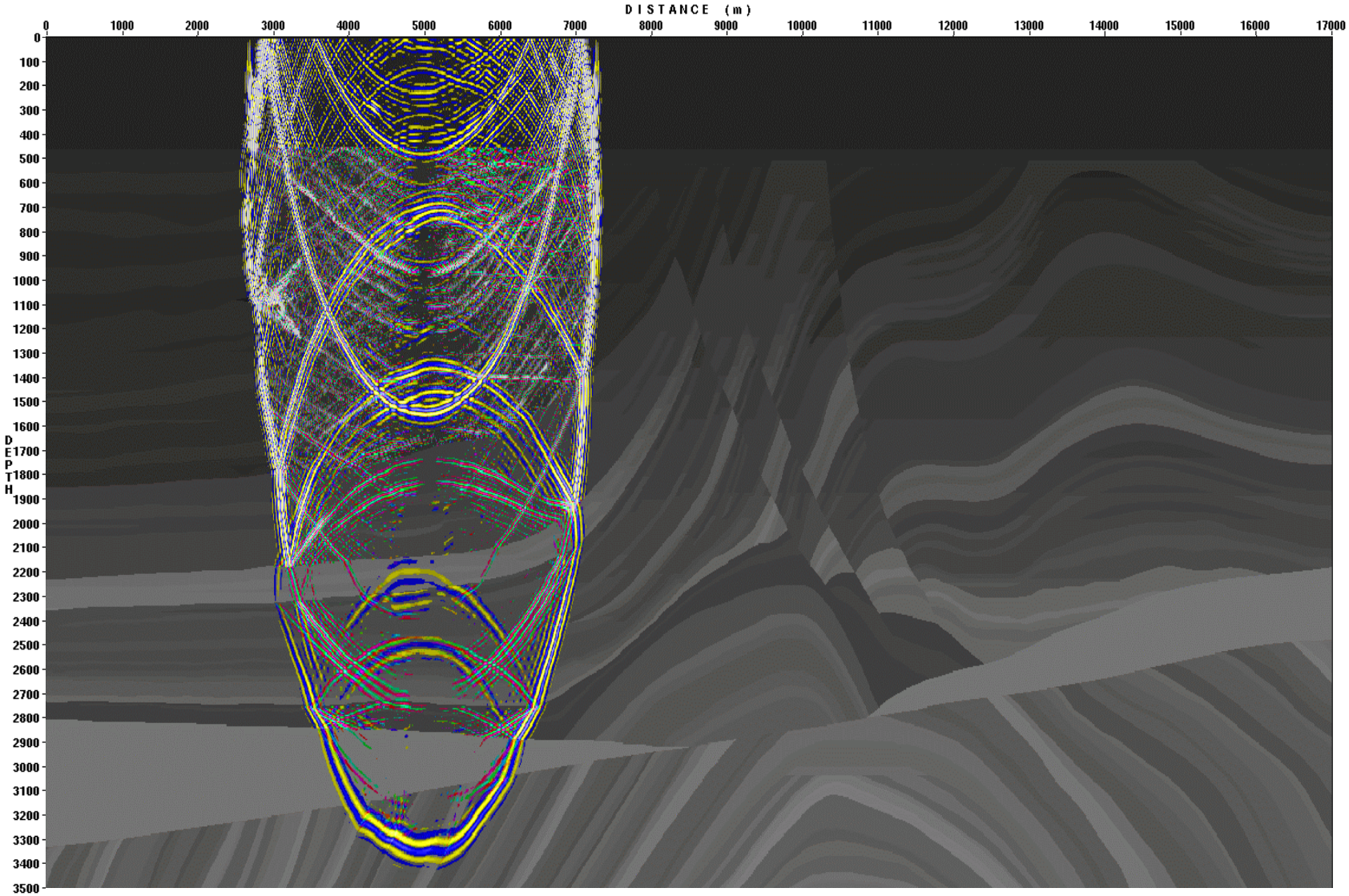

Figure 3.20. Wave propagation snapshot at t=1.6s. P-waves are blue-yellow, S-waves are red-green, model is greyscale

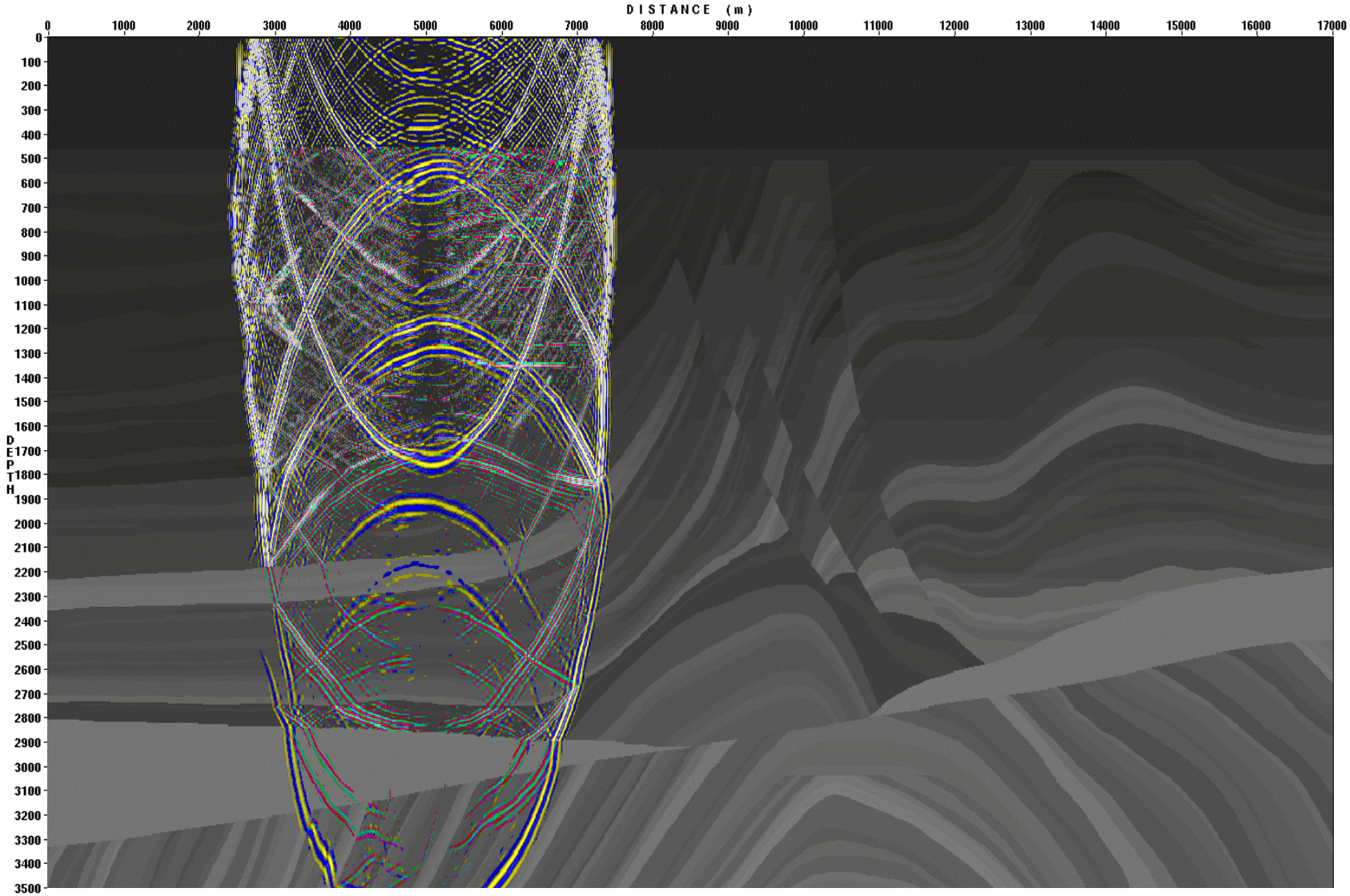

Figure 3.21. Wave propagation snapshot at t=1.7s. P-waves are blue-yellow, S-waves are red-green, model is greyscale

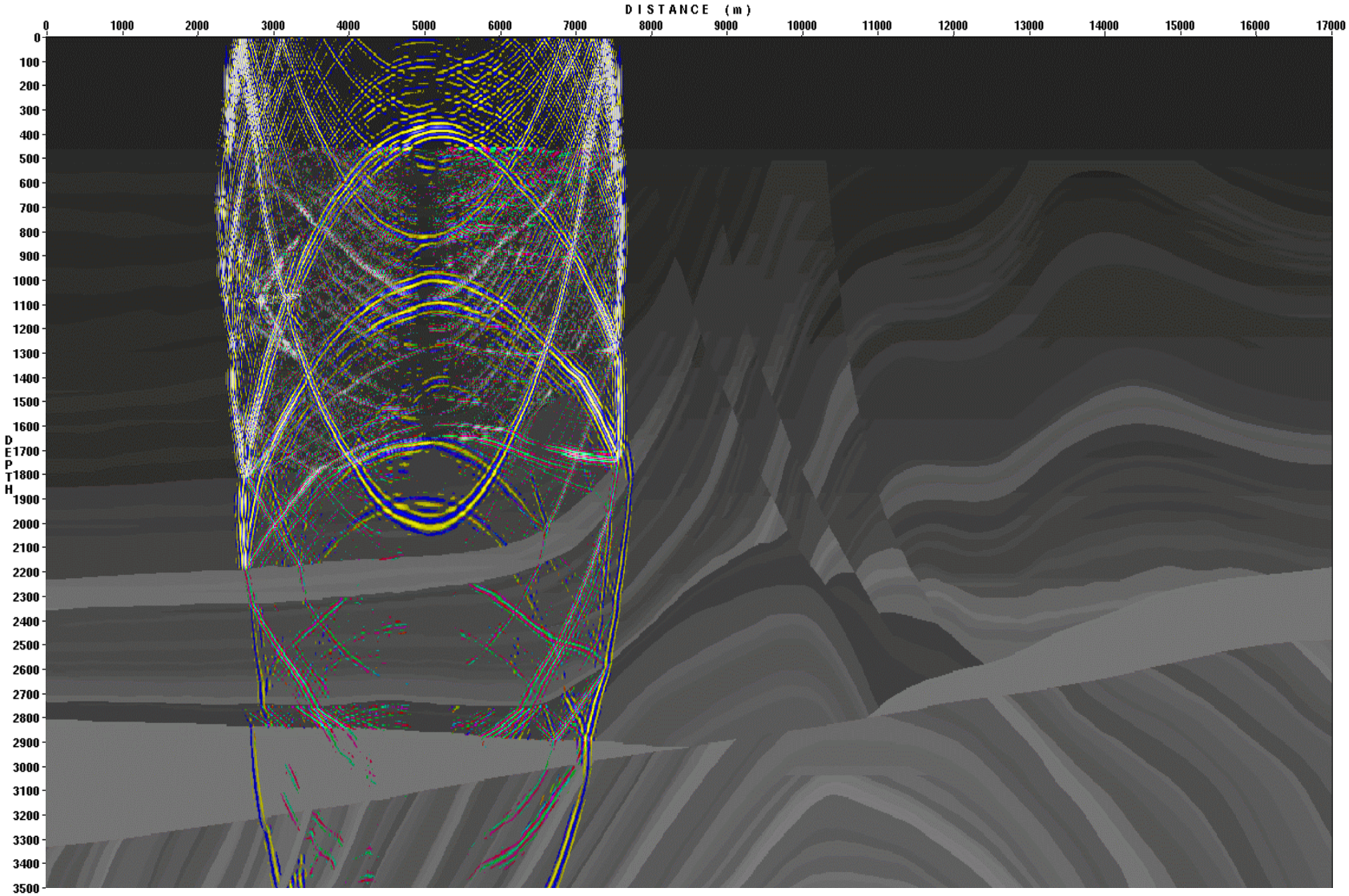

Figure 3.22. Wave propagation snapshot at t=1.8s. P-waves are blue-yellow, S-waves are red-green, model is greyscale

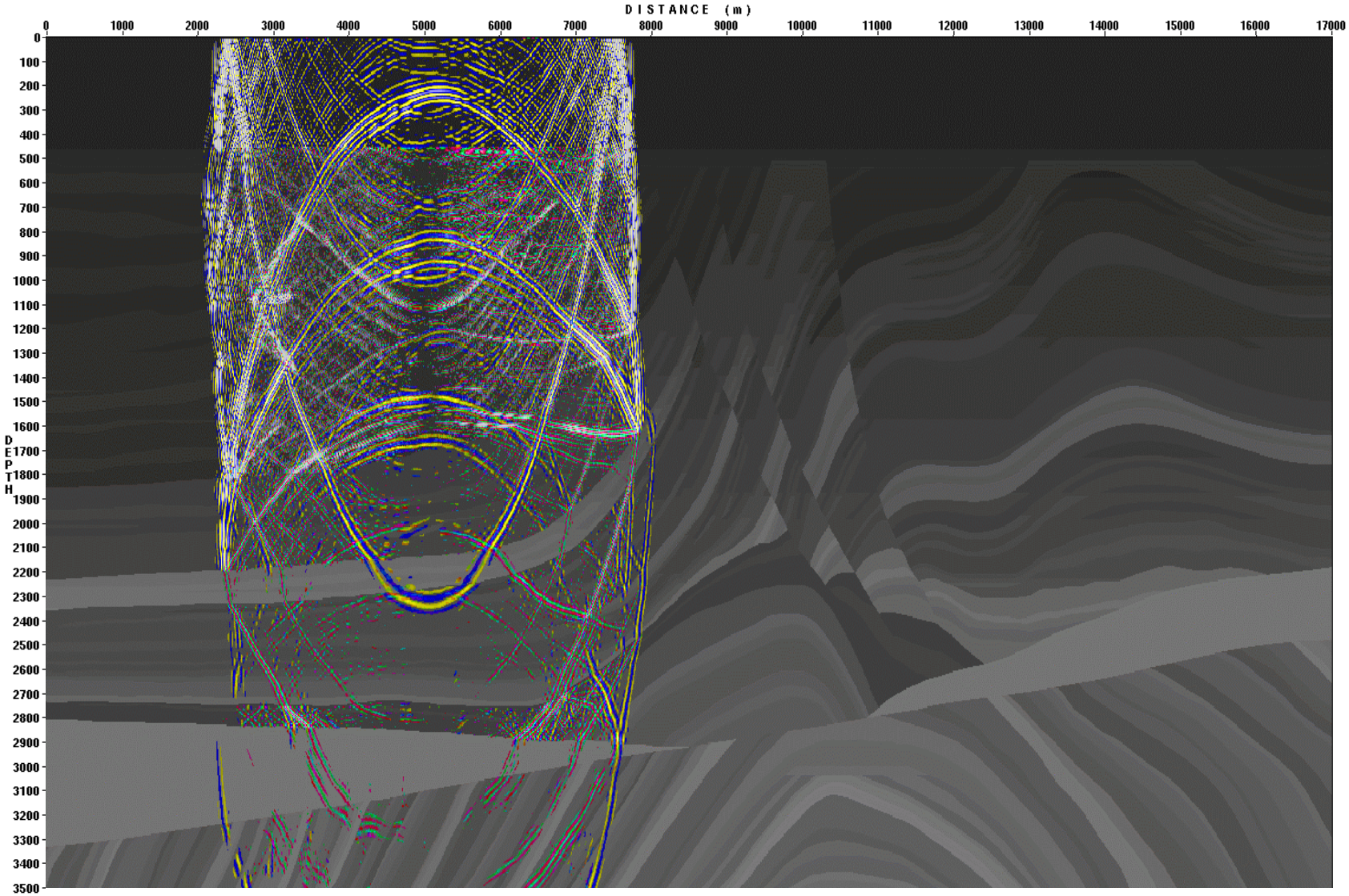

Figure 3.23. Wave propagation snapshot at t=1.9s. P-waves are blue-yellow, S-waves are red-green, model is greyscale

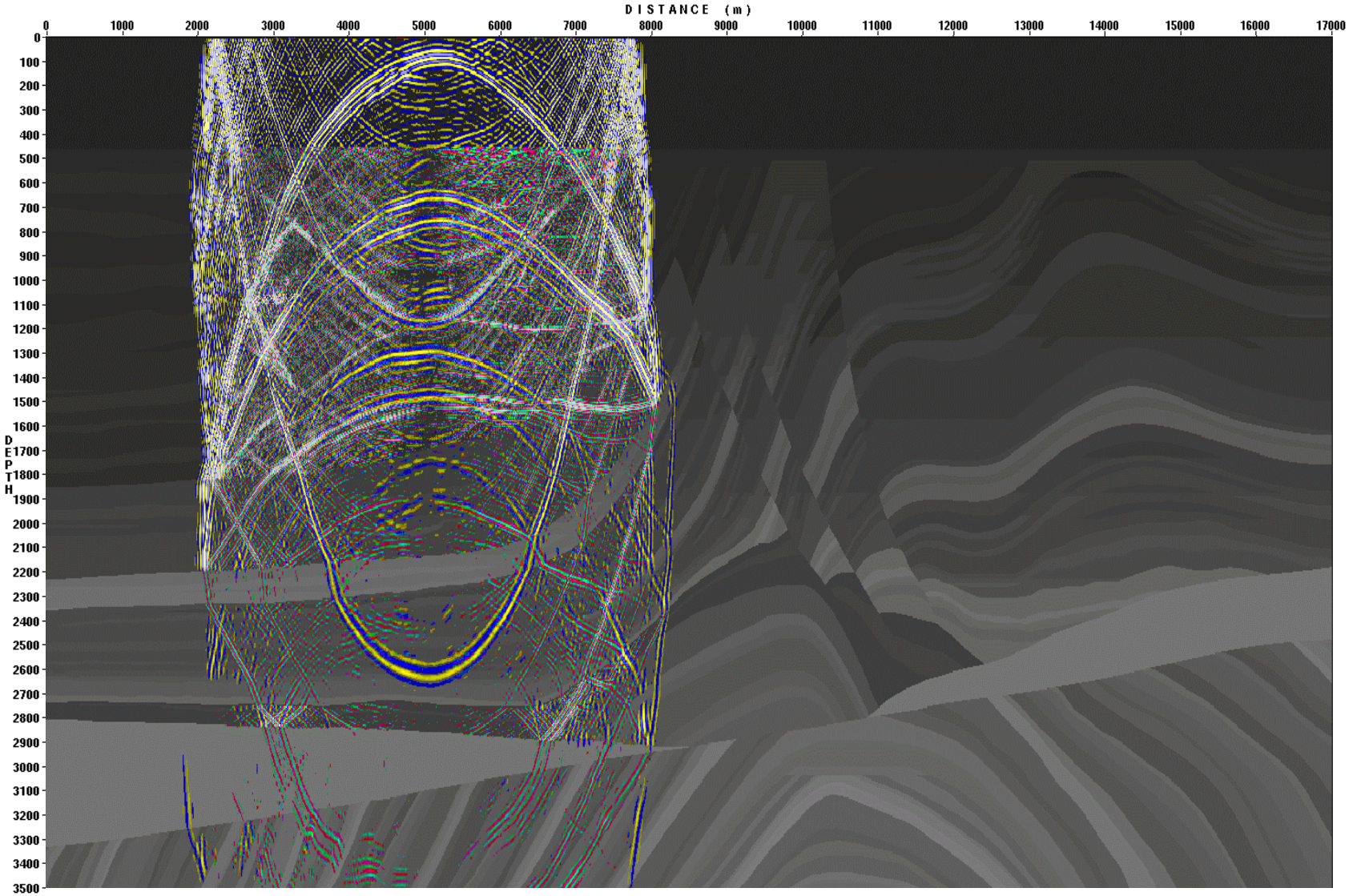

Figure 3.24. Wave propagation snapshot at t=2.0s. P-waves are blue-yellow, S-waves are red-green, model is greyscale

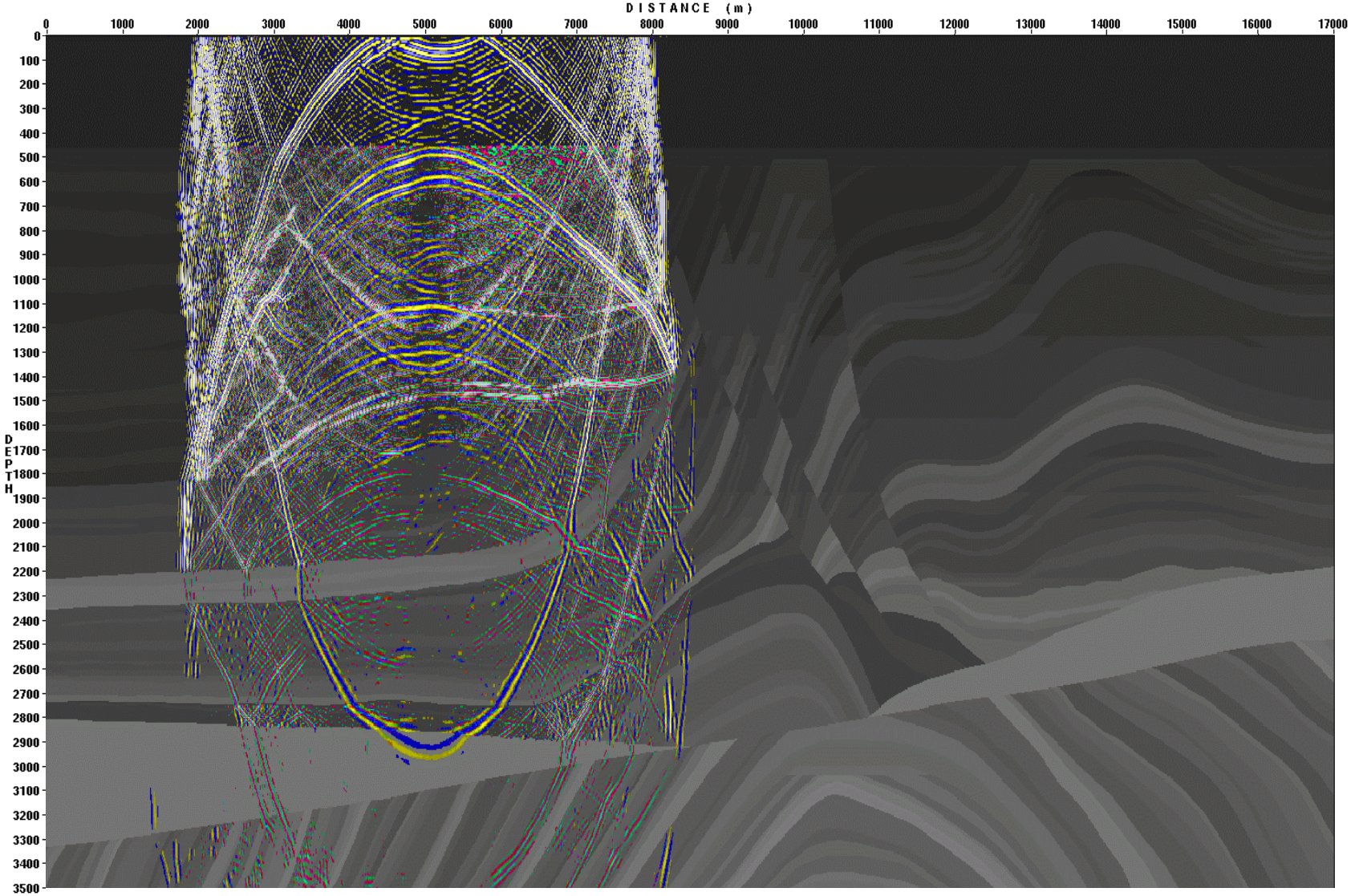

Figure 3.25. Wave propagation snapshot at t=2.1s. P-waves are blue-yellow, S-waves are red-green, model is greyscale

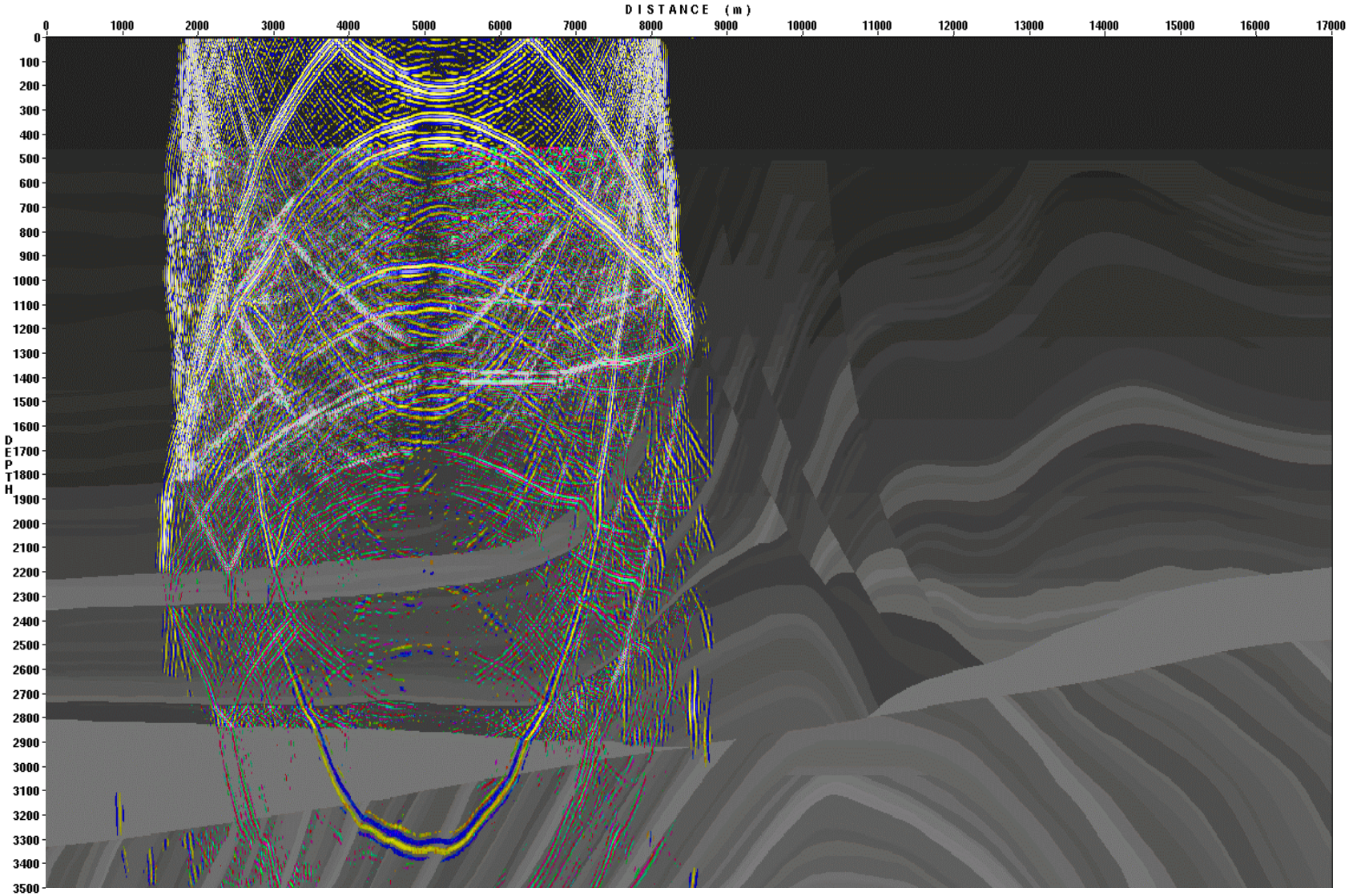

Figure 3.26. Wave propagation snapshot at t=2.2s. P-waves are blue-yellow, S-waves are red-green, model is greyscale

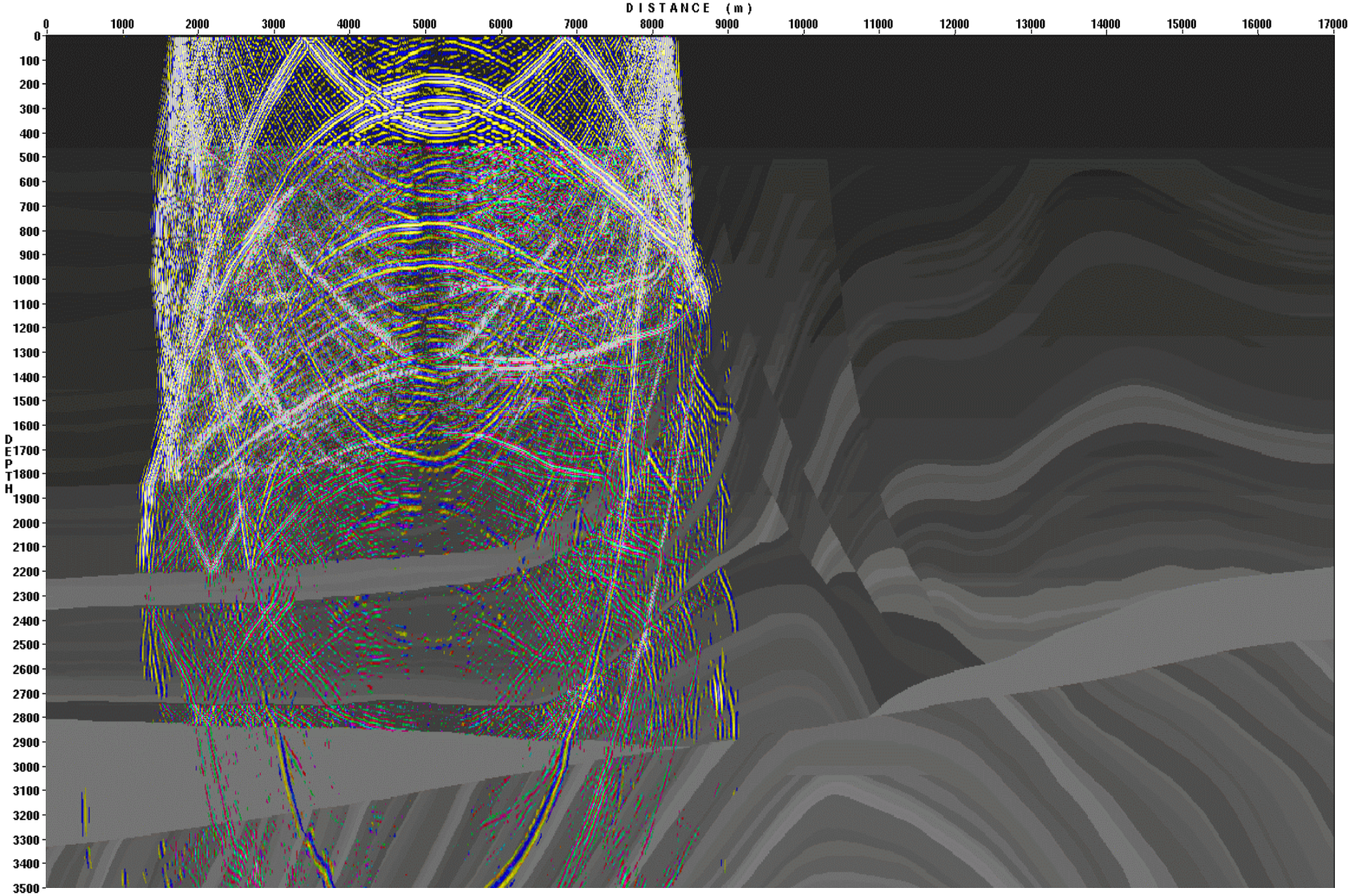

Figure 3.27. Wave propagation snapshot at t=2.3s. P-waves are blue-yellow, S-waves are red-green, model is greyscale

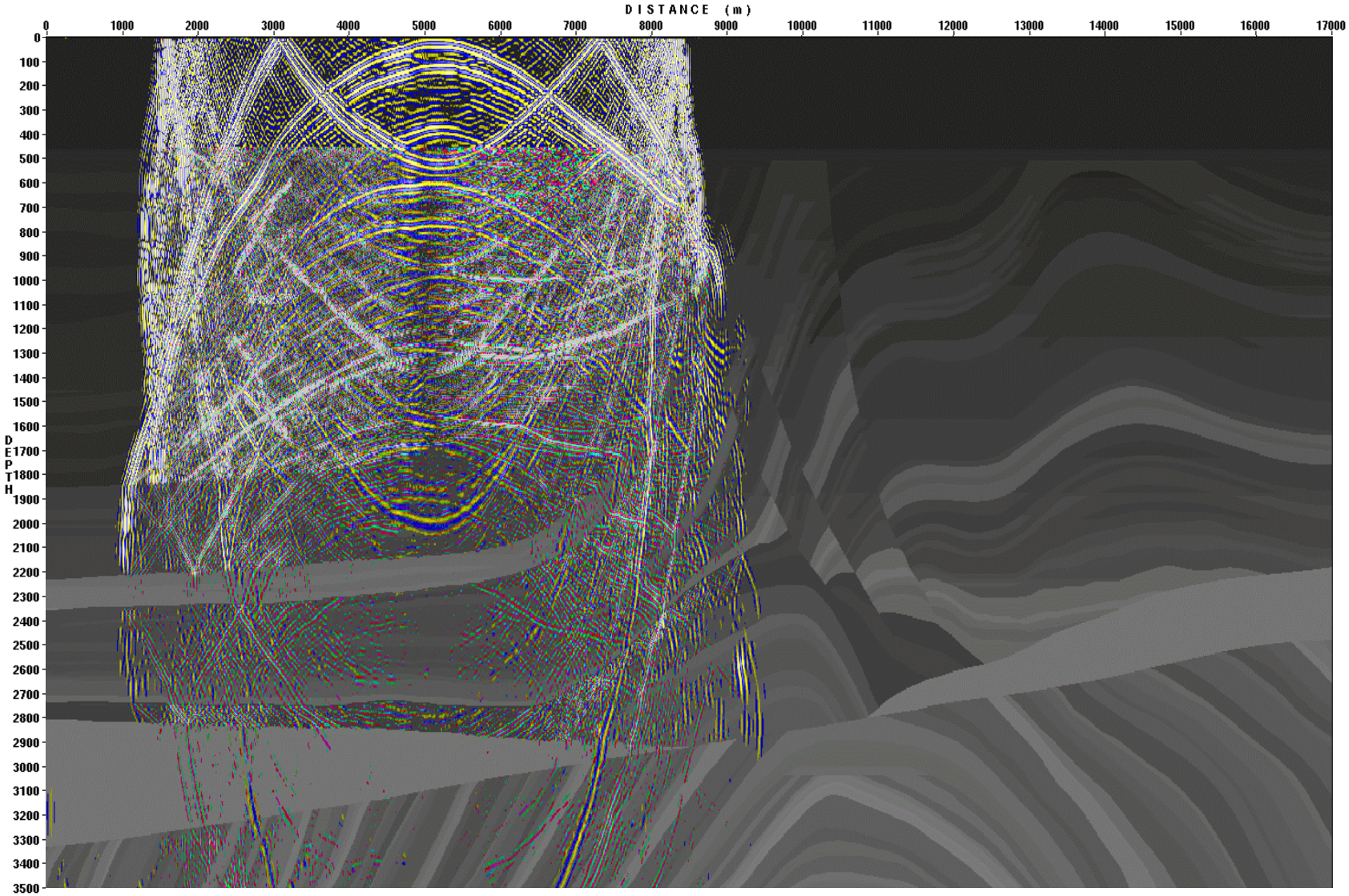

Figure 3.28. Wave propagation snapshot at t=2.4s. P-waves are blue-yellow, S-waves are red-green, model is greyscale

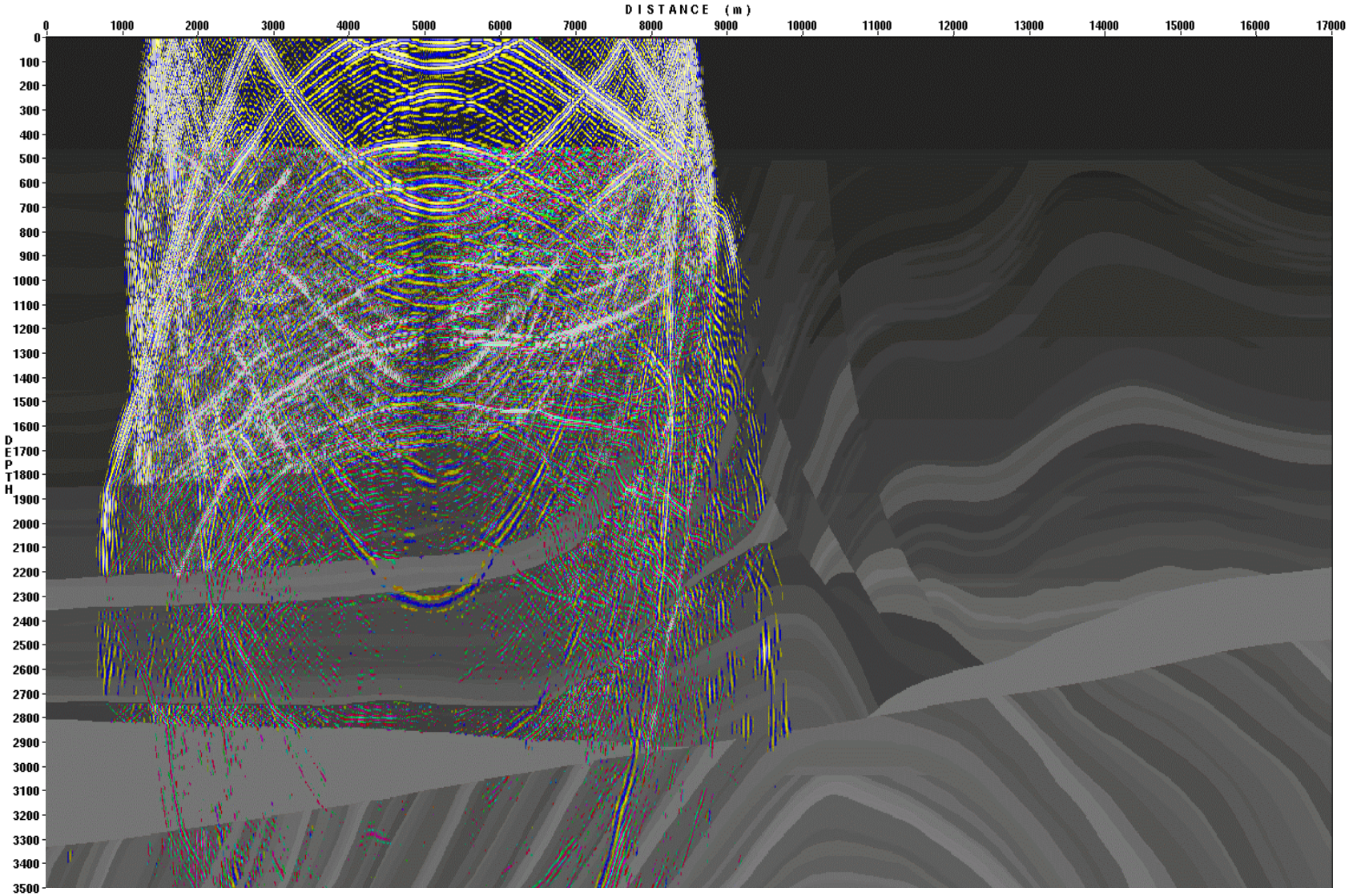

Figure 3.29. Wave propagation snapshot at t=2.5s. P-waves are blue-yellow, S-waves are red-green, model is greyscale

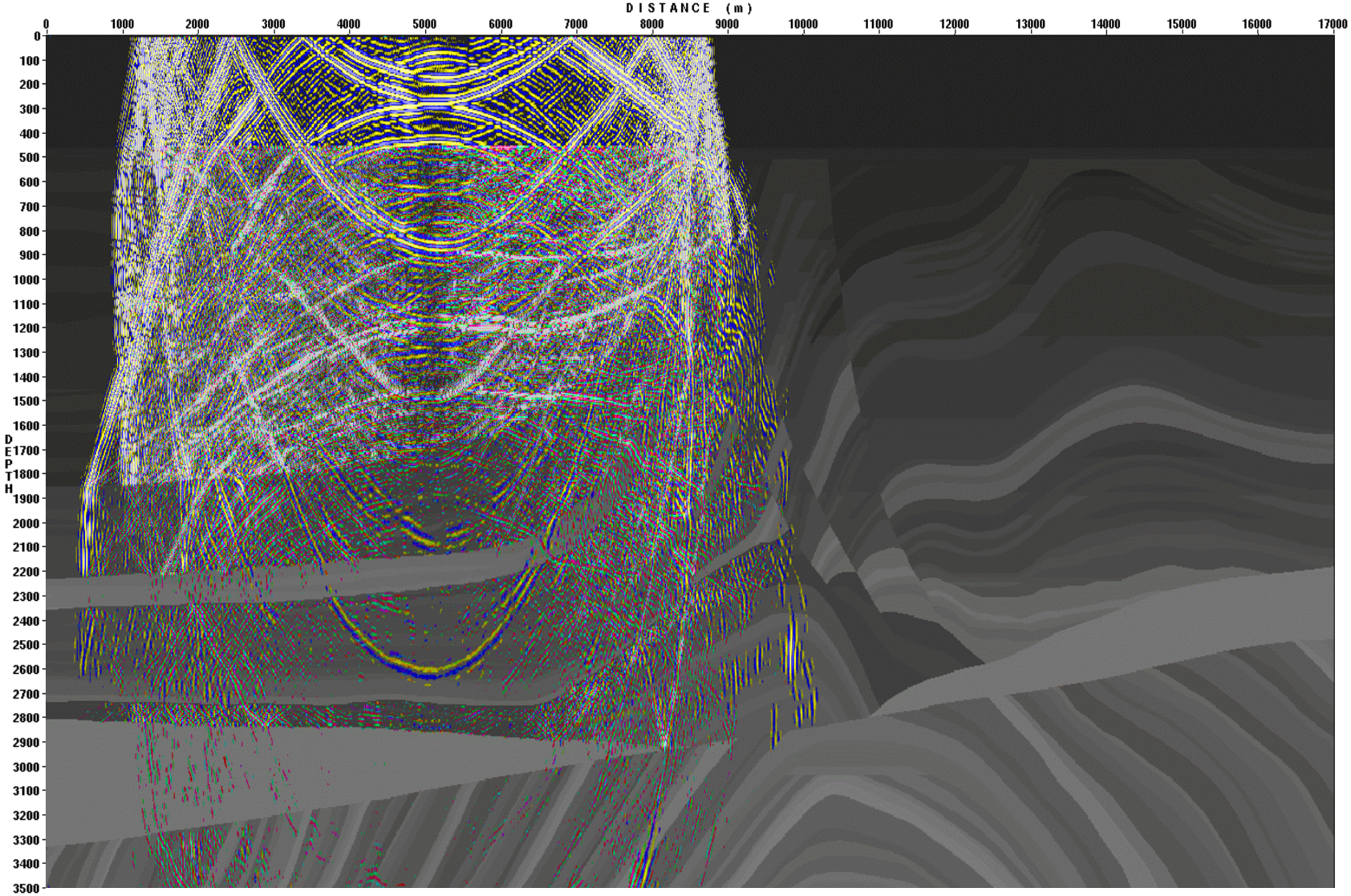

Figure 3.30. Wave propagation snapshot at t=2.6s. P-waves are blue-yellow, S-waves are red-green, model is greyscale

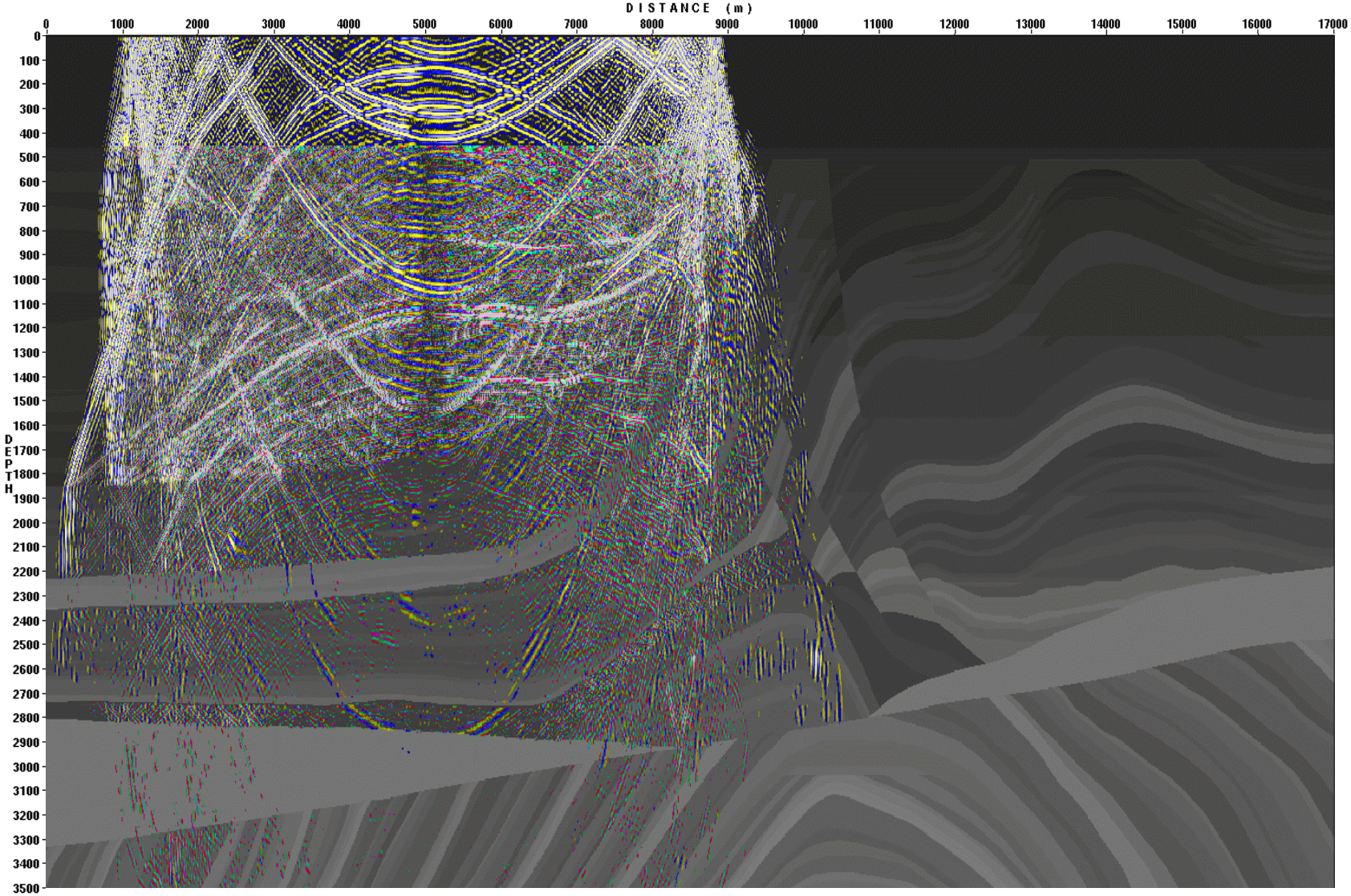

Figure 3.31. Wave propagation snapshot at t=2.7s. P-waves are blue-yellow, S-waves are red-green, model is greyscale

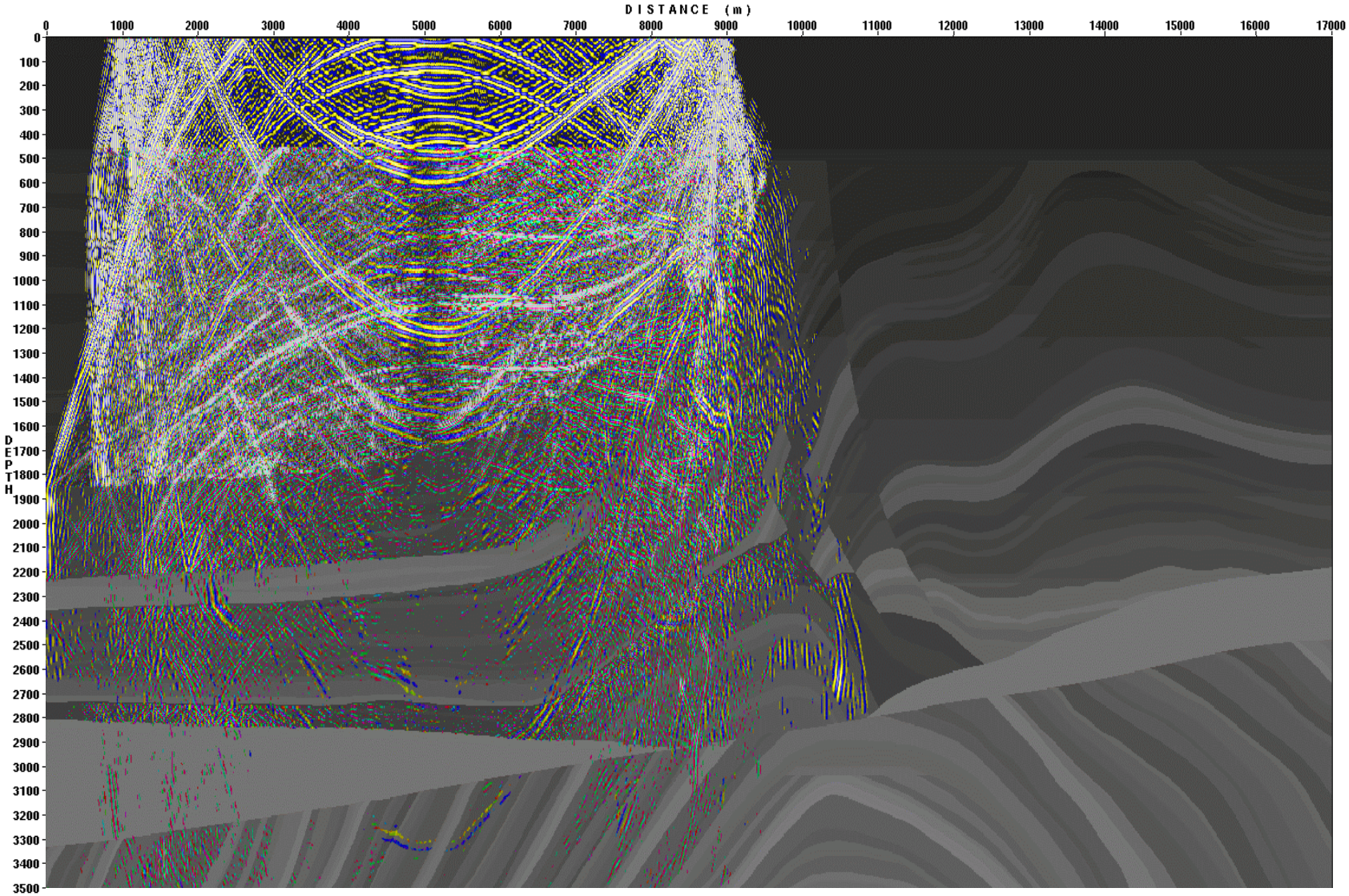

Figure 3.32. Wave propagation snapshot at t=2.8s. P-waves are blue-yellow, S-waves are red-green, model is greyscale

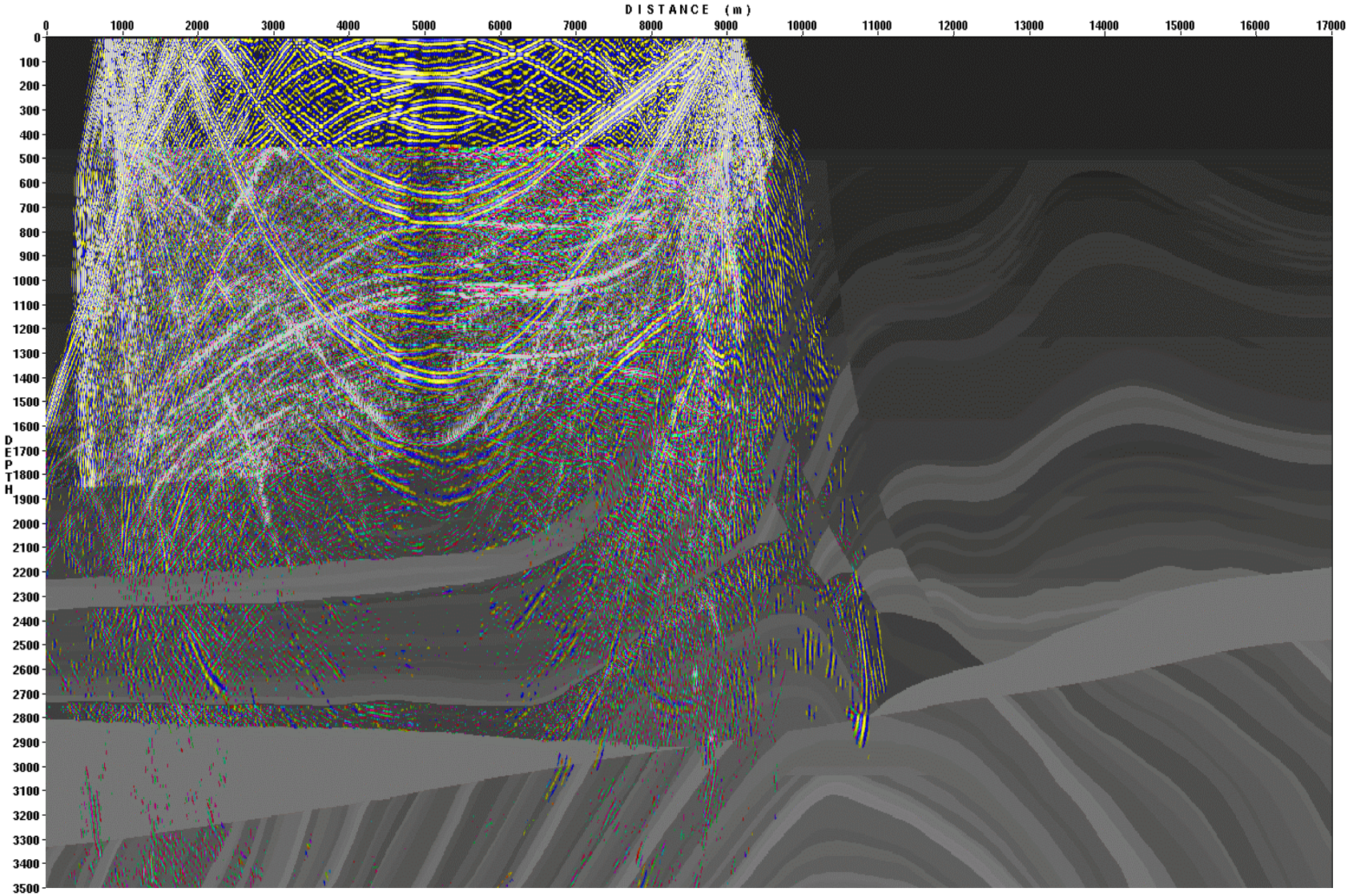

Figure 3.33. Wave propagation snapshot at t=2.9s. P-waves are blue-yellow, S-waves are red-green, model is greyscale

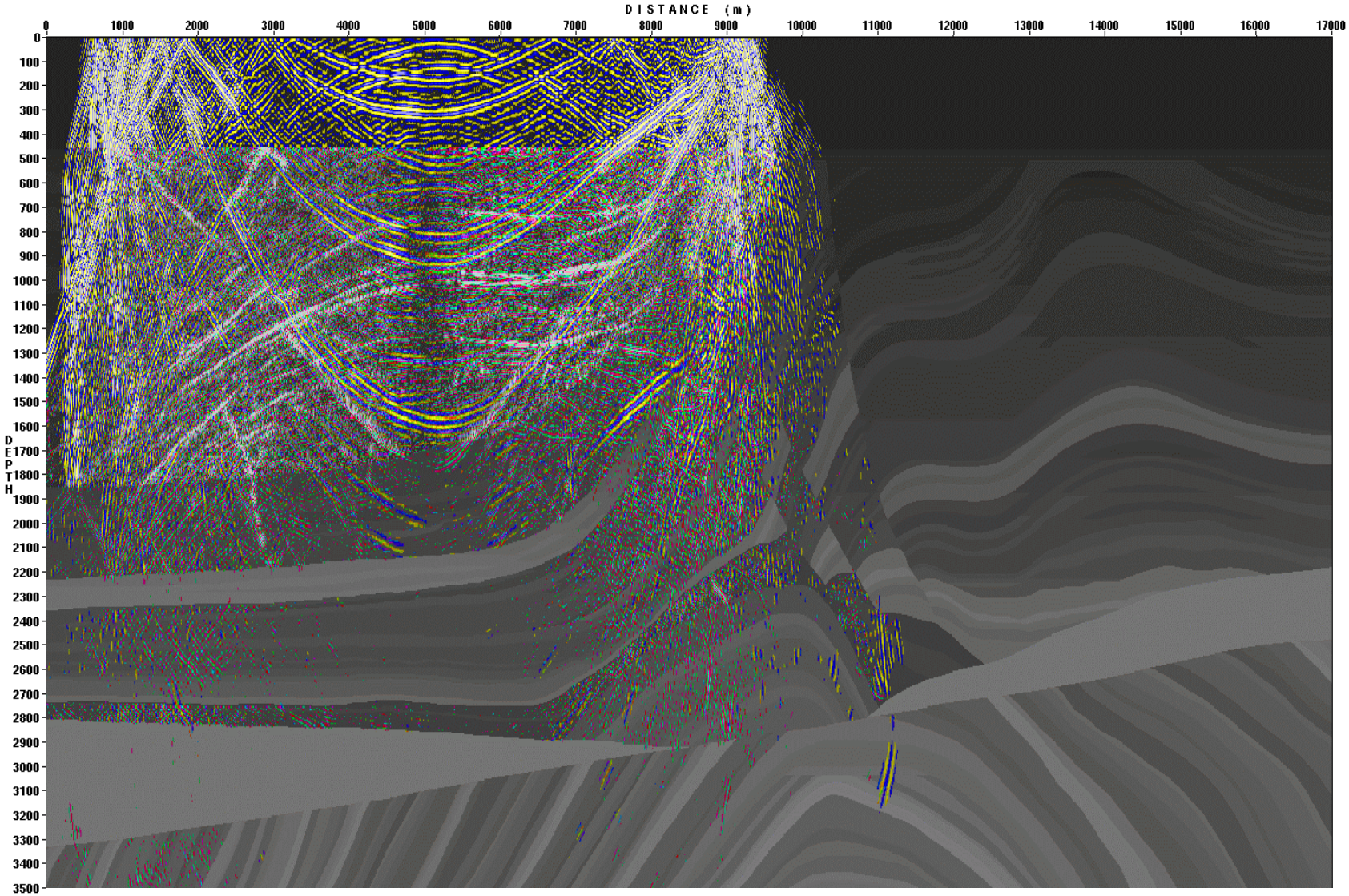

Figure 3.34. Wave propagation snapshot at t=3.0s. P-waves are blue-yellow, S-waves are red-green, model is greyscale

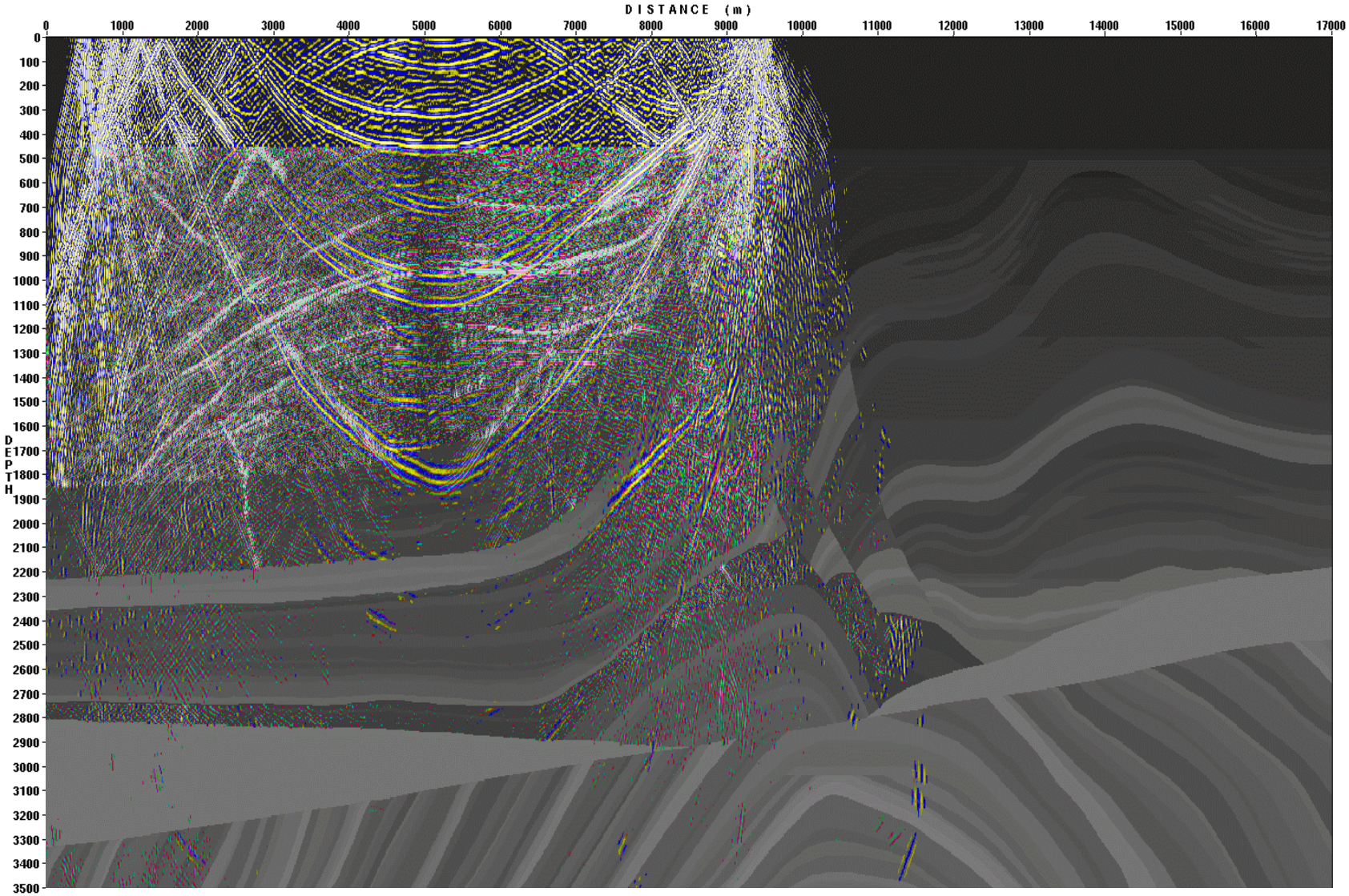

Figure 3.35. Wave propagation snapshot at t=3.1s. P-waves are blue-yellow, S-waves are red-green, model is greyscale

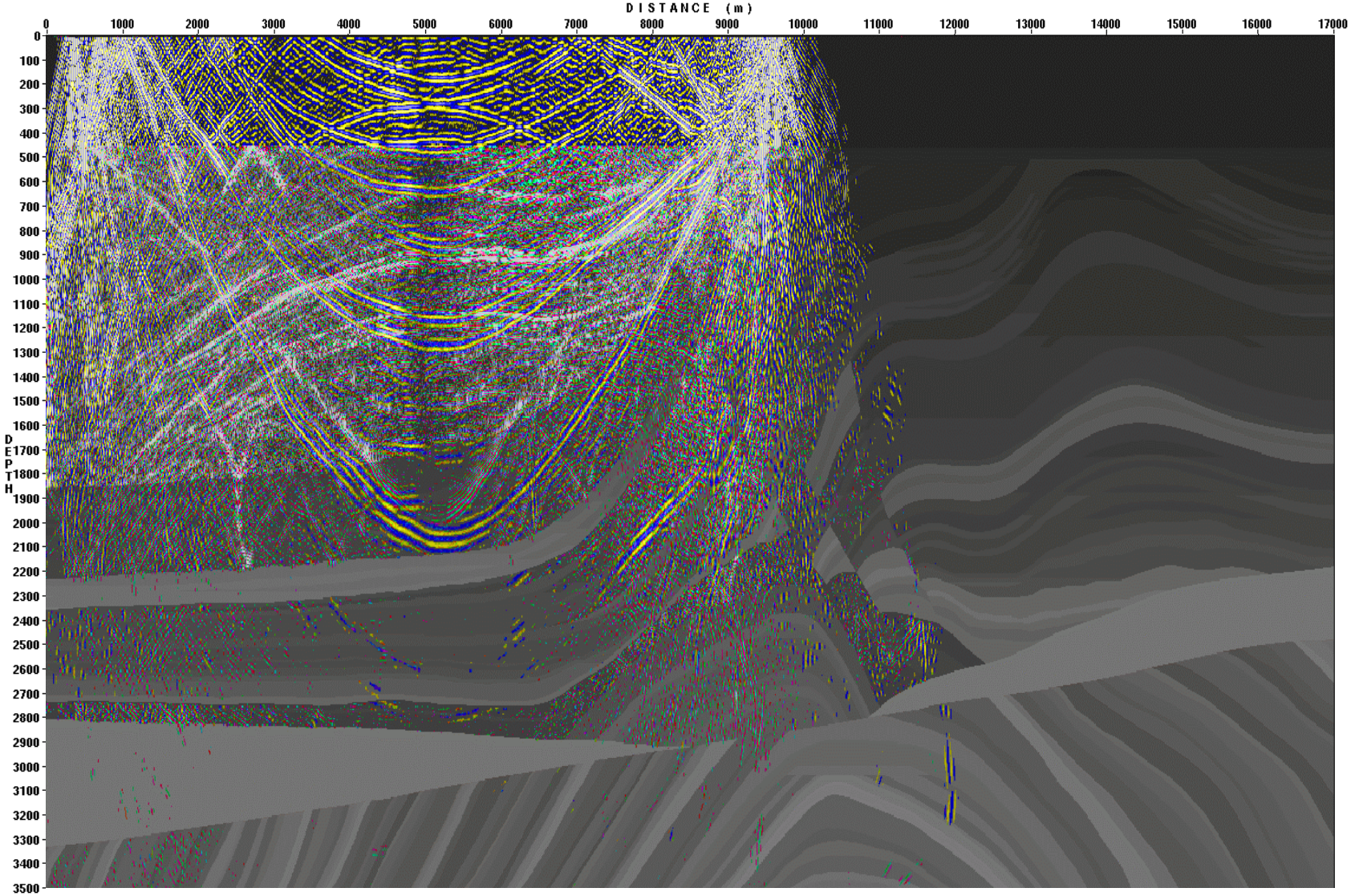

Figure 3.36. Wave propagation snapshot at t=3.2s. P-waves are blue-yellow, S-waves are red-green, model is greyscale

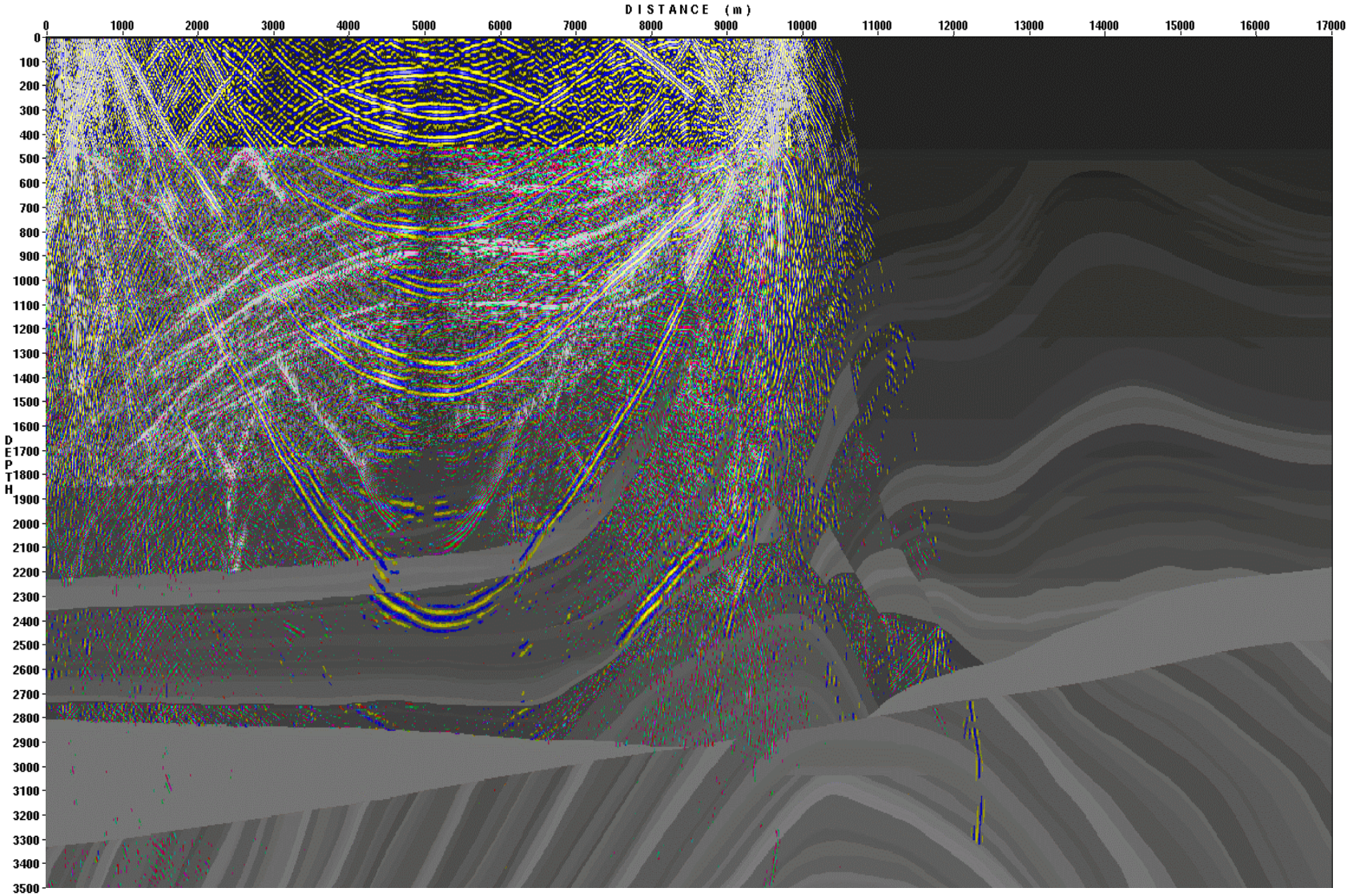

Figure 3.37. Wave propagation snapshot at t=3.3s. P-waves are blue-yellow, S-waves are red-green, model is greyscale

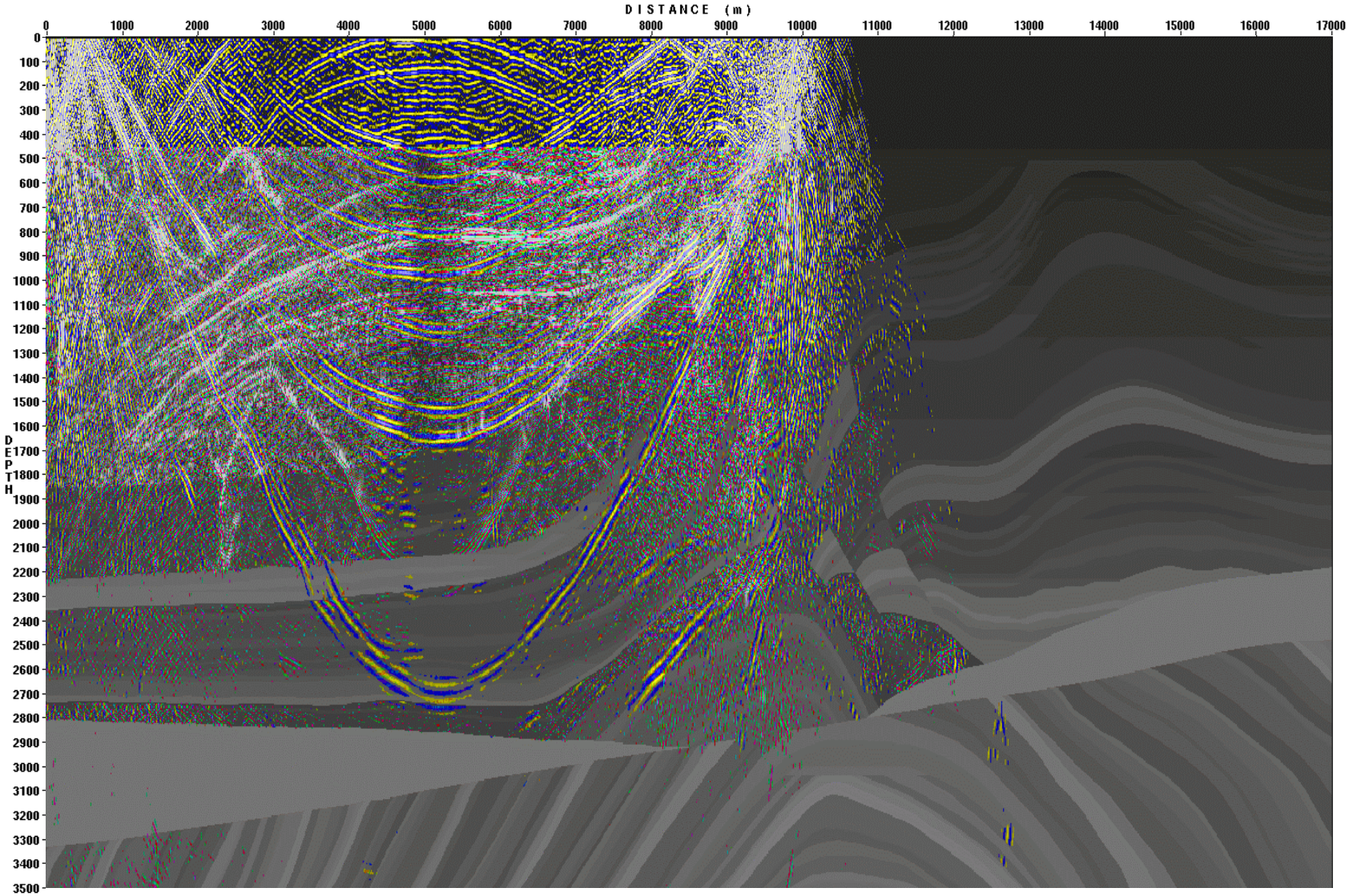

Figure 3.38. Wave propagation snapshot at t=3.4s. P-waves are blue-yellow, S-waves are red-green, model is greyscale

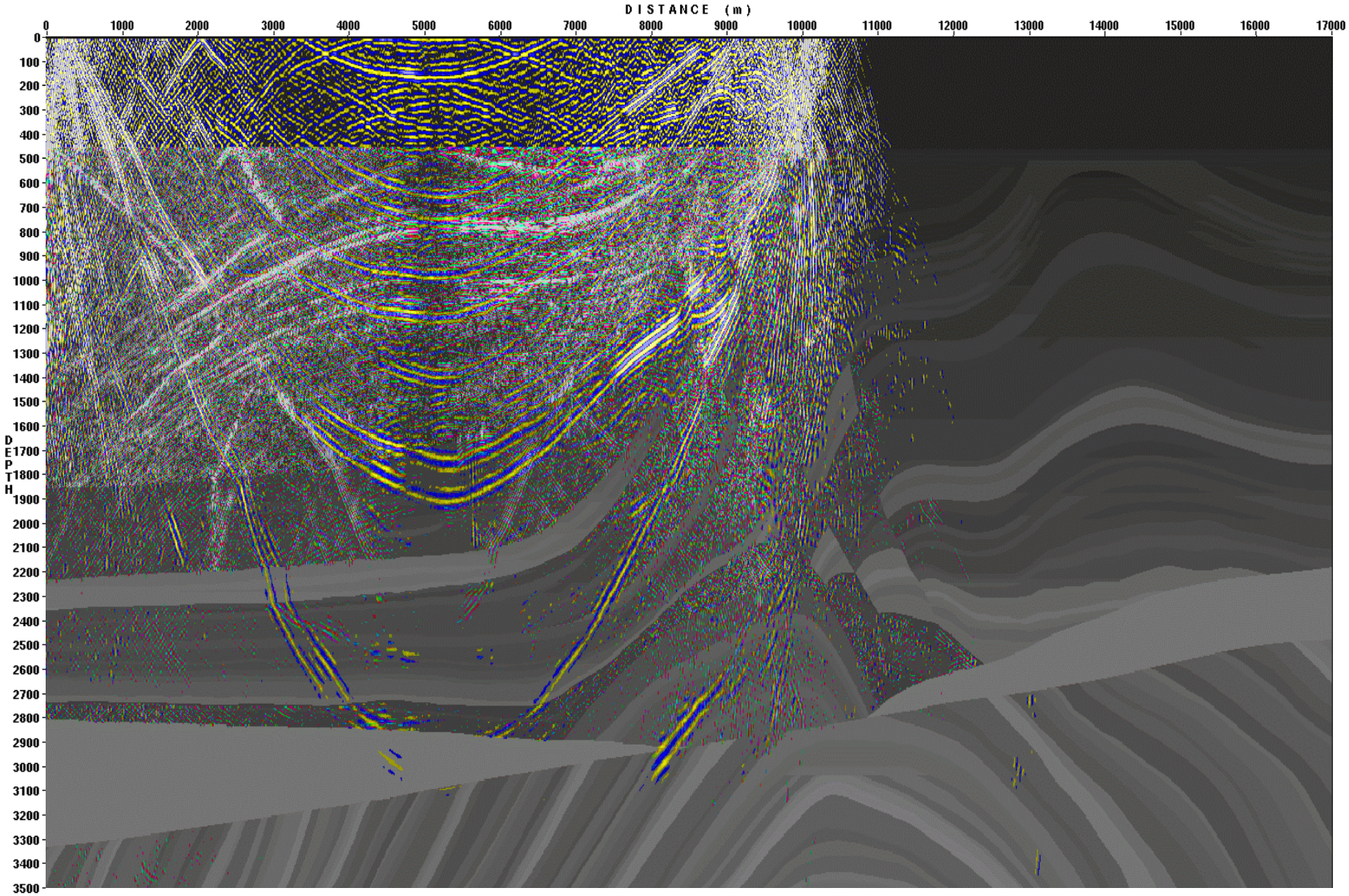

Figure 3.39. Wave propagation snapshot at t=3.5s. P-waves are blue-yellow, S-waves are red-green, model is greyscale

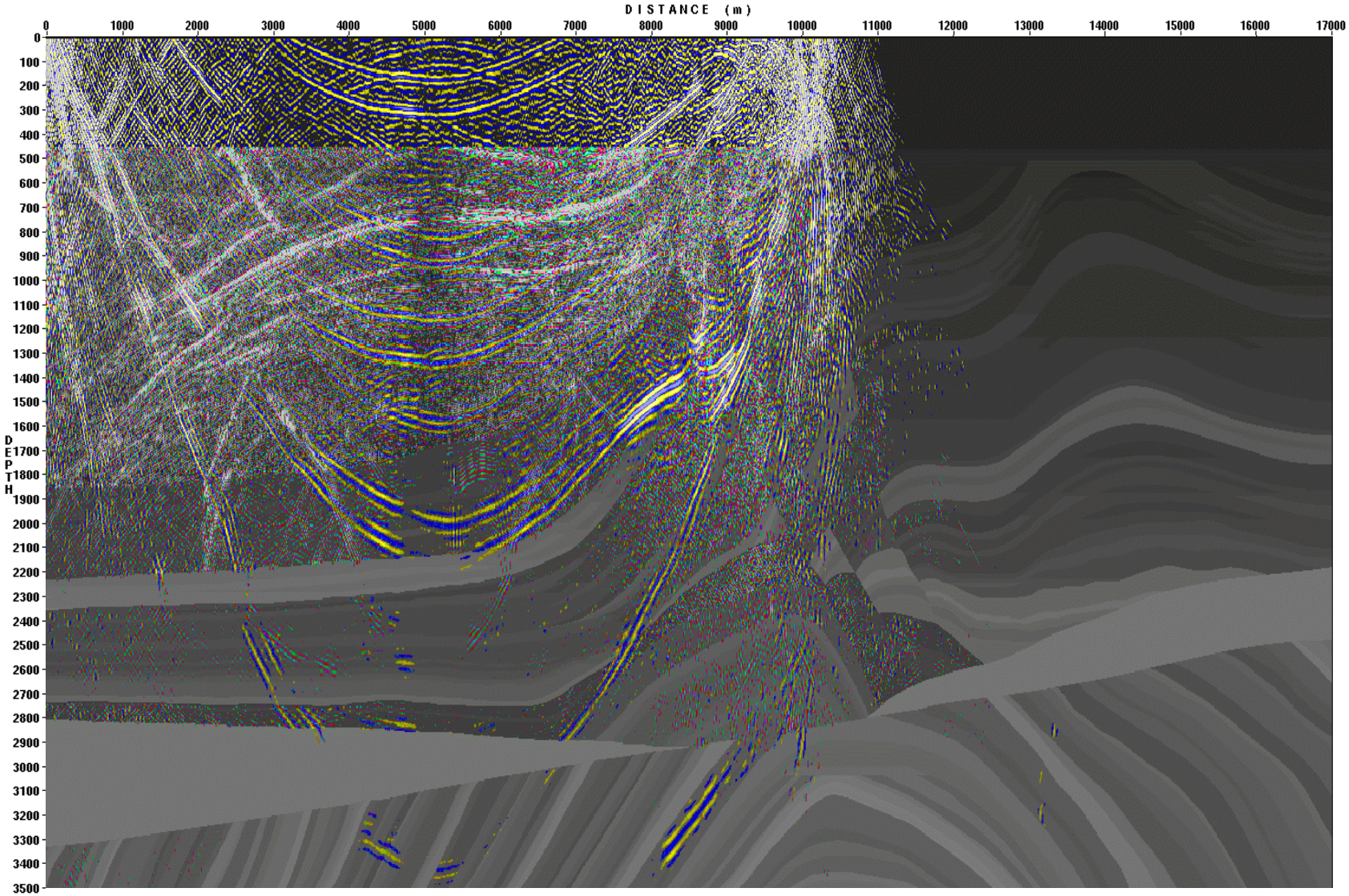

Figure 3.40. Wave propagation snapshot at t=3.6s. P-waves are blue-yellow, S-waves are red-green, model is greyscale

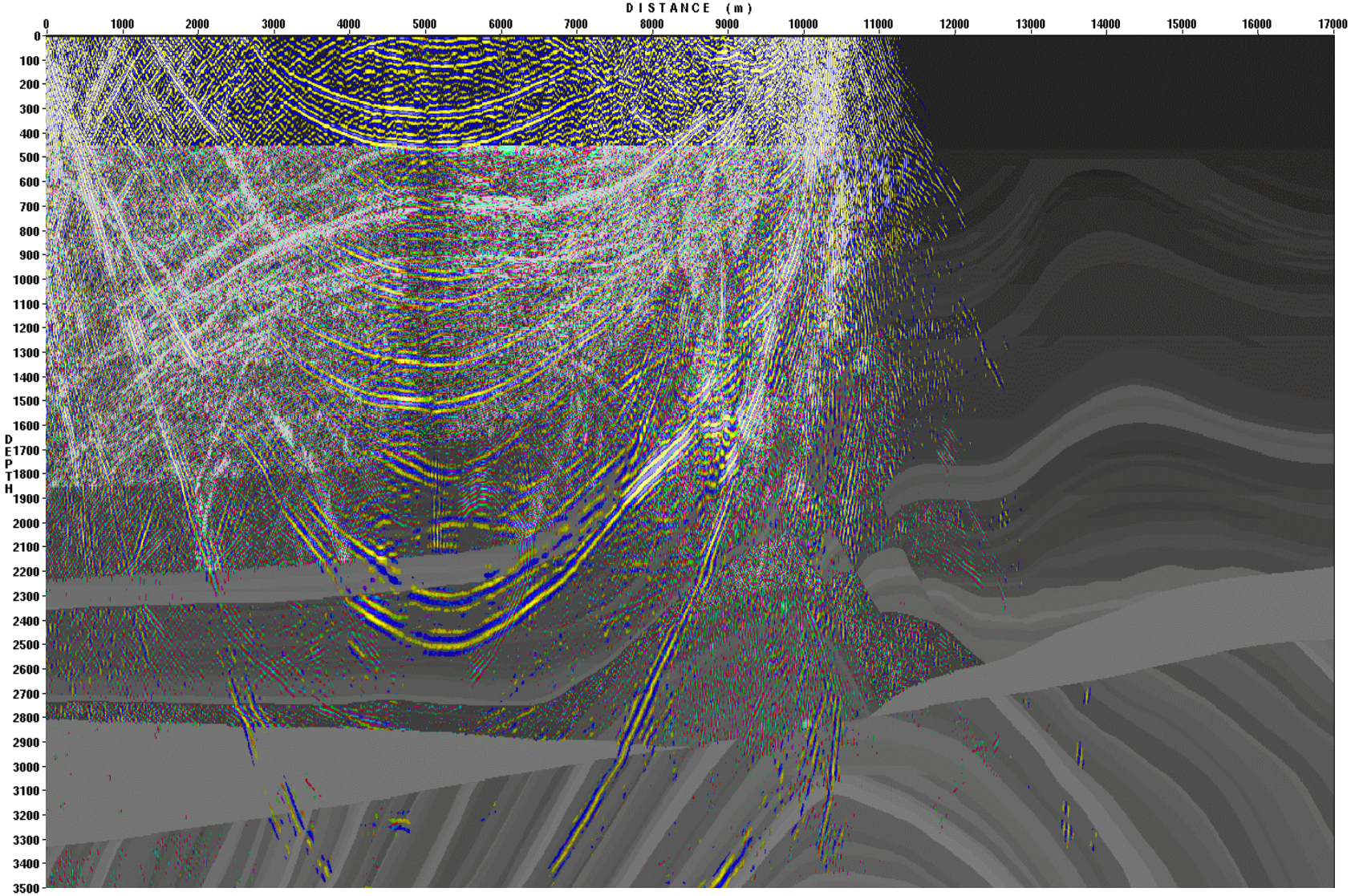

Figure 3.41. Wave propagation snapshot at t=3.7s. P-waves are blue-yellow, S-waves are red-green, model is greyscale

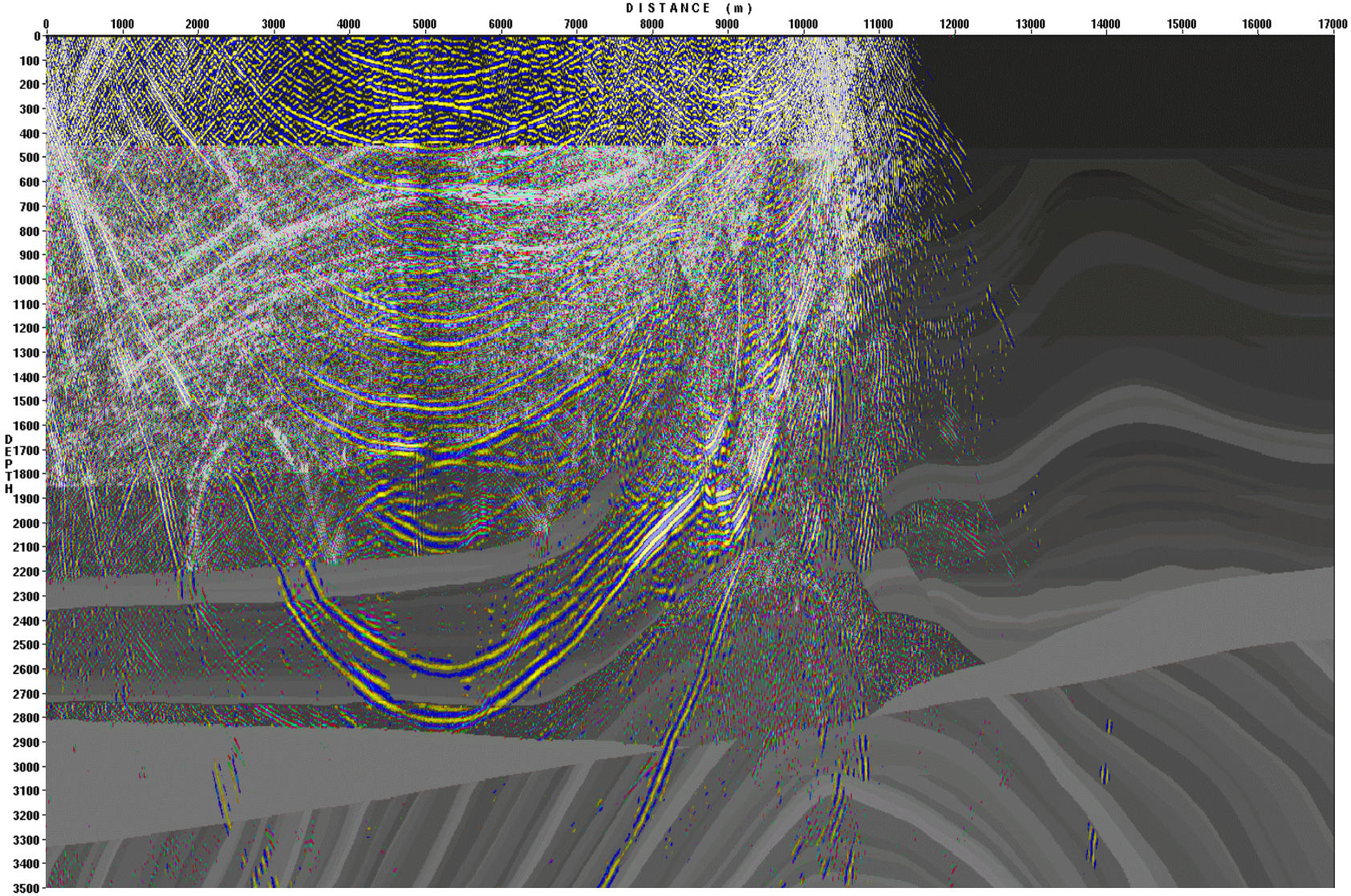

Figure 3.42. Wave propagation snapshot at t=3.8s. P-waves are blue-yellow, S-waves are red-green, model is greyscale

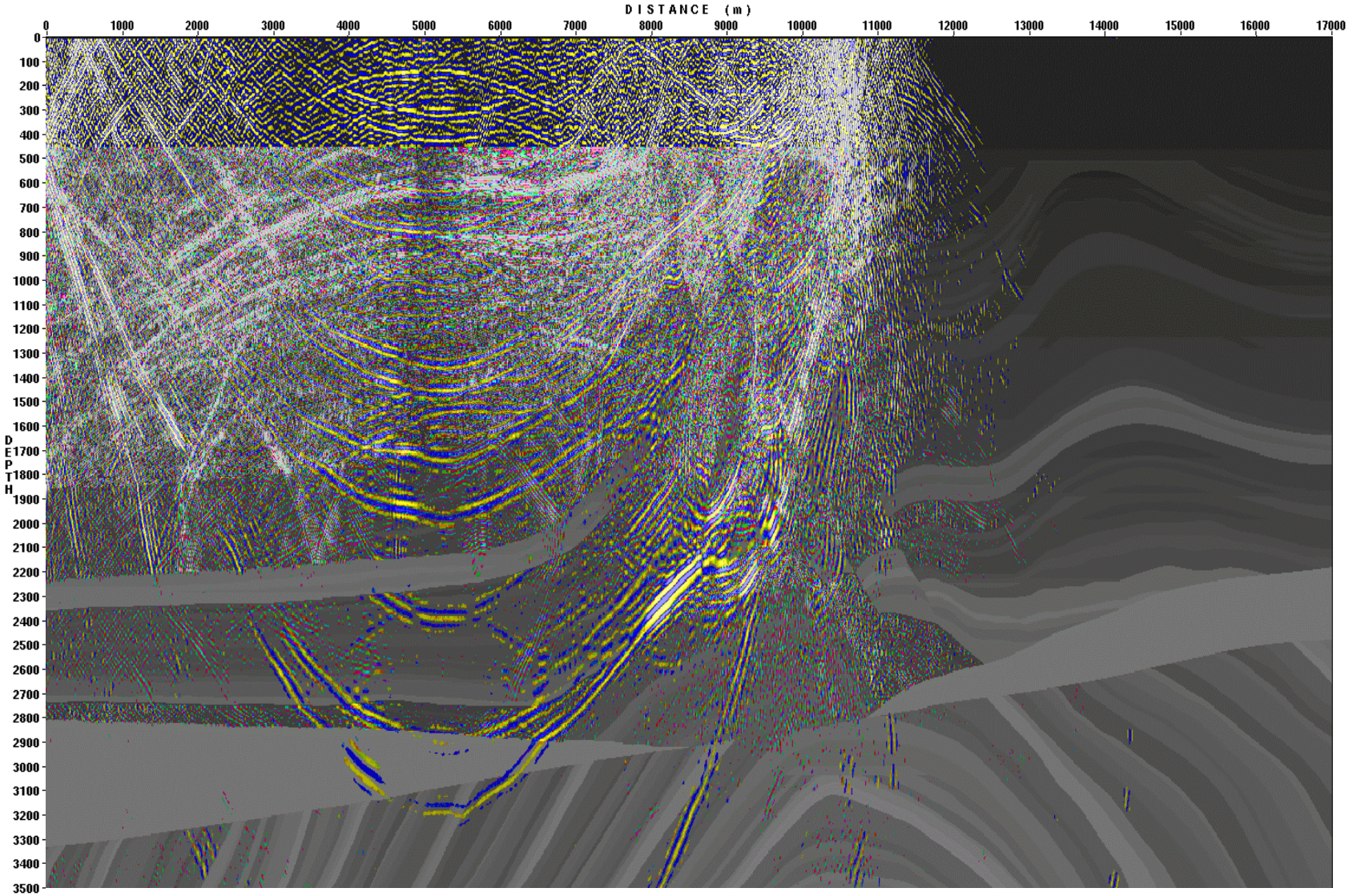

Figure 3.43. Wave propagation snapshot at t=3.9s. P-waves are blue-yellow, S-waves are red-green, model is greyscale

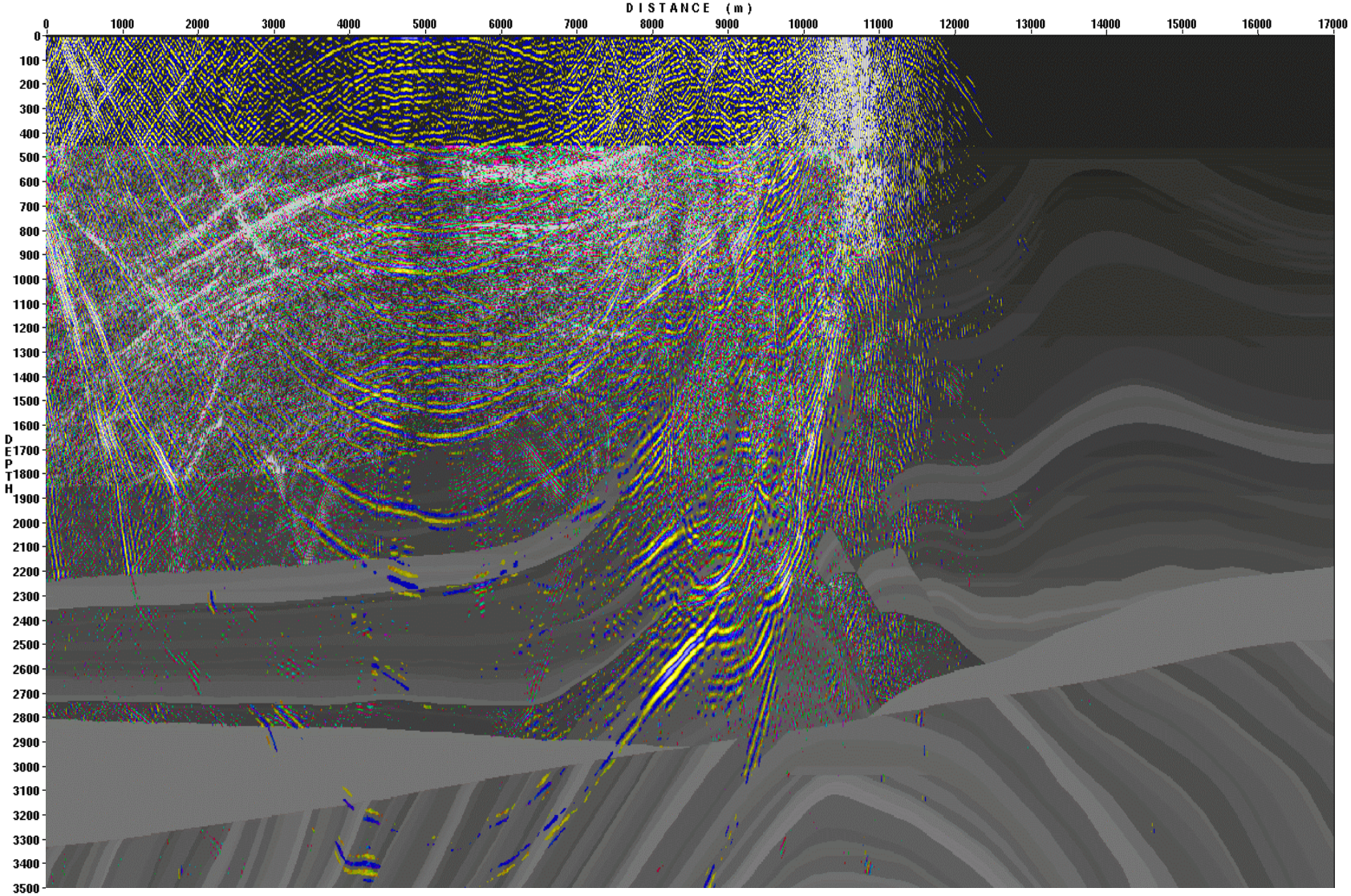

Figure 3.44. Wave propagation snapshot at t=4.0s. P-waves are blue-yellow, S-waves are red-green, model is greyscale

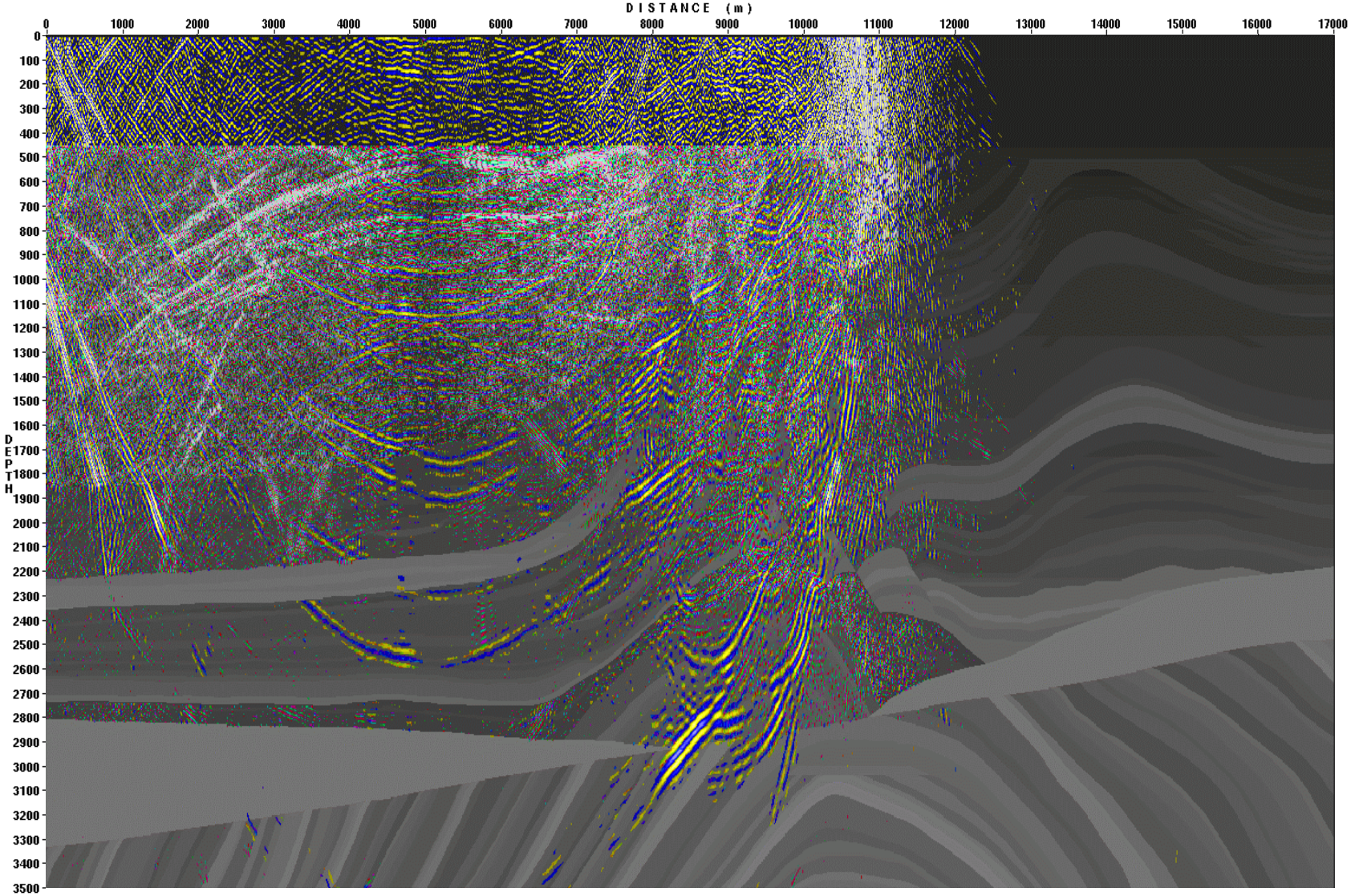

Figure 3.45. Wave propagation snapshot at t=4.1s. P-waves are blue-yellow, S-waves are red-green, model is greyscale

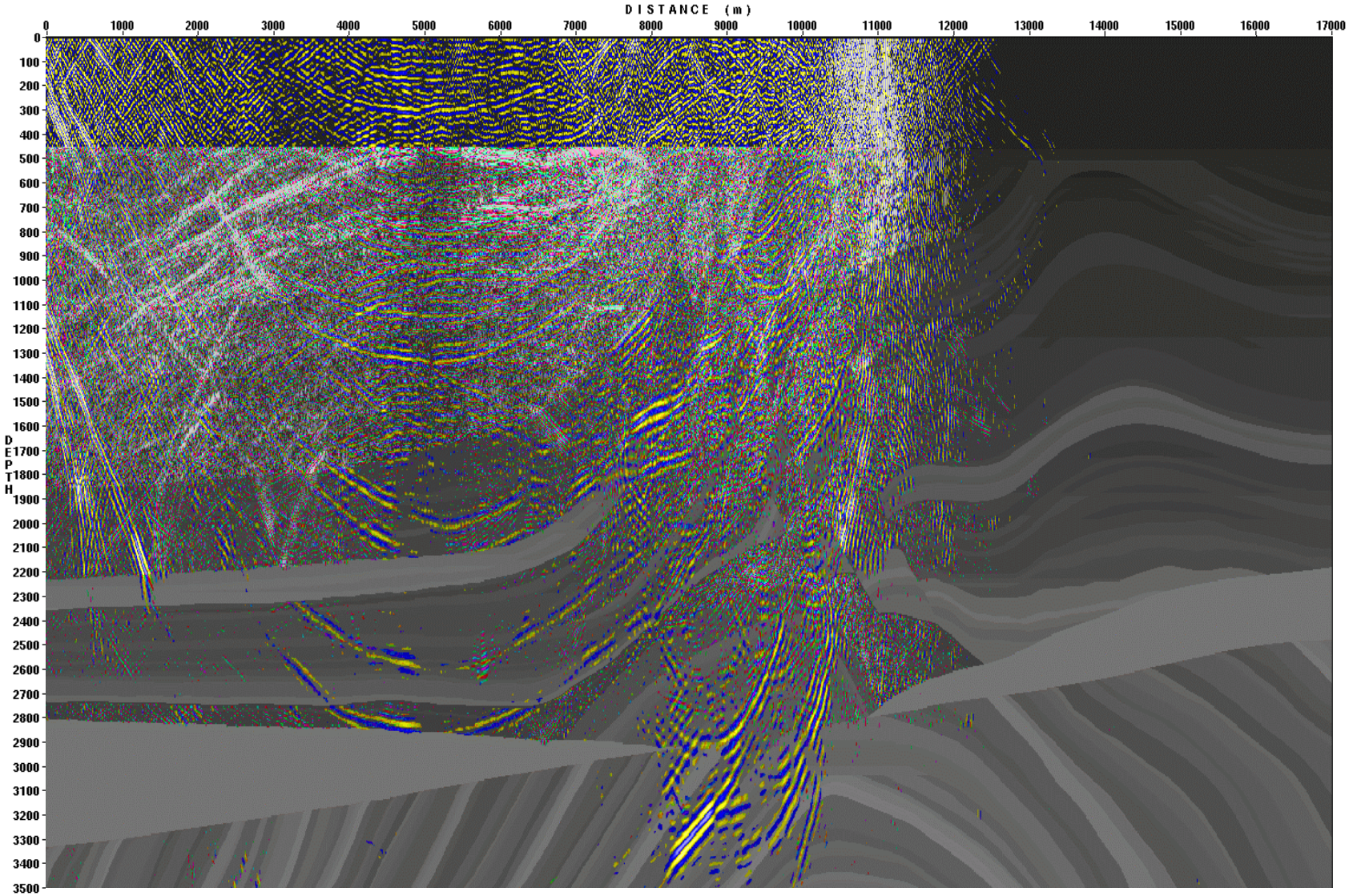

Figure 3.46. Wave propagation snapshot at t=4.2s. P-waves are blue-yellow, S-waves are red-green, model is greyscale

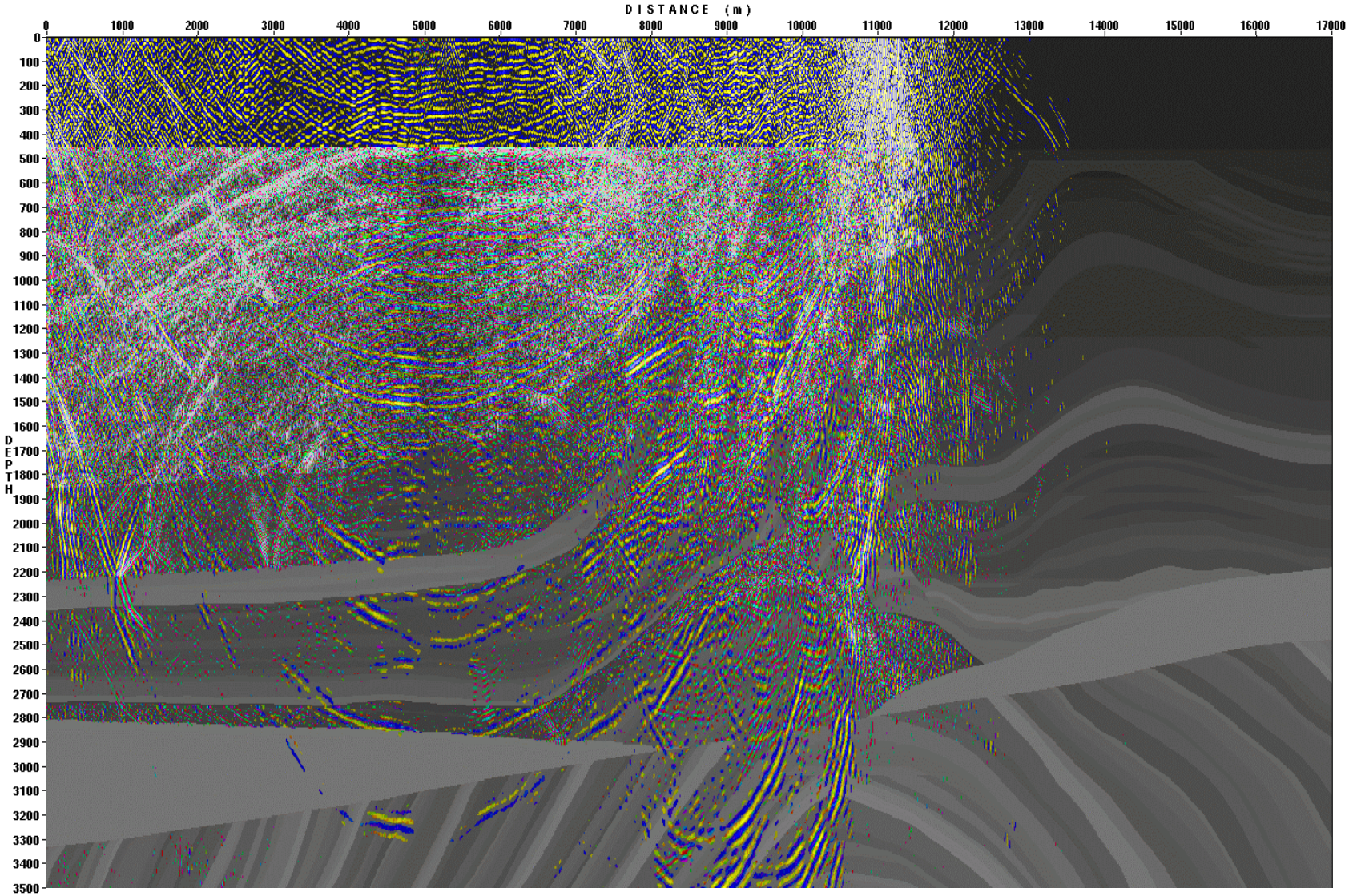

Figure 3.47. Wave propagation snapshot at t=4.3s. P-waves are blue-yellow, S-waves are red-green, model is greyscale

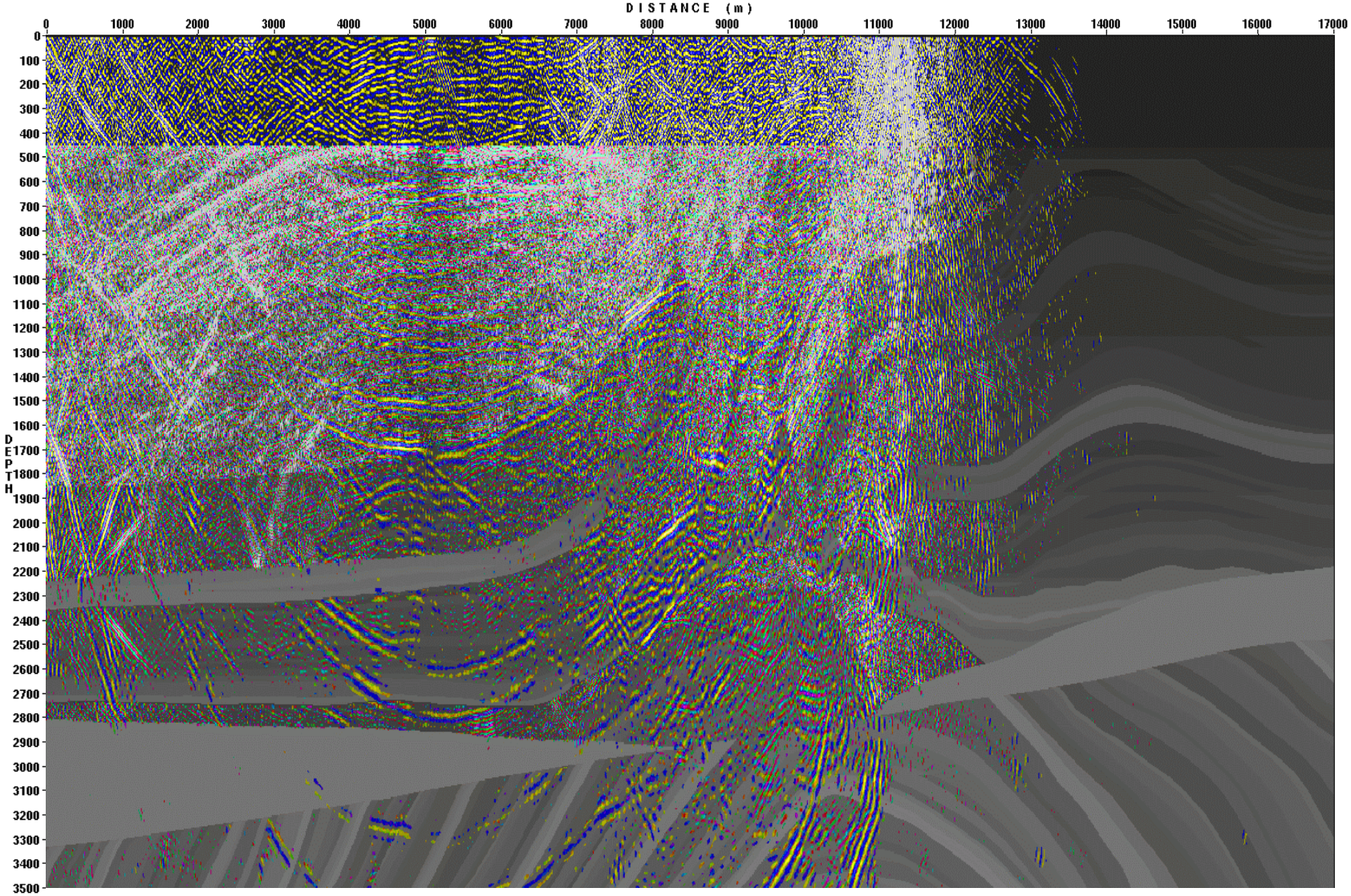

Figure 3.48. Wave propagation snapshot at t=4.4s. P-waves are blue-yellow, S-waves are red-green, model is greyscale

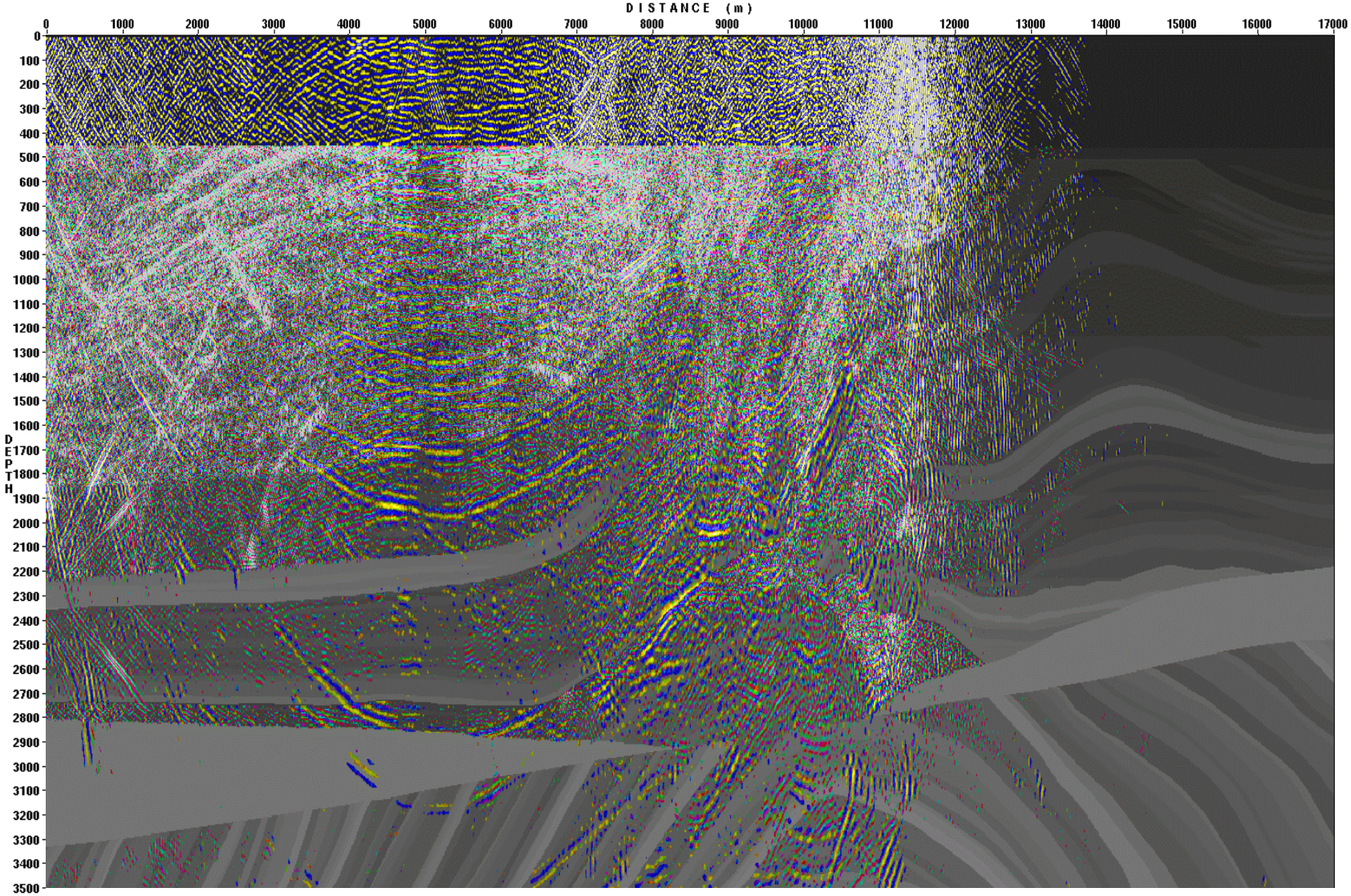

Figure 3.49. Wave propagation snapshot at t=4.5s. P-waves are blue-yellow, S-waves are red-green, model is greyscale

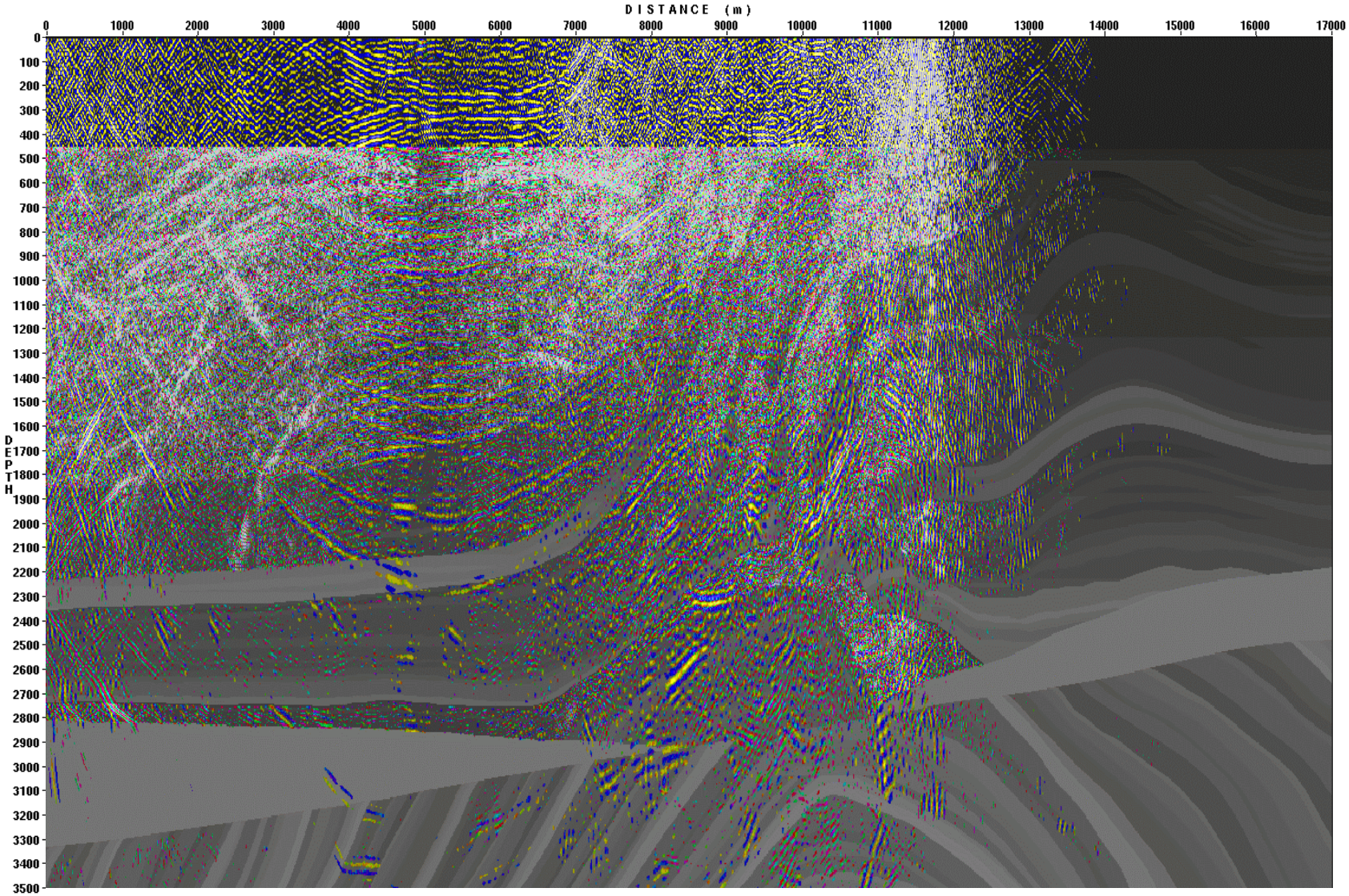

Figure 3.50. Wave propagation snapshot at t=4.6s. P-waves are blue-yellow, S-waves are red-green, model is greyscale

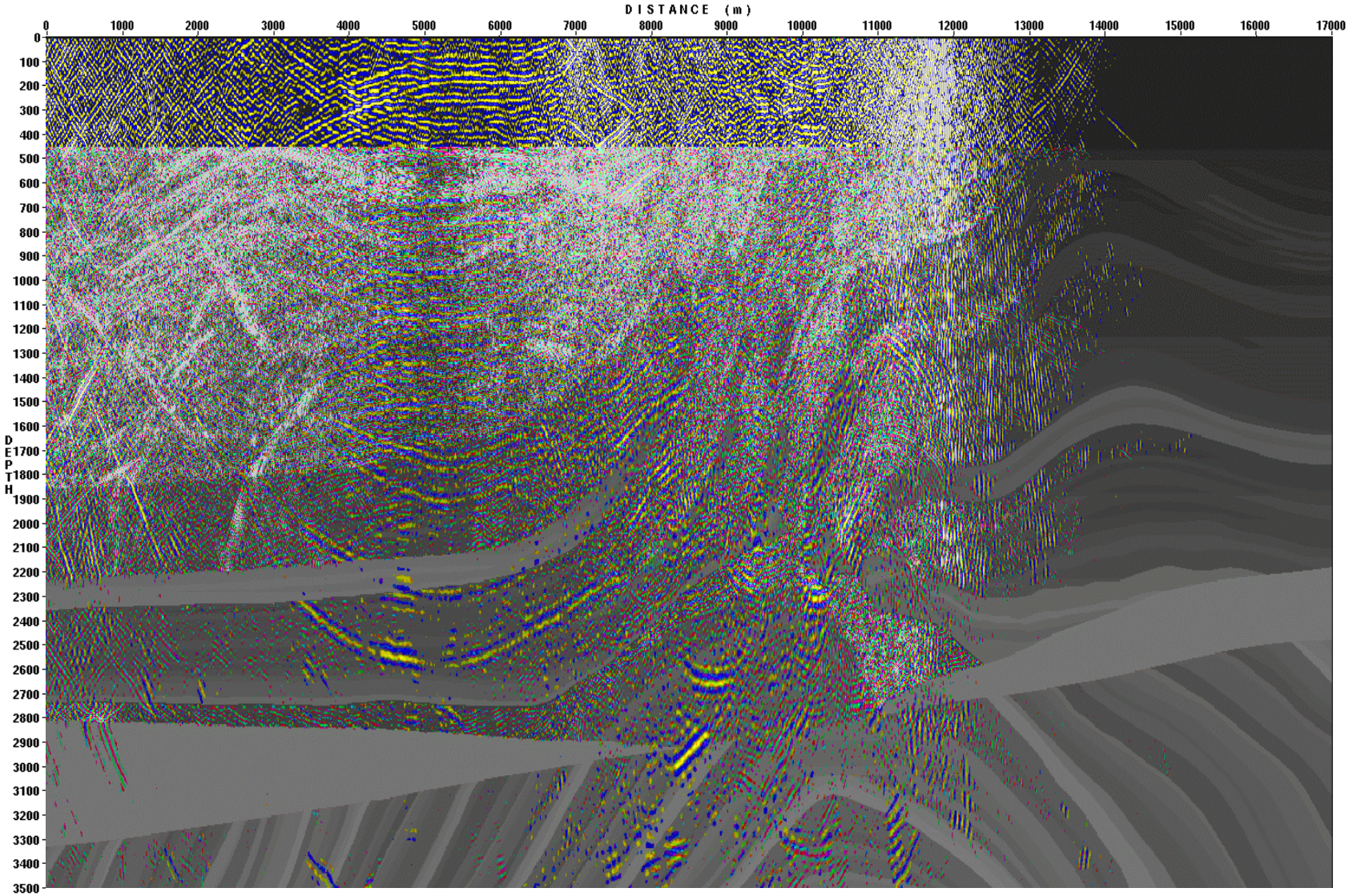

Figure 3.51. Wave propagation snapshot at t=4.7s. P-waves are blue-yellow, S-waves are red-green, model is greyscale

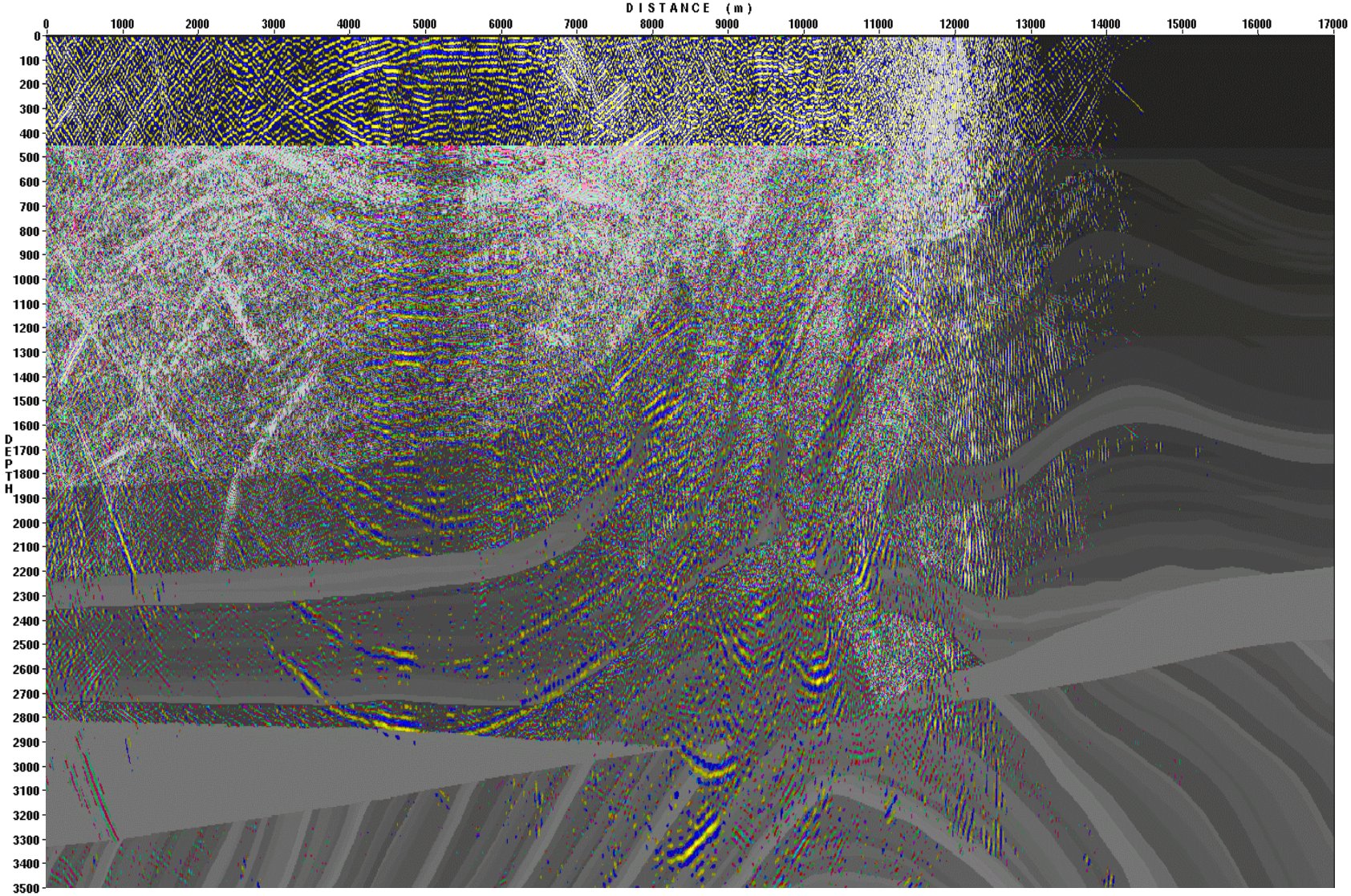

Figure 3.52. Wave propagation snapshot at t=4.8s. P-waves are blue-yellow, S-waves are red-green, model is greyscale

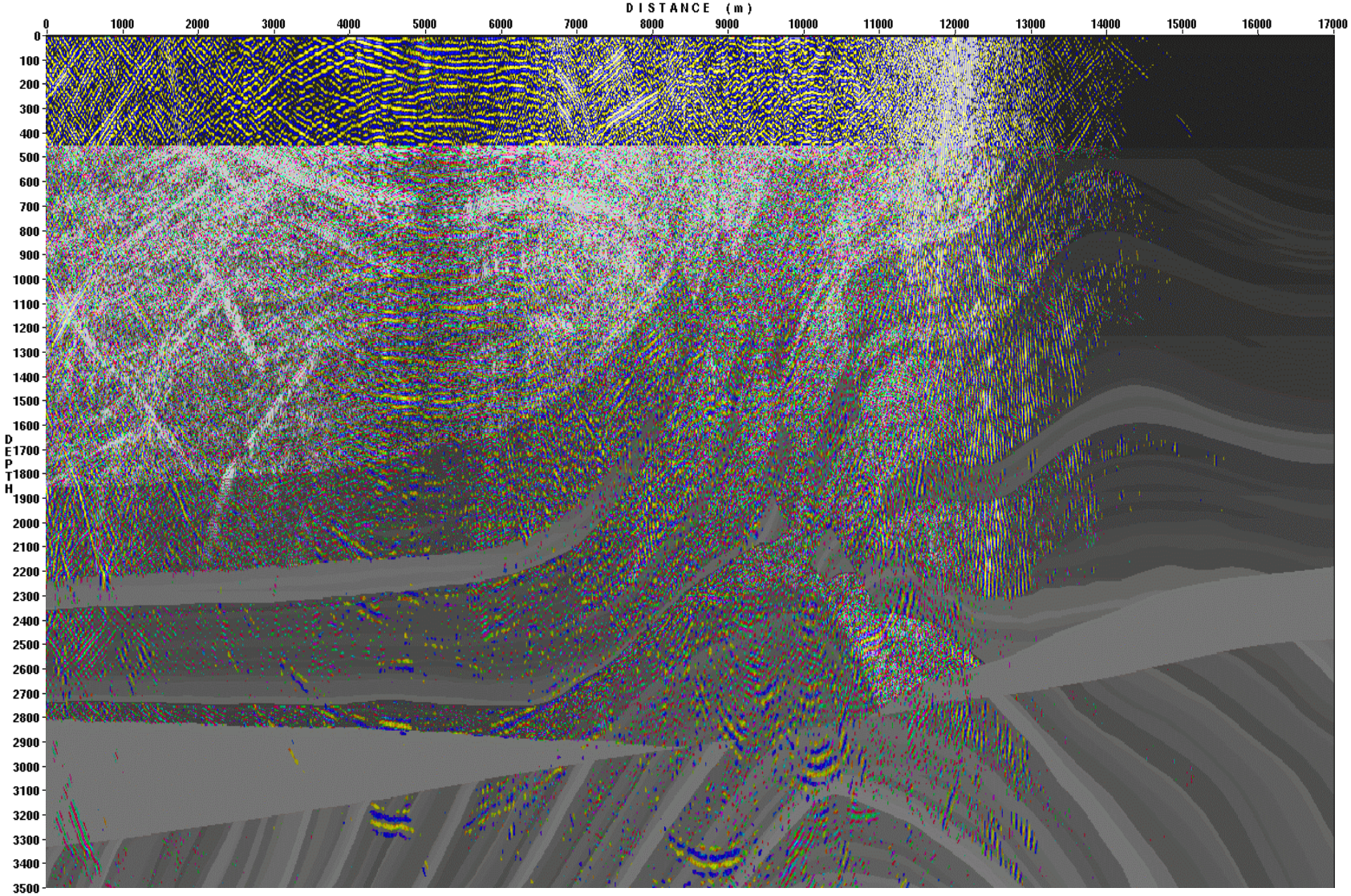

Figure 3.53. Wave propagation snapshot at t=4.9s. P-waves are blue-yellow, S-waves are red-green, model is greyscale

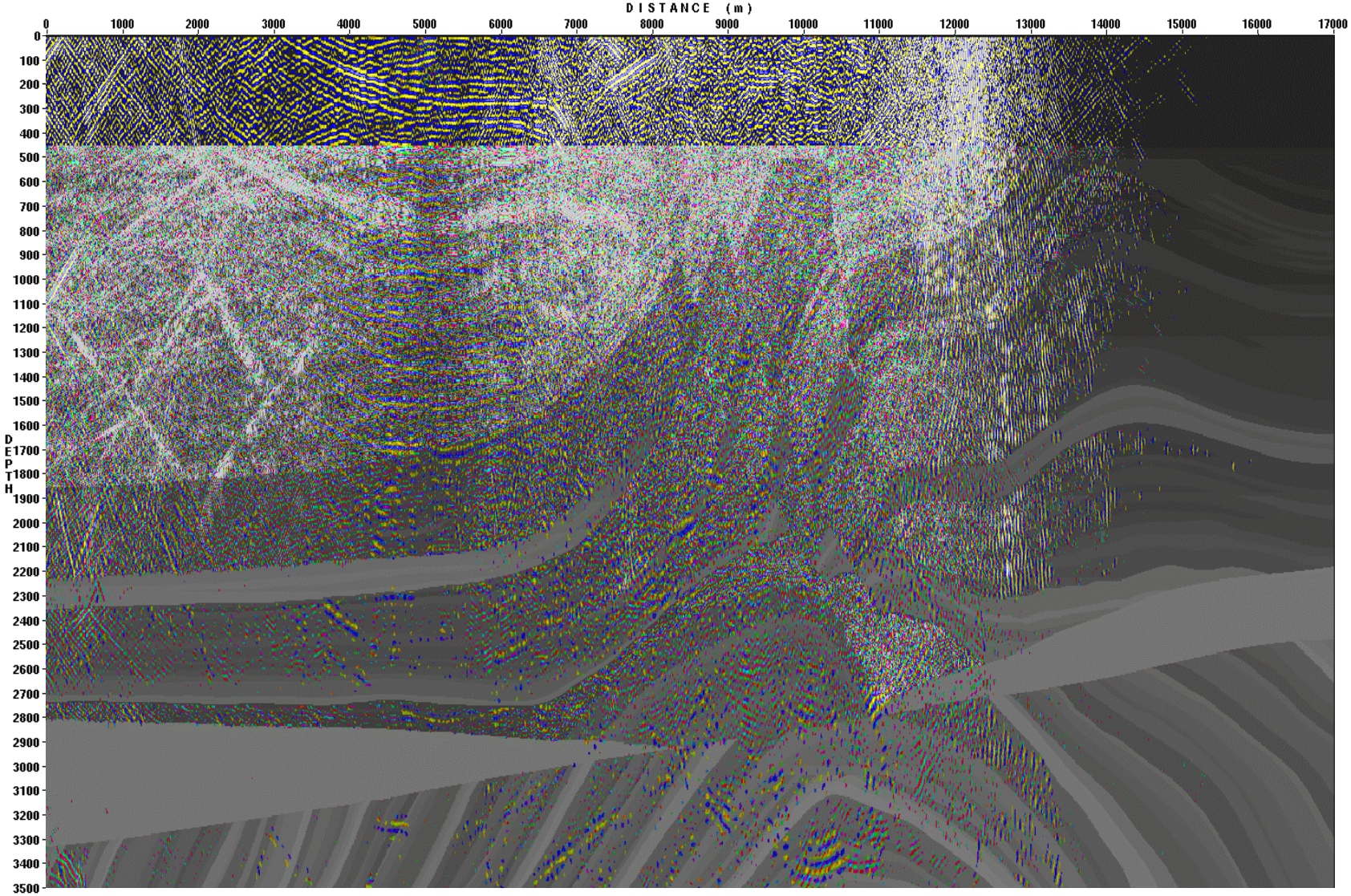

Figure 3.54. Wave propagation snapshot at t=5.0s. P-waves are blue-yellow, S-waves are red-green, model is greyscale

4. Data Processing

4.1 Marine Streamer Subset

My colleagues at the AGL performed an initial sorting of the data to create a "marine streamer" subset of the data. For each of the sources, only the receivers that would be present given a 6km towed streamer acquisition geometry were extracted. The geometry of the marine streamer configuration is given in Figure 4.1 and Table 4.1.

Source		**Receiver**	
Type	airgun	Type	hydrophone
Depth	10m	Depth	5m
First source number	121	First group number	1
First source location	3000m	Offset of first group	-6000m
Shot spacing	25m	Group interval	12.5m
Last source number	600	Last group number	480
Last source location	14975	Offset of last group	-12.5m
Number of sources	480	Number of receiver groups	480

Table 4.1. Marmousi2 "Marine Streamer" subset geometry

The towed streamer subset was used exclusively as the input for the processing, migration, and AVO analysis presented in this and the following chapters.

4.2 Processing Steps

I performed the seismic data processing using Landmark Graphics Corporation's ProMAX software, and GX Technology's imaging software.

Since the data are synthetic, many of the most commonly applied processing steps are not necessary, such as swell noise removal, cable strum noise removal, seismic interference noise removal, temperature/salinity statics, feathering issues,

filtering of bubble energy, *etc*. Therefore I applied a fairly simple processing flow as described in Figure 4.2.

4.3 Geometry

I created a geometry assignment as described in Figure 4.3. I assigned a common midpoint binning (CDP) starting with CDP 1 at X=0m, and a CDP interval of 6.25m. I provide the relationships between X, CDP, and shot number in Table 4.2 and Table 4.3.

	X	**CDP**	**Shot**
X		X=6.25(CDP-1)	X=25(Shot-1)
CDP	CDP=(X/6.25)+1		CDP=(4Shot)-3
Shot	Shot=(X/25)+1	Shot=(0.25CDP)+0.75	

Table 4.2. Relationships between CDP, shot, and distance (m).

	X(m)	**CDP#**	**Shot#**
Origin of velocity model	0	1	1
First CDP	0	1	1
First CDP with live traces	1500	241	61
First full fold CDP	2975	477	120
First shot	3000	481	121
First shot with all receivers inside the model	6000	961	241
Last full fold CDP	11993.75	1920	480.75
Last CDP with live traces	14968.75	2396	599.75
Last shot	14975	2397	600
End of velocity model	17000	2721	681

Table 4.3. CDP, shot, and distance at key locations. Note that some of the listed CDP and source numbers are outside of the real ranges (gray text).

The full fold portion of the line lies within the CDP range of 477-1920 (2975m-11993.75m). In this portion the fold is 90, since there are 4 CDPs for every shot (and 480/4=90). The fold tapers more rapidly at the low X end of the line. This is due to the

fact that the model stops abruptly at X=0 and for the shots in the X range of 3000-6000m some of the receivers were not present.

4.4 Datum Corrections

I processed the data such that the source and receiver depths were correctly compensated by applying a simple static shift to the traces.

The data required a secondary static shift to compensate for the input wavelet, *i.e.* to position the central peak of the wavelet at zero time, as discussed in Chapter 3. I applied a simple static shift of 72ms. The static shift was estimated from the data, but ideally the exact shift from the modeling experiment should be used. The publicly available synthetic data will be shifted so that this correction is not necessary.

4.5 Multiple Attenuation

The data contain a large amount of multiple energy. Since multiple energy is typically considered as noise in conventional data processing and imaging, it is desirable to remove it from the data. The multiples are particularly harmful if they interfere with primary events in the areas of interest.

I applied an adaptive free-surface multiple attenuation scheme to the shot records. The technique is a proprietary GX Technology implementation based on theory developed by the Delphi consortium, (e.g. Verschuur and Berkhout, 1992, 1997; Berkhout and Verschuur, 1997). The technique requires no prior knowledge of the subsurface and predicts and removes multiples that have a bounce at the free surface (water-air interface).

The first step is to extrapolate the traces to the near offset. I then muted the direct arrivals and predicted the multiples. I muted the multiple traces, to remove the numerical noise prior to the time of the first multiple, before adaptively matching and subtracting them from the input data.

Since the model is 2D the technique in general works extremely well, removing the free-surface multiples indicated in Figure 4.4a without degrading the primary reflections. The waterbottom multiples are seen to be almost completely removed in Figure 4.4b, as are some other strong multiple events highlighted in Figure 4.4a. Since the data itself drives the multiple prediction, the effectiveness of the method is reduced towards the edges of the data. This is observed in Figures 4.5 and 4.6 which show the NMO stack of the data before and after multiple attenuation. The yellow arrow indicates the area of diminished multiple attenuation.

Next, in Figures 4.7 – 4.12 I demonstrate the effectiveness of the multiple attenuation with respect to the prestack depth migration. The figures highlight four areas that are worthy of further discussion. Area 1 (Figure 4.9) shows a portion of the first waterbottom multiple. In the depth domain the previously flat multiple is now complex due to lateral and vertical variations in velocity. It is very effectively removed without harm to primary reflections. Area 2 (Figure 4.10) shows a deep portion of the result that is contaminated with multiples of contrasting dip. The multiples are very effectively removed. Area 3 (Figure 4.11) possesses multiples, some of which are attenuated, and others which are not. The multiples that are removed are the surface related multiples from events labeled as B and C in Figures 4.4 – 4.6. The multiples that are not removed are interbed multiples, and, since they do not have a bounce at the free surface, they are not removed using the surface multiple prediction algorithm. Area D (Figure 4.12) shows

the reduction in algorithm efficacy as the edge of the data is reached. In addition, a prominent interbed multiple is shown. The red line sketched onto the figure shows that the multiple results from a bounce within the gas sand layer. The multiple does not have a bounce at the free surface, and thus is not removed. The curious artifact that is highlighted probably results from the application of the multiple attenuation, especially as it is located in the zone where the multiple prediction would become challenging (not enough data).

A residual Radon multiple attenuation pass is often used on field data, but was not applied to the synthetic data since the remaining multiple energy is not significant in the areas of greatest interest.

4.6 Imaging

4.6.1 Imaging Overview

Imaging is the component of seismic processing that attempts to create an interpretable subsurface image.

Common mid-point sorting, followed by normal moveout correction (NMO) and stacking often provides the first estimate of the subsurface image. The method utilizes the redundancy of acquisition sampling, and assumes generally flat lying interfaces. In areas with dipping or complex geologic structures the NMO approximation fails, and migration is required in order to obtain an accurate image of the subsurface.

Migration is a process that moves dipping reflectors to their true (or at least more accurate) subsurface positions and collapses diffractions. Given the structural

complexity and lateral velocity heterogeneity of Marmousi2, it is evident that migration is very much required.

There are several families of migration methods which have significant differences in input requirements, cost, accuracy, and interpreter interaction. Typically, all migrations may be categorized by a few criteria, namely; 2D or 3D migration, poststack or prestack migration of the input traces, time or depth domain migration, and by the migration algorithm.

The dimensionality of the acquired data determines whether 2D or 3D methods should be used. 2D migrations are appropriate for data collected by 2D acquisition, such as Marmousi2.

Poststack migration involves a two step procedure, first, the hyperbolic stacking of the input traces (NMO), followed by a migration of the stacked traces. The migration is relatively fast due to the reduction (by stacking) of the quantity of input traces. The method tends to suffer when seismogram events are non hyperbolic, which is typical of mildly complex to complex geologic environments. Prestack migration handles the non hyperbolic nature of events by migrating them all, and performing NMO and stacking during the migration. The method is of course more expensive since many more input traces must be processed, but it is the method of choice for complicated geologic environments.

Imaging methods in the time domain are suitable for mildly varying velocity regimes since lateral velocity changes are ignored and no raypath bending is allowed. Depth domain migration takes into account lateral changes in interval velocity, including the associated raypath bending, and therefore is suitable for any geological situation that

results in rapid lateral velocity variations. The difference between time and depth imaging is easily understood by a raypath characterization (*e.g*. Fagin, 1999), as shown in Figure 4.13.

There are two means of propagating the seismic energy into the subsurface; Kirchhoff summation, or wavefield extrapolation. Kirchhoff methods utilize a diffraction summation technique, which is based on the summation of amplitudes along a diffraction hyperbola, where the hyperbolic curvature is governed by the velocity of the medium. A common variant in implementation is to 'scatter' the amplitude of an input seismic sample along an output subsurface ellipsoid. Amplitude and phase corrections are typically applied to the amplitudes (*e.g*. Schneider, 1978), and have been applied by the algorithms used in this study. Kirchhoff methods are computationally fast, can image steep dips, but may suffer in areas of complex velocity due to the requirement of raytracing to estimate the traveltimes. Usually only a single traveltime arrival is allowed, which means complex areas impinged by multiple wavefronts may not be well imaged. Wavefield methods work by downward continuing the recorded data to successively lower datums, typically using the one way (scalar) wave equation. At the image point, the downward continued samples are extracted and placed into the final image *(e.g*. Claerbout and Doherty, 1972). Wavefield methods are typically more computer intensive, and in regions of complex structure with multiple raypaths into the subsurface, provide more accurate results. They do not require raytracing and all arrivals are utilized.

None of the discussed methods are able to correctly handle multiple reflections, converted waves, surface waves, or noise. Therefore, the input data must be preprocessed to avoid imaging these 'extra' events as false subsurface scatterers.

4.6.2 Imaging Marmousi2

I applied a suite of representative seismic imaging methods to the processed data. These ranged from very simple to state of the art methods. I used various tools at my disposal including ProMAX and GX Technology Corporation's proprietary algorithms. I expect these images will serve as a 'benchmark' against which other scientists can compare their work and improve their algorithms. The methods are summarized in Table 4.4.

#	Description	Velocity model	Migration Domain	Migration Algorithm	Output Domain	Output Type
1	Simple NMO/Stack	Vrms	-	-	time	stack
2	Kirchhoff PoSTM	Vrms	poststack	Kirchhoff	time	stack
3	Kirchhoff PoSDM	Vinterval	poststack	Kirchhoff	depth	stack
4	Kirchhoff PreSTM	Vrms	prestack	Kirchhoff	time	offset gathers
5	Kirchhoff PreSDM (shortest path)	Vinterval	prestack	Kirchhoff	depth	offset gathers
6	Kirchhoff PreSDM (max. energy)	Vinterval	prestack	Kirchhoff	depth	offset gathers
7	Wave-equation PreSDM	Vinterval	prestack	wave-equation	depth	angle gathers

Table 4.4. Imaging methods applied to Marmousi2

4.6.3 Imaging Velocity

The input migration velocity models are shown in Figures 4.14 – 4.16. Wave equation migration does not require a smoothed velocity; therefore I used an unaltered version of the model interval velocity grid, Figure 4.14. The Kirchhoff depth migration method is very sensitive to sharp lateral changes in interval velocity since ray paths may be scattered, causing an uneven ray coverage and therefore uneven and discontinuous traveltime information. I performed a series of migration tests with different smoothing parameters before accepting the velocity grid shown in Figure 4.15. The smoothing was

performed in the slowness domain and included both horizontal high cut filtering and variable length boxcar smoothing in both directions. The time migrations require an RMS velocity, which I created from the interval velocity, Figure 4.16. I smoothed the RMS velocity so that large lateral changes in the RMS velocity, which can introduce migration artifacts, were removed.

4.6.4 Post migration processing

Due to the significant velocity variations within the model, there is a large amount of wavelet stretch with offset. This can be clearly identified in Figure 4.17. The stretched wavelet, if included in the stack, produces undesirable results. I removed the stretch effect by applying a simple outer mute to the input data for the poststack migrations. I applied a simple outer mute to the image gathers (before stack) for the prestack migrations. The prestack outer mute is shown in Figure 4.17.

The mute described by Figure 4.17 reveals that much of the imaged information is not captured by the final stacked image. In some cases amplitudes are low in the near offsets but increase substantially in the mid and far offsets due to AVO effects. The stack includes only the near offsets, resulting in some events being poorly represented. Careful mute picking can be performed to incorporate the information from the further offsets without degrading the stacked result. In practice, automated picking methods are required, and this may be an area for future research.

4.6.5 Comparison of results

In order to ascertain the quality of the resultant images, I converted all of the images to depth, so that they could be compared to the velocity model, Figure 4.18. However, direct comparison of seismic images to a velocity model is somewhat difficult.

In order to provide an easier means of quality control I calculated a synthetic seismogram.

Simple vertical raytracing (one vertical ray for each CDP) was performed and the resultant amplitude was convolved with the Ormsby 5-10-60-80Hz wavelet. Initially the match between the synthetic and the imaged results was poor due to the ghosts not being taken into account by the simple synthetic. Figure 4.19a shows a schematic of the travel paths. A single arrival for each reflection event is obtained when ghosts are not considered, Figure 4.19b, and four arrivals are obtained when the ghosts are considered, Figure 4.19c. Convolution with the wavelet produces Figures 4.19d and 4.19e which are without and with ghosts respectively. The addition of the ghosts has the net effect of applying approximately a 180 degree phase shift to the data, and time-shifts the maximum energy of the envelope, as indicated by the blue arrows in Figures 4.19d and 4.19e.

The Marmousi2 model has a velocity gradient at the waterbottom, which may also affect the phase and timing of the wavelet. The vertical raytracing solution does not take into account the gradient since there are no samples (reflection events) within the sediment layer. In order to determine whether this would be a significant factor I created additional thin layers within the top two sediment layers. A total of eleven 5m thick layers were placed between the waterbottom and the base of horizon H003, which represents the base of the soft sedimentary transition zone, Figure 4.20. I computed the vertical synthetic with and without ghosts, and no discernable changes could be observed compared to the unmodified Marmousi2 model results. The extremely low acoustic impedance contrasts between the layers produces extremely small amplitudes, which explains why the results are practically identical.

The final vertical synthetic result was converted to depth for comparison to the migrated depth sections, Figure 4.21. The “jitter” observed on the horizons in the simple synthetic is a result of the depth conversion. Using a smoother velocity for the depth conversion removes the jitter, but also leads to incorrect depths. Therefore the jitter should be ignored; the perfect solution should be smooth.

The timing and phase of the imaged results and the vertical synthetic were compared for a couple of key events to ensure that their comparison is valid. The waterbottom and the shallow low velocity gas sand were used as reference locations for the calibration since at these locations the acoustic impedance contrasts are large and unambiguous. A detailed inspection of the traces imaged at the waterbottom is presented in Figure 4.22. There are some slight differences between the results, but the wavelet shape generally matches the vertical synthetic, *i.e.* a symmetrical trough, time shifted beneath the waterbottom by about 10ms (8m). A similar detailed inspection at the shallow gas sand is presented in Figure 4.23. The top of the sand is represented by a large symmetrical peak time shifted below the actual interface. The base is represented by a large trough with symmetrical large amplitude side lobes. The imaged results show the same features. It is interesting to note that the vertical sampling of the velocity grid (1.25m) and the imaged output (5m) appear to be coarse when these details are studied. The wavelets have not been interpolated in order to emphasize the ‘stepped’ nature present in the results. The Kirchhoff poststack and prestack depth migrated results, Figures 4.23d and 4.23f show considerable timing differences compared to the synthetic and the other results. These timing differences are due to the velocity smoothing that is necessary to obtain a good image. To prove this hypothesis I

imaged the data without smoothing, using a 1m imaging depth step. The result is displayed in Figure 4.23g, and the timing is comparable with the other methods.

Generally, the results show the imaging improvements that result from applying the appropriate imaging method to the geological complexity of the area of study. The Marmousi2 model is a complex model with structural dip and extremely variable interval velocity. In such regimes the prestack depth migration methods have an obvious edge over less rigorous methods.

4.6.5.1 Simple NMO/Stack (#1)

The resultant image is shown in Figure 4.24, and enlarged portions are shown in Figures 4.31 – 4.34. The result is interpretable in the flat lying areas, and in these areas the horizons are imaged at the correct depth. As the dip increases the image quality gradually degrades and the horizons are laterally mispositioned. The diffractions are not collapsed since no migration has been applied. The diffractions totally obscure the complex central area which is not interpretable, and some textbook examples of 'bow ties' for some small synclinal structures are present.

4.6.5.2 Kirchhoff poststack time migration (#2)

The resultant image is shown in Figure 4.25, and enlarged portions are shown in Figures 4.31 – 4.34. The poststack time migration provides a decent image in most of the section. The diffractions are fully collapsed, converting the bow-ties into synclines, and providing hints regarding the structural complexity in the faulted zone which is not well imaged. Events with moderate dip are mispositioned. Some deep events under the unconformity are imaged, but are accordingly mispositioned. The deep area under the complex zone shows artifacts related to the depth to time conversion.

4.6.5.3 Kirchhoff poststack depth migration (#3)

The resultant image is shown in Figure 4.26, and enlarged portions are shown in Figures 4.31 – 4.34. The poststack depth migration shows an improvement from the poststack time migration since the complex velocity variations are taken into account. A decent image in most of the section is obtained. The diffractions are fully collapsed and events are more correctly positioned. The central complex area is not well imaged, but shows considerable improvement from the poststack time migration. The deep area under the complex zone possesses less noise than the poststack time migration. Steep reflectors under the unconformity are imaged, and are correctly positioned.

4.6.5.4 Kirchhoff prestack time migration (#4)

The resultant image is shown in Figure 4.27, and enlarged portions are shown in Figures 4.31 – 4.34. The prestack time migration has the advantage of migrating all the input traces, but is limited by the simplistic velocity assumptions. The imaging of the flat and shallow dipping areas is excellent, but the imaging and positioning deteriorates in the complex part of the model. A greater number of horizons are imaged compared to the post stack migrations, even in the deeper parts of the model. The deep area under the complex zone shows artifacts related to the depth to time conversion.

4.6.5.5 Kirchhoff prestack depth migration (shortest travel path) (#5)

The resultant image is shown in Figure 4.28, and enlarged portions are shown in Figures 4.31 – 4.34. Prestack depth migration methods are well suited to the imaging problem since each prestack input trace is migrated without NMO and stack degradation, and lateral velocity variations are taken into account. Very good imaging of most of the model is obtained, with horizon depth and lateral position matching the

model very well. The shallow/moderate depth horizons are almost perfect and faults are well defined. The imaging deteriorates in the central portion (the marl cored anticline and the anticline under the unconformity) and the amplitude is much weaker. The Kirchhoff implementation includes amplitude corrections computed during raytracing that result in the lower amplitudes in this difficult imaging zone. In many cases the reflections can often be seen, but they have a low signal to noise ratio.

4.6.5.6 Kirchhoff prestack depth migration (max. energy) (#6)

The resultant image is shown in Figure 4.29, and enlarged portions are shown in Figures 4.31 – 4.34. This method provides a very similar result to the shortest travel path result. To the flanks of the structure the result is identical since both raytracing travelpaths are identical. In the complex area the raypaths are different, resulting in slightly different imaging. The central, deeper portion is slightly better imaged using the maximum energy arrival rather than the shortest travel path arrival. The amplitudes are stronger and events can be traced for greater distances.

4.6.5.7 Shot-profile wavefield prestack depth migration (#7)

The resultant image is shown in Figure 4.30, and enlarged portions are shown in Figures 4.31 – 4.34. The wave-equation migration has the advantage of incorporating all travelpaths simultaneously, and does not require the velocity model to be smoothed. This method produces the superior result. The imaging is equivalent to the Kirchhoff prestack depth migration results in most of the model, but the complex area is vastly improved, and fault planes are much better defined. Commonly, wavefield methods are characterized by the inability to image steep dips, but this is usually due to computational constraints (cost) which force the computational grid size to be too large,

the frequency bandwidth to be restricted, and the input data to be decimated. This example shows that if the frequency and grid size are appropriately small, the imaging of the fault planes is far superior to the Kirchhoff methods. Almost all events are correctly positioned in space and are traceable across the whole model.

4.6.6 Image Gathers

The stretch muted NMO gathers and unmuted prestack migrated image gathers are shown in Figures 4.35 – 4.40. For presentation, every 40th image gather is displayed. The offset stretch at far offsets is observed. The prestack time gathers show events that are not always flat due to the limitations of the method, Figure 4.36. The prestack depth migrated image gathers show events that are generally flat, Figures 4.37 – 4.40, which is expected given that the exact velocity model was used. Two sets of gathers are presented for the wavefield migration. Familiar offset gathers (similar to those generated by the Kirchhoff methods) are shown in Figure 4.39, and subsurface angle gathers are shown in Figure 4.40. The wavefield offset gathers were computed before the SRME multiple attenuation processing and therefore contain free surface multiples.

4.6.7 Imaging problems

All of the results contain noise that can be attributed to many sources; remaining multiples, converted waves, head waves, *etc.* The noise is less evident where strong events are present, but it contributes significantly in areas of low or absent signal, such as inside the salt. Theoretically the salt body should be devoid of any data as shown by the simple synthetic. In areas of very complex imaging the coherent noise may be the dominant signal, which may lead to erroneous interpretation.

An interesting problem at the left side of the section appears to be a migration artifact, possibly caused by spikes in the dataset. However, detailed inspection of the input shot records shows the real cause of the problem, Figure 4.41. During acquisition Clayton-Engquist boundary conditions were used at the edges of the velocity model to provide an absorbing boundary. If the boundary conditions are sufficient, waves will be fully absorbed and will not be able to bounce back into the model. However, the figure clearly shows that events are reflected back into the data where the model terminates. The problem only occurs where the receivers extend outside of the model (shots 121 to ~251). The imaging methods cannot discriminate against this data and the result is that the energy is spread across the migrated image, appearing as an imaging artifact. The data reflected from the model boundary could probably be easily removed by applying a filter that can discriminate using the dip, such as an fk filter.

Another artifact common to all migrations is the shallow anomaly shown in Figure 4.12. This has already been discussed, and is related to the multiple attenuation.

A few interesting artifacts are highlighted in Figure 4.42. Event A appears to be an interbed multiple (trapped between the two bright reflectors) or a mode conversion event. Event B is possibly a mode converted event. The origin of event C is currently unknown.

4.6.8 Computational Considerations

The attainment of better results by applying more advanced imaging methods is not without cost. The superior methods require more rigorous input in terms of the velocity model (not an issue for synthetic data such as Marmousi2 since the exact model

is known), and in terms of runtime. The approximate runtimes in CPU minutes are shown in Figure 4.43.

Although the runtimes appear to grow at an alarming rate, modern PC clustering technology allows these tasks to be run in parallel and results can be provided within tens of minutes for the Kirchhoff prestack migrations, and several hours for the wavefield methods.

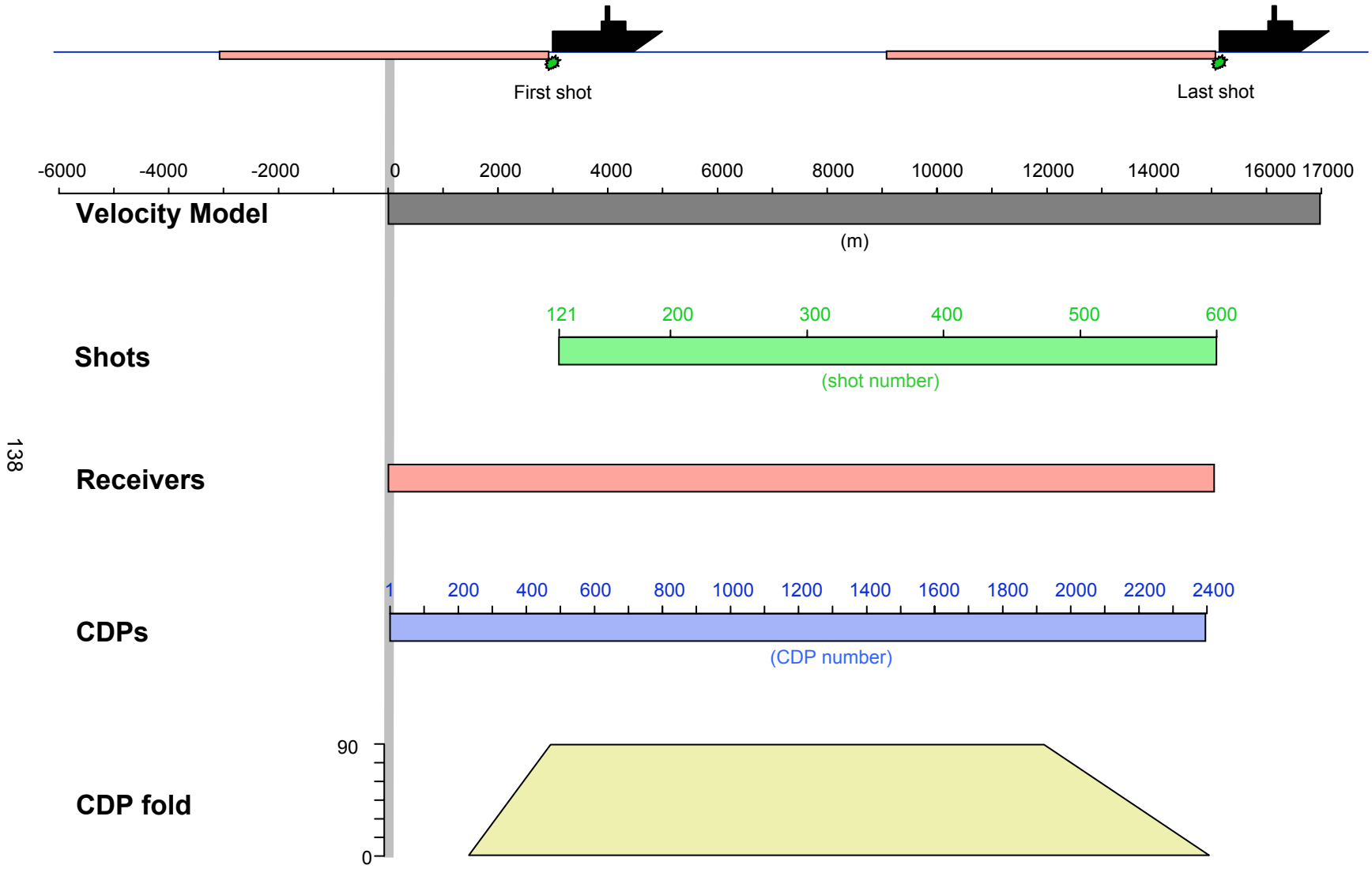

Figure 4.3. Marmousi2 "Marine Streamer" subset. Coverage of velocity model, sources, receivers, CDPs, and CDP fold.

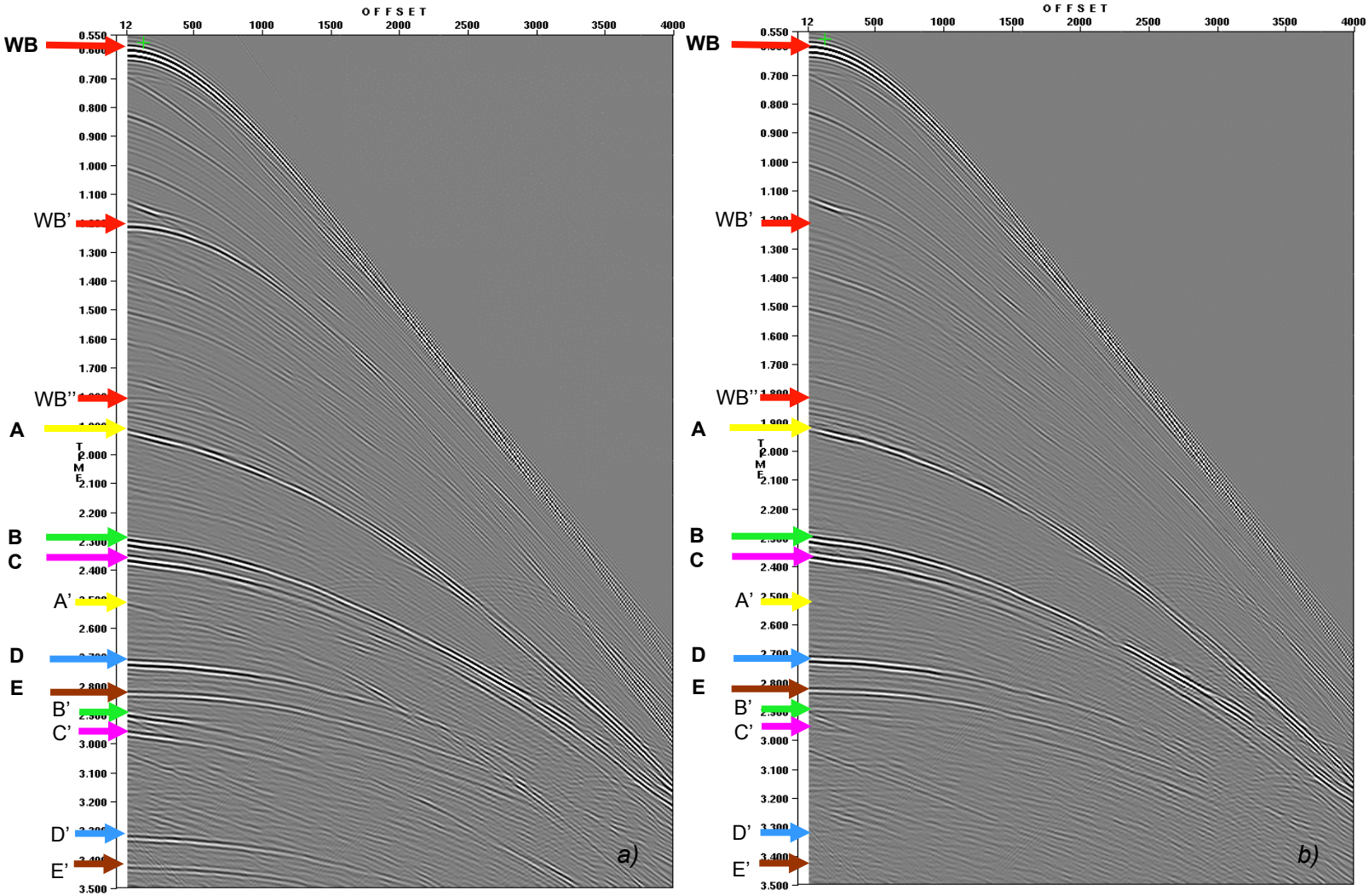

Figure 4.4. Shot gathers for shot #245 (at x=6100). a) before multiple attenuation, b) after multiple attenuation. Selected multiple generators and multiple reflectors are shown. Large arrows indicate primaries and are labeled in bold case. Small arrows indicate multiples and are labeled with a single prime, ', for 1st multiple, and with a double prime, '', for 2nd multiple. Arrow colors are consistent for each reflector.

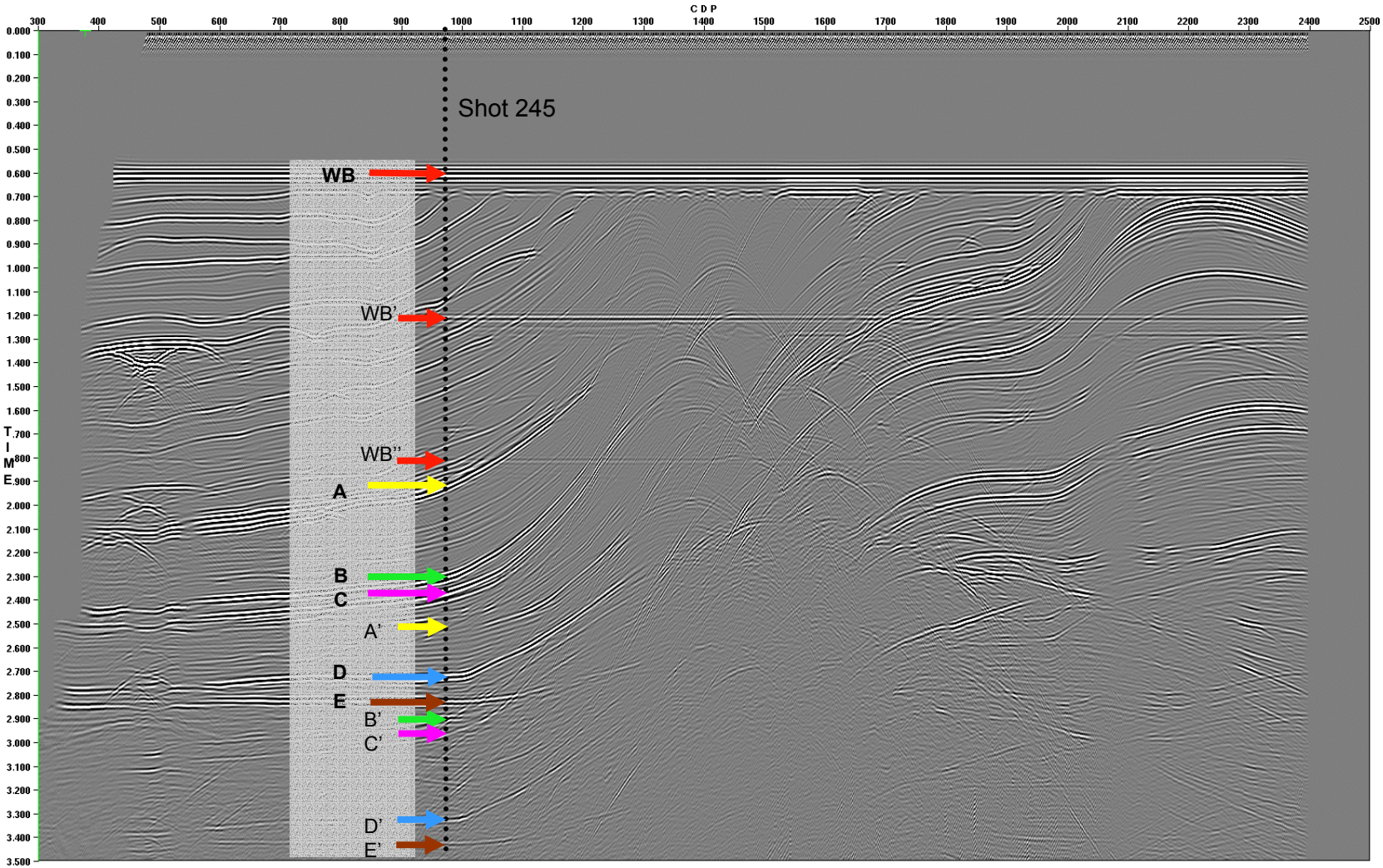

Figure 4.5. NMO-stack (time) before multiple attenuation. Dashed line shows location of shot record #245 showed in Figure 4.5. Large arrows indicate primaries and are labeled in bold case. Small arrows indicate multiples and are labeled with a single prime, ', for 1st multiple, and with a double prime, '', for 2nd multiple. Selected events only are labeled. Arrow colors are consistent for each reflector.

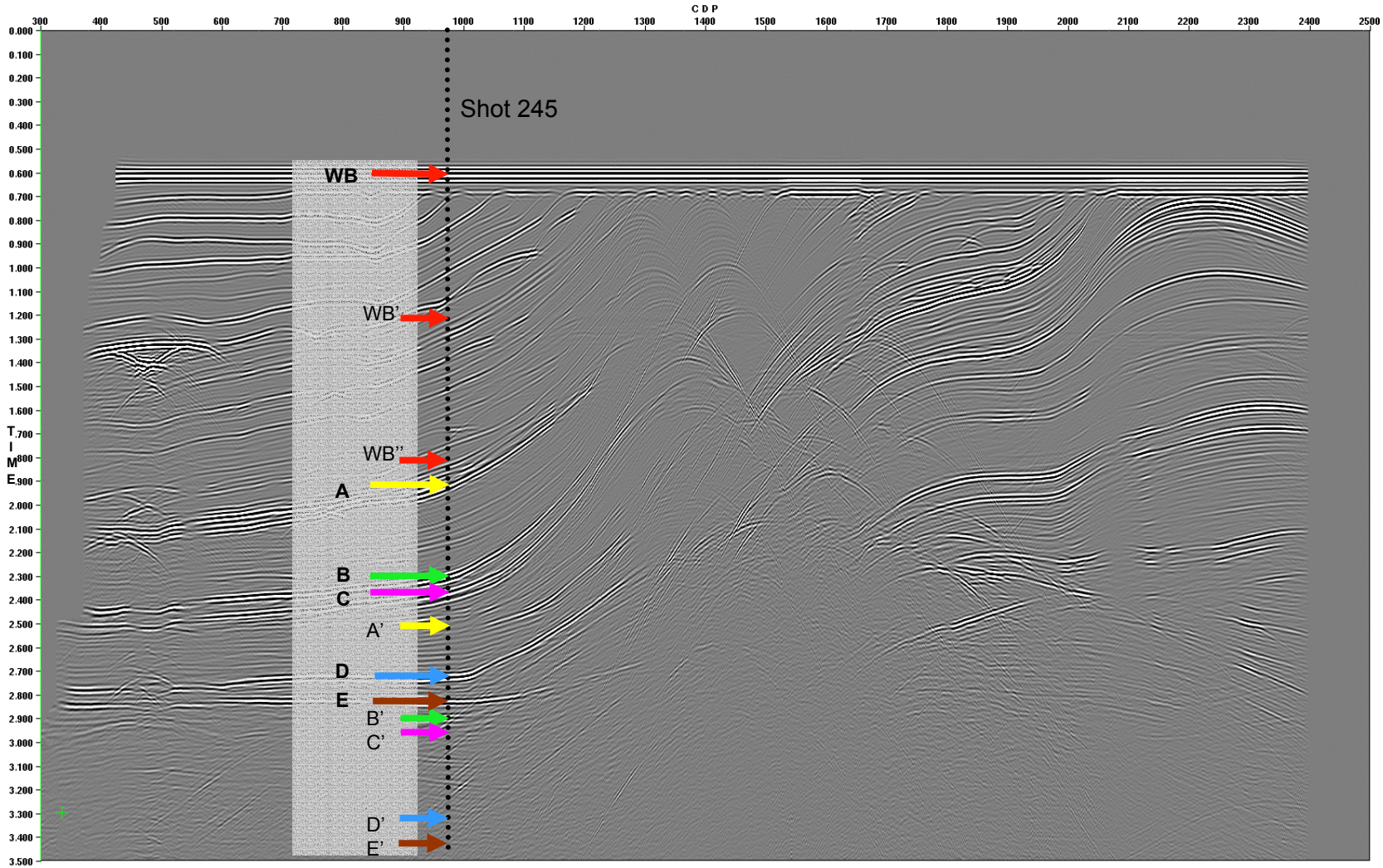

Figure 4.6. NMO-stack (time) after multiple attenuation. Dashed line shows location of shot record #245 showed in Figure 4.5. Large arrows indicate primaries and are labeled in bold case. Small arrows indicate locations of multiples shown in Figure 4.6 and are labeled with ' for 1st multiple, and '' for 2nd multiple. Selected events only are labeled. Arrow colors are consistent for each reflector.

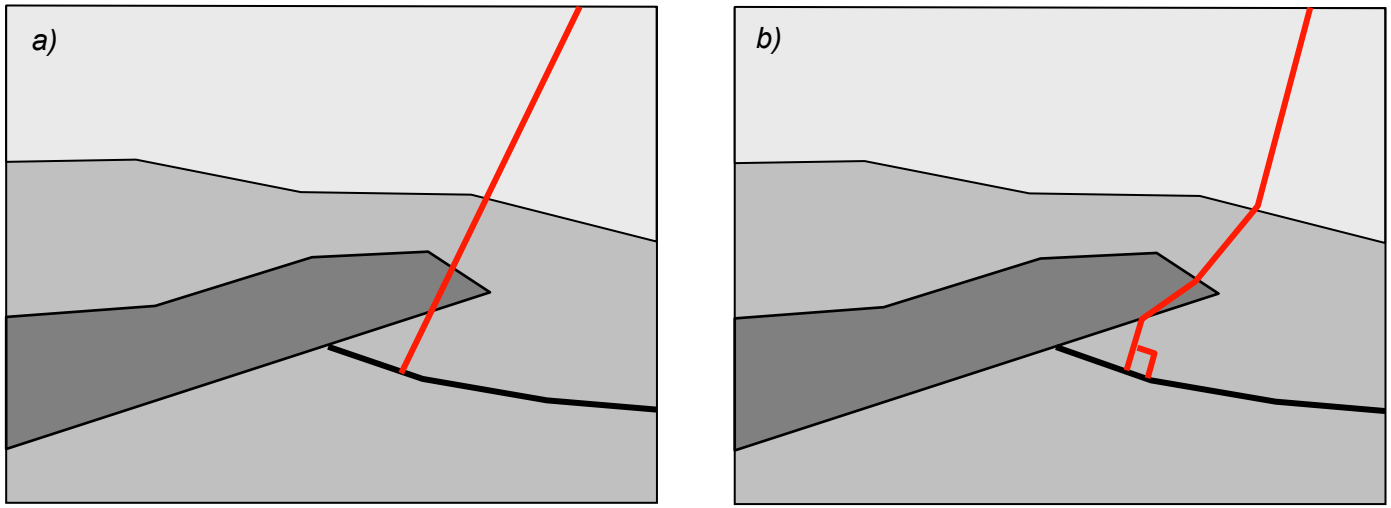

Figure 4.13. Raypath characterization of the difference between a) time and b) depth migration. Time migration does not account for the complex raypath of the true velocity model. Figure taken from Fagin (1999).

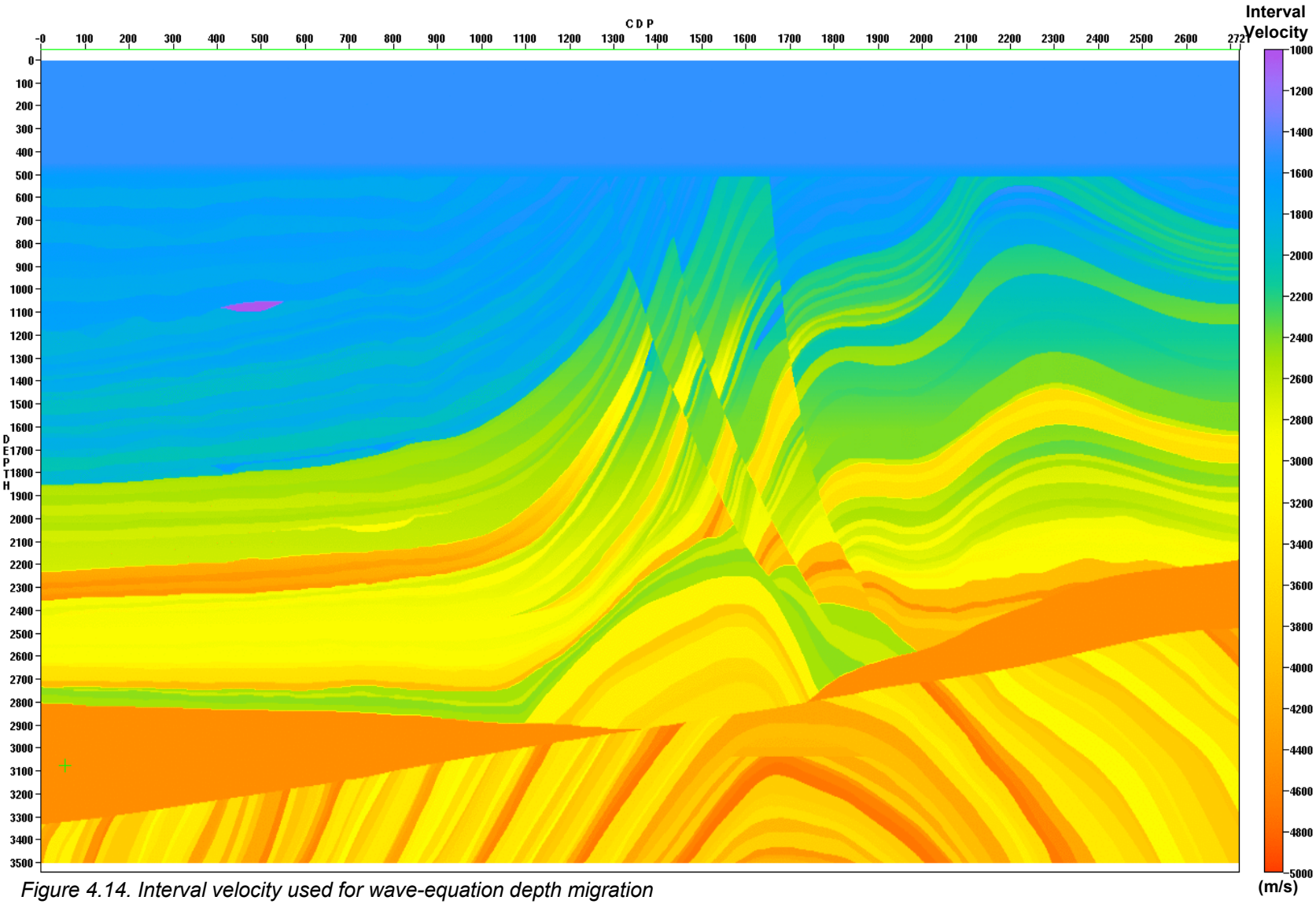

Figure 4.14. Interval velocity used for wave-equation depth migration

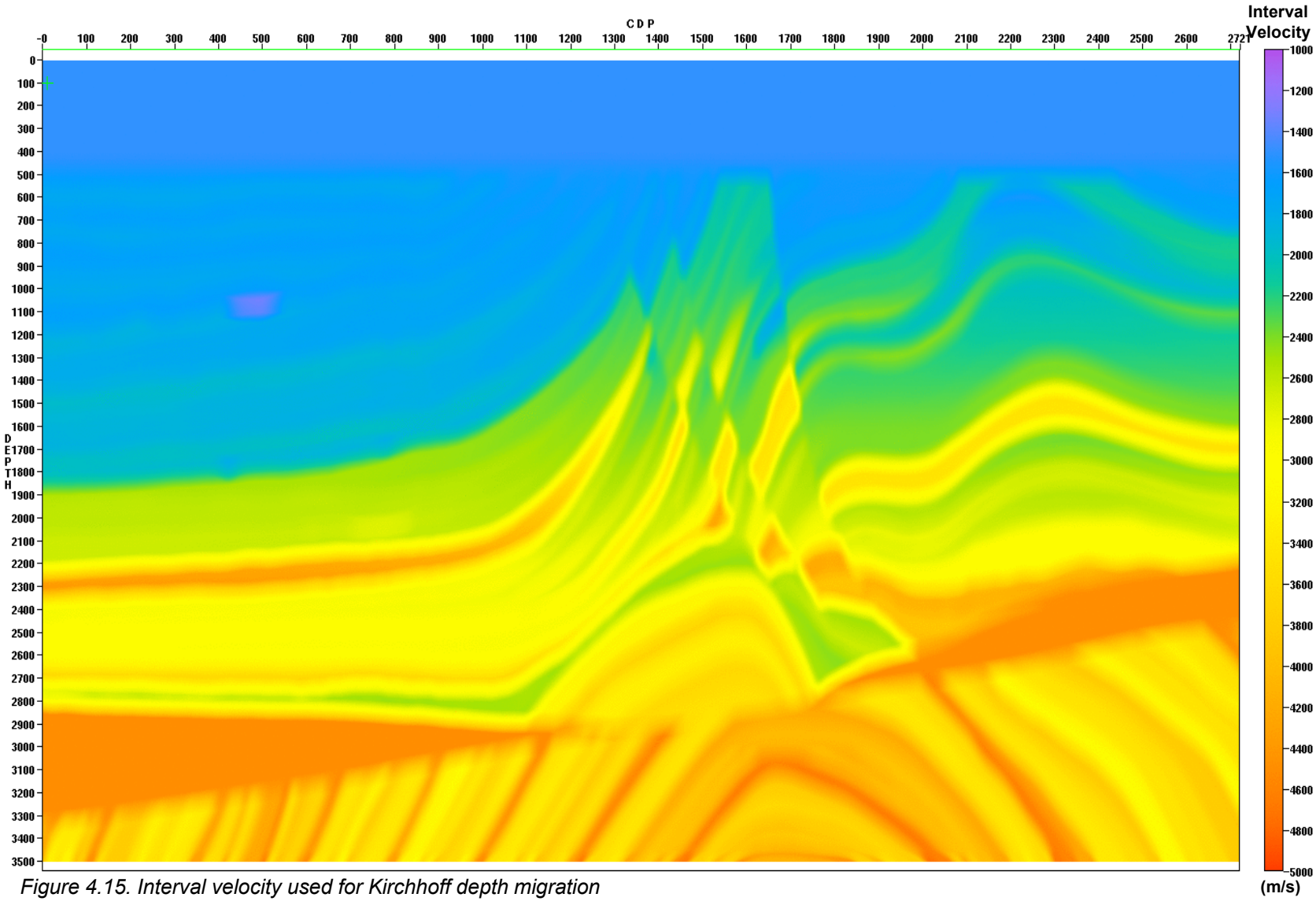

Figure 4.15. Interval velocity used for Kirchhoff depth migration

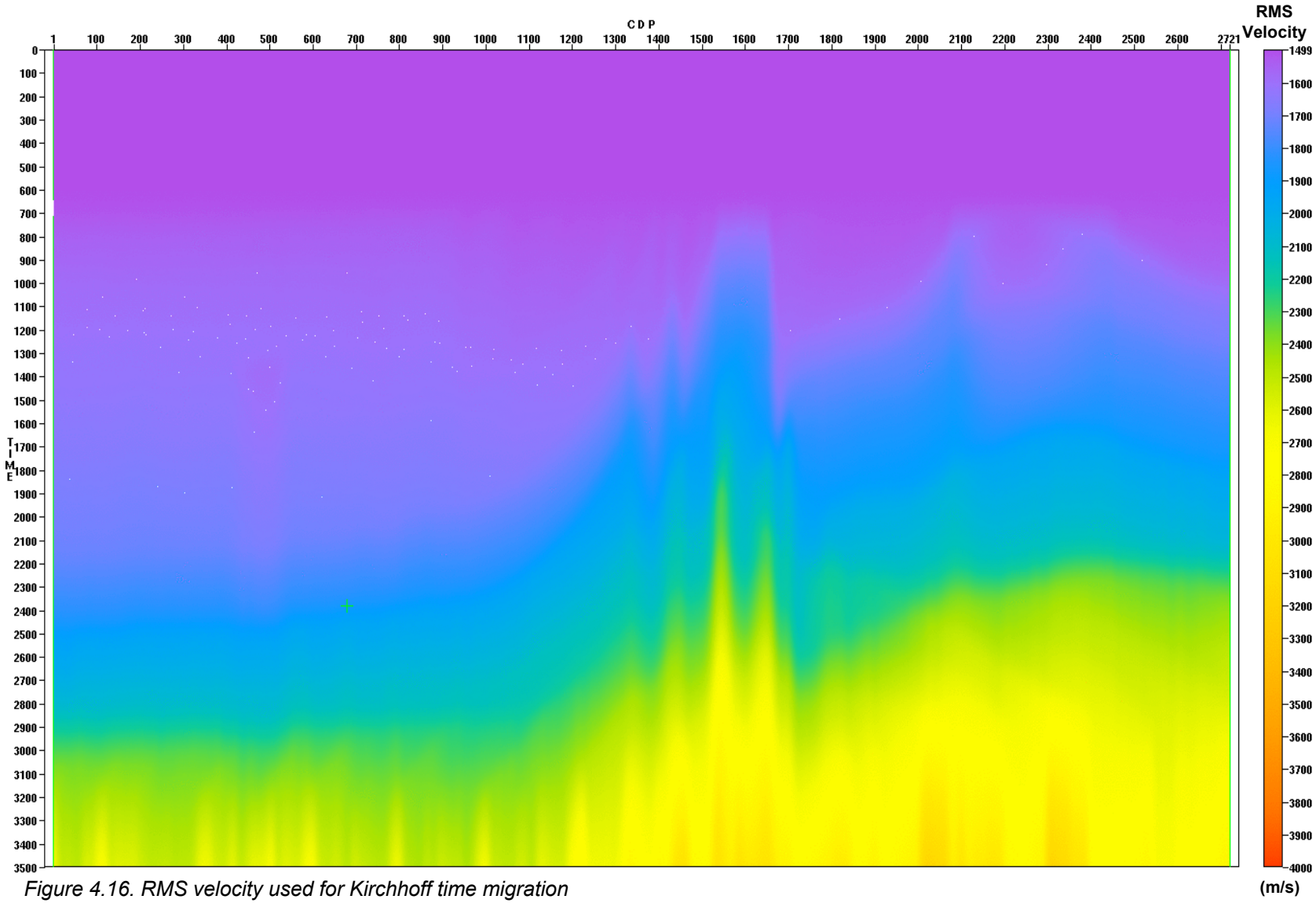

Figure 4.16. RMS velocity used for Kirchhoff time migration

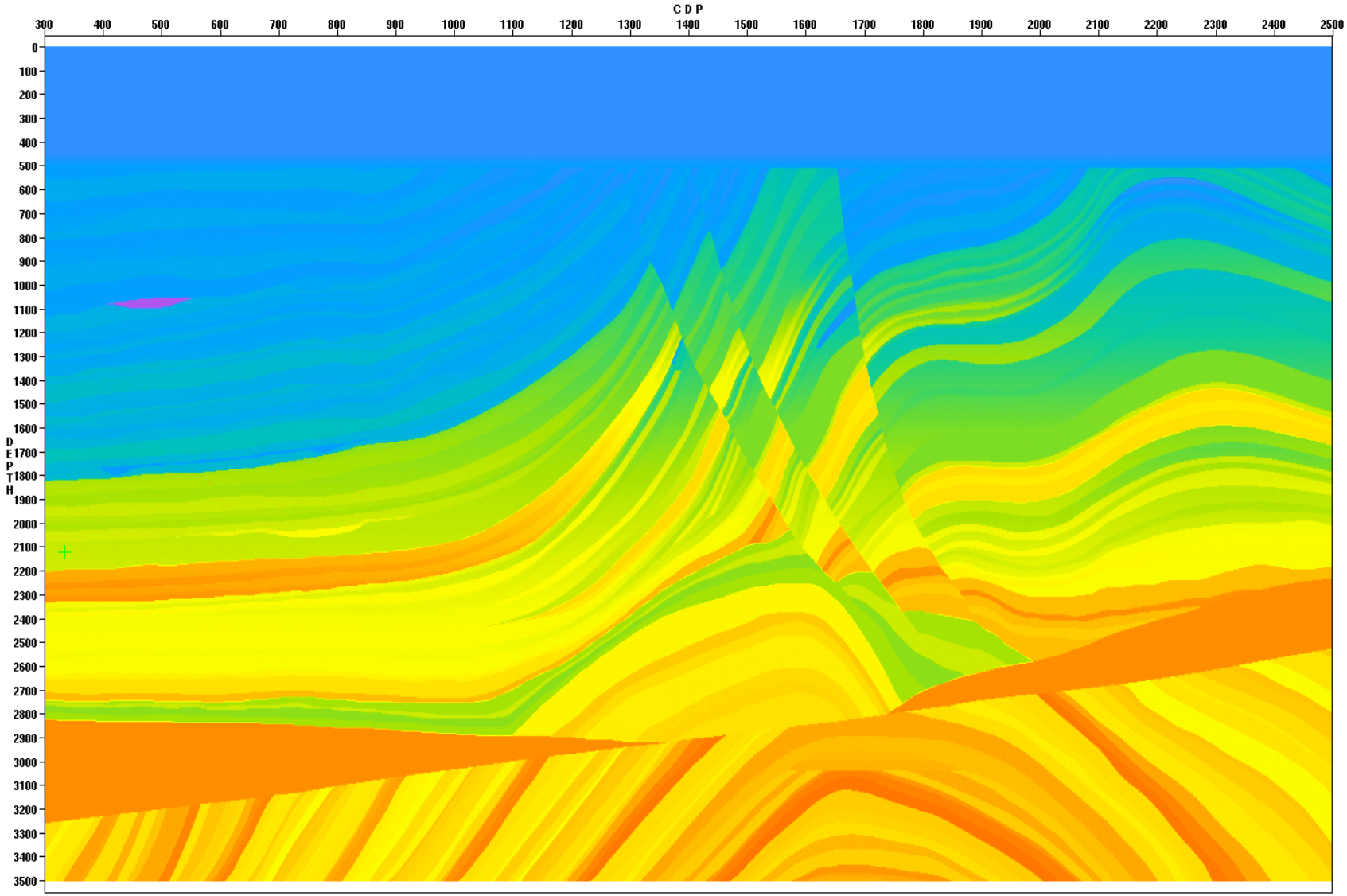

Figure 4.18. Marmousi2 interval velocity at the same size as the migration results (Figures 4.24 – 4.30).

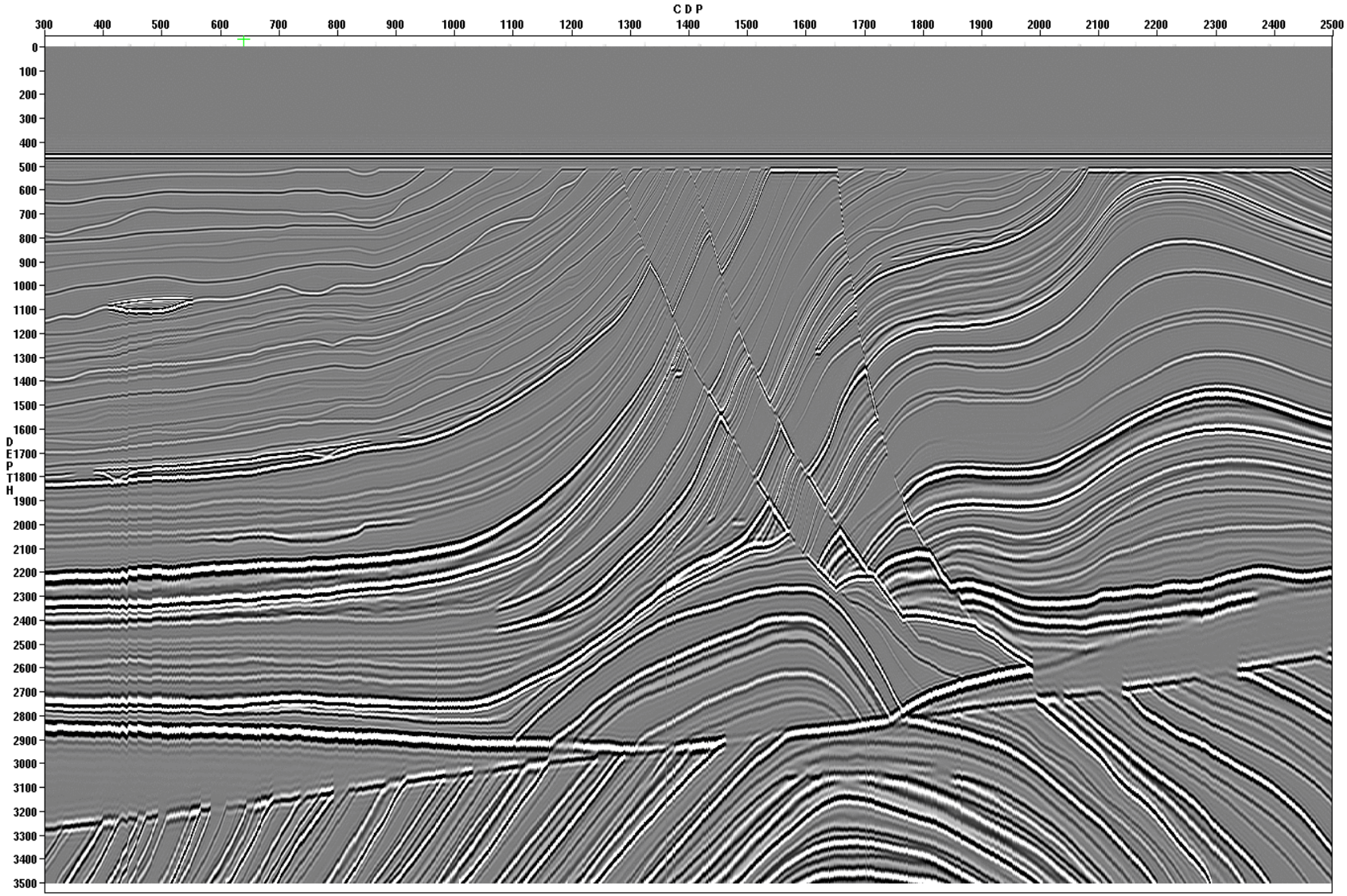

Figure 4.21 . Simple vertical raytracing synthetic (including ghosts), converted to depth

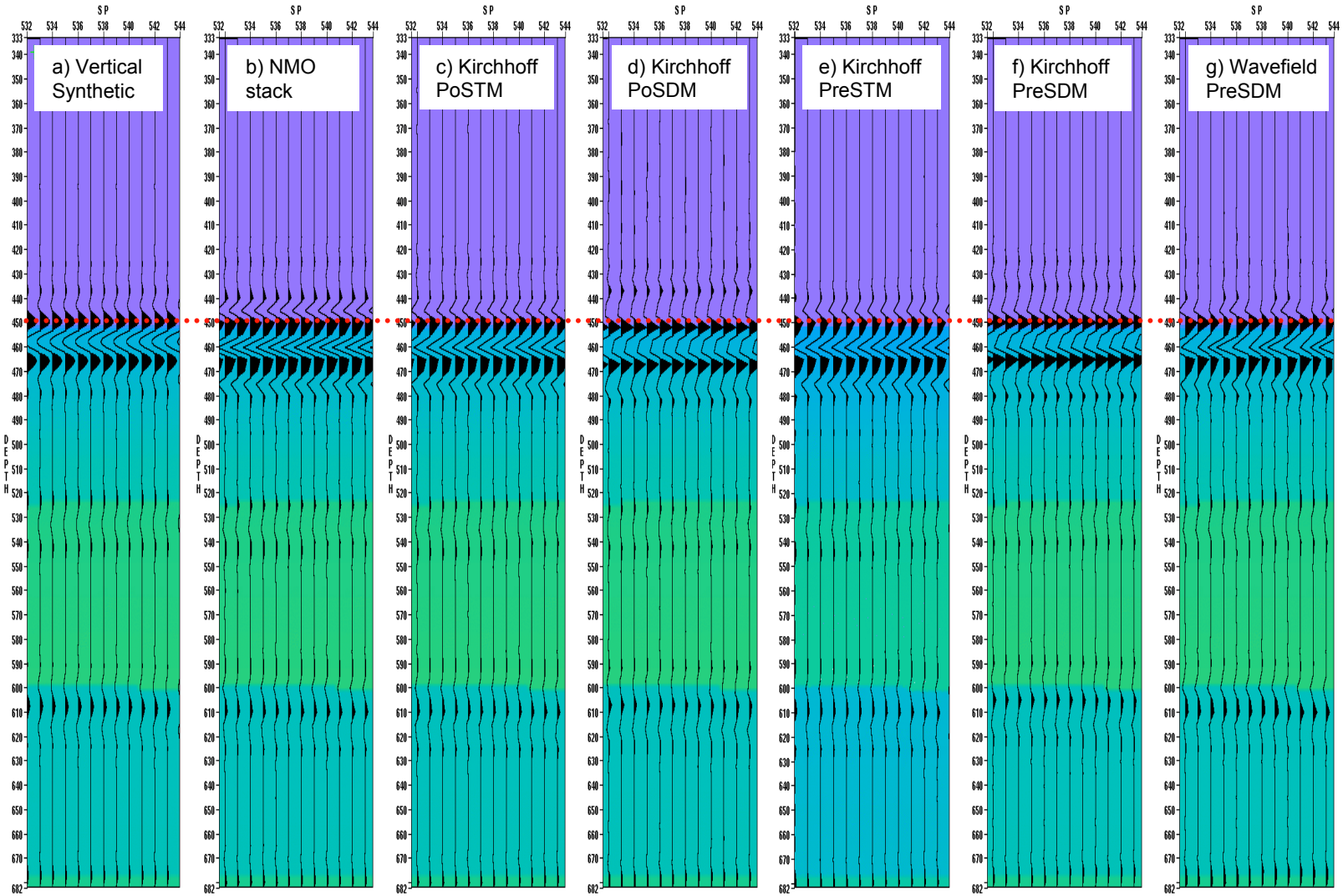

Figure 4.22. Timing and phase quality control at the waterbottom (red line), interval velocity is shown as color. a) simple vertical synthetic (with ghosts), b) NMO stack, c) Kirchhoff poststack time migration, d) Kirchhoff poststack depth migration, e) Kirchhoff prestack time migration, f) Kirchhoff prestack depth migration, g) wavefield prestack depth migration.

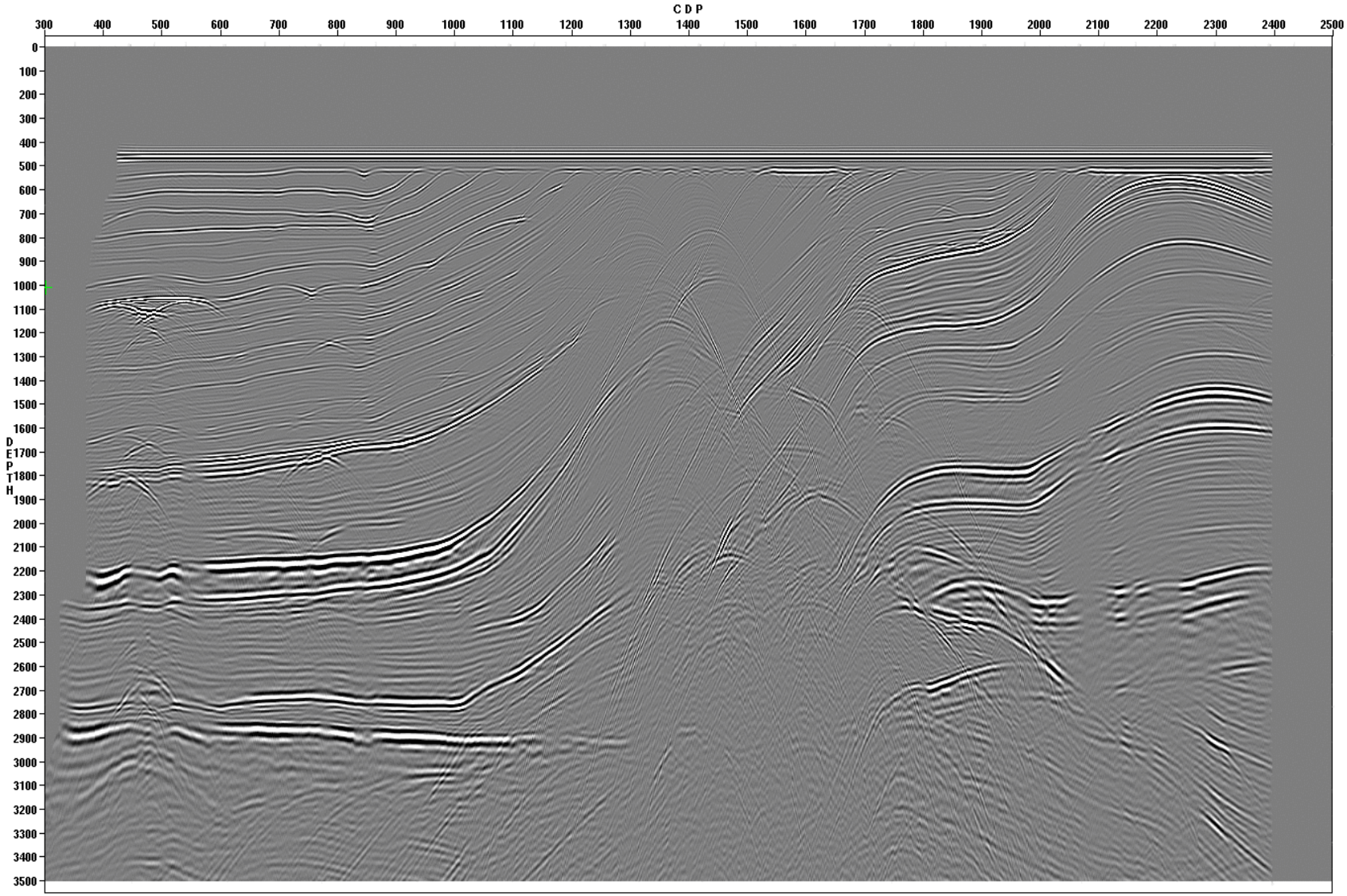

Figure 4.24. NMO-stack converted to depth

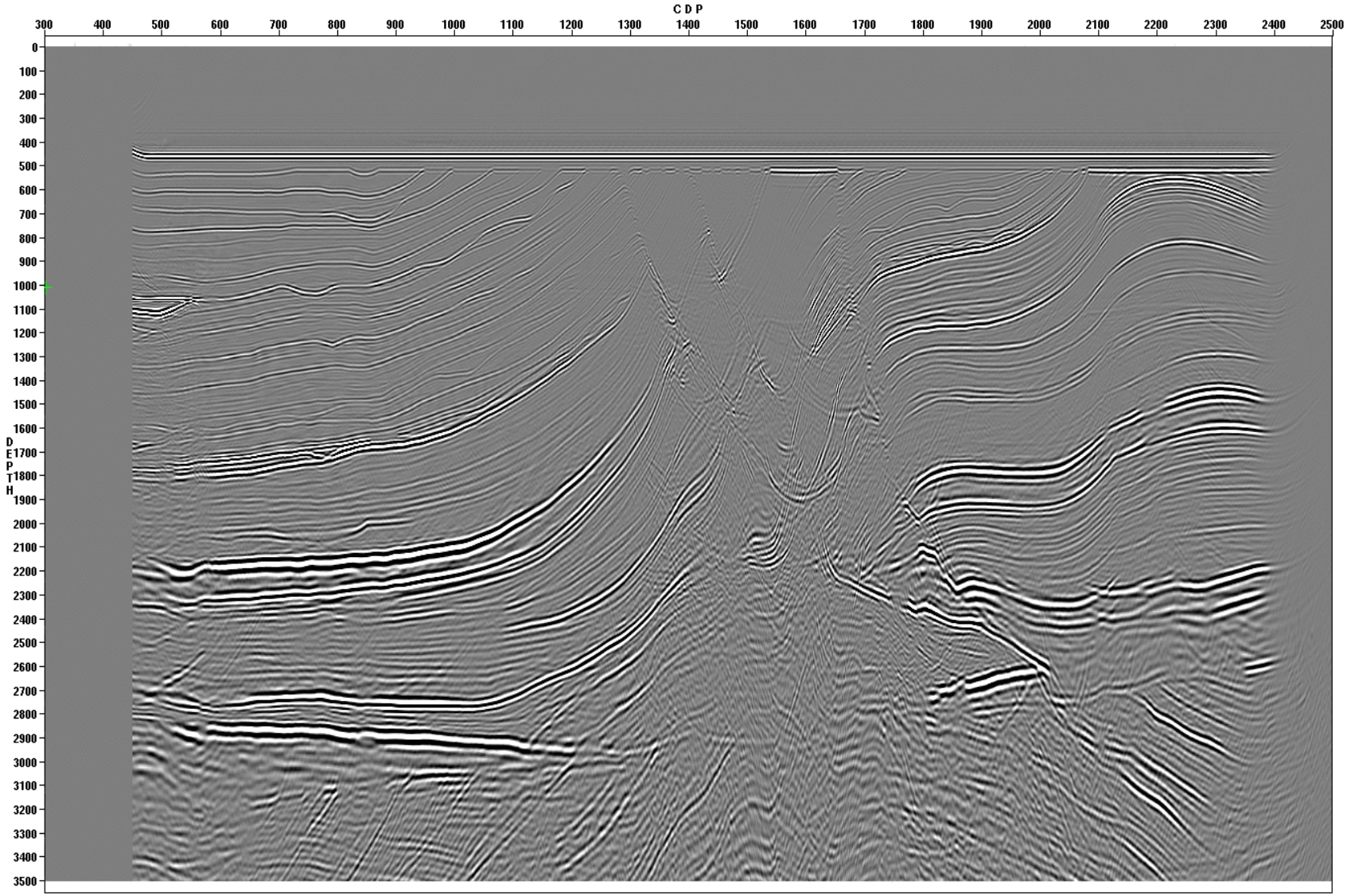

Figure 4.25. Kirchhoff poststack time migration (converted to depth).

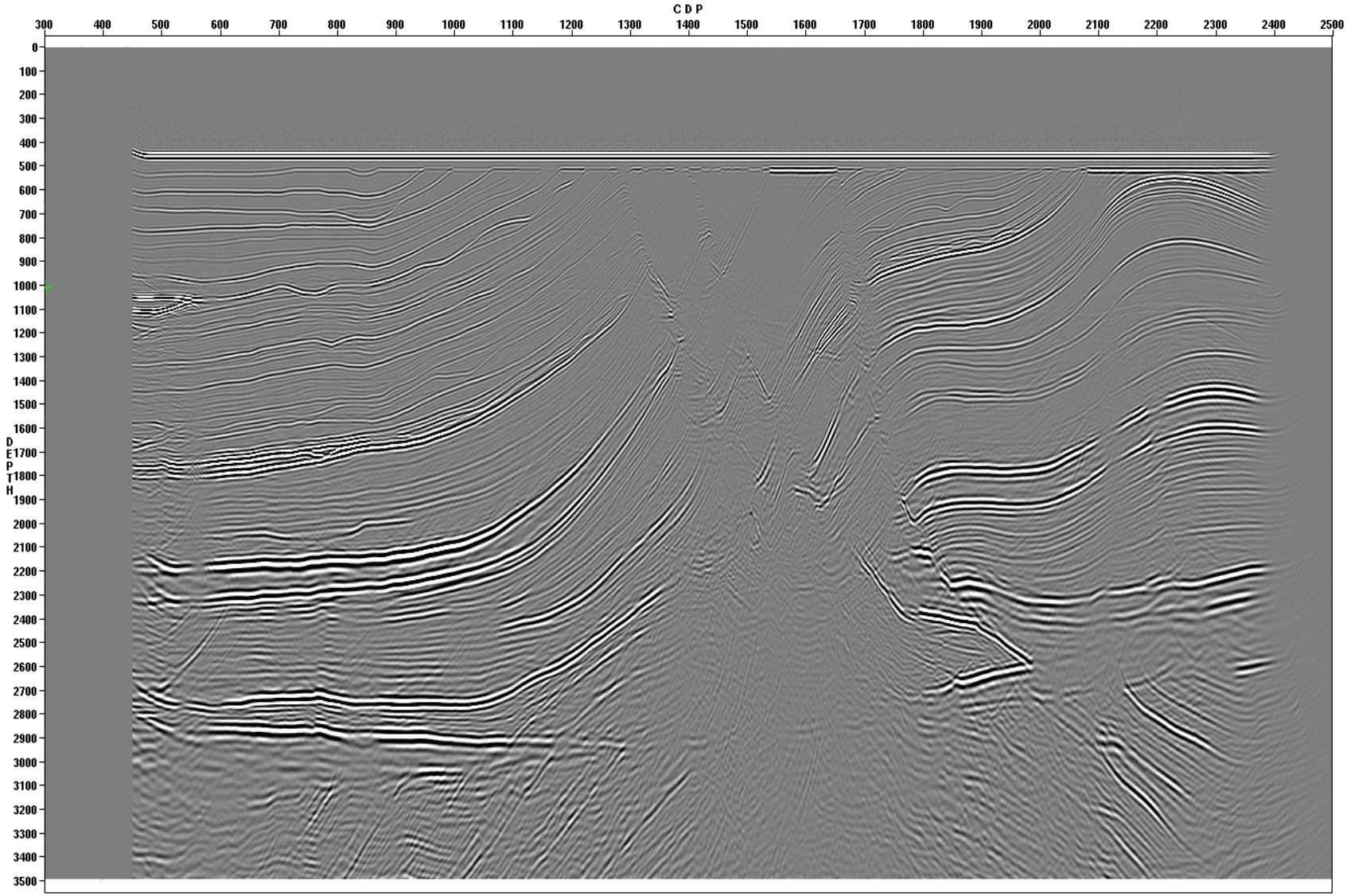

Figure 4.26. Kirchhoff poststack depth migration.

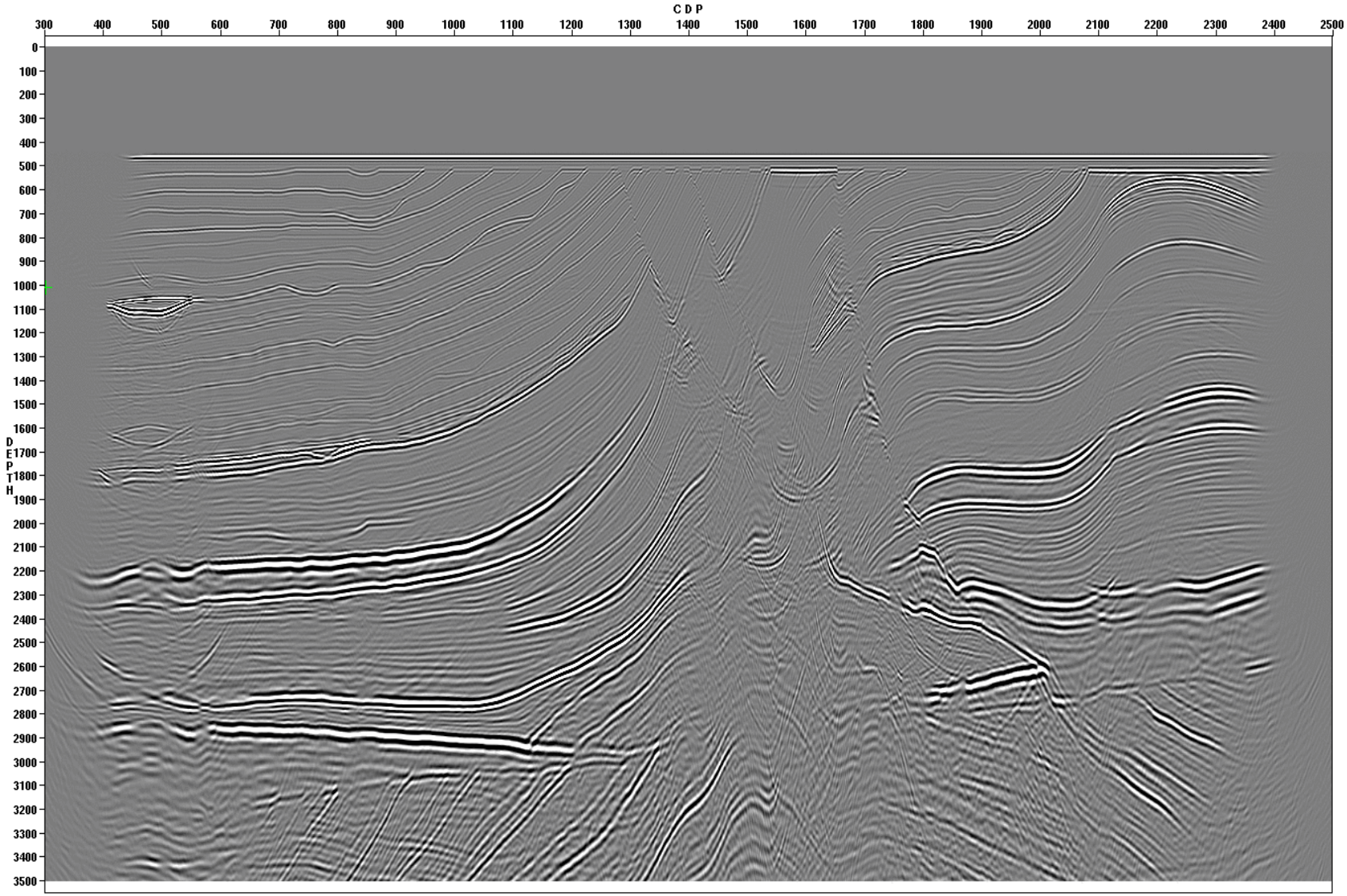

Figure 4.27. Kirchhoff prestack time migration, converted to depth.

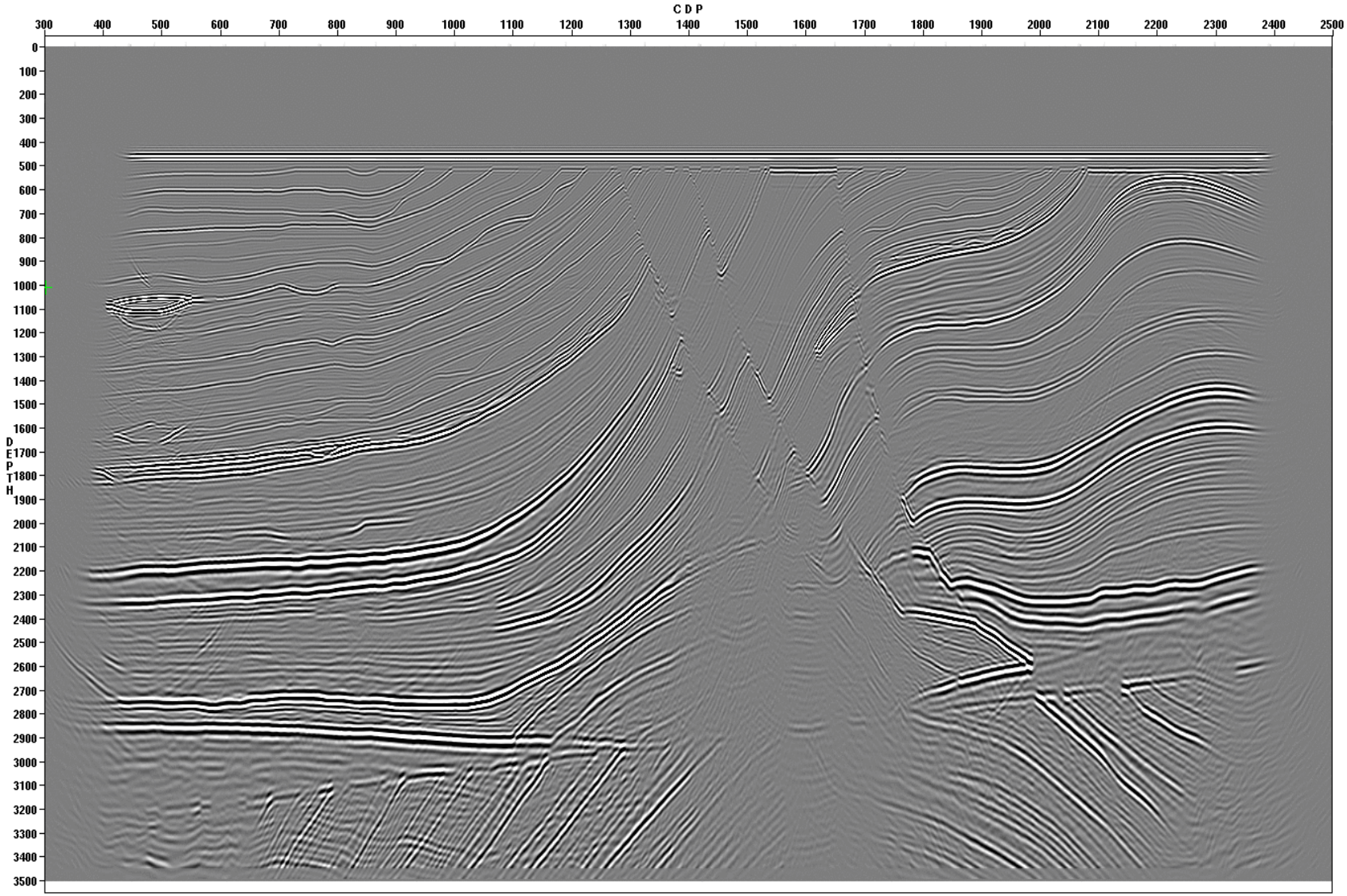

Figure 4.28. Kirchhoff prestack depth migration, with shortest travel path raytracing

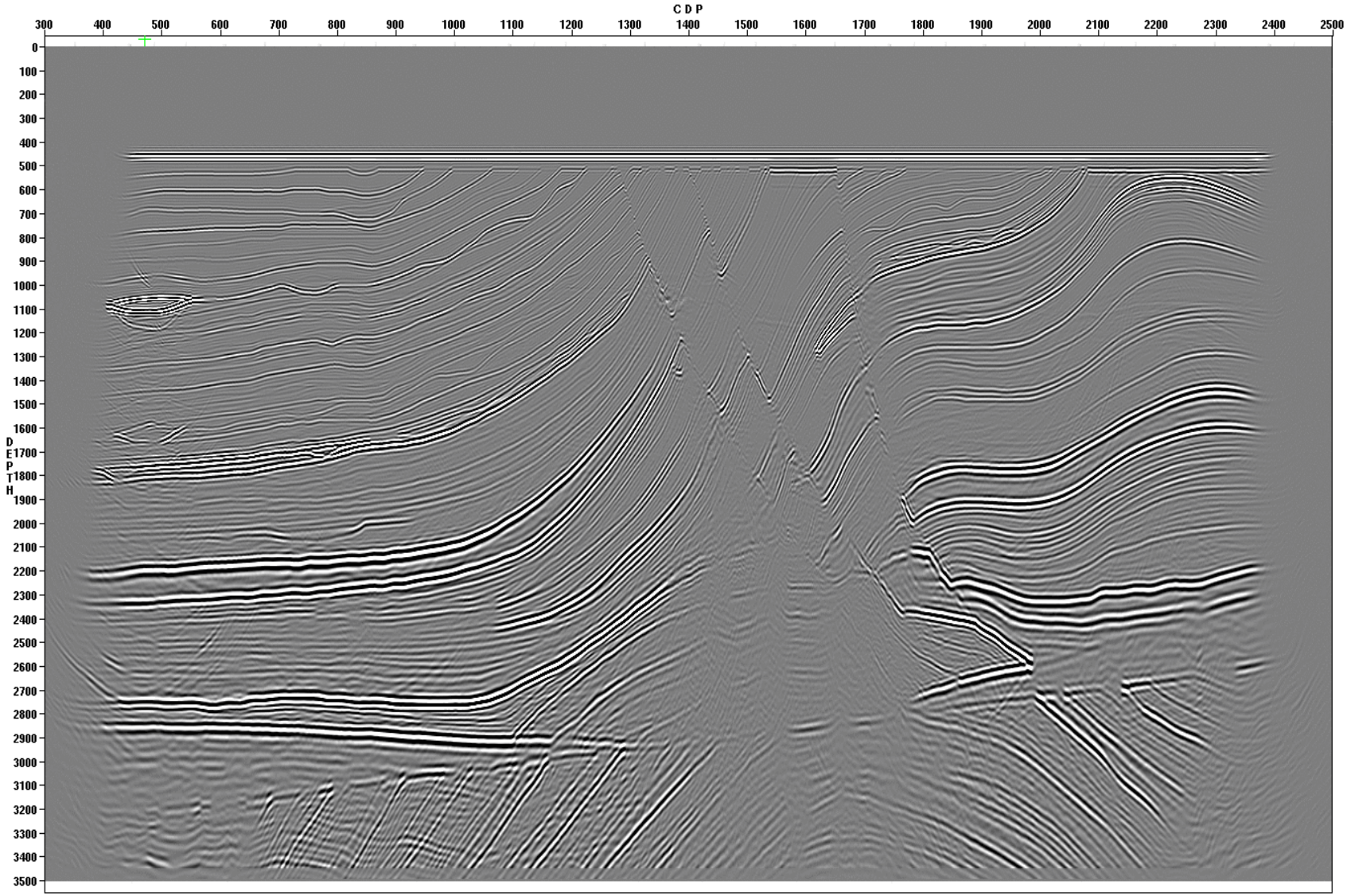

Figure 4.29. Kirchhoff prestack depth migration, with maximum energy raytracing

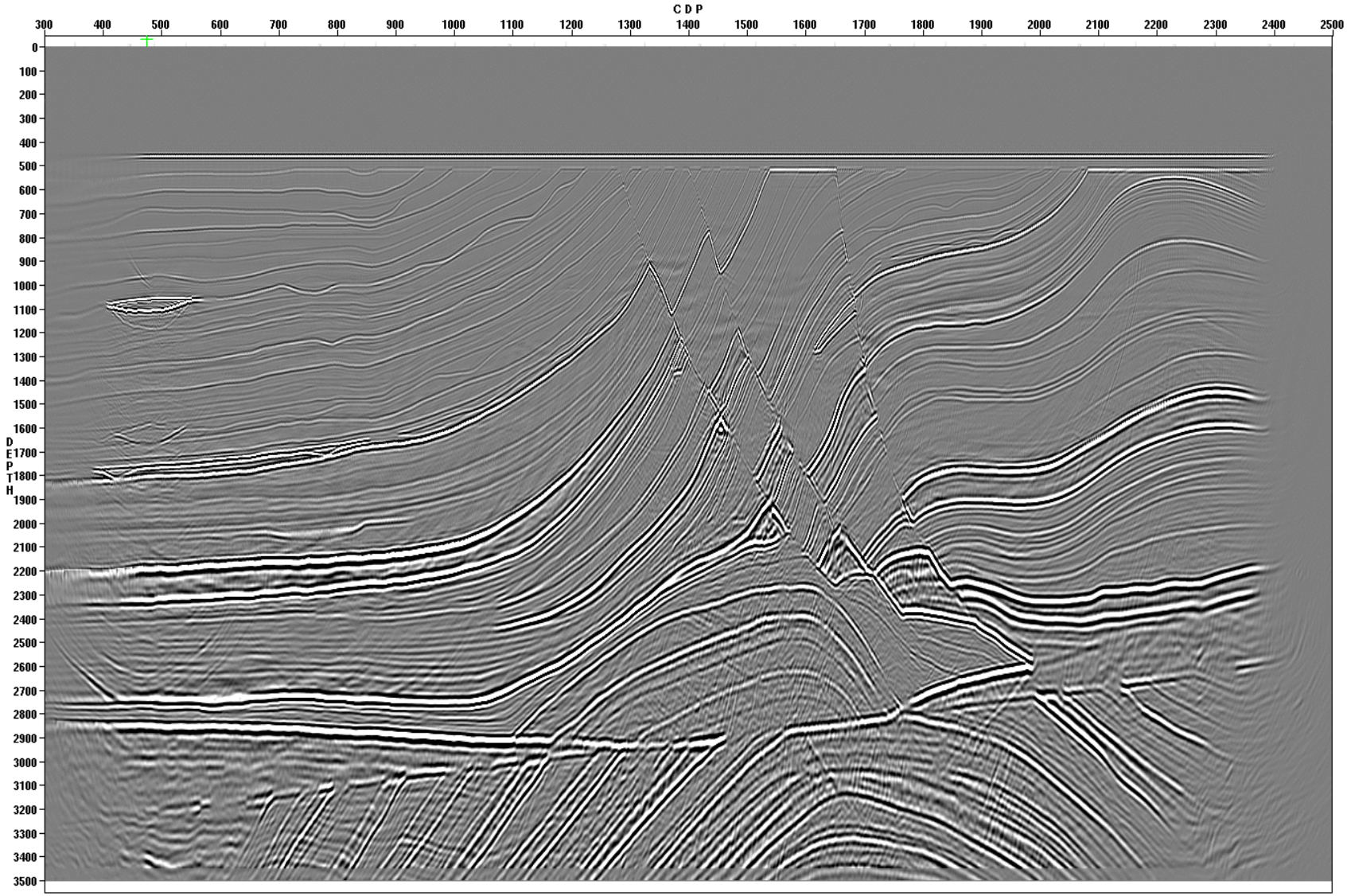

Figure 4.30. Shot profile wave equation prestack depth migration

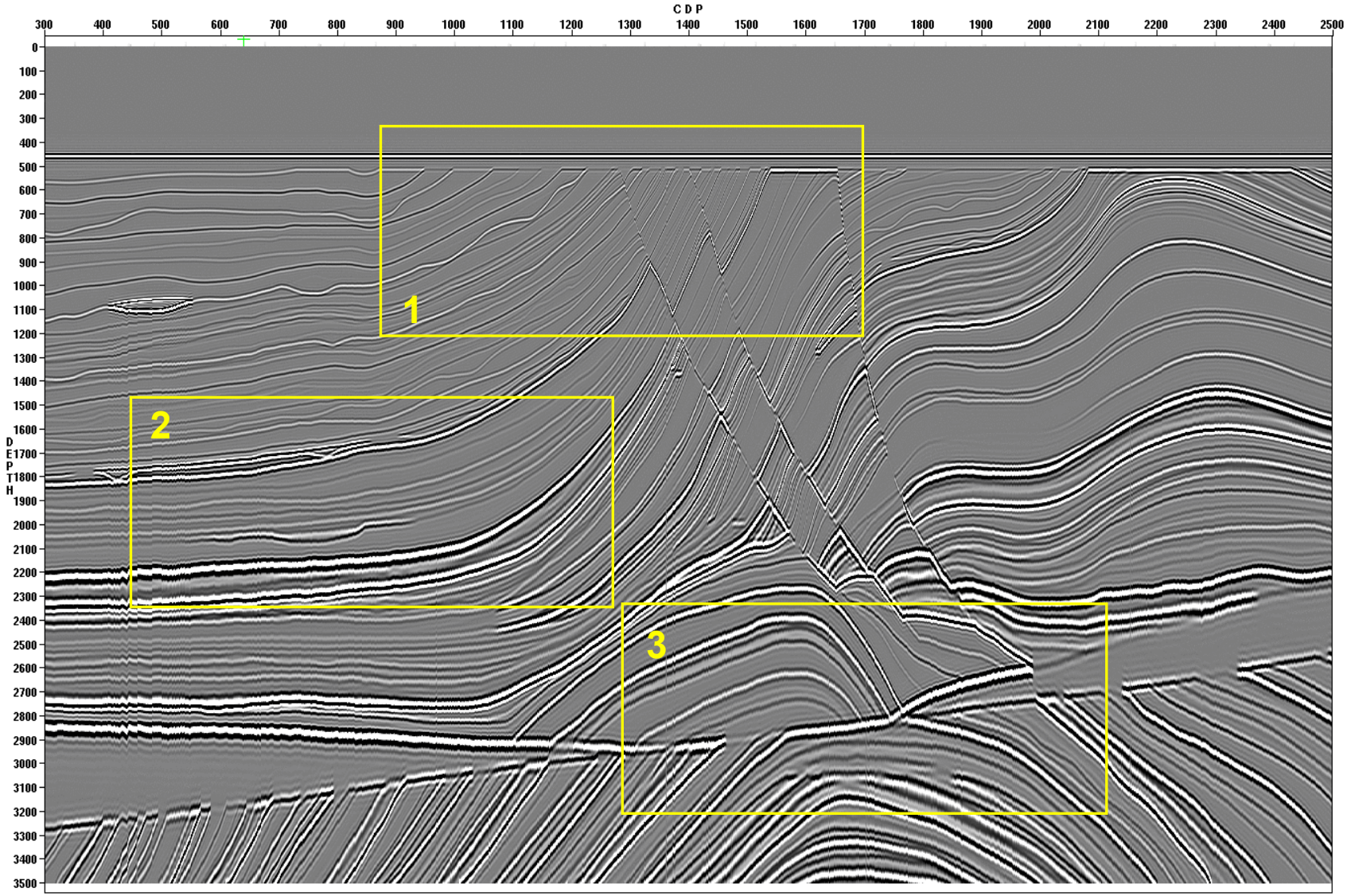

Figure 4.31. Location of detailed inspection of migration results. Background image is the vertical synthetic.

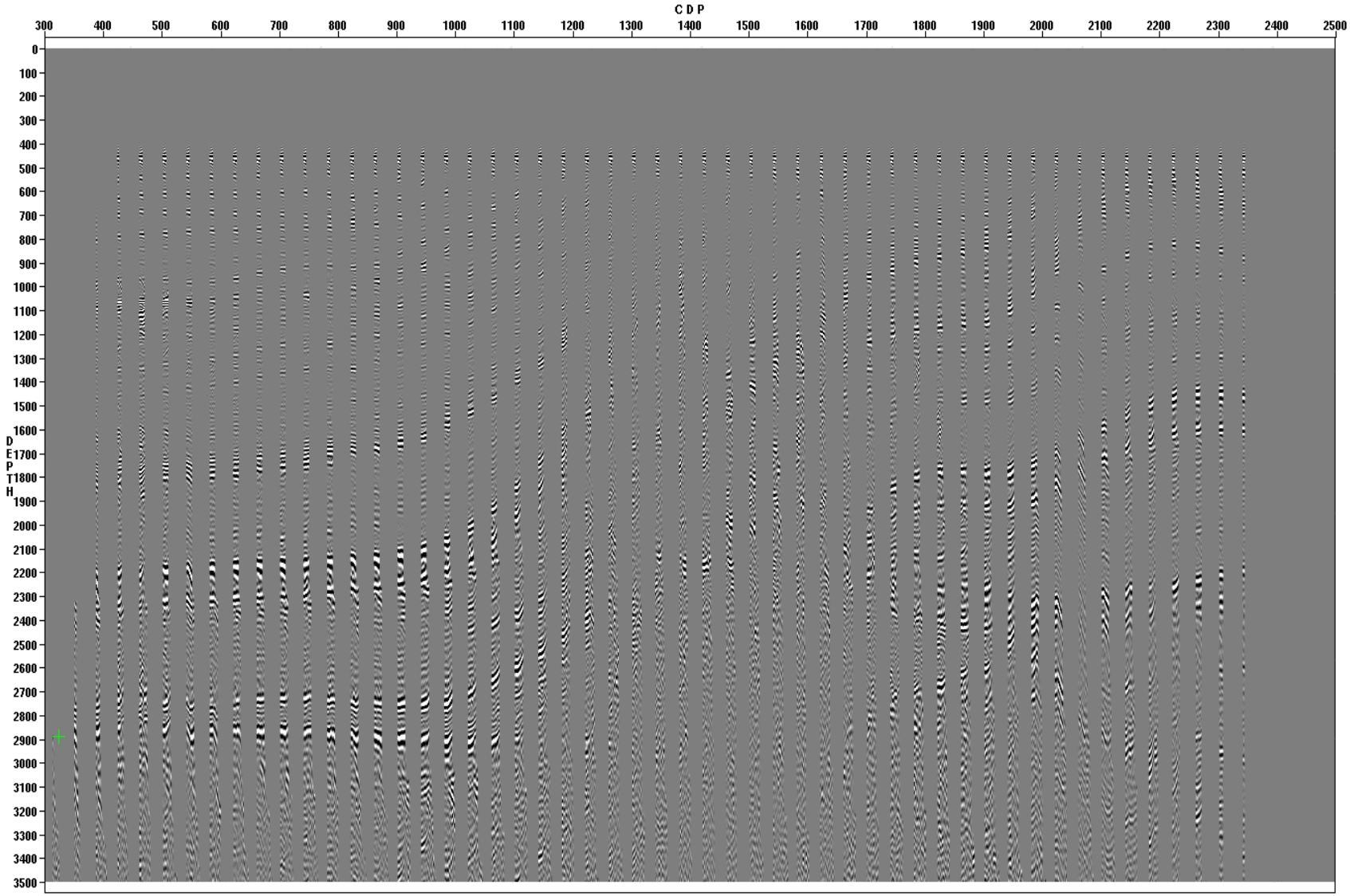

Figure 4.35. NMO corrected CMP gathers, converted to depth. Every 40th gather is shown.

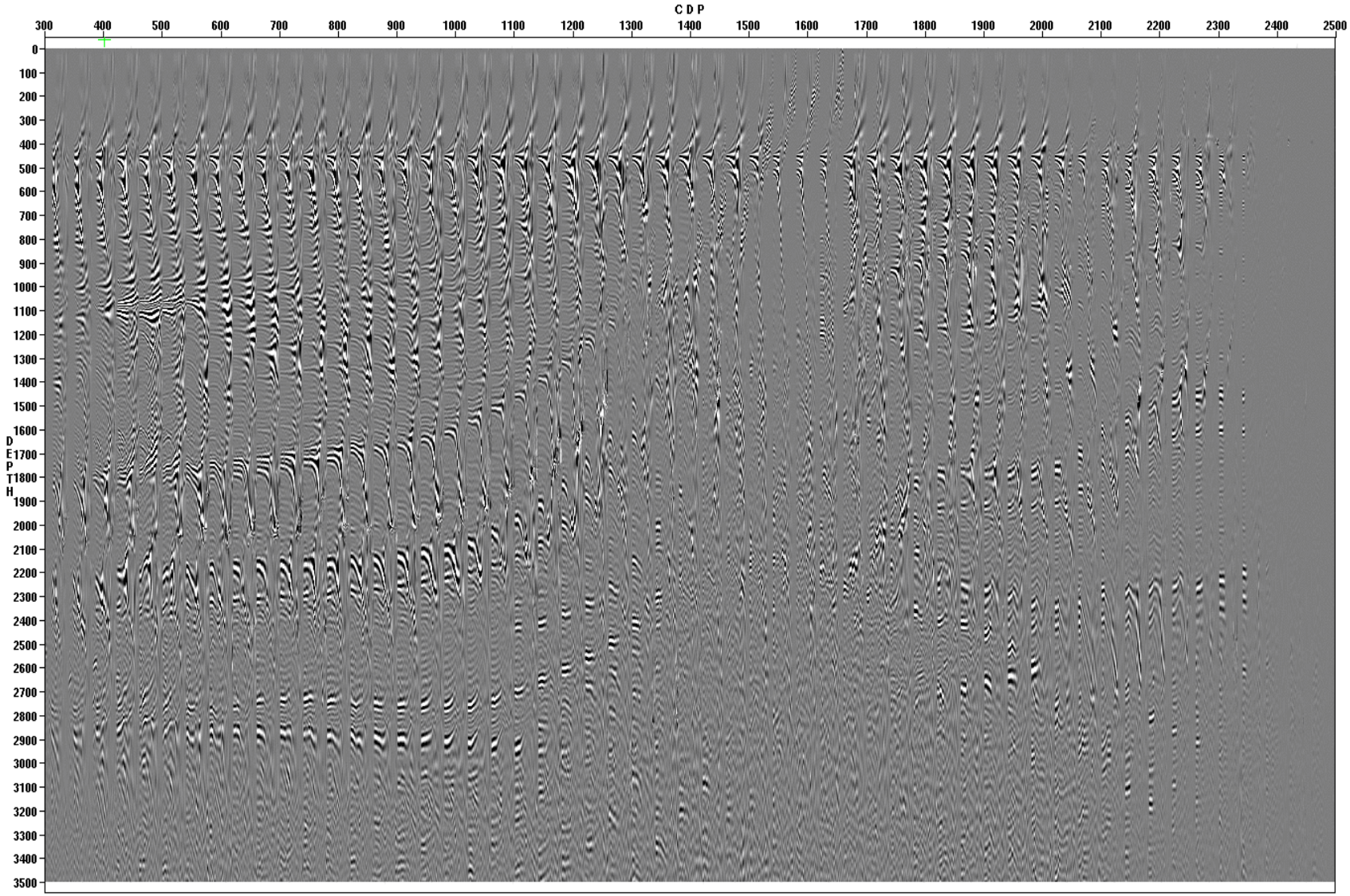

Figure 4.36. Kirchhoff prestack time migrated image gathers, converted to depth. Every 40th gather is shown.

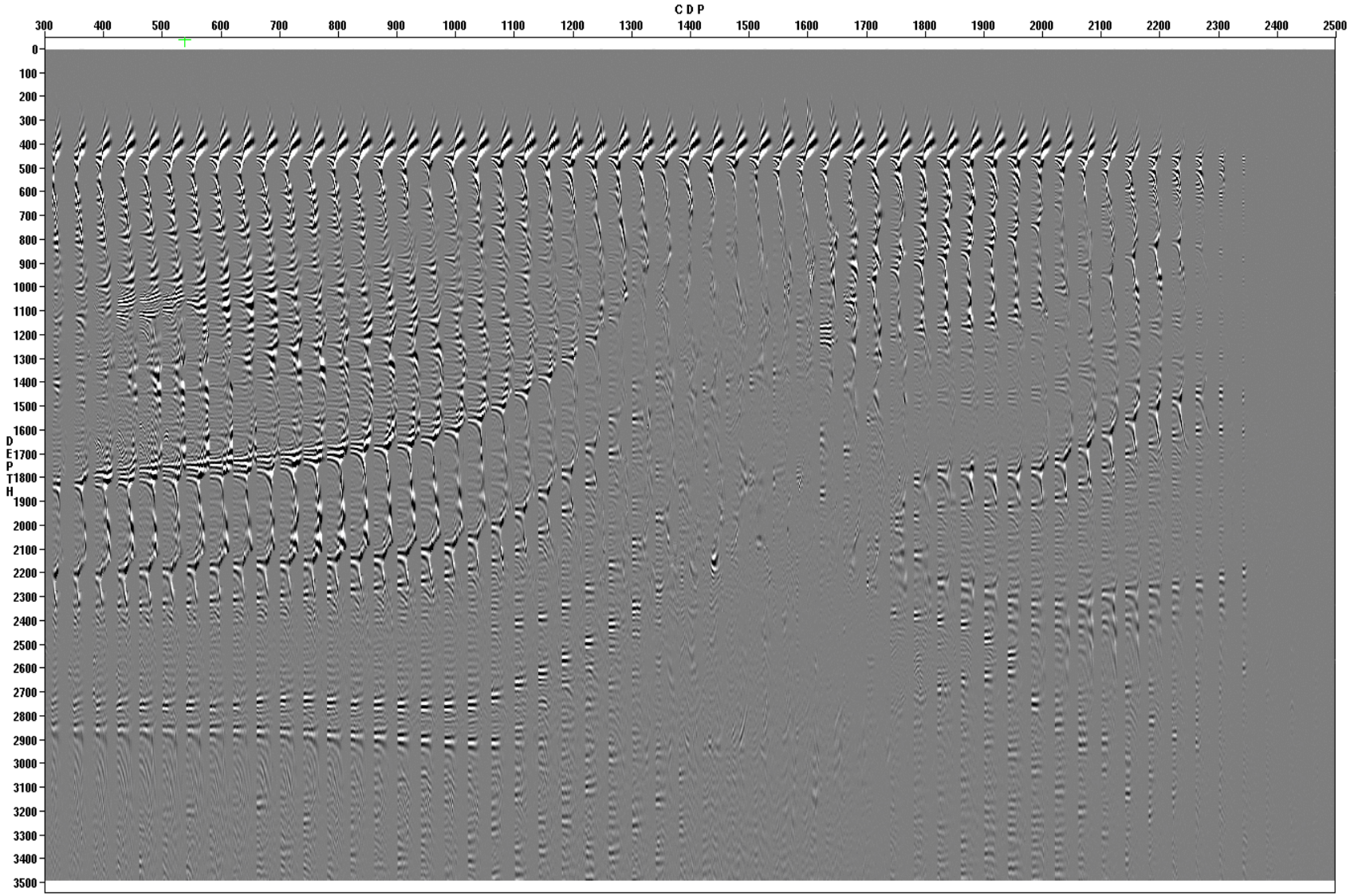

Figure 4.37. Kirchhoff prestack depth migrated image gathers (shortest raypath). Every 40th gather is shown.

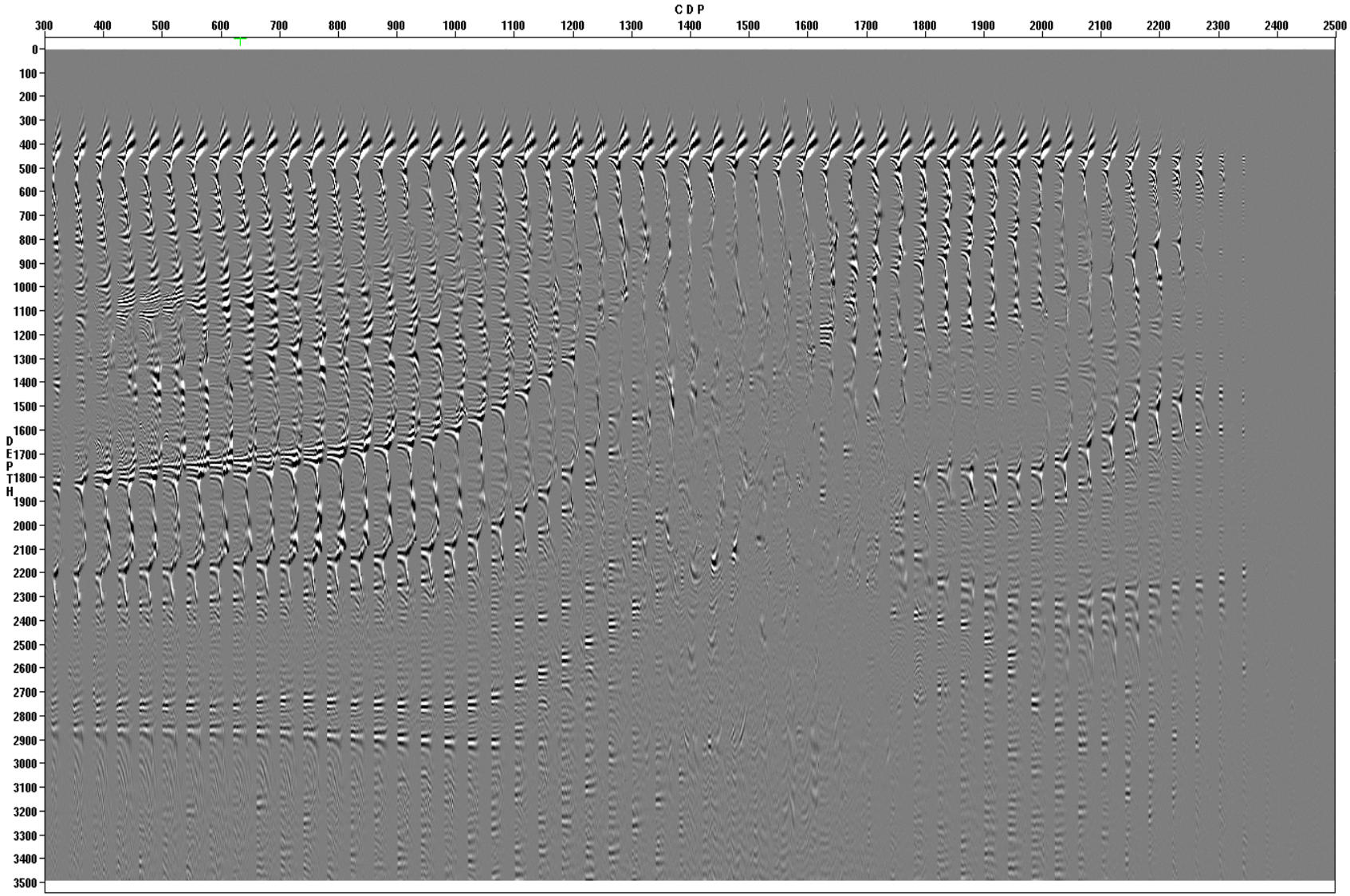

Figure 4.38. Kirchhoff prestack depth migrated image gathers (maximum energy). Every 40th gather is shown.

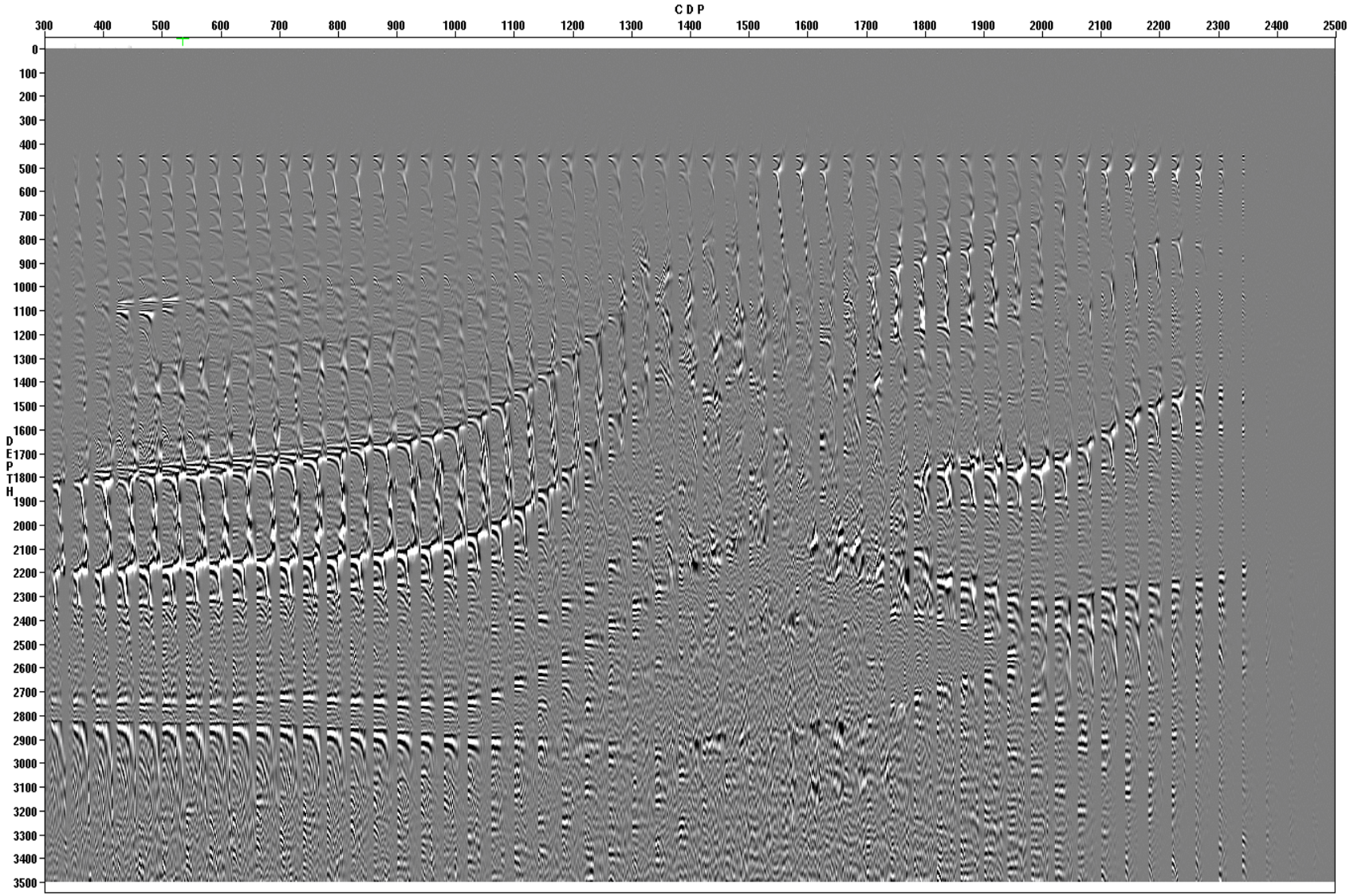

Figure 4.39. Wavefield prestack depth migrated image gathers (offset), no multiple attenuation applied. Every 40th gather is shown.

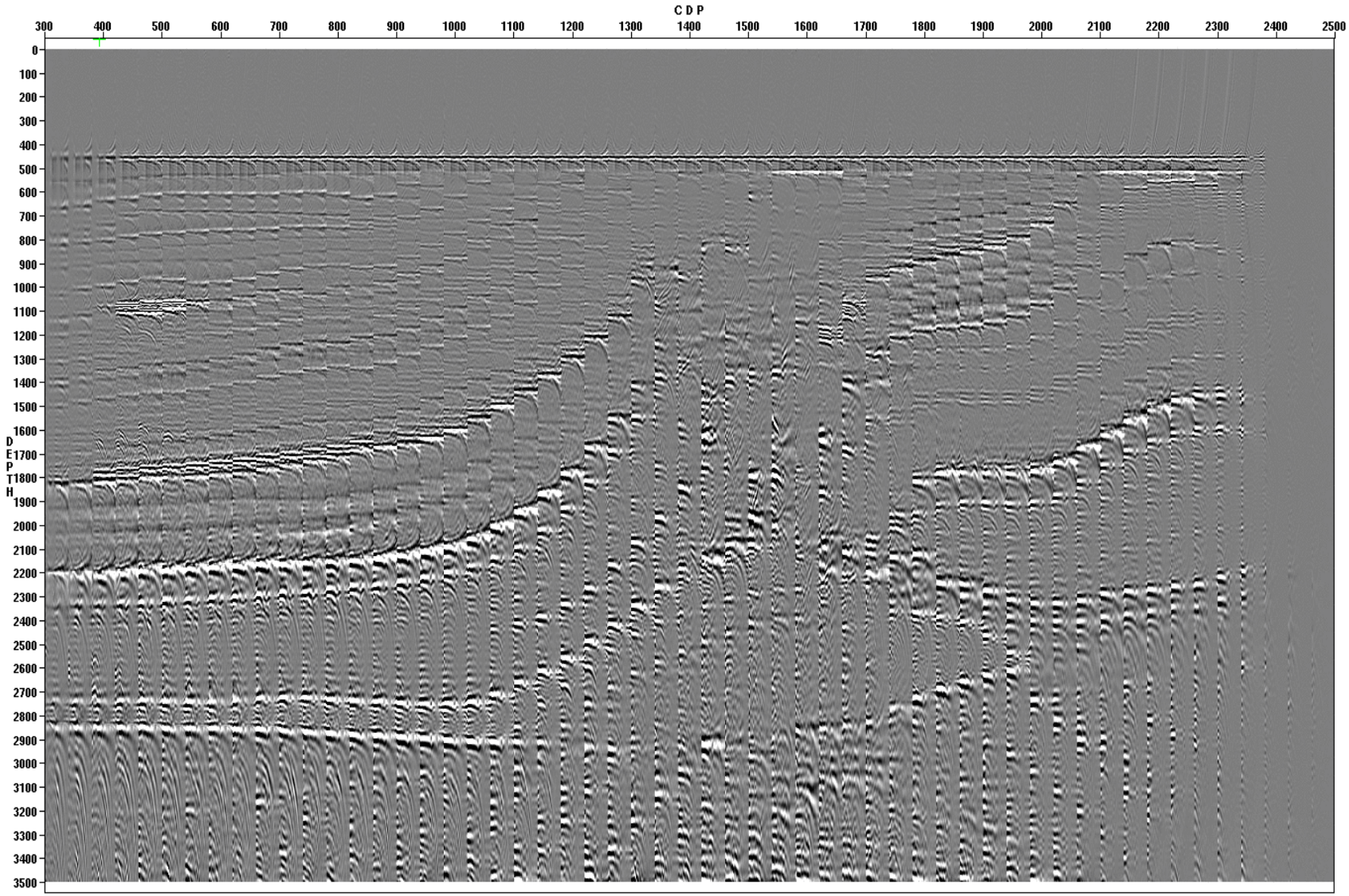

Figure 4.40. Wavefield prestack depth migrated image gathers (angle). Every 40th gather is shown.

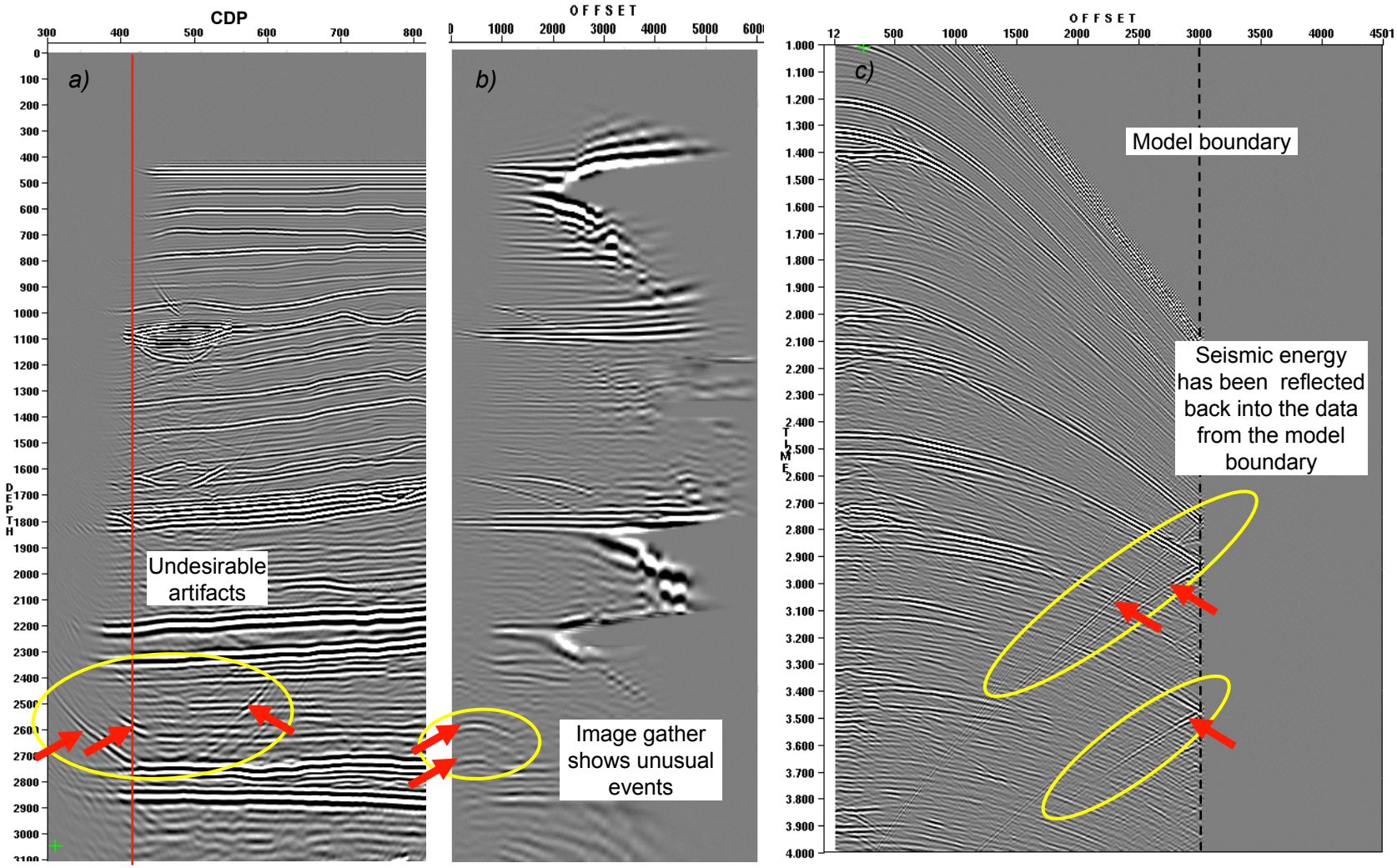

Figure 4.41. Imaging problems due to model padding inadequacies. a) Kirchhoff prestack depth migration. Arrows highlight energy that does not fit the velocity model. b) Image gather at CDP 410 as indicated by the red line in a). Arrows point to anomalous horizons. c) Shot record (shot 121, at x=3000m) shows that energy is reflected back into the data from the edge of the velocity model, which is the source of many of the image anomalies on the left side of the line.

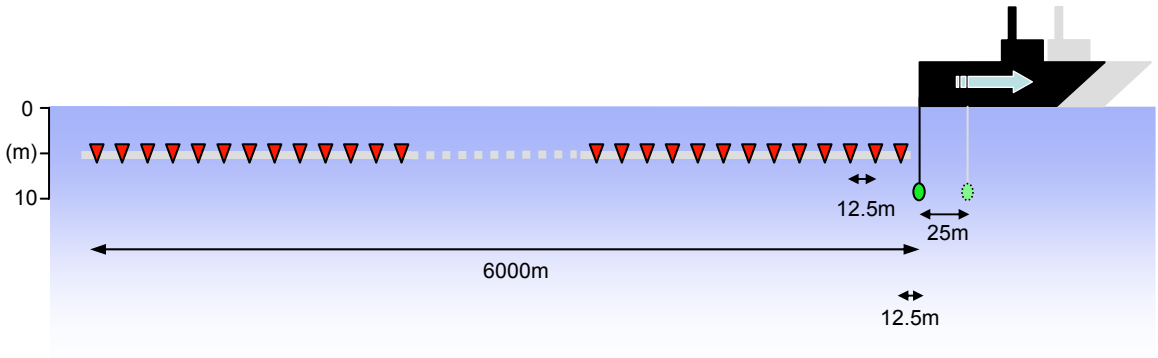

Figure 4.1. Marmousi2 "Marine Streamer" subset geometry

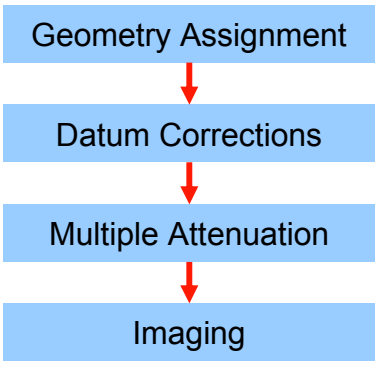

Figure 4.2. Processing flowchart

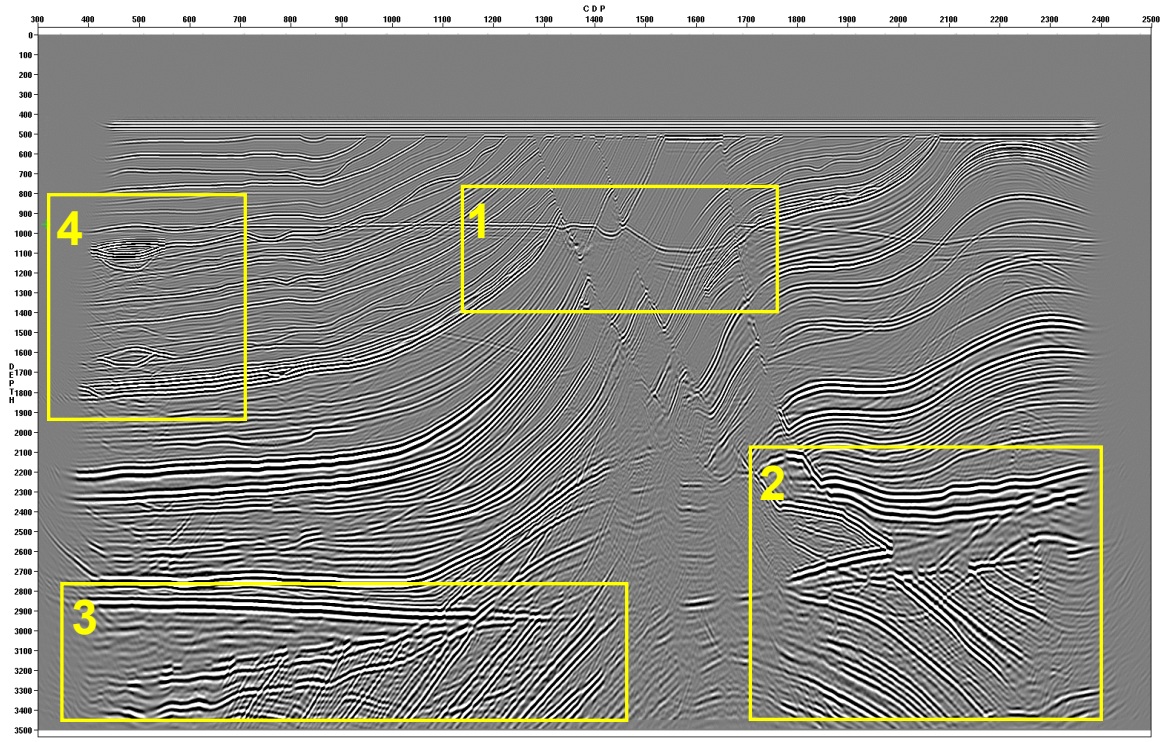

Figure 4.7. Kirchhoff prestack depth migration before surface multiple attenuation. Areas 1-4 are shown in greater detail in Figures 4.10-4.14.

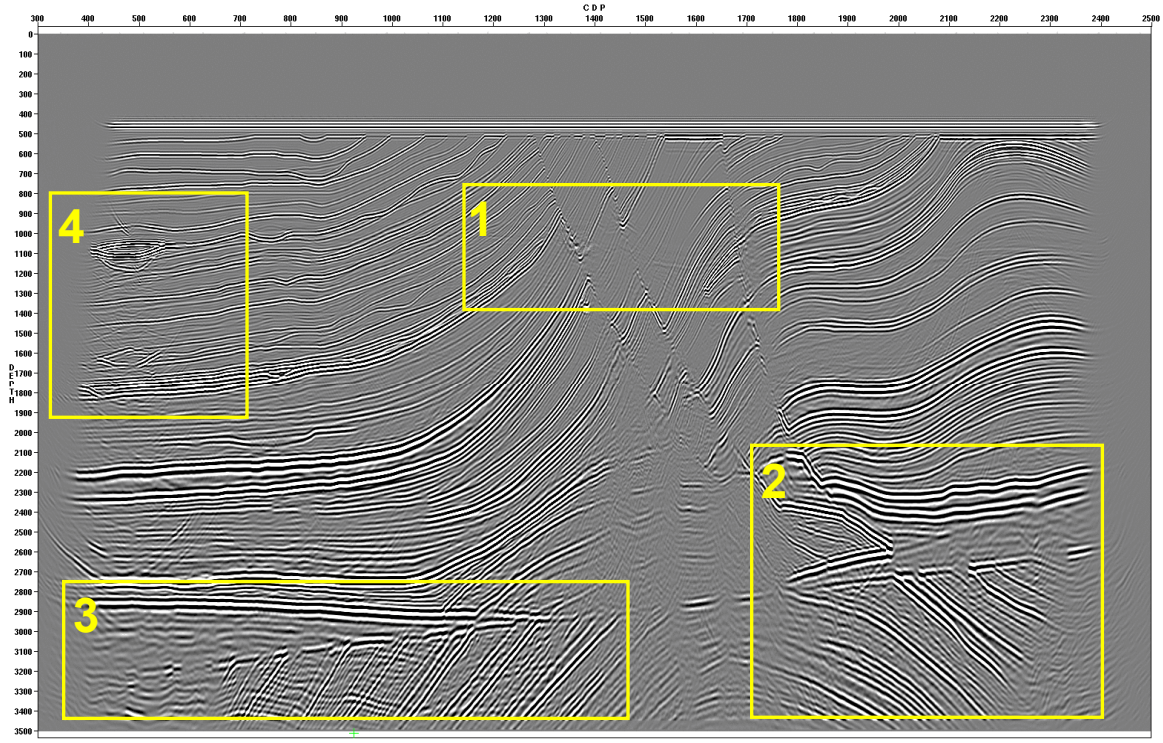

Figure 4.8. Kirchhoff prestack depth migration after surface multiple attenuation. Areas 1-4 are shown in greater detail in Figures 4.10-4.14.

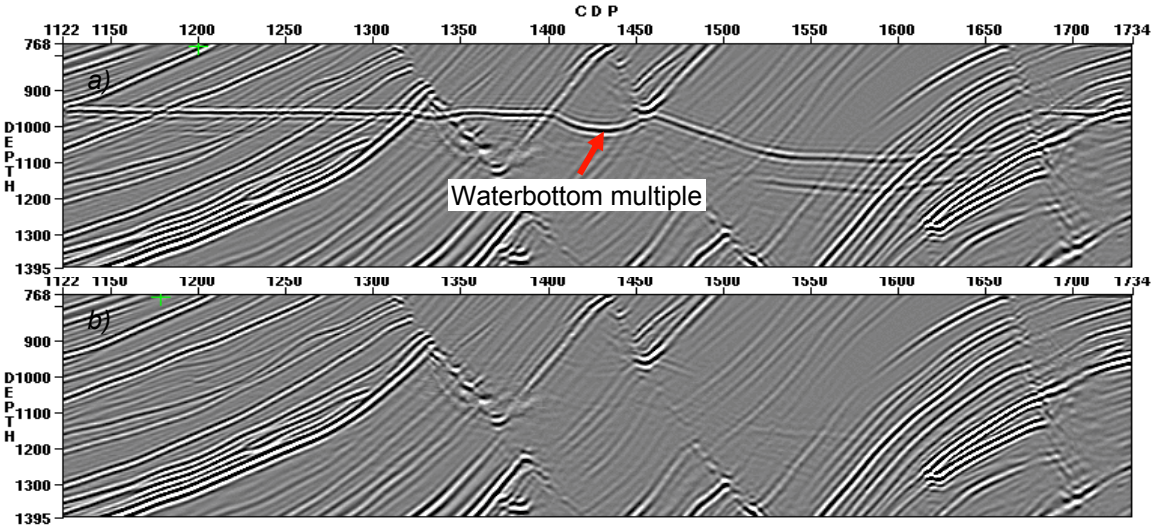

Figure 4.9. Kirchhoff prestack depth migration, a) before multiple attenuation, and b) after SRME multiple attenuation. This area (area 1 from Figure 4.8 and 4.9) shows a portion of the first waterbottom multiple. In the depth domain the previously flat multiple is now complex due to variations in velocity. It is very effectively removed without harm to primary reflections.

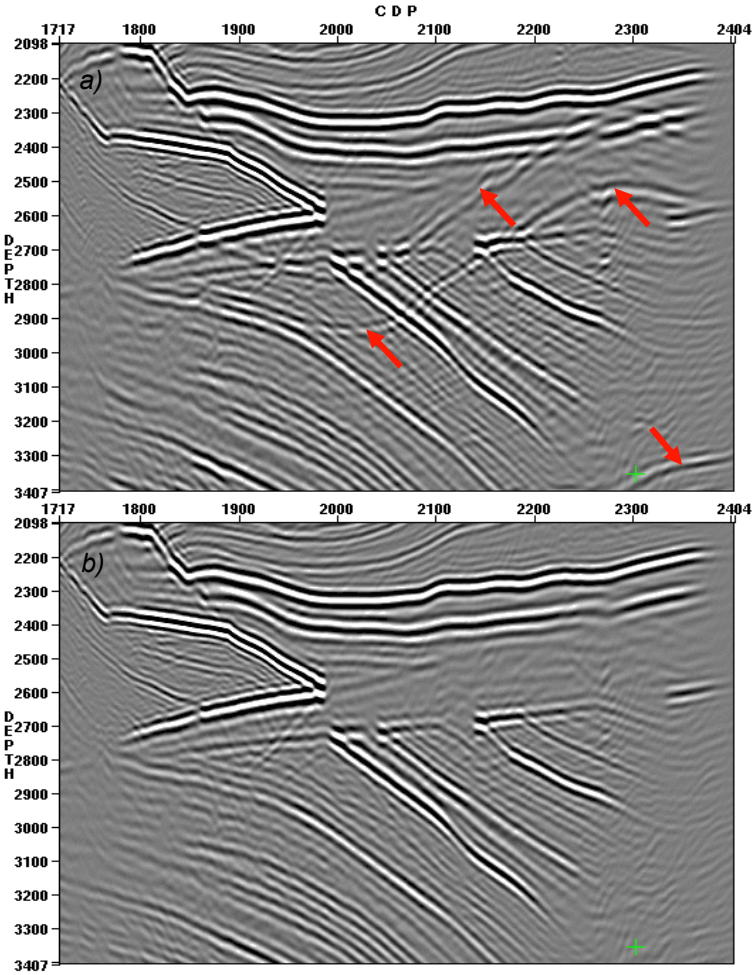

Figure 4.10. Kirchhoff prestack depth migration, a) before multiple attenuation, and b) after SRME multiple attenuation. This area (area 2 from Figure 4.8 and 4.9) shows a deep portion of the result that is contaminated with multiples of contrasting dip as indicated by the arrows. The multiples are very effectively removed.

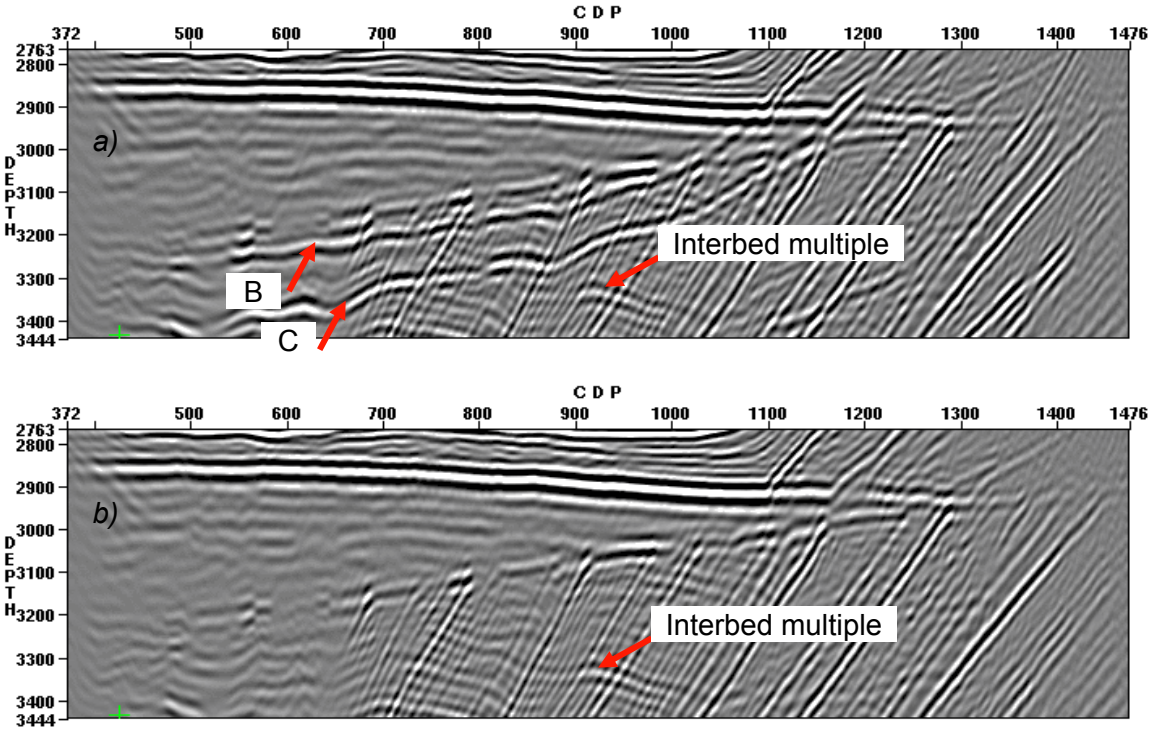

Figure 4.11. Kirchhoff prestack depth migration, a) before multiple attenuation, and b) after multiple attenuation. This area (area 3 from Figure 4.8 and 4.9) possesses multiples, some of which are attenuated, and others which are not. The multiples that are removed are the surface related multiples from events labeled as B and C in Figures 4.5 – 4.7. The multiples that are not removed are interbed multiples, and, since they do not have a bounce at the free surface, they are not removed.

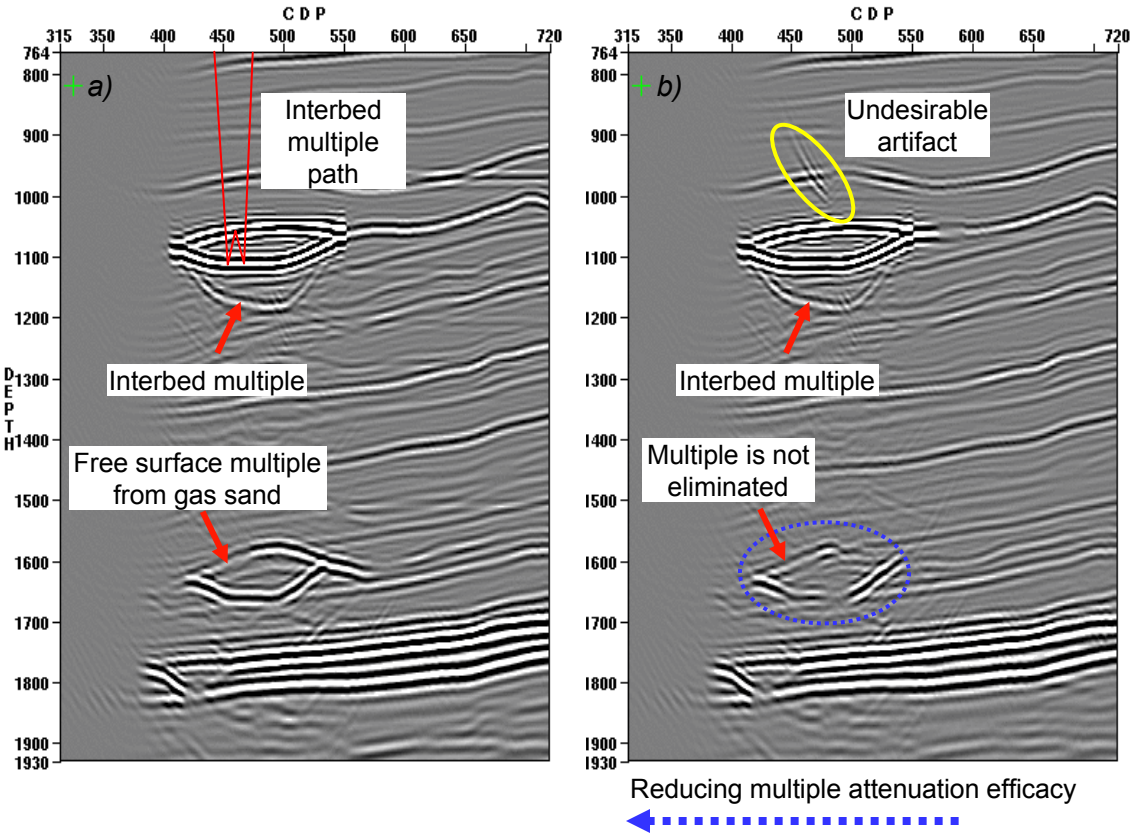

Figure 4.12. Kirchhoff prestack depth migration, a) before multiple attenuation, and b) after SRME multiple attenuation. This area (area 4 from Figure 4.8 and 4.9) shows the reduction in algorithm efficacy as the edge of the data is reached. The free surface multiple from the gas sand is poorly attenuated (blue dashed circle). Generally the effectiveness of the multiple attenuation diminishes as the edge of the data is reached, as indicated by the blue dashed arrow. A prominent interbed multiple is shown (red arrow). The red line sketched onto a) shows that the interbed results from a bounce within the gas sand layer. The multiple does not have a bounce at the free surface, and thus is not removed. The curious artifact that is highlighted in the yellow oval (in (b)) probably results from a problem with the parameterization of the multiple attenuation, especially as it is located in the zone where the multiple prediction becomes challenging (not enough data).

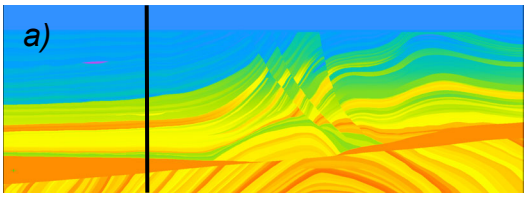

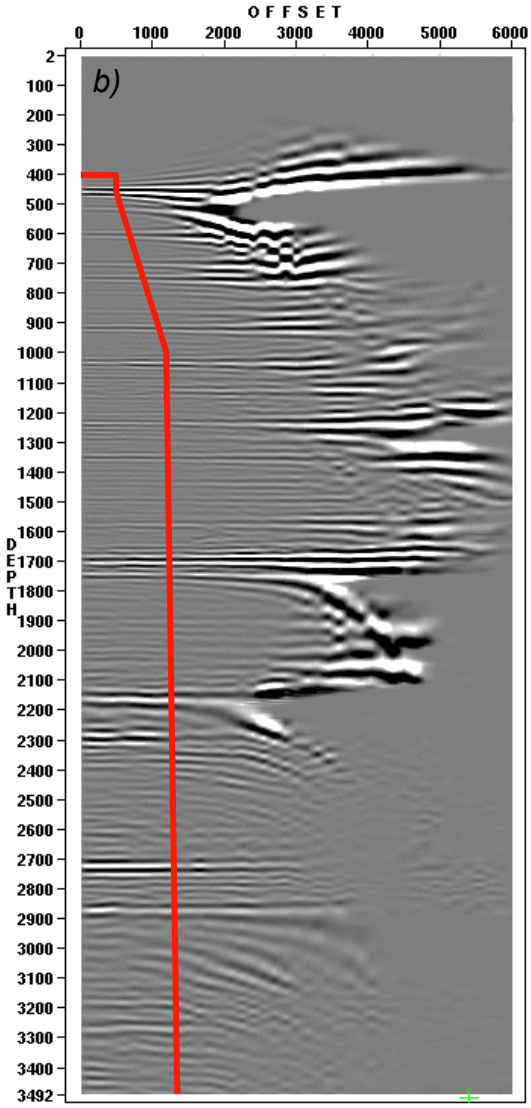

Figure 4.17. a) location of depth migrated offset gather shown in b), b) depth migrated offset gather from CDP 750 (X=4681.25). Large amounts of wavelet stretch are observed for horizons representing a substantial change in interval velocity. To avoid incorporating too much stretch into the stacked result an aggressive outer mute was used. Red line shows the simple outer mute that was used before stacking the data.

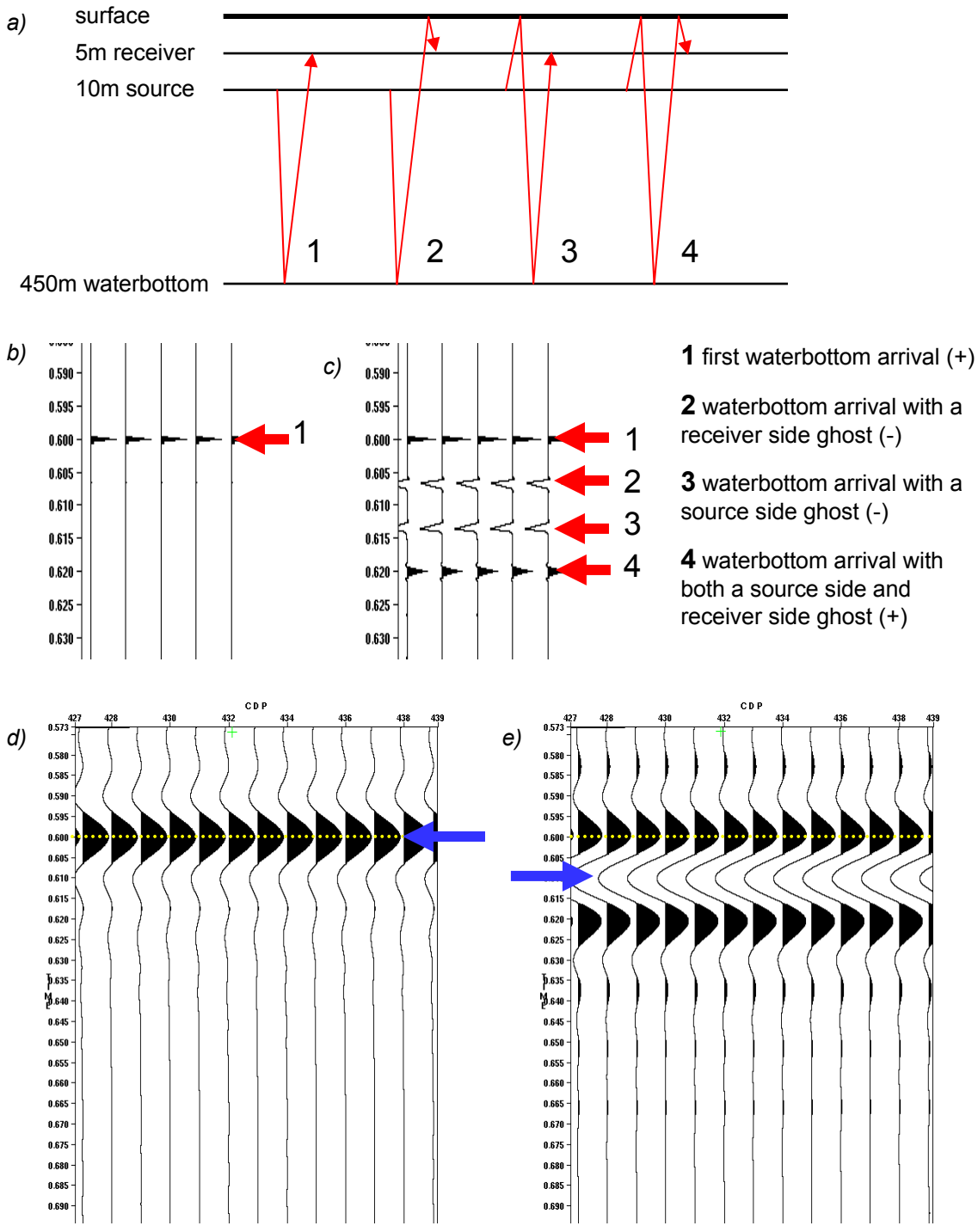

Figure 4.19. Importance of the ghost for calibrating the vertical synthetic to the imaged data. a) schematic showing direct reflection and the ghost travelpaths for the waterbottom, b) arrival (spike) without ghosts, c) arrivals (spikes) including ghosts, d) convolution with 5-10-60-80Hz Ormsby wavelet without ghosts, e) convolution with 5-10-60-80Hz Ormsby wavelet including the ghosts. The waterbottom (yellow line) and maximum energy of the envelope (blue arrows) are indicated on d) and e).

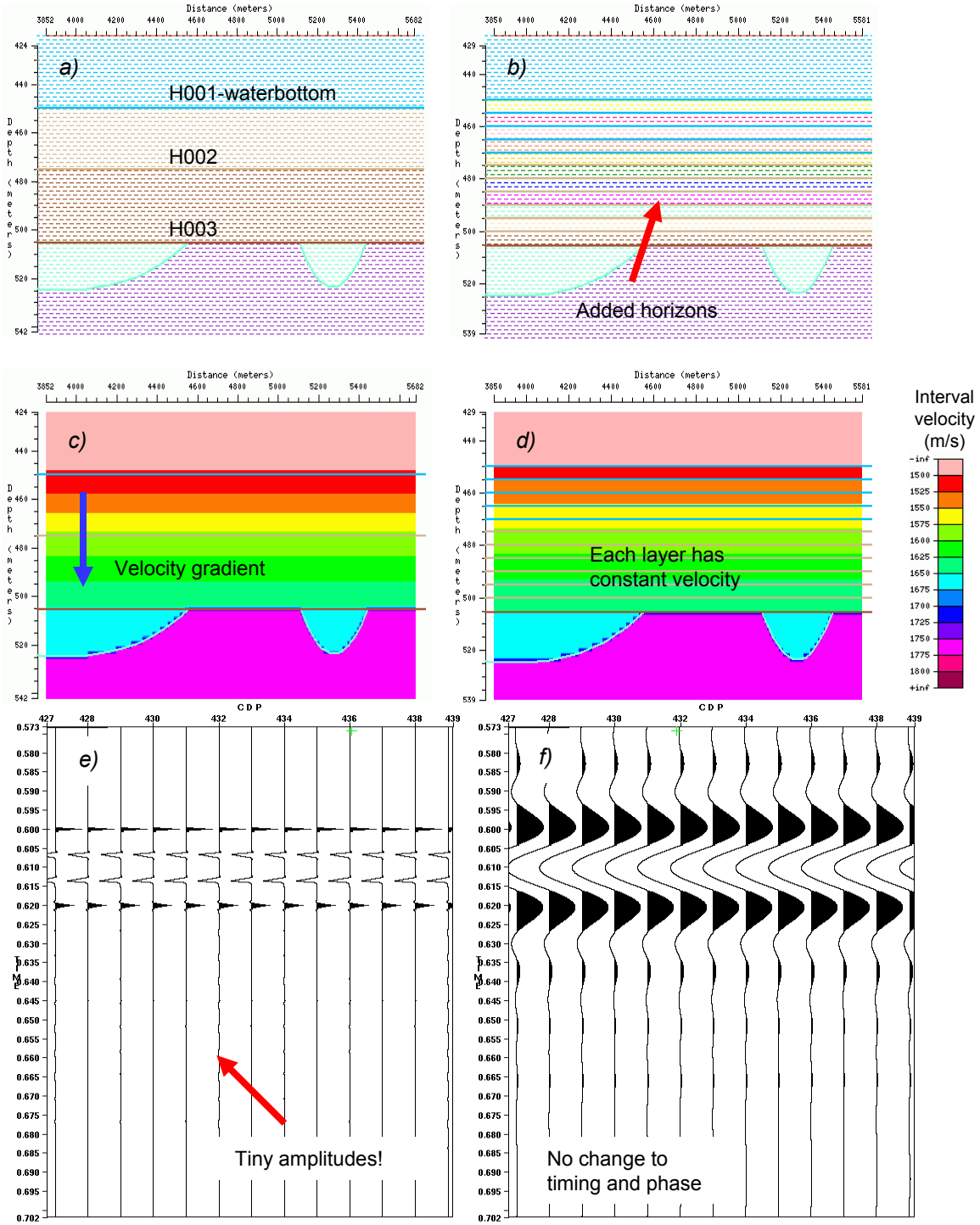

Figure 4.20. a) Marmousi2 model showing the waterbottom and shallow sediments, b) modified model to include a series of events within the soft sediment layers, c) Marmousi2 interval velocity defined by gradients in the first two sedimentary layers, d) modified model with constant velocity in each thin layer, velocity values estimated from Marmousi2, e) arrivals for the modified model, amplitudes for the thin interfaces are extremely small, f) spikes convolved with the Orsmby wavelet show that the additional thin layers have approximately no effect on the resultant phase and timing.

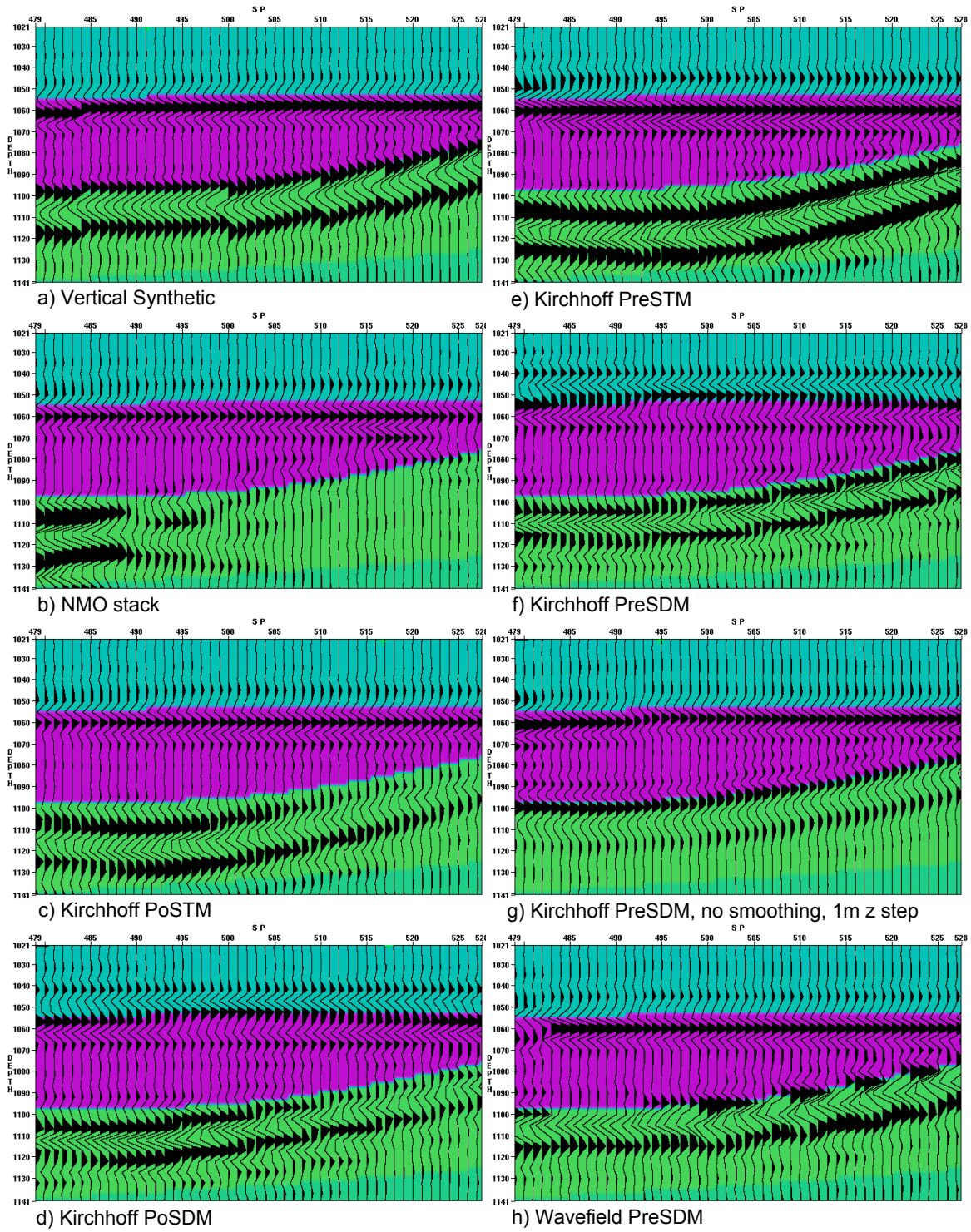

Figure 4.23. Timing and phase quality control at the gas sand (indicated by the purple), interval velocity is shown as color. a) simple vertical synthetic (with ghosts), b) NMO stack, c) Kirchhoff poststack time migration, d) Kirchhoff poststack depth migration, e) Kirchhoff prestack time migration, f) Kirchhoff prestack depth migration, g) Kirchhoff prestack depth migration with no smoothing and a 1m depth step, h) wavefield prestack depth migration.

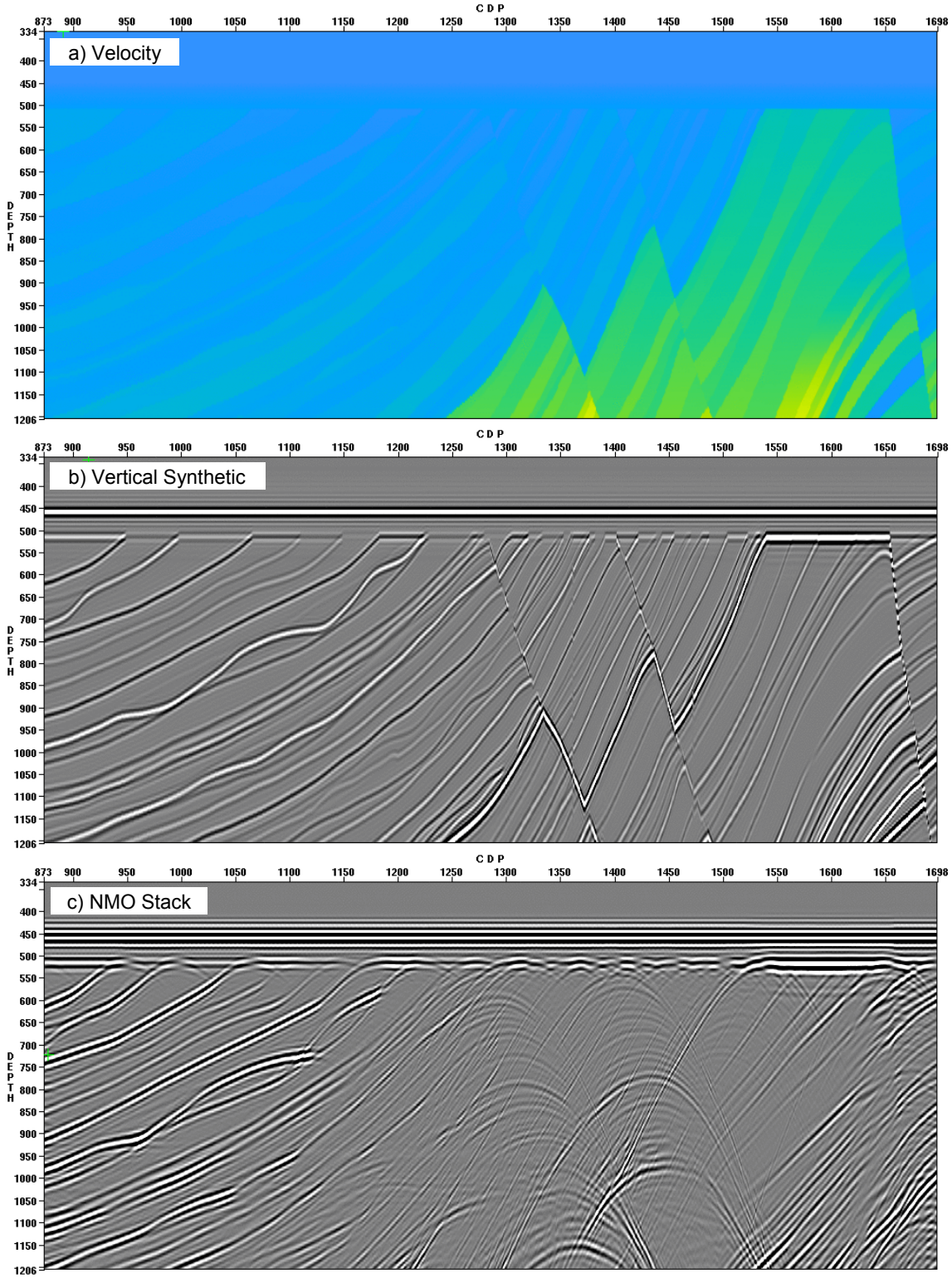

Figure 4.32. Imaging details from area 1. a) interval velocity, b) vertically raytraced synthetic, c) simple NMO stack.

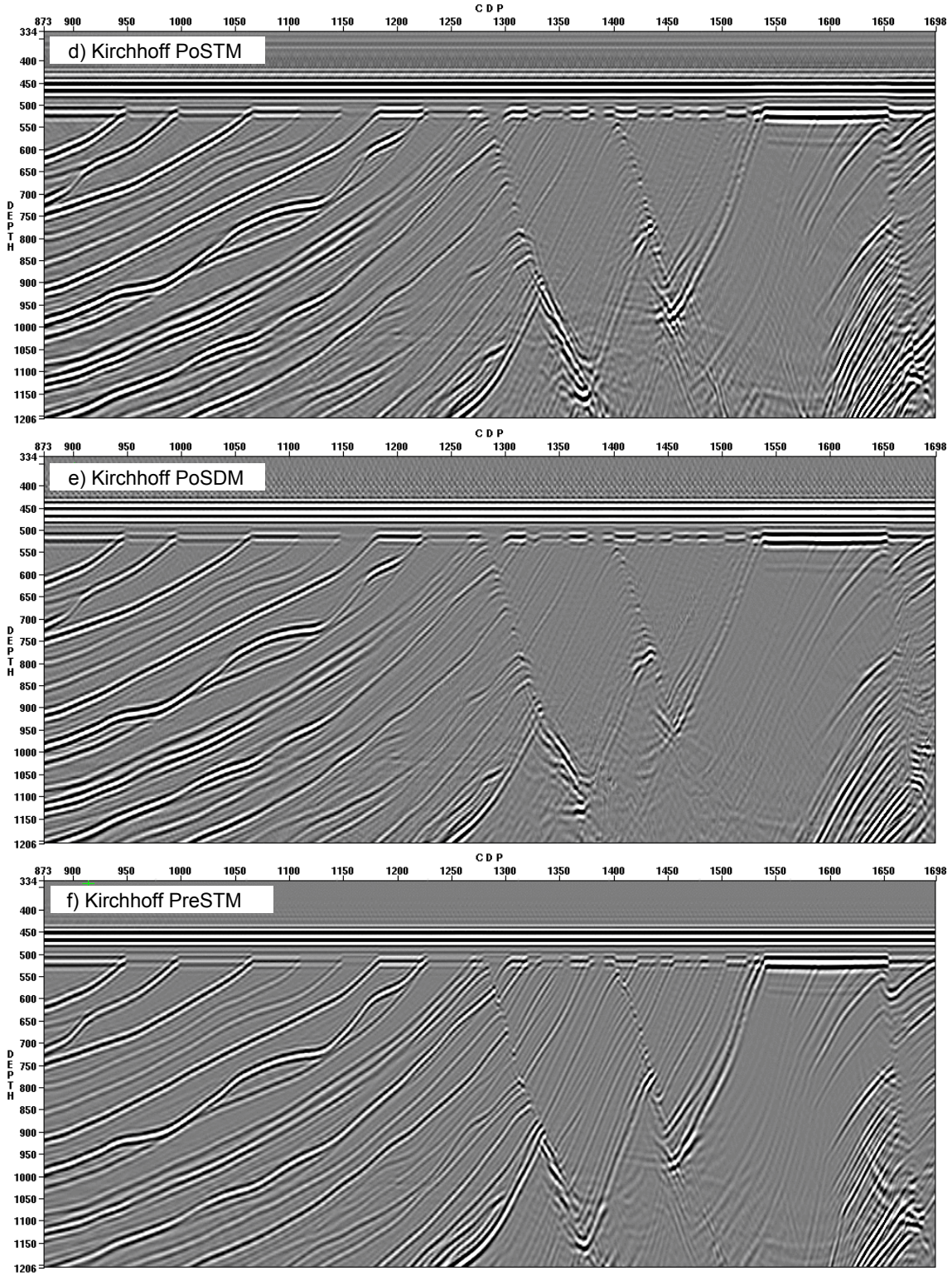

Figure 4.32. Imaging details from area 1. d) Kirchhoff poststack time migration, e) Kirchhoff poststack depth migration, f) Kirchhoff prestack time migration.

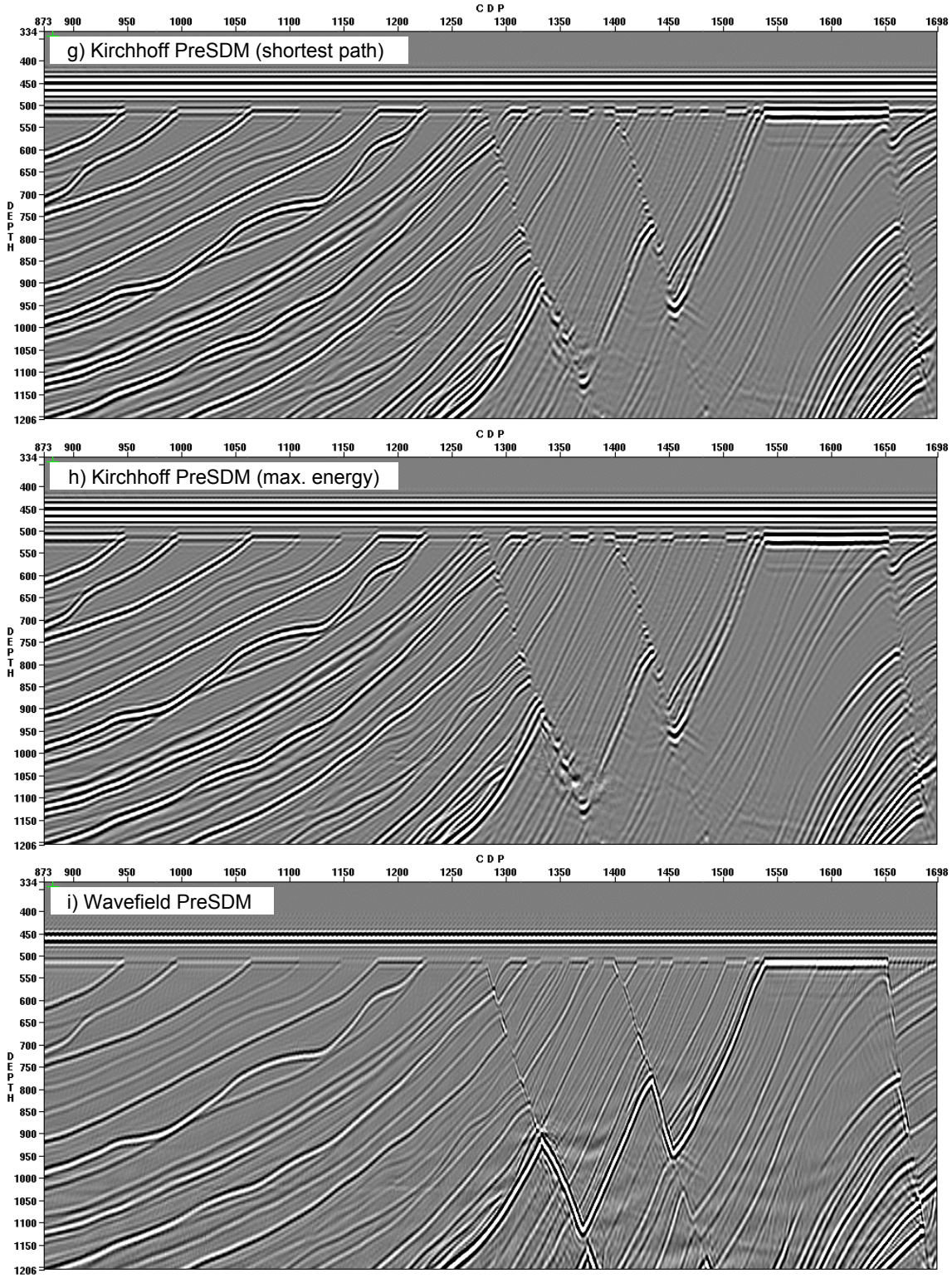

Figure 4.32. Imaging details from area 1. g) Kirchhoff prestack depth migration using shortest path raytracing, h) Kirchhoff prestack depth migration using maximum energy raytracing, i) shot profile wave-equation prestack depth migration.

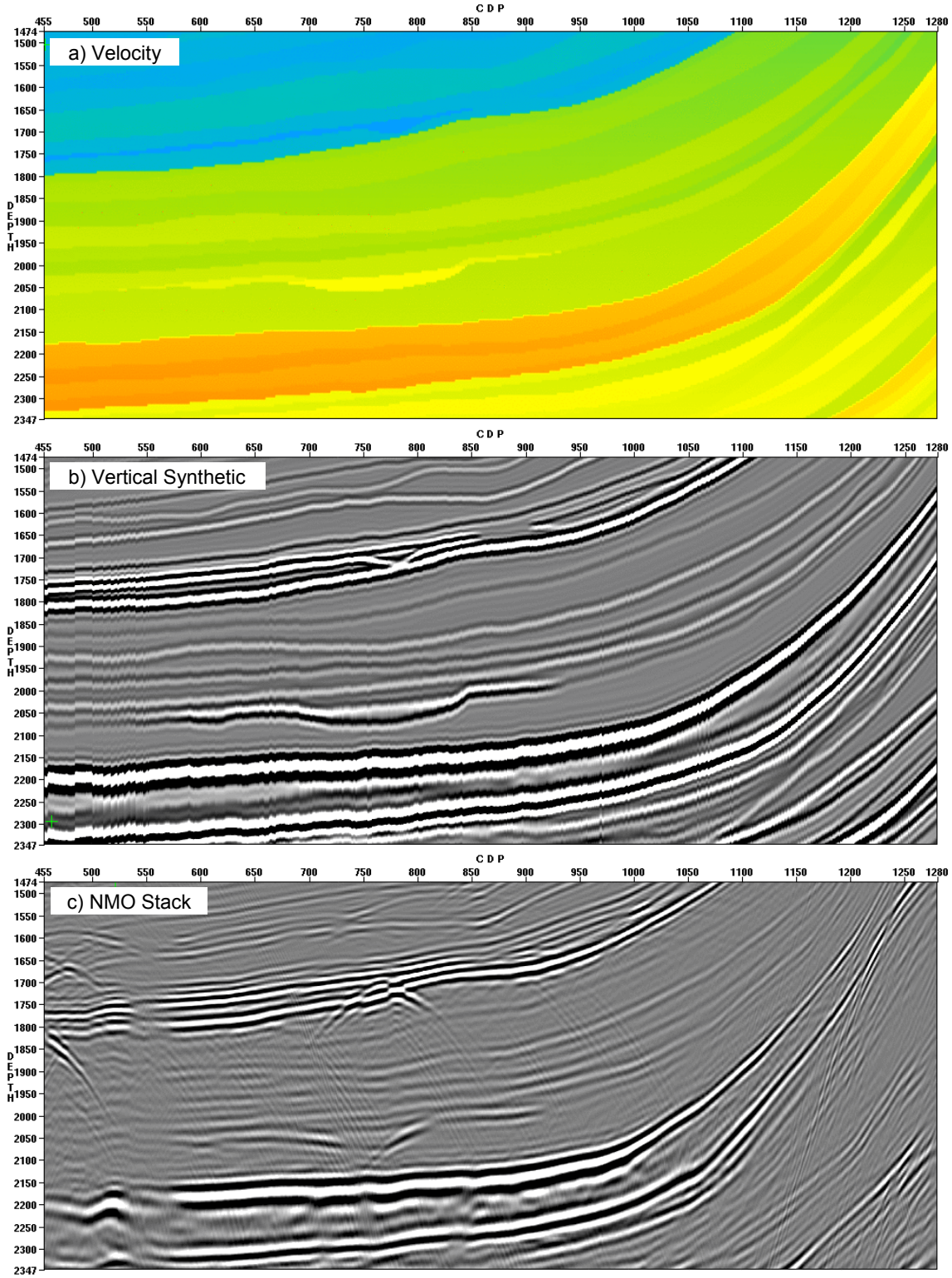

Figure 4.33. Imaging details from area 2. a) interval velocity, b) vertically raytraced synthetic, c) simple NMO stack.

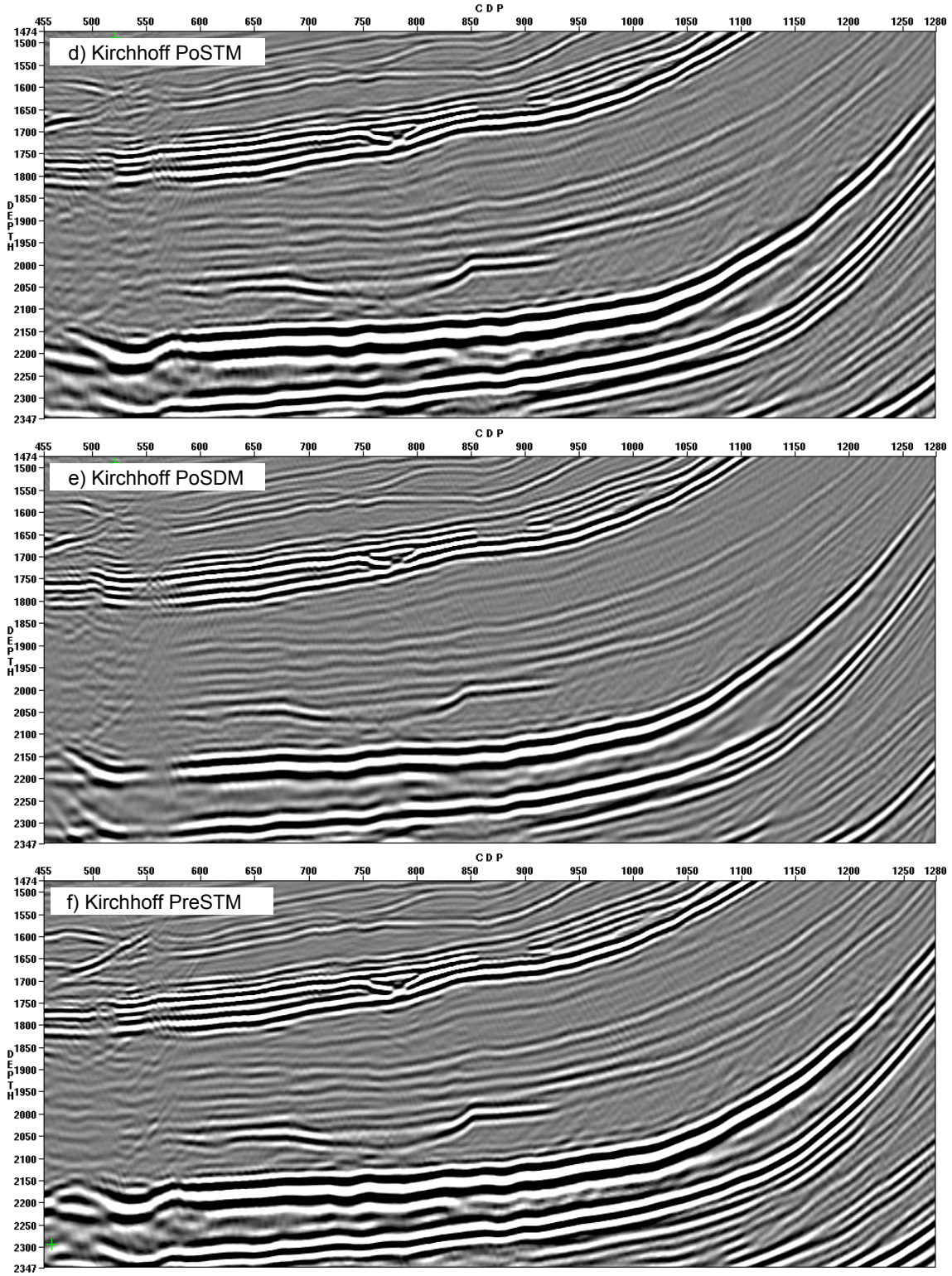

Figure 4.33. Imaging details from area 2. d) Kirchhoff poststack time migration, e) Kirchhoff poststack depth migration, f) Kirchhoff prestack time migration.

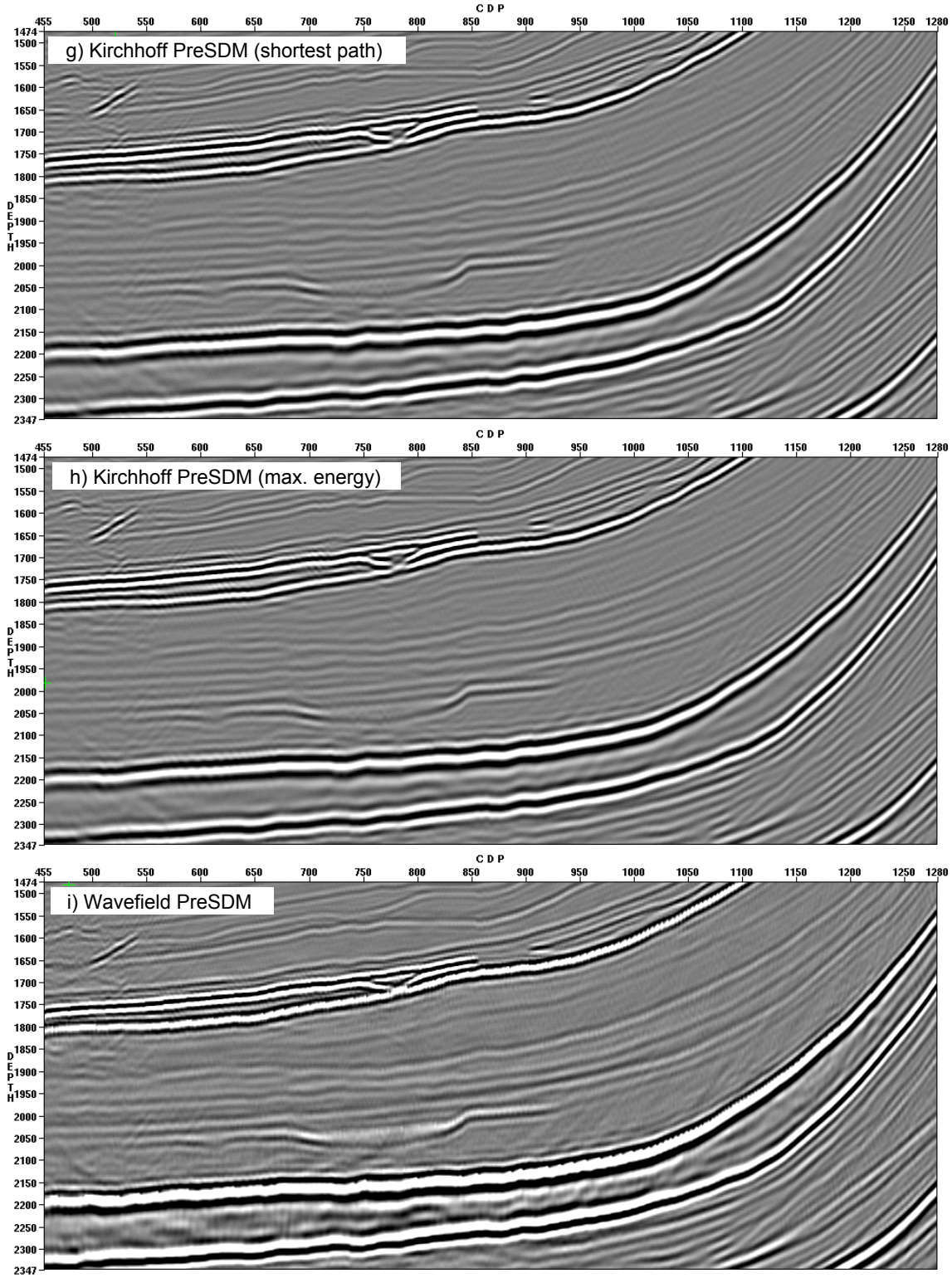

Figure 4.33. Imaging details from area 2. g) Kirchhoff prestack depth migration using shortest path raytracing, h) Kirchhoff prestack depth migration using maximum energy raytracing, i) shot profile wave-equation prestack depth migration.

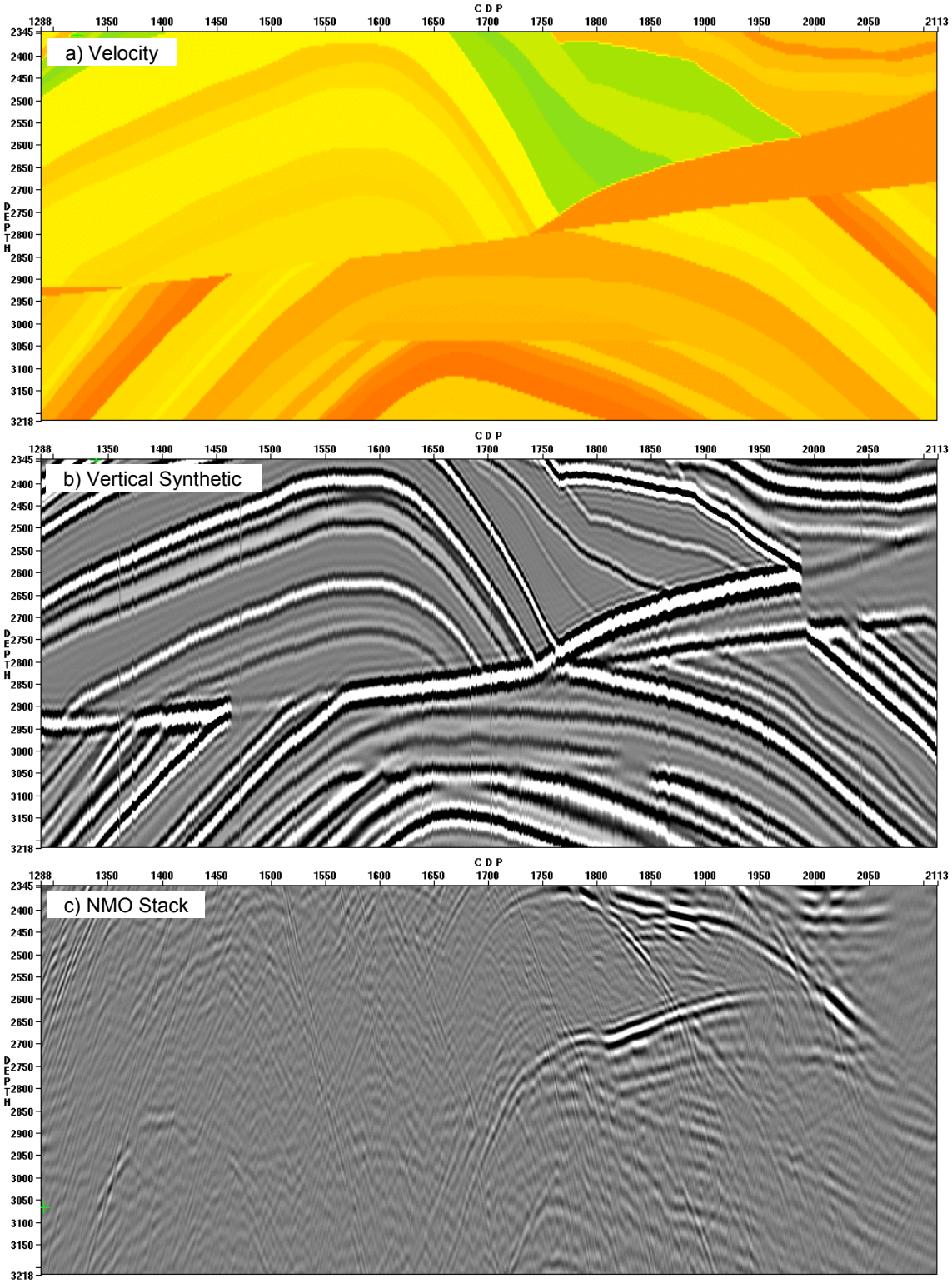

Figure 4.34. Imaging details from area 3. a) interval velocity, b) vertically raytraced synthetic, c) simple NMO stack.

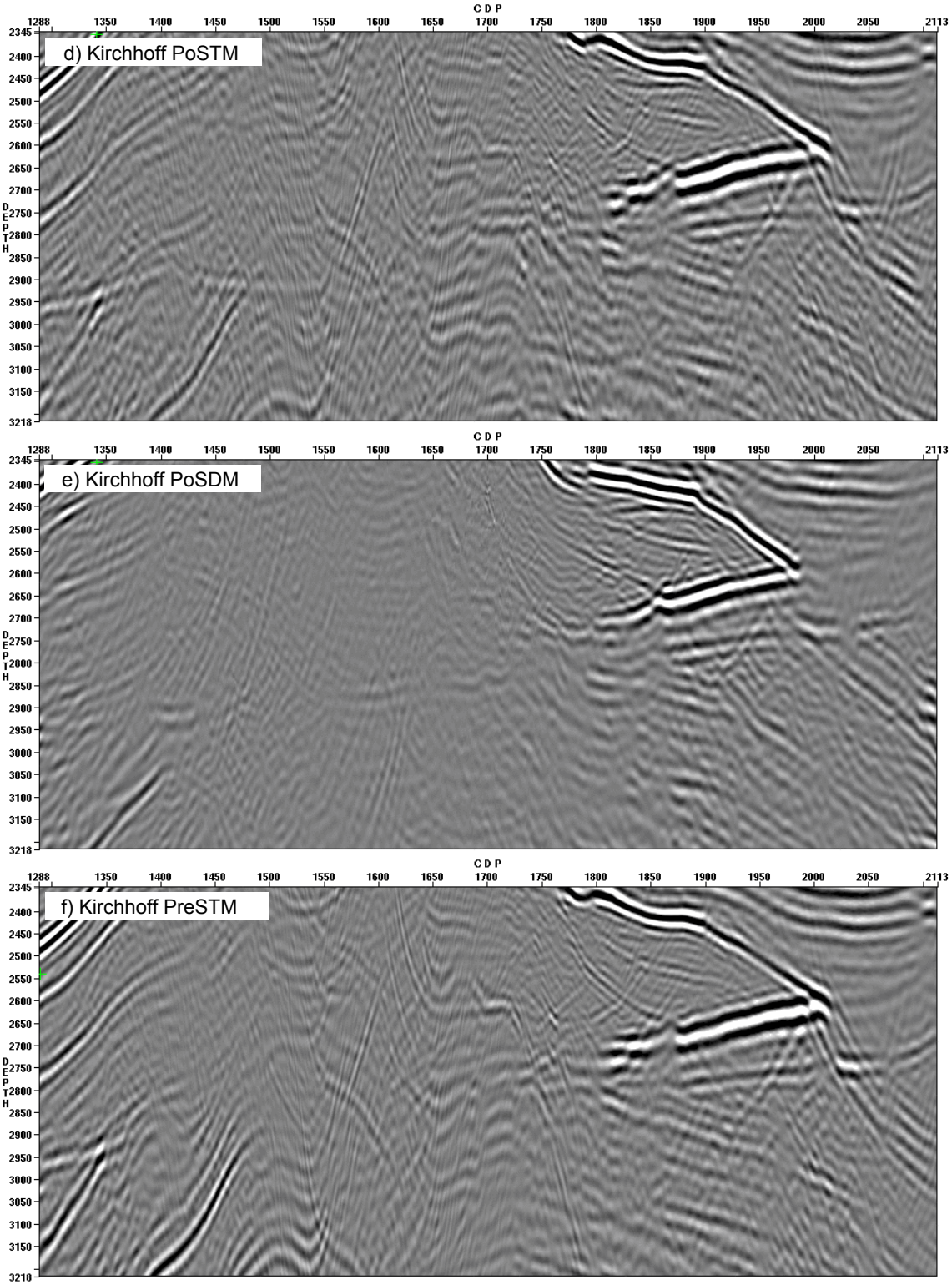

Figure 4.34. Imaging details from area 3. d) Kirchhoff poststack time migration, e) Kirchhoff poststack depth migration, f) Kirchhoff prestack time migration.

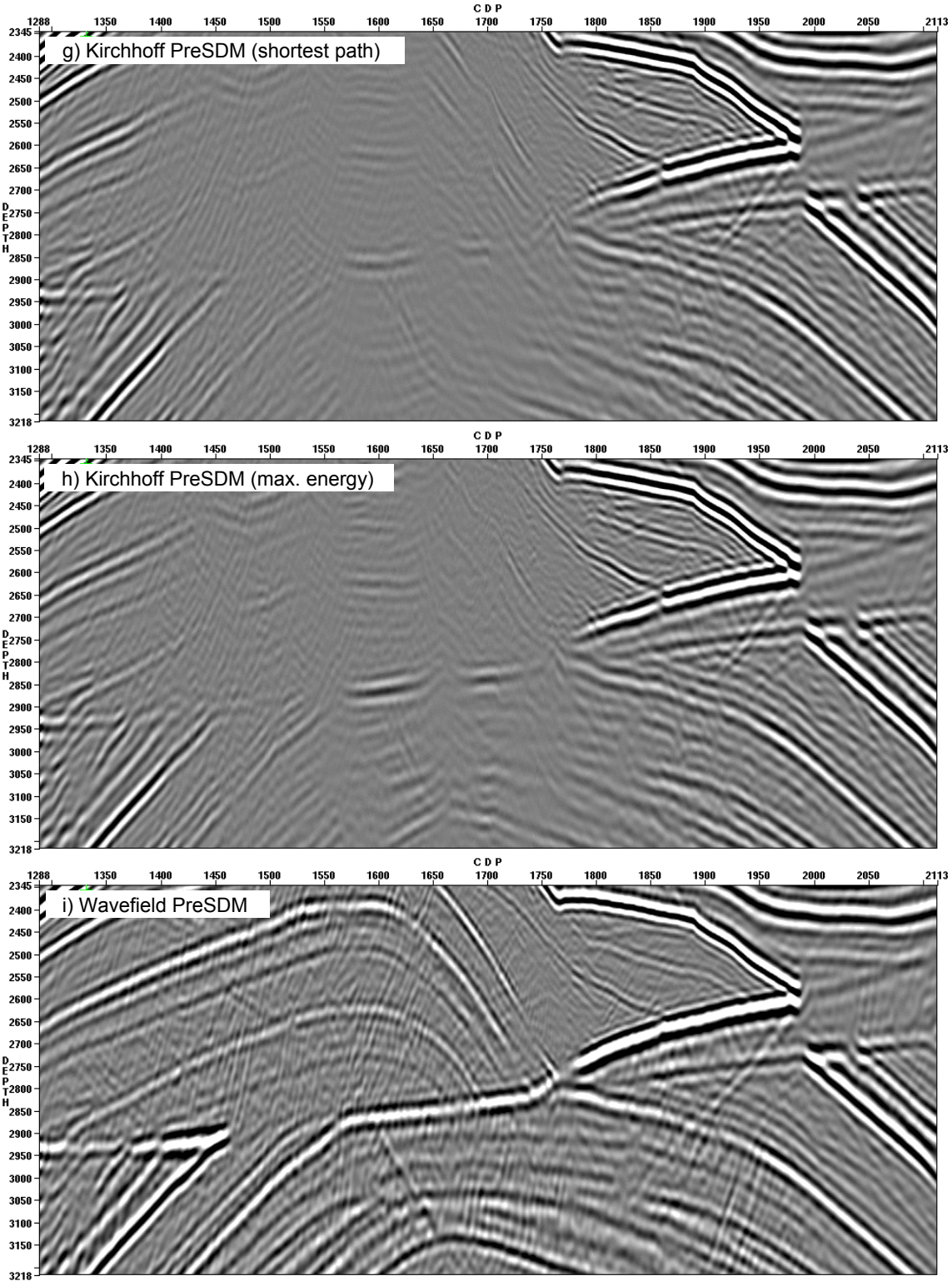

Figure 4.34. Imaging details from area 3. g) Kirchhoff prestack depth migration using shortest path raytracing, h) Kirchhoff prestack depth migration using maximum energy raytracing, i) shot profile wave-equation prestack depth migration.

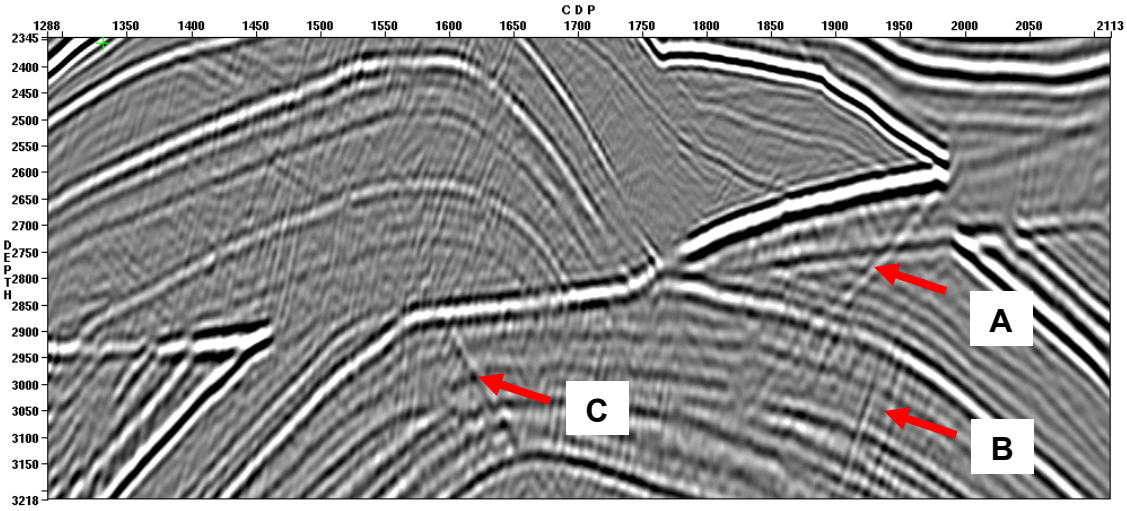

Figure 4.42 Artifacts in the deeper section.

#	Description	Runtime (mins)
1	Simple NMO/Stack	5
2	Kirchhoff PoSTM	9
3	Kirchhoff PoSDM	11
4	Kirchhoff PreSTM	540
5	Kirchhoff PreSDM shortest path	550
6	Kirchhoff PreSDM max. energy	550
7	Wave-equation PreSDM	15000

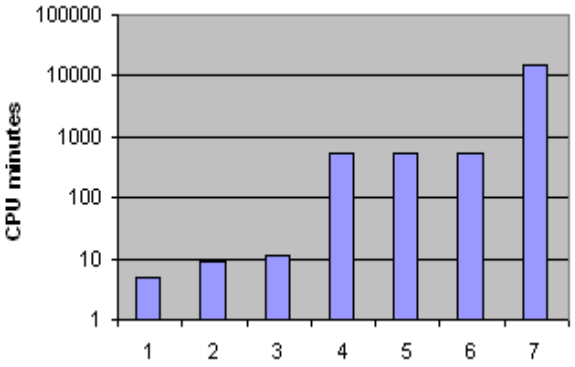

Figure 4.43. Migration runtimes. Runtimes are approximate for a single CPU workstation. Graph is shown in logarithmic scale.

5. AVO Analysis

The Marmousi2 model possesses a set of hydrocarbon bodies with varying sizes, hydrocarbon content, and structural location, as described in Chapter 2. An analysis of the seismic imaging and seismic amplitude variations with offset that are associated with the hydrocarbons are presented in this chapter, with the aim of ascertaining whether current seismic processing methodologies and simple AVO analysis will allow the detection of these bodies.

5.1 Brief overview of AVO

The ability to detect hydrocarbon bearing rocks using seismic amplitude has been practiced in the USA since the late 1960s, using bright spot analysis. True AVO methods were first published in the 1980s (*e.g.* Ostrander, 1982), and are continuously evolving, with many papers published annually in the geophysical literature.

The theory of AVO is based upon the changes to the physical properties of rocks that occur when they are filled with hydrocarbons, and the ability of seismic methods to distinguish them from water filled rocks. Pore fluid content affects the compressional wave (P-wave) velocity, whereas the shear wave (S-wave) velocity is more dependent upon the rock framework (matrix). Oil and gas generally have the effect of lowering the P-wave velocity of the rock, with only small changes to the S-wave velocity. The modification of the ratio between the P-wave velocity and the S-wave velocity causes changes in the partitioning of an incident wave upon the horizon, which can result in anomalous amplitude variations with offset that can be observed on seismic gathers. Since hydrocarbons are not present in the vast majority of rocks, the search for them is

based around the detection of an anomaly, *i.e.* the recognition of a pattern that is different to the normal situation.

Traditionally AVO methods have been applied to CMP gathers. However, as structural complexity increases, the basic assumptions of the CMP method begin to fail, and obtaining an interpretable image of the subsurface is no longer possible, let alone the use of the gathers for AVO analysis. Typical processing flows now include prestack migrations, in time and/or depth in order to obtain satisfactory subsurface images. The prestack, post-migration gathers (image gathers) are now routinely used for AVO analyses in such areas.

5.2 Detecting the Marmousi2 hydrocarbon units using AVO

In order to ascertain whether the real data contains a signature of AVO consistent with theory it is necessary to first predict the theoretical responses. The prediction of the theoretical response takes into account many factors including: depth of burial, thickness of unit, rock properties of the unit, *etc*., as presented in Chapter 2. However, the complexity of the overburden and structural dip (*i.e.* imaging complexity) and ghost effect is not taken into account. The predicted responses are shown in Figures 2.11 – 2.20, and are summarized in Table 2.7. Due to the ghost, which causes an approximate 180 phase rotation, all peaks are troughs and *vice-versa*.

AVO anomaly detection methods require the analysis of prestack seismic amplitudes. Prestack amplitudes are provided by simplistic methods such as common mid-point binning (CMP), or by more advanced prestack migration techniques which provide image gathers. Seismic gathers were generated by the processing methods described in the previous chapter. For analysis, the depth gathers were converted to the

time domain, since typically AVO analysis is performed in this domain; where wavelet stretch caused by velocity variations is minimized.

Figure 5.1 shows the vertical synthetic time section, the location of the Marmousi2 hydrocarbon units, and a central CDP location for each unit. The analysis of AVO is based entirely upon the data at the central CDP location, which is assumed to be representative of the hydrocarbon body. The corresponding locations in the depth domain are presented in Figure 5.2.

Figures 5.3 – 5.9 show the imaging results in the areas of the hydrocarbons, and indicate the location of the central CDP. Figures 5.10 – 5.17 show a detailed examination of the image gathers in the hydrocarbon zones, and also show the modeled (predicted) AVO effect. Remember, because of the ghost the modeled result is 180 degrees out of phase compared to the imaged data.

5.2.1 Hydrocarbon A (shallow gas sand)

The imaging results and image gathers are presented in Figures 5.3 and 5.4. It is immediately apparent that the imaging depth step of 5m is quite coarse for detailed analysis of features such as the gas sand, which has a maximum vertical thickness of approximately 40m, representing only 8 samples. The depth step can be clearly identified on the wiggle displays by the jagged appearance of the wiggles. The wavefield migration events are very broken and step like compared to the Kirchhoff results. This is due to the coarseness of the imaging depth step and associated velocity model. It should be noted that typical production processing of large 2D and 3D surveys using wavefield methods does not utilize grid dimensions this small (6.26m x 5m), and

results similar and worse (in terms of sampling limitations) to those shown for Marmousi2 should therefore be expected.

The observed AVO effect closely mirrors the modeled result in most cases. The top and base are bright spots, with a minor increase of amplitude with offset. In this shallow, more or less flat-lying case even the NMO gathers show the expected result for the top of the sand. The base shows the opposite effect, a decrease of amplitude with offset, but analysis of the stacked image shows that the base is not well imaged, and is complicated by interfering diffractions, and is therefore not suitable for AVO analysis. Both sets of Kirchhoff gathers show the expected AVO result. The Kirchhoff PreSTM gathers are good, but the result deteriorates at offsets greater than twice the depth, and the event appears to be under-corrected, probably due to the limitations of PreSTM and the velocity smoothing. The Kirchhoff PreSDM gathers are similar to the PreSTM gathers, with a less severe under-correction at offsets greater than twice the depth. Both sets of wavefield migration gathers are flatter than the Kirchhoff gathers, and do not suffer from undercorrection, but no AVO effect is observed. The wavefield method employed does not yet satisfy the “amplitude preserving” or more rigorous “true amplitude” criteria, and is therefore not expected to preserve the amplitudes necessary for AVO analysis.

5.2.2 Hydrocarbon B (oil sand)

The imaging results and image gathers are presented in Figures 5.5 and 5.6. The oil sand is just thick enough (~40m) to be reasonably well imaged in its thickest location, but for most of its length the unit is too thin to resolve the top and base. Even at this location the base is not uniquely identifiable due to the close proximity of other

events. The observed AVO effect from the top matches the expected result of a very mild increase of amplitude with offset. The amplitudes at the top have a similar magnitude to the surrounding sediments, with negligible increase of amplitude with offset. In this shallow, more or less flat-lying case even the NMO gathers show the expected result. The migrated image gathers are also good, but the result deteriorates at offsets greater than twice the depth. At these offsets anomalously large amplitudes are encountered in the Kirchhoff results and the wavefield offset gathers, but they are not related to AVO.

5.2.3 Hydrocarbon C1 (gas sand)

The imaging results and image gathers are presented in Figures 5.7 and 5.8. The gas sand is very thin (~26m) and located in a more structurally complex area. Consequently, the NMO technique fails miserably, and the event is not detectable on the stack, let alone on the gathers. It is possible to identify the top of the sand on the PreSTM stacked image, but not on the image gathers. The Kirchhoff PreSDM correctly images the top of the sand and the gas-water contact is also imaged. The unit is too thin to identify the base. The top of the sand is associated with approximately constant amplitude with offset, but the Kirchhoff PreSDM gathers show a mild increase of amplitude with offset out to offsets up to one and a half times the depth. The sand is best imaged by the wavefield migration, and both sets of gathers show variable, but more or less constant amplitude with offset.

5.2.4 Hydrocarbon C2 (gas sand)

The imaging results and image gathers are presented in Figures 5.7 and 5.8. Despite the additional thickness of this unit (~55m), it is poorly imaged. The NMO stack

and PreSTM cannot resolve the structural complexity, and thus the event cannot be located on the gathers. The Kirchhoff PreSDM shows a dim structural top, and a bright gas-water contact, but there is little reflectivity observed for the base. The reflectivity for the top is so dim that it is difficult to identify the event, and therefore an AVO effect cannot be observed. The wavefield migration performs well, and the stacked image is very good. However, the analysis location is too close to the left edge of the feature and the top interferes with the bright gas-water contact. The compound reflection exhibits a strong amplitude increase with offset, which is present on all three depth migrated image gathers.

5.2.5 Hydrocarbon C3 (gas sand)

The imaging results and image gathers are presented in Figures 5.9 and 5.10. The gas sand is reasonably well imaged by all methods except for the NMO stack. Consequently, it is impossible to detect the unit using the NMO gathers. The PreSTM image is mispositioned, and somewhat broken up. The top and base are detectable on the PreSTM gathers, and a mild AVO effect, at least at the top, is observed for the near offsets. The moderate offsets pass through more complicated geology, and the events are lost. The Kirchhoff and wavefield PreSDM methods provide a satisfactory image of events. All of the depth migrations provide image gathers on which both the top and base can be traced for offsets up to twice the depth. Beyond that there are some anomalous amplitudes not related to any realistic AVO. The Kirchhoff gathers show agreement with the modeled results, *i.e.* moderate increase of amplitude with offset. This effect is not observed on the wavefield gathers, as expected.

5.2.6 Hydrocarbon C4 (gas sand)

The imaging results and image gathers are presented in Figures 5.11 and 5.12. The deeper C4 unit is not imaged using the NMO stack, and the gathers are not useful in identifying the event or any AVO effect. The events are imaged by the PreSTM, but the gathers show some interesting trends. There is very little near offset reflectivity, which gives way to undercorrected events towards the mid offsets, and then flattish high amplitudes in the further offsets! The Kirchhoff PreSDM provides an adequate image of the events, although the amplitude is weak. The gathers show increasing amplitude with offset as expected from the modeling. The weak amplitudes on the stack are due to the aggressive outer mute, such that the strong mid-offsets were not included. The wavefield PreSDM again provides the best imaging solution, but the gathers are not useful for AVO purposes.

5.2.7 Hydrocarbon D1 (oil sand)

The imaging results and image gathers are presented in Figures 5.13 and 5.14. The oil filled D1 unit has a relatively small acoustic impedance contrast compared to the surrounding rocks, which, along with the complex location, results in a very difficult imaging problem. The NMO and Kirchhoff methods do not achieve an interpretable result in this area, and the events are not detectable on the gathers either. The wavefield PreSDM again performs well, although the top and base have very low amplitudes (as predicted). Given the low amplitudes and a minor AVO effect, it is not surprising that an AVO effect is not observable.

5.2.8 Hydrocarbon D2 (oil sand)

The imaging results and image gathers are presented in Figures 5.13 and 5.15. The D2 sand exhibits almost identical characteristics to the D1 sand. It has very low amplitudes, and is in a difficult structural location to image. Only the wavefield PreSDM methods manages to adequately image the reflectors, but given the steepness of the events, the identification of the events on the gathers is difficult, and thus any observation of the very mild AVO would be very challenging, even if the wavefield gathers did preserve the AVO signature.

5.2.9 Hydrocarbon E1 (gas sand)

The imaging results and image gathers are presented in Figures 5.16 and 5.17. The anticlinal D1 sand is tenuously imaged by the wavefield PreSDM method. There is significant interference of the wavelets from the top and base of the gas sand, and it is not possible to credibly identify any AVO effect on the gathers.

5.2.10 Hydrocarbon E2 (oil sand)

The imaging results and image gathers are presented in Figures 5.16 and 5.17. Similar to E1, the E2 sand is only tenuously imaged by the wavefield PreSDM method. Again, there is significant interference of the wavelets from the top and base of the gas sand, and it is not possible to identify any AVO effect on the gathers.

5.3 Summary

The connection between imaging and AVO is apparent. Units that are not at least reasonably imaged in the stacked section, have an even poorer representation on

the image gathers, and therefore the analysis of these gathers for AVO anomalies is tenuous at best.

As structural complexity increases more sophisticated imaging methods are required, including prestack depth migration using Kirchhoff and wavefield methods. The Kirchhoff methods are “amplitude preserving” or “AVO friendly” and carry the AVO information, such that the gathers may be used for exploration for hydrocarbons. The wavefield method does not currently preserve AVO information, and the gathers should not be used for analysis. This is a shame given the better imaging performance.

The small scale of many of the hydrocarbon units, their placement in difficult imaging locations, associated with the minor (realistic) changes to fluid properties, and close proximity to other reflecting horizons makes their detection difficult. In this study AVO analysis did not yield useful information for some known hydrocarbons. As such, the dataset provides a good test for imaging and AVO methods.

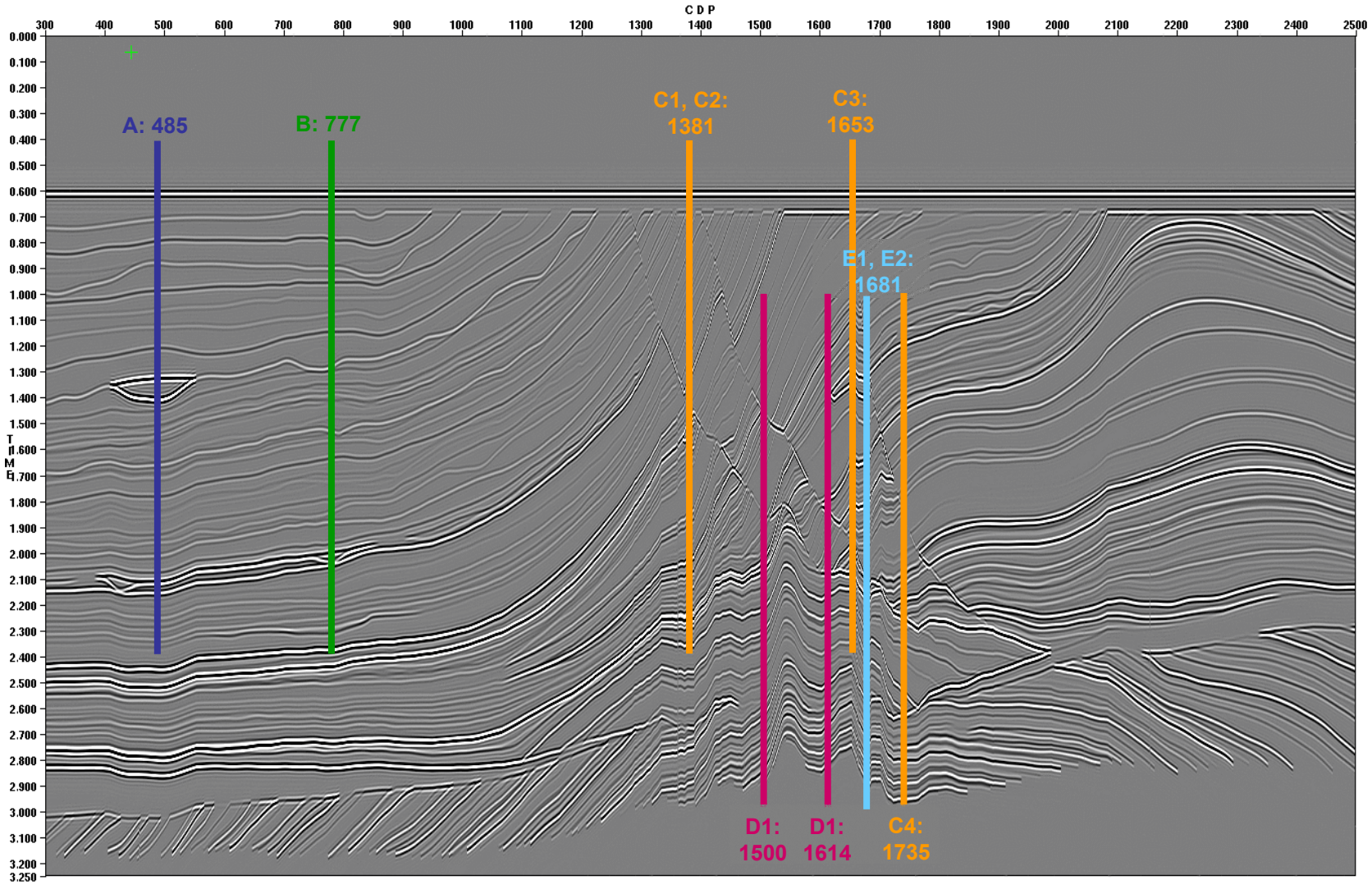

Figure 5.1. Simple vertical raytracing synthetic. Location of AVO analysis gathers are shown by the vertical lines. Each line is labeled by the CDP location and hydrocarbon identifier.

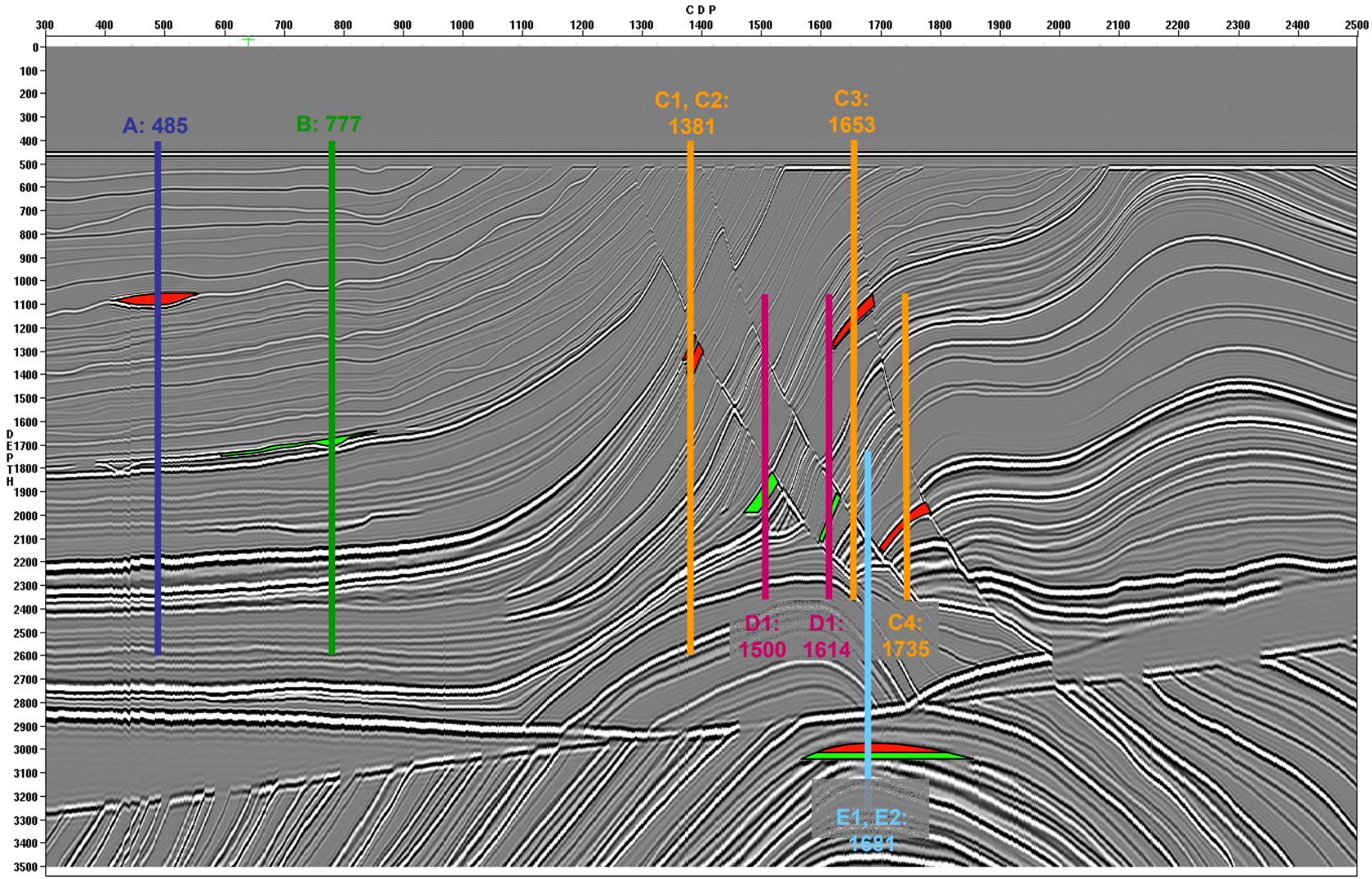

Figure 5.2 . Simple vertical raytracing synthetic, converted to depth. Location of AVO analysis gathers are shown by the vertical lines. Each line is labeled by the CDP location and hydrocarbon identifier.

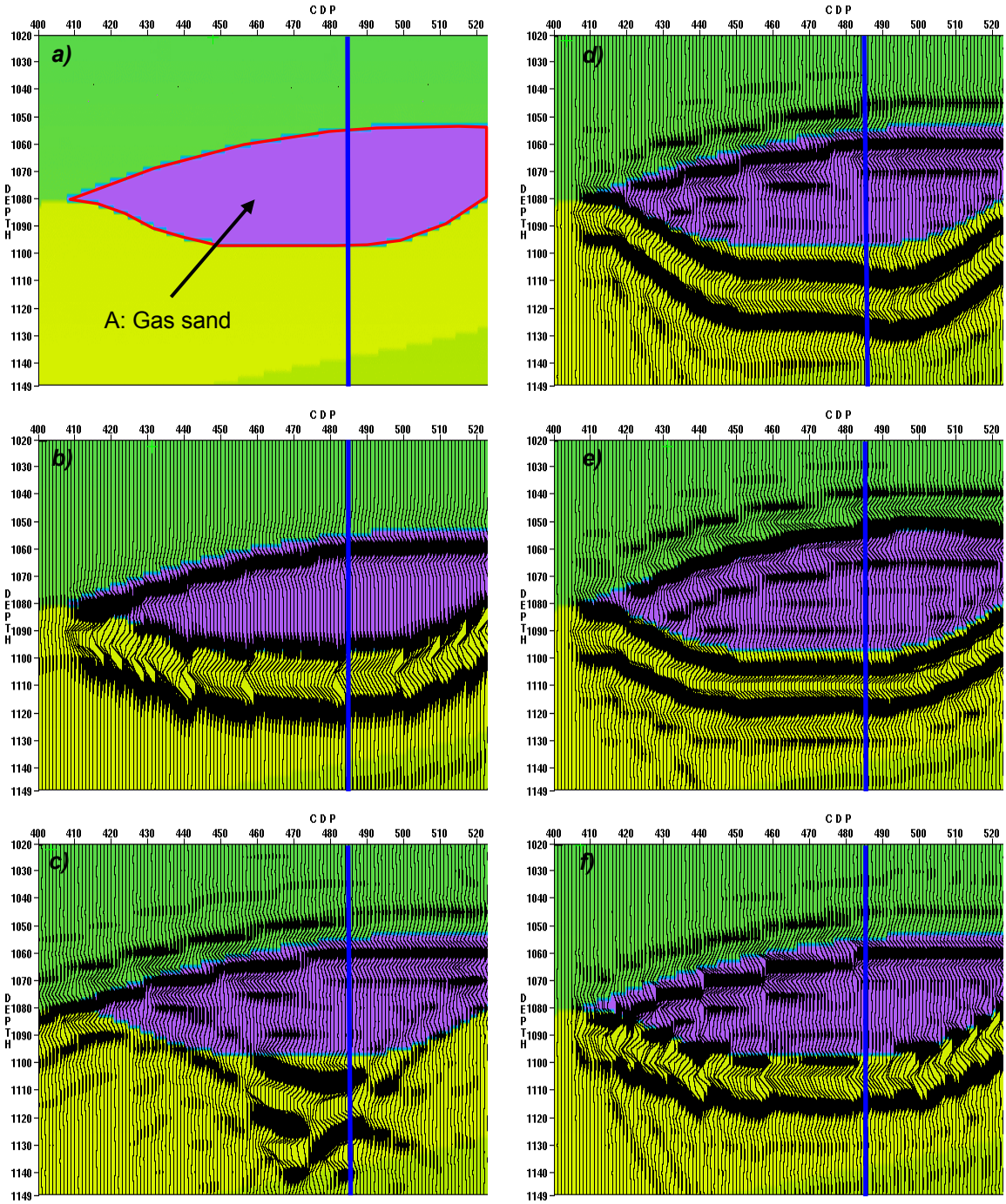

Figure 5.3. Hydrocarbon A, depth cross sections. Vertical line shows placement of analysis at CDP 485. a) velocity and cartoon of hydrocarbon, b) vertical synthetic section, c) NMO stack, d) Kirchhoff prestack time migration, e) Kirchhoff prestack depth migration, f) wavefield prestack depth migration.

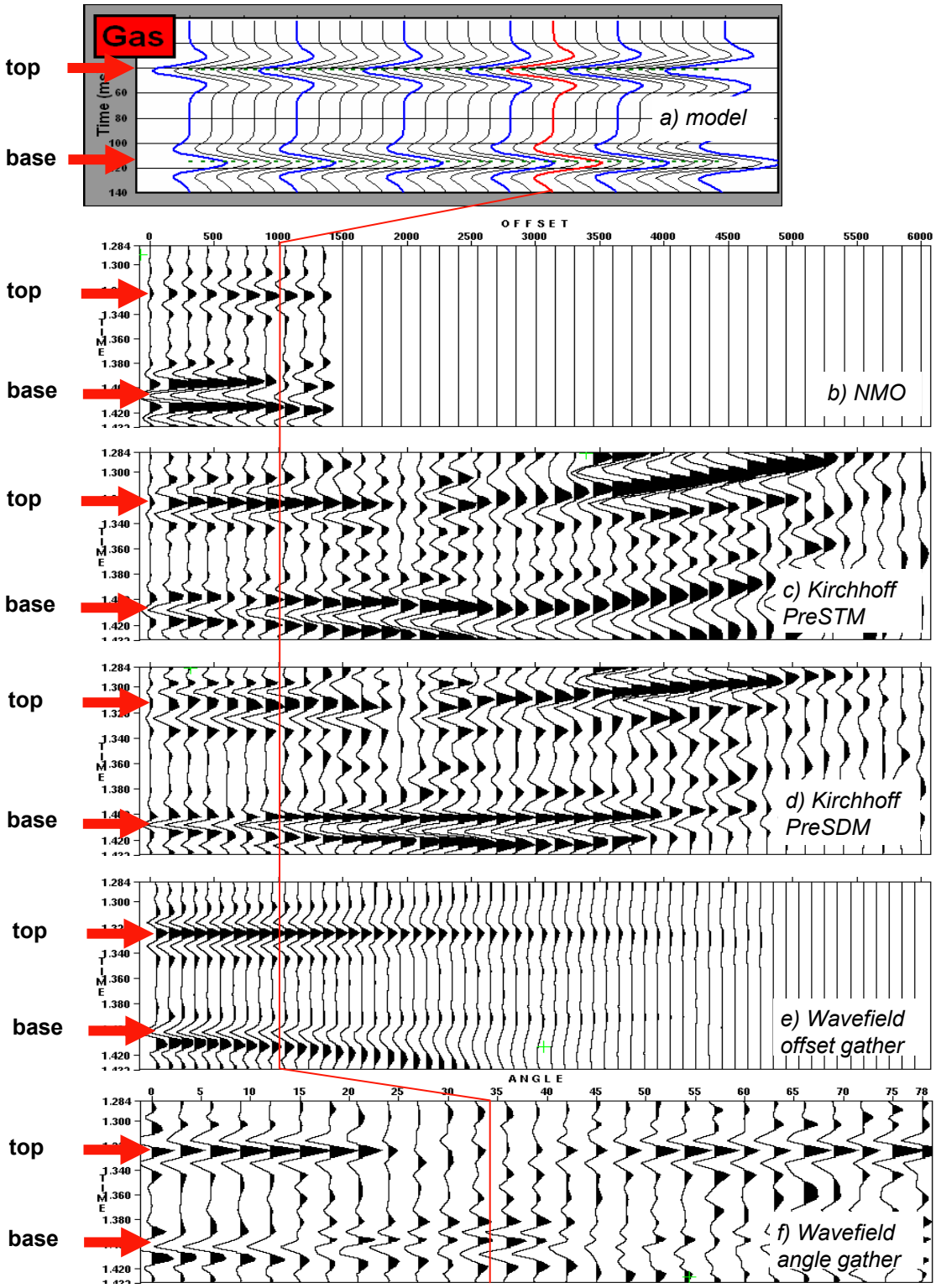

Figure 5.4. Analysis of AVO response for hydrocarbon A at CDP 485. a) synthetic response, b) NMO gathers, c) Kirchhoff PreSTM image gathers, d) Kirchhoff PreSDM image gathers, e) wavefield PreSDM offset image gathers, f) wavefield PreSDM angle gathers. Offset=depth is indicated by the red line.

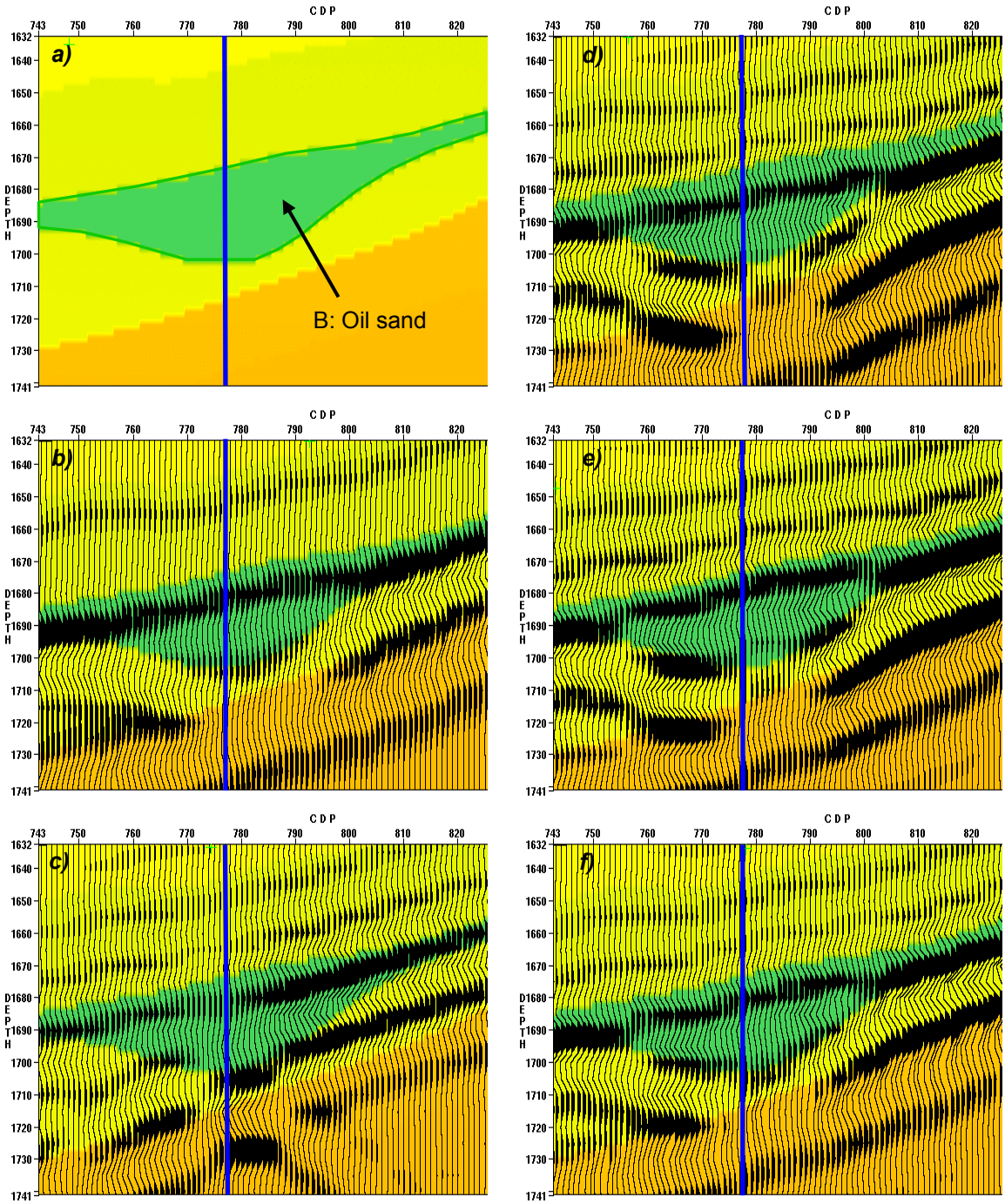

Figure 5.5. Hydrocarbon B, depth cross sections. Vertical line shows placement of analysis at CDP 777. a) velocity and cartoon of hydrocarbon, b) vertical synthetic section, c) NMO stack, d) Kirchhoff prestack time migration, e) Kirchhoff prestack depth migration, f) wavefield prestack depth migration.

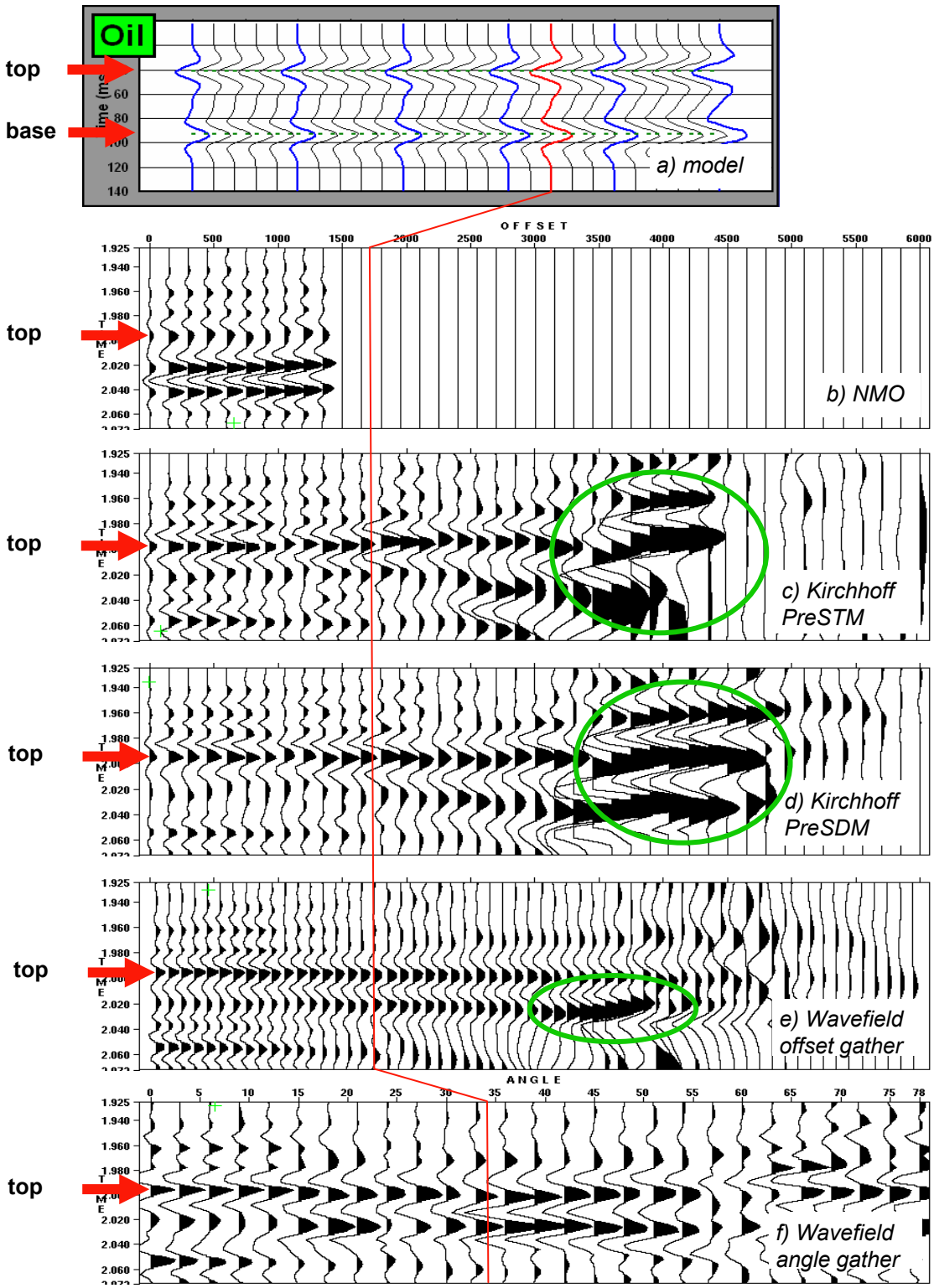

Figure 5.6. Analysis of AVO response for hydrocarbon B at CDP 777. a) synthetic response, b) NMO gathers, c) Kirchhoff PreSTM image gathers, d) Kirchhoff PreSDM image gathers, e) wavefield PreSDM image gathers, f) wavefield PreSDM angle gathers. Offset=depth is indicated by the red line. Green outline indicates area of anomalous amplitude, not an AVO effect.

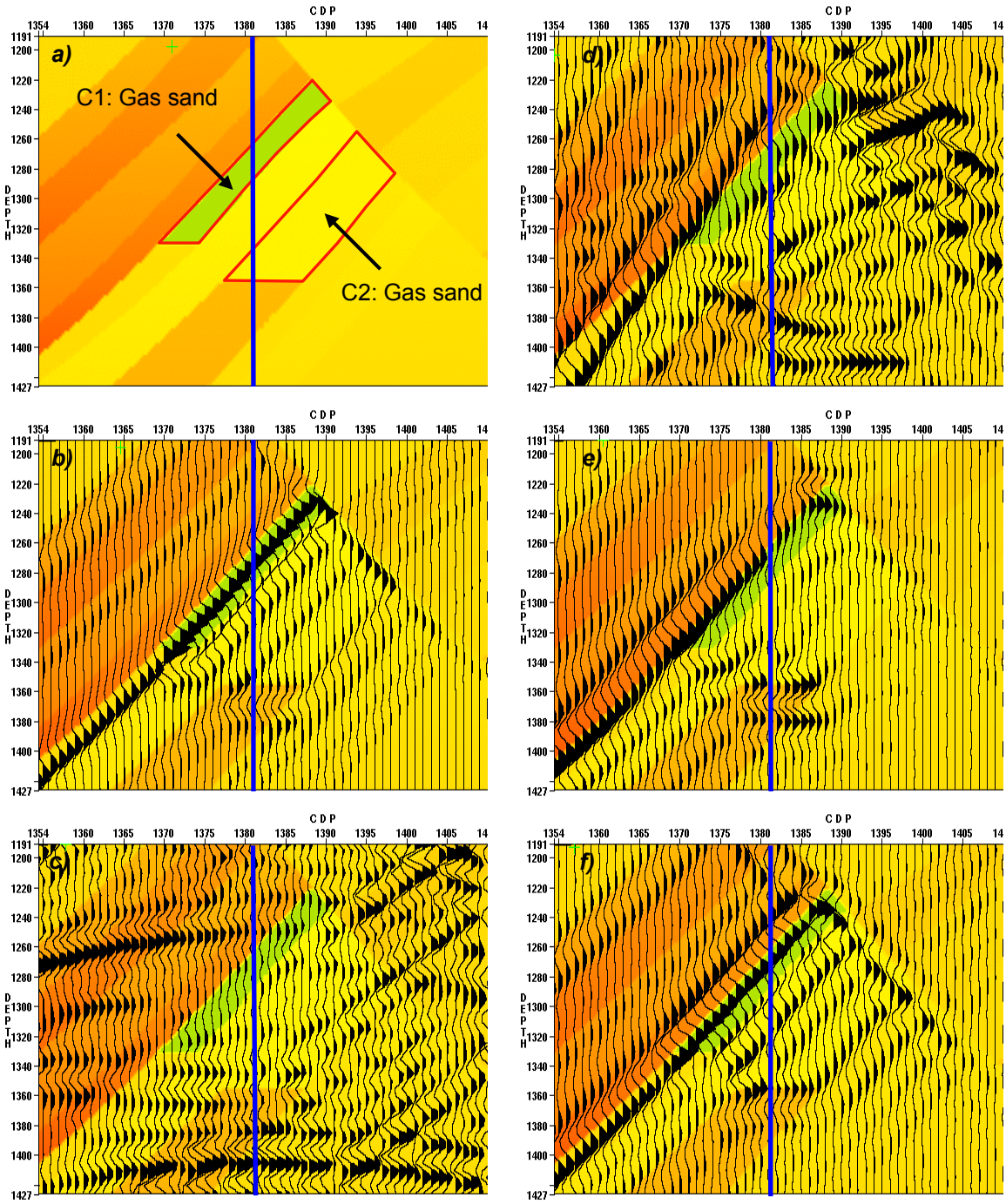

Figure 5.7. Hydrocarbon C1 and C2, depth cross sections. Vertical line shows placement of analysis at CDP 1381. a) velocity and cartoon of hydrocarbon, b) vertical synthetic section, c) NMO stack, d) Kirchhoff prestack time migration, e) Kirchhoff prestack depth migration, f) wavefield prestack depth migration.

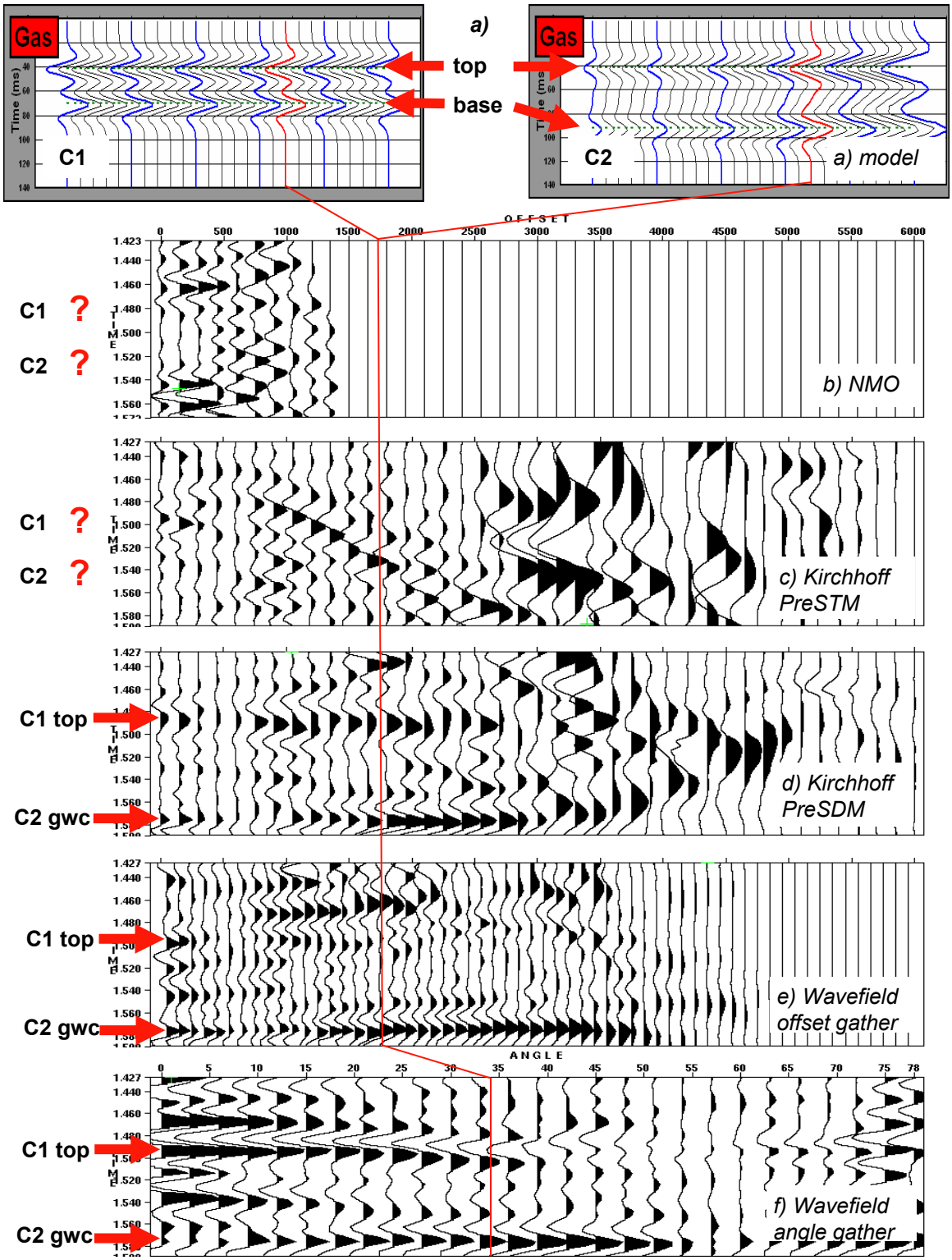

Figure 5.8. Analysis of AVO response for hydrocarbon C1 and C2 at CDP 1381. a) synthetic response, b) NMO gathers, c) Kirchhoff PreSTM image gathers, d) Kirchhoff PreSDM image gathers, e) wavefield PreSDM image gathers, f) wavefield PreSDM angle gathers. Offset=depth is indicated by the red line. gwc is the gas-water contact.

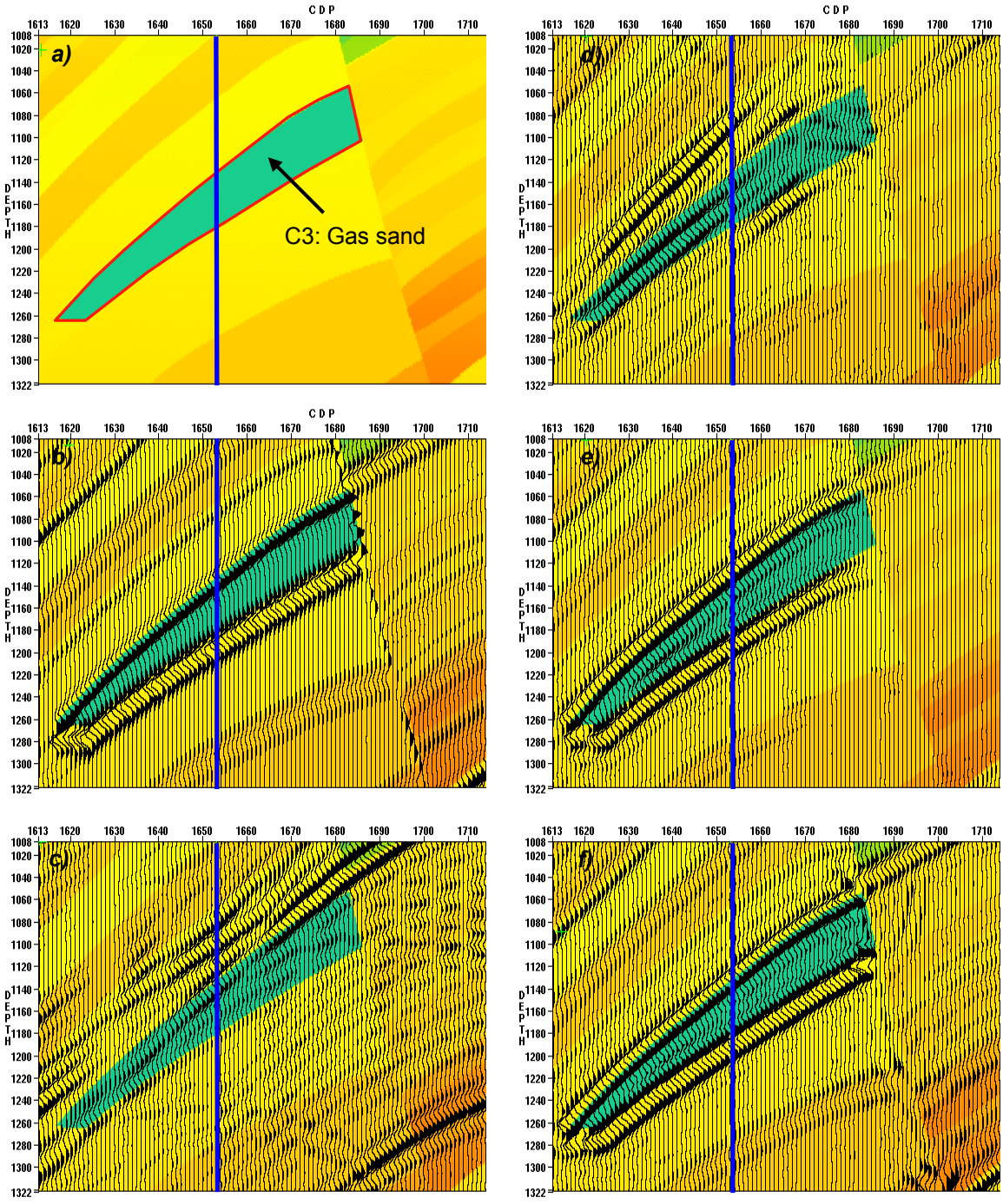

Figure 5.9. Hydrocarbon C3, depth cross sections. Vertical line shows placement of analysis at CDP 1653. a) velocity and cartoon of hydrocarbon, b) vertical synthetic section, c) NMO stack, d) Kirchhoff prestack time migration, e) Kirchhoff prestack depth migration, f) wavefield prestack depth migration.

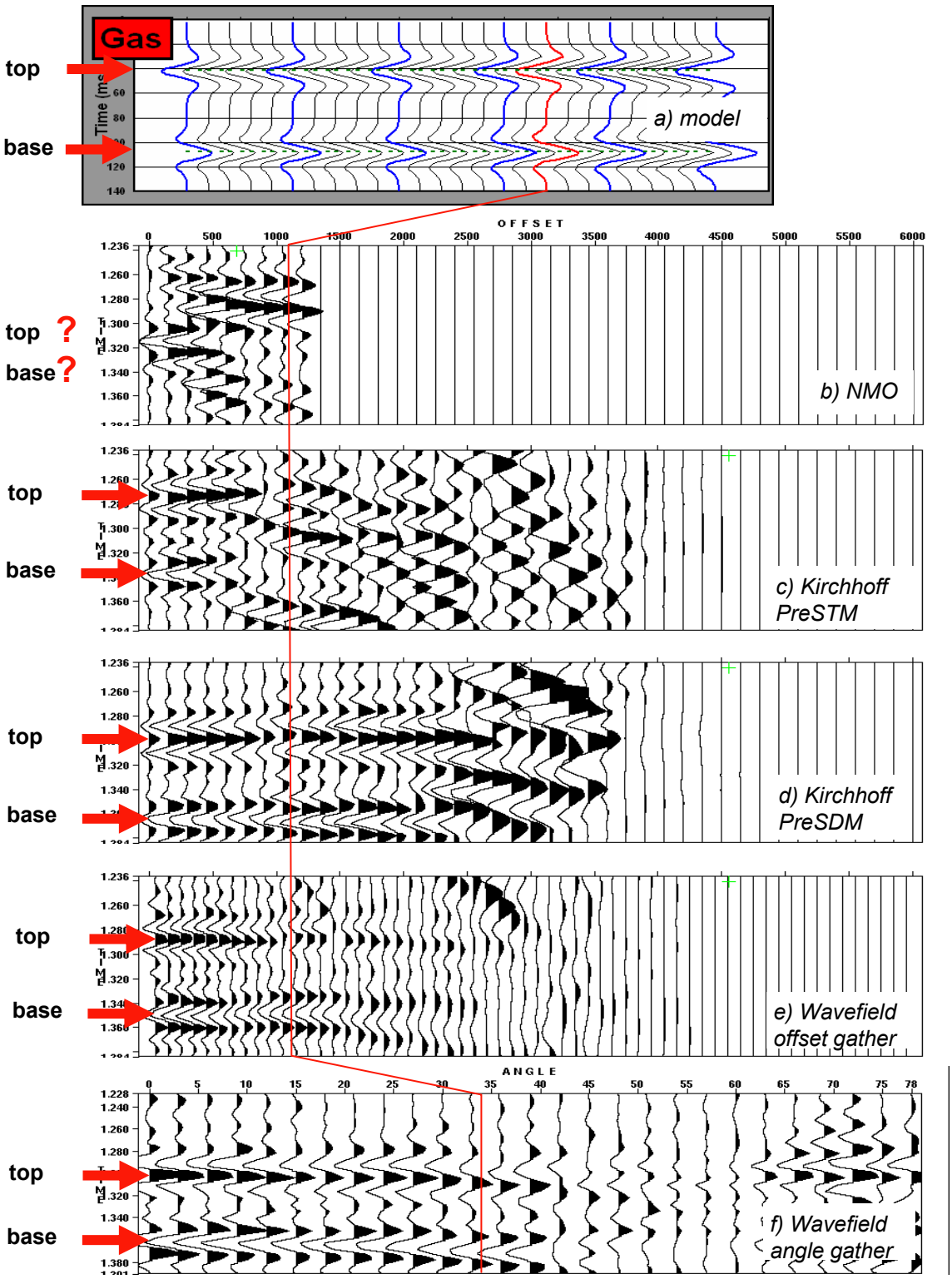

Figure 5.10. Analysis of AVO response for hydrocarbon C3 at CDP 1653. a) synthetic response, b) NMO gathers, c) Kirchhoff PreSTM image gathers, d) Kirchhoff PreSDM image gathers, e) wavefield PreSDM image gathers, f) wavefield PreSDM angle gathers. Offset=depth is indicated by the red line.

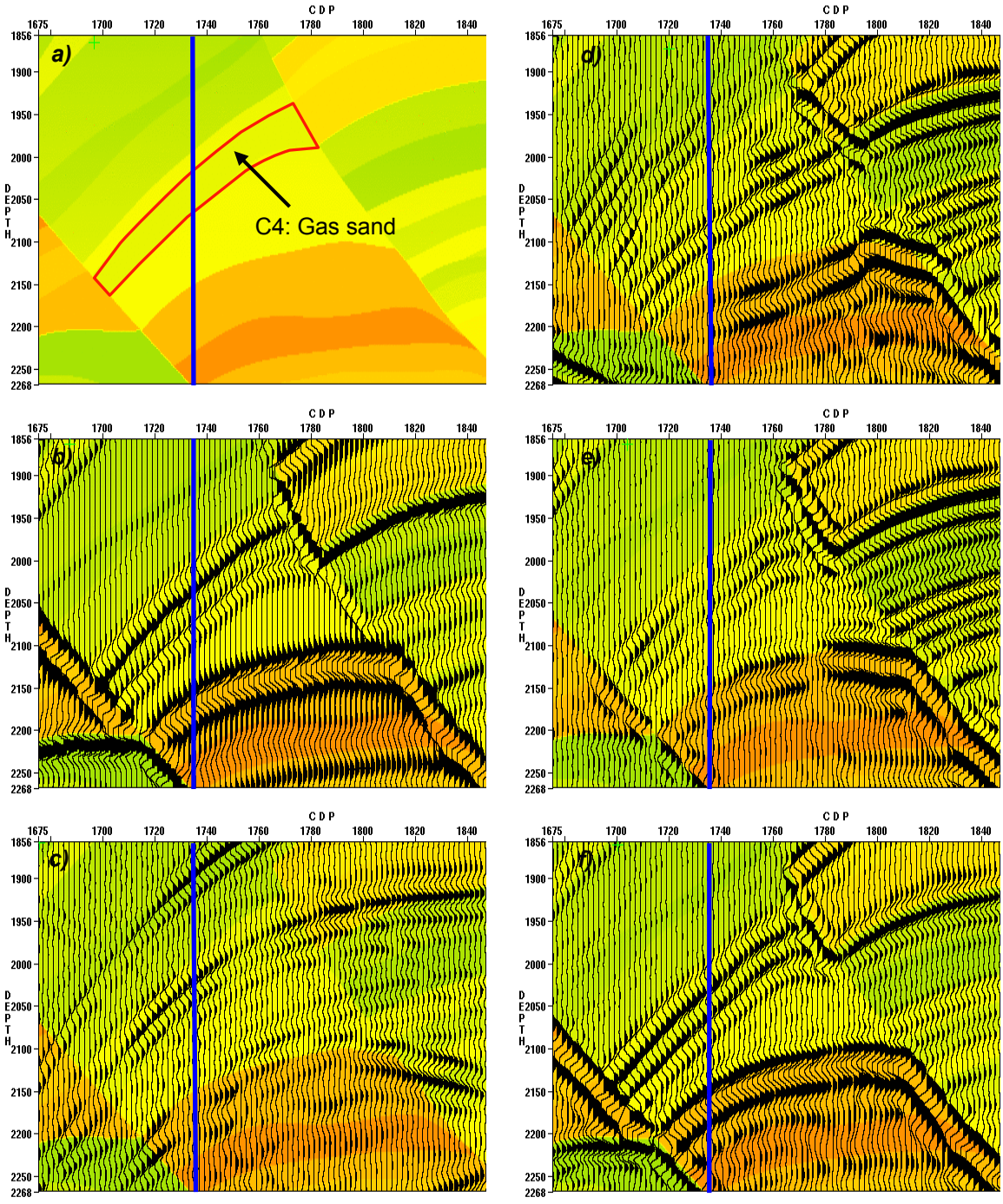

Figure 5.11. Hydrocarbon C4, depth cross sections. Vertical line shows placement of analysis at CDP 1735. a) velocity and cartoon of hydrocarbon, b) vertical synthetic section, c) NMO stack, d) Kirchhoff prestack time migration, e) Kirchhoff prestack depth migration, f) wavefield prestack depth migration.

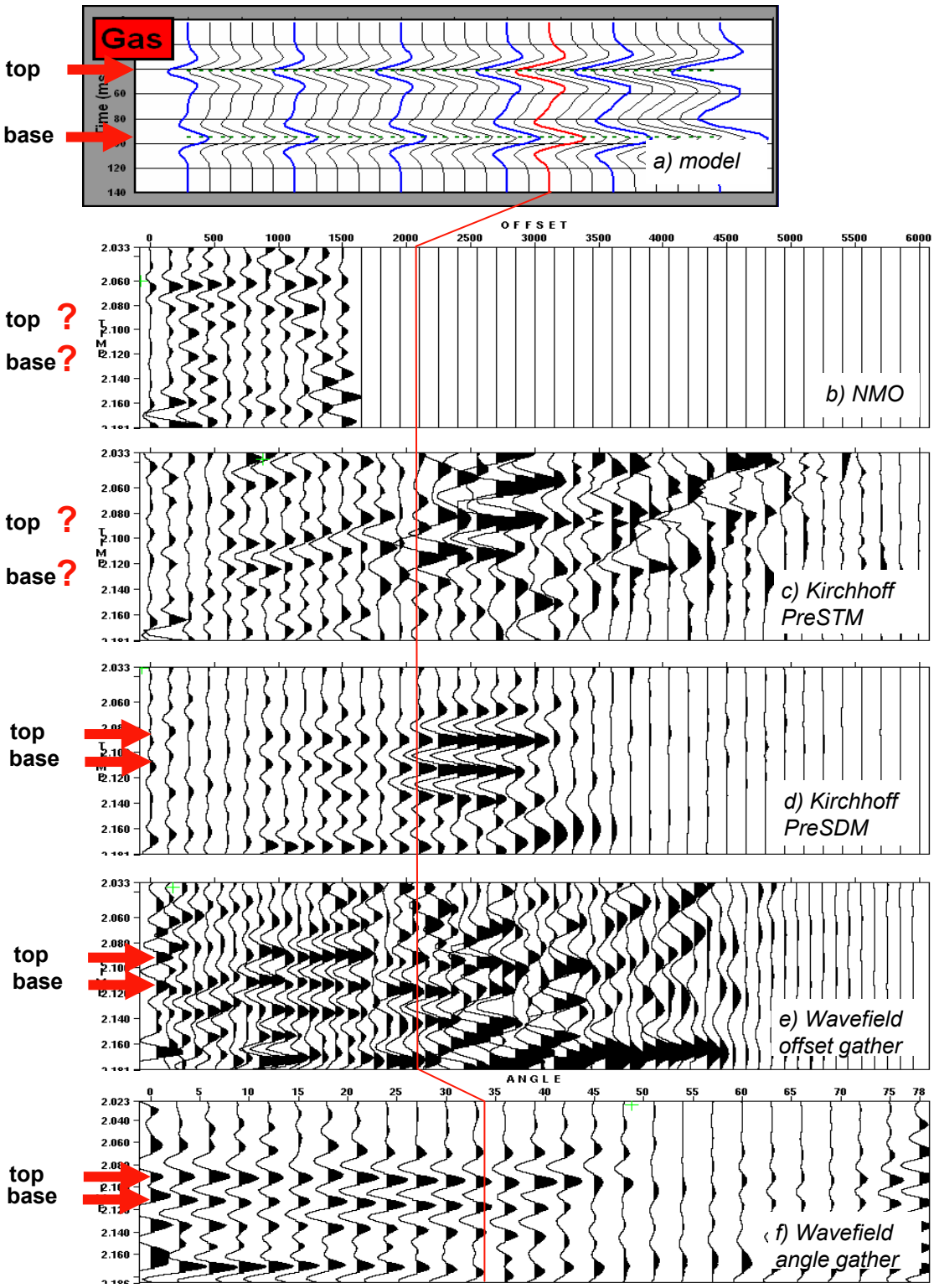

Figure 5.12. Analysis of AVO response for hydrocarbon C4 at CDP 1735. a) synthetic response, b) NMO gathers, c) Kirchhoff PreSTM image gathers, d) Kirchhoff PreSDM image gathers, e) wavefield PreSDM image gathers, f) wavefield PreSDM angle gathers. Offset=depth is indicated by the red line.

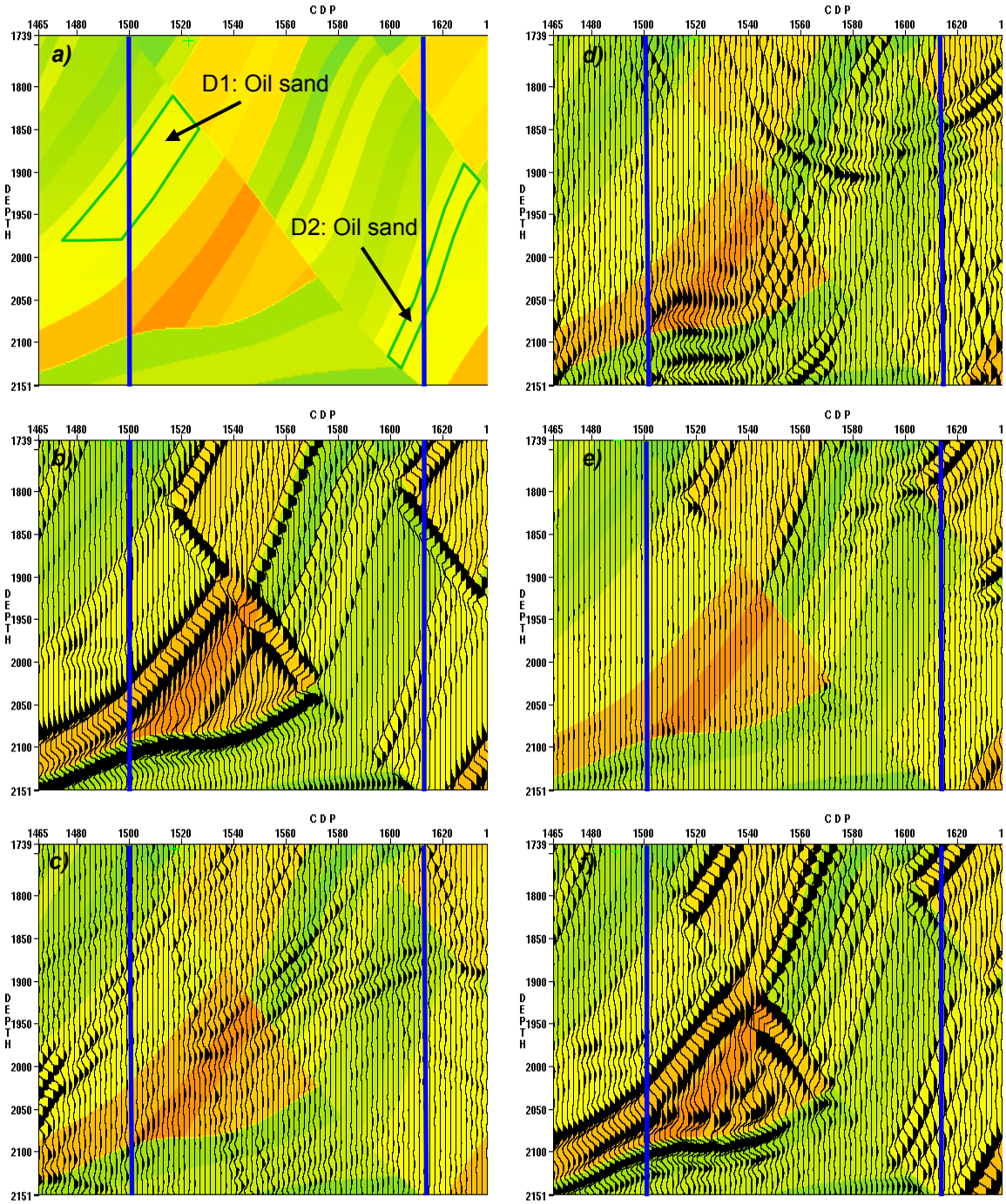

Figure 5.13. Hydrocarbon D1 and D2, depth cross sections. Vertical line shows placement of analysis at CDPs 1500 and 1614. a) velocity and cartoon of hydrocarbon, b) vertical synthetic section, c) NMO stack, d) Kirchhoff prestack time migration, e) Kirchhoff prestack depth migration, f) wavefield prestack depth migration.

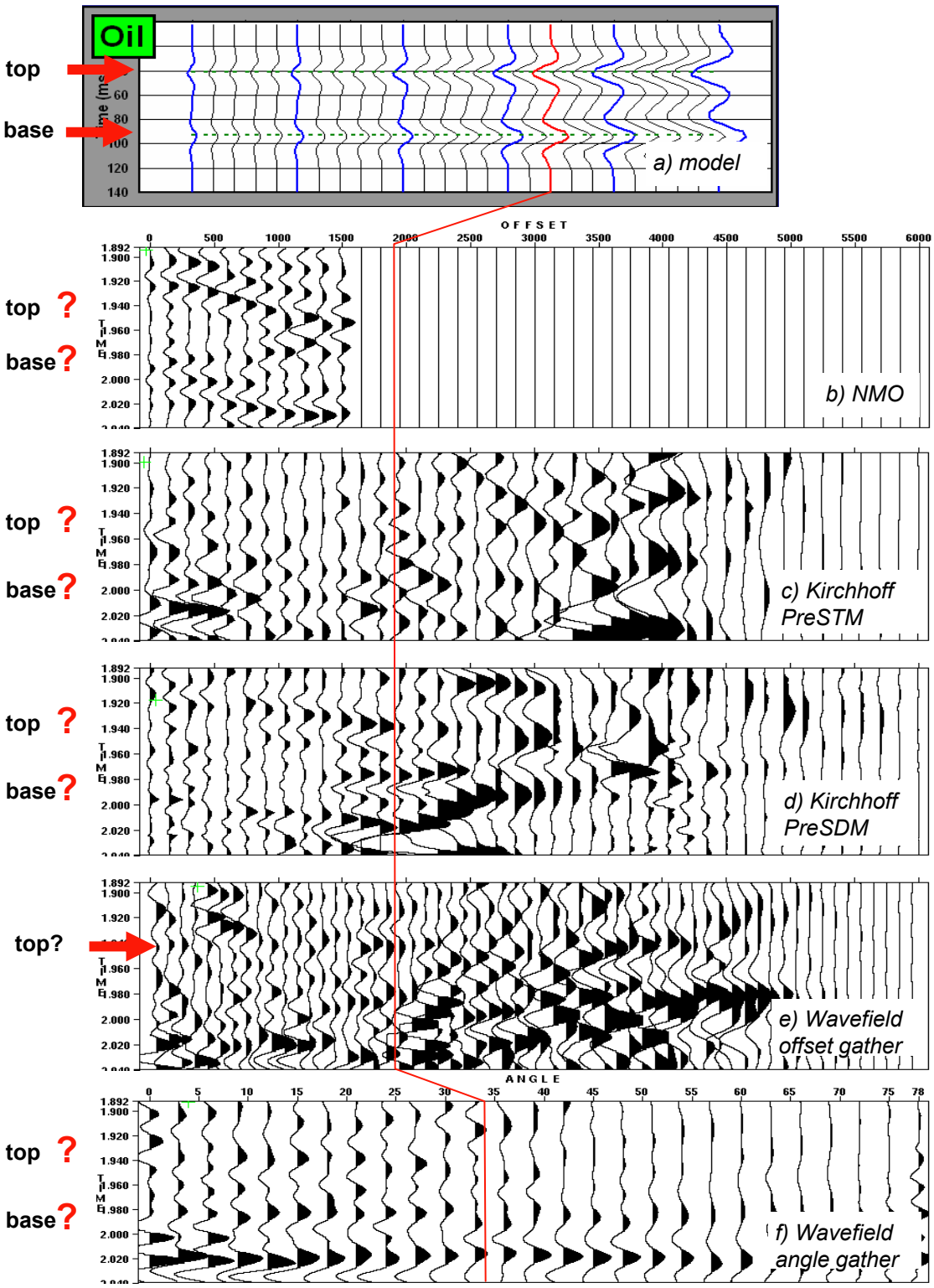

Figure 5.14. Analysis of AVO response for hydrocarbon D1 at CDP 1500. a) synthetic response, b) NMO gathers, c) Kirchhoff PreSTM image gathers, d) Kirchhoff PreSDM image gathers, e) wavefield PreSDM image gathers, f) wavefield PreSDM angle gathers. Offset~depth is indicated by the red line.

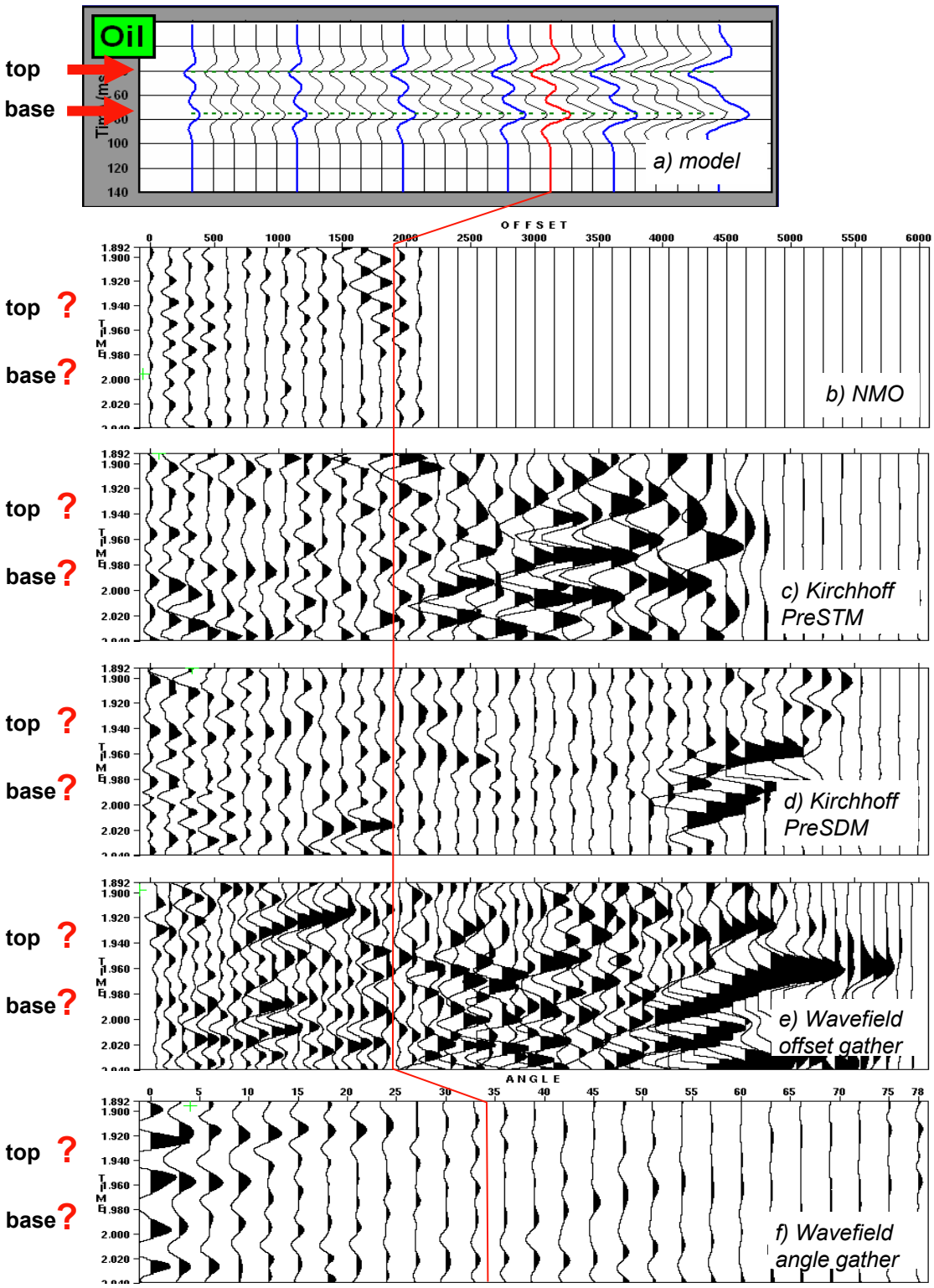

Figure 5.15. Analysis of AVO response for hydrocarbon D2 at CDP 1614. a) synthetic response, b) NMO gathers, c) Kirchhoff PreSTM image gathers, d) Kirchhoff PreSDM image gathers, e) wavefield PreSDM image gathers, f) wavefield PreSDM angle gathers. Offset~depth is indicated by the red line.

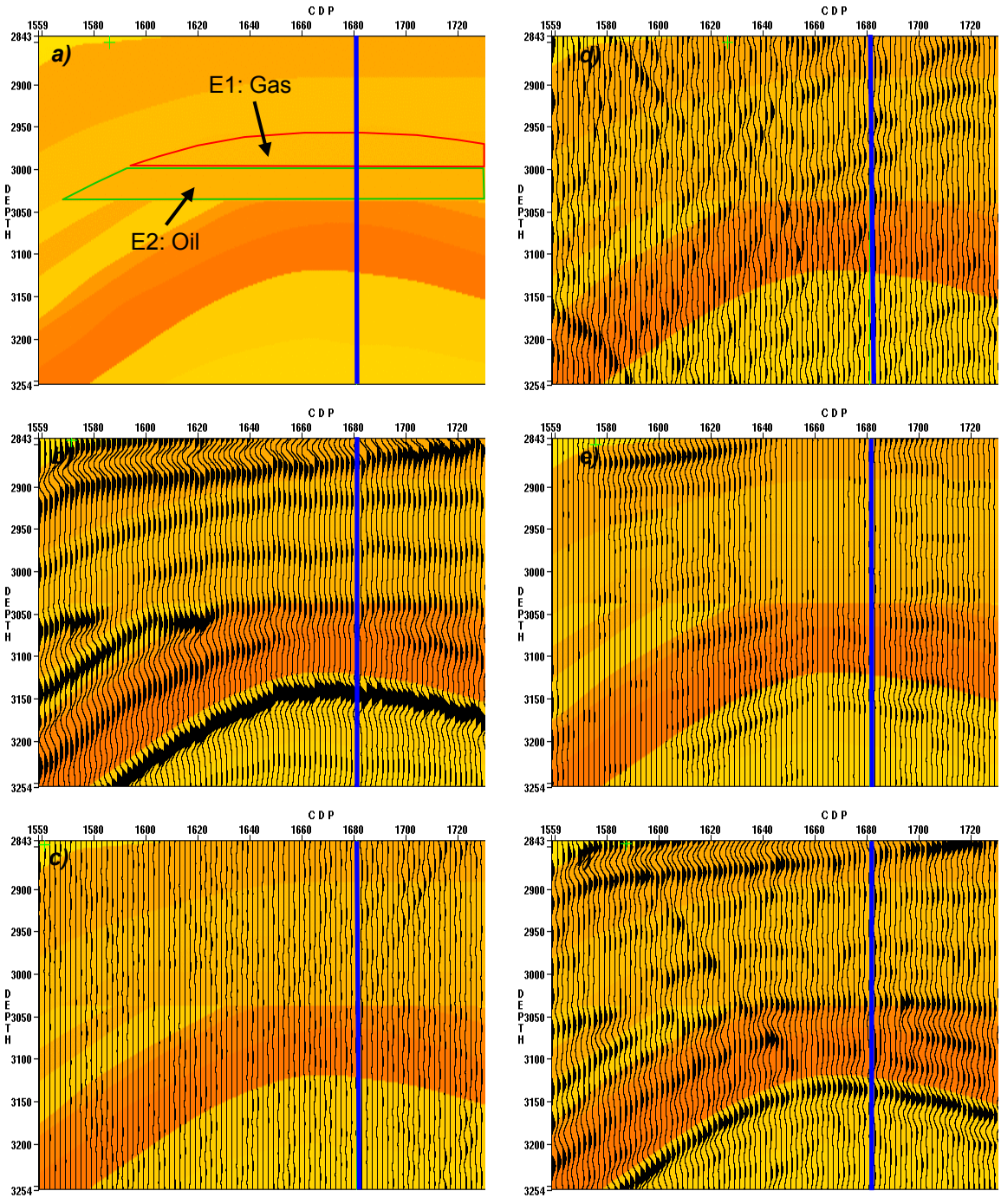

Figure 5.16. Hydrocarbon E1 and E2, depth cross sections. Vertical line shows placement of analysis at CDP 1681. a) velocity and cartoon of hydrocarbon, b) vertical synthetic section, c) NMO stack, d) Kirchhoff prestack time migration, e) Kirchhoff prestack depth migration, f) wavefield prestack depth migration.

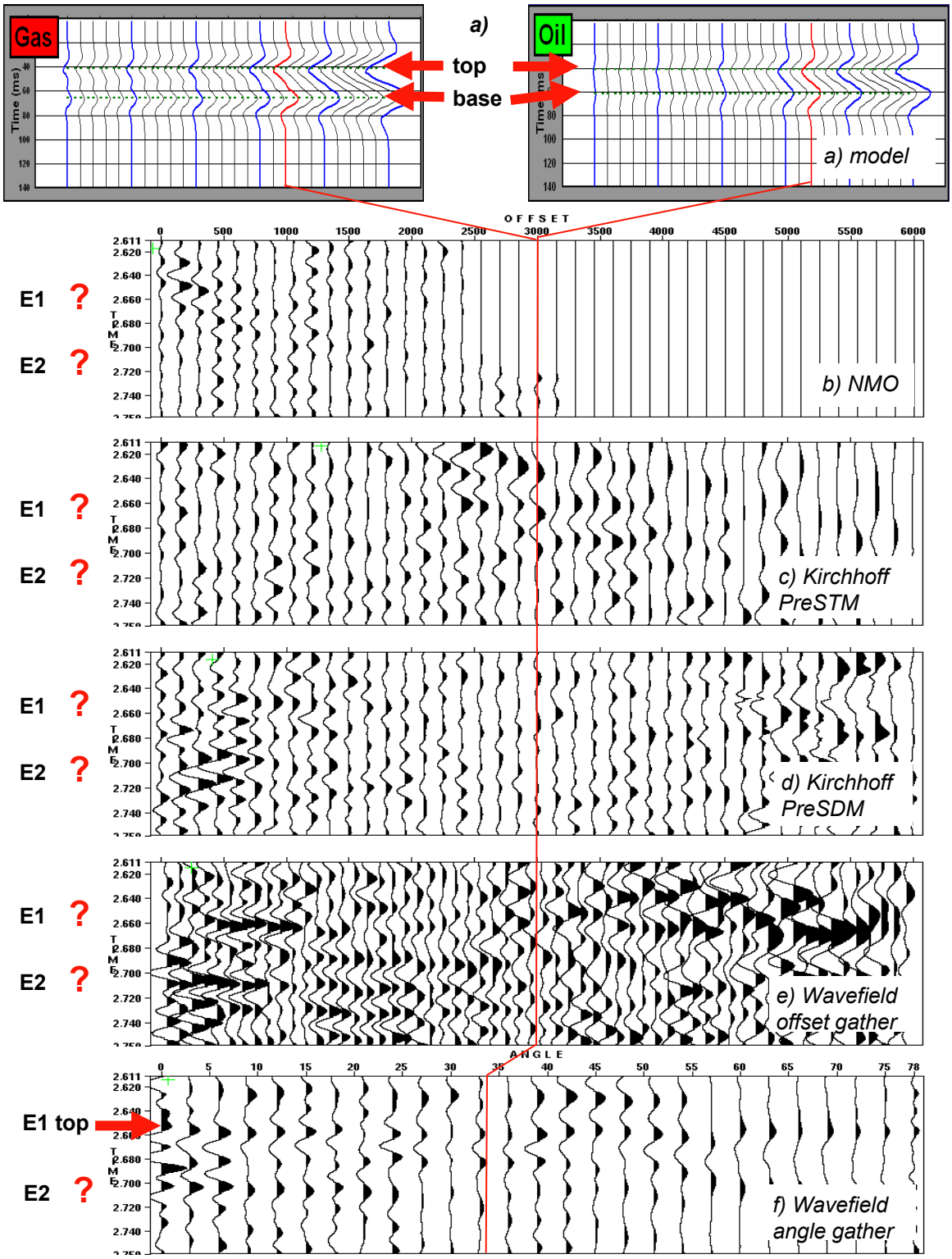

Figure 5.17. Analysis of AVO response for hydrocarbon E1 and E2 at CDP 1681. a) synthetic response, b) NMO gathers, c) Kirchhoff PreSTM image gathers, d) Kirchhoff PreSDM image gathers, e) wavefield PreSDM image gathers, f) wavefield PreSDM angle gathers. Offset=depth is indicated by the red line.

6. Conclusion

I have created an updated 2D fully elastic extension of the Marmousi model for the calibration of velocity analysis, seismic imaging, AVO, and inversion for the geophysical research community at large. The new model is named Marmousi2 and maintains the structure and velocity variations present in the original model. The new model is almost twice the initial length, and is buried under 450m of water, and 55m of soft sediments. The added structure on both sides of the model is relatively simple, and does not contain complexity comparable to the central portion. Similar to the original, Marmousi2 contains hundreds of individually defined horizons, which define the layers of varying physical properties. I retained the P-wave velocity of the original model, except for the salt, which has a new velocity of 4500m/s. The S-wave velocity and density for each layer were defined using industry standard transforms, and by assigning lithologies to the model. I added ten hydrocarbon units of varying size, shape, and hydrocarbon content in locations of varying structural and imaging complexity. I applied fluid substitution methods to ensure that the hydrocarbon saturated rock properties were realistic.

Elastic finite difference 2D modeling was performed using Sun Microsystems' Geoscience Center of Excellence at the University of Houston. The modeling utilized 20 clustered Solaris computers, and consumed some 5 months of calendar time. The modeling was performed with a high frequency wavelet (up to 80Hz), which, associated with the low shear wave velocities, required a very small computational grid size (1.25m) in order to avoid numerical problems. Using finite difference approaches enabled the simultaneous acquisition on different surfaces with different receiver types. A surface

streamer (hydrophone only) dataset, an OBC multi-component dataset, a VSP multi-component dataset, and wavefront snapshots (for both P-waves and S-waves) were created. Analysis of the raw records shows that the datasets are indeed high fidelity, high frequency datasets.

The model and data should be suitable for many types of geophysical research and testing including; conventional imaging, velocity estimation, AVO calibration, multi-component imaging, VSP calibration, multiple suppression, *etc.* The major limitation is that the data are 2D. The Marmousi2 model and synthetic data have already been made available to many researchers throughout the world. A web site is currently being constructed to host the information and data related to Marmousi2.

To form a benchmark, and as the first step towards the actual use of the Marmousi2 model, I have processed and imaged the marine streamer subset using state of the art algorithms available to me at GX Technology. I leave it to my colleagues at UH, GXT, and the industry at large to exploit the value of the multi-component or VSP data.

I applied a simple geometry assignment, datum corrections, and multiple attenuation as pre-processing steps before imaging. Multiple attenuation is very important since it affects the ability to interpret the geology. I used a S.R.M.E. technique which performed very well on Marmousi2, removing almost all traces of the free surface multiples. The performance is degraded at the edges of the data, since the technique is data driven, and in this case an artifact has been added to the data. More careful QC and parameterization should remove this anomaly.

A suite of imaging methods were applied to the data; simple NMO and stacking, Kirchhoff poststack time and depth migration, Kirchhoff prestack time and depth imaging, and wave-equation prestack depth migration. I calibrated the images with a simple synthetic in order to ascertain the quality of the results. The imaging examples indicate that the choice of an appropriate imaging method is very important to achieve an interpretable result. In particular, to obtain an image of the whole section, prestack depth imaging is necessary. Typically, more rigorous algorithms produce better results, with a higher cost in terms of compute time. For Marmousi2 the shot profile wave-equation prestack depth migration produced the best image. No decimation was used, and the imaging grid size was small compared to typical surveys. This allowed excellent imaging of the shallow, high frequency data, including the fault planes, as well as the deep complex structure. A key element that has been overlooked in terms of grading the result is velocity. For this synthetic study, the velocity is precisely known, and this can be used to obtain very good imaging with most algorithms. Small and medium size perturbations from the exact model may lead to different conclusions in terms of the best imaging solution, but this was not tested in the study.

Despite generally good imaging results, the identification of the hydrocarbon bodies may be difficult. This is especially true of the hydrocarbons located in the central complex zone, whether the hydrocarbons are small, thin, and steeply dipping, or if they are deeper, with minor acoustic impedance contrasts. As the level of the complexity increases, more rigorous imaging methods are required. Some of the hydrocarbons were only imaged by the wavefield method.

Imaging and AVO are inextricably linked. In areas of mild to complex structure simple NMO and stacking will not image the events and AVO analysis is impossible. In

these areas, prestack migrations are required. Poorly imaged events on the stacked section typically do not have amplitude distributions on the image gathers that are entirely reliable, and therefore the analysis of these gathers for the identification of AVO anomalies is questionable. Generally, the depth migrated gathers are more reliable in areas of complex velocity. The time migrated gathers are not as flat as the depth gathers, even using the perfect velocity model, and may require additional residual flattening before performing AVO analysis. The wavefield migration gathers appear to have the greatest continuity of amplitude across the gathers, although in this case the AVO effect is not preserved by the algorithm. The Kirchhoff prestack migration methods contain the AVO information, and the gathers are generally useful for exploration for hydrocarbons.

The preliminary imaging and AVO analysis I have performed will serve as the 'baseline' for forthcoming studies by other researchers. I sincerely hope that others may find this data useful. Certainly there are a large number of possibilities for future work.

References

Alkhalifah, T., 2000, Prestack phase-shift migration of separate offsets, Geophysics, **65**, 1179-1194.

Berkhout, A.J., and Verschuur, D.J., 1997, Estimation of multiple scattering by iterative inversion, Part I: Theoretical considerations, Geophysics, **62**, 1586-1595.

Bishop, K., Keliher, K., Paffenholz, J., Stoughton, D., Mitchell, S., Ergas, R., and Hadidi, M., 2001, Investigation of vendor demultiple technology for complex subsalt geology, Society of Exploration Geophysics, Expanded Abstracts.

Castagna, J.P., and Backus, M.M., eds., 1993, Offset-dependent reflectivity – Theory and practice of AVO anomalies, Society of Exploration Geophysics. Investigations in Geophysics no. **8.**

Castagna, J.P., Batzle, M.L., and Kan, T.K., 1993, Rock Physics – The link between rock properties and AVO response: *in* Castagna, J.P., and Backus, M.M., eds., Offset-dependent reflectivity – Theory and practice of AVO anomalies, Society of Exploration Geophysics. Investigations in Geophysics no. **8**, 135-171.

Claerbout, J.F., and Doherty, S.M., 1972, Downward continuation of moveout corrected seismograms, Geophysics, **37**, 741-768.

Clayton, R. W., and Engquist, B., 1990, Absorbing boundary conditions for acoustic and elastic wave equations, *in* Kelly, K. R., and Marfurt, K. J., Eds., Numerical modeling of seismic wave propagation, **13**: Soc. of Expl. Geophys., 448-459. (* Reprinted from Bulletin of the Seismological Society of America, Volume 67:6, 1529-1540).

Ehinger, A., Lailly, P., and Marfurt, K.J., 1996, Green's function implementation of common-offset, wave-equation migration, Geophysics, **61**, 1813-1821.

Fagin, S., 1999, Model-based depth imaging, Society of Exploration Geophysics. SEG course notes series, No.**10**.

Gray, S.H., Etgen, J., Dellinger, J., and Whitmore, D., 2001, Y2K review article. Seismic migration problems and solutions, Geophysics, **66**, 1622-1640.

Greenburg, M.L., and Castagna, J.P., 1992, Shear-wave velocity estimation in porous rocks: Theoretical formulation, preliminary verification and applications, Geophysical Prospecting, **40**, 195-210.

Hill, R.W., 1952, The elastic behavior of crystalline aggregate, Proceedings of the Physical Society, London, **A65**, 349-354.

Hill, N.R., 2001, Prestack Gaussian-beam migration, Geophysics, **66**, 1240-1250.

Hilterman, F.J., 2001, Seismic amplitude interpretation, Society of Exploration Geophysics. SEG distinguished instructor short course, No.**4**.

House, L., Fehler, M., Aminzadeh, F., Barhen, J. and Larson, S., 1996, A national laboratory-industry collaboration to use the SEG/EAEG model data sets: The Leading Edge, **15**, 135-136.

Larsen, S., and J. Grieger, 1998, Elastic modeling initiative, Part III: 3-D computational modeling, Society of Exploration Geophysicists. Expanded Abstracts., **68**, 1803-1806.

Levander, A. R., 1988, Fourth-order finite-difference P-SV seismograms, Geophysics, **53**, 1425-1436.

Ogilvie, J. S., and G. W. Purnell, 1996, Effects of salt-related mode conversions on subsalt prospecting, Geophysics, **61**, 331-348.

Ostrander, W.J., 1982, Plane wave reflection coefficients for gas sands at nonnormal angles of incidence, Geophysics, **49**, 1637-1648.

Schneider, W., 1978, Integral formulation for migration in two and three dimensions, Geophysics, **43**, 49-76.

Versteeg, R., 1994, The Marmousi experience: Velocity model determination on a synthetic complex data set, The Leading Edge, **13**, 927-936.

Verschuur, D. J., Berkhout, A. J., and Wapenaar, C.P.A., 1992, Adaptive surface-related multiple elimination, Geophysics, **57**, 1166-1177.

Verschuur, D.J., and Berkhout, 1997, Estimation of multiple scattering by iterative inversion, Part II: Practical aspects and examples, Geophysics,**62**, 1596-1611

Zhu, J., and Lines, L.R., 1998, Comparison of Kirchhoff and reverse-time migration methods with applications to prestack depth imaging of complex structures, Geophysics, **63**, 1166-1176.

Zoeppritz, K., 1919, Erdbebenwellen VIIIB, On the reflection and propagation of seismic waves: Gottinger Nachrichten, **I**, 66-84.